

University of Warwick institutional repository: <http://go.warwick.ac.uk/wrap>

**A Thesis Submitted for the Degree of PhD at the University of Warwick**

<http://go.warwick.ac.uk/wrap/76173>

This thesis is made available online and is protected by original copyright.

Please scroll down to view the document itself.

Please refer to the repository record for this item for information to help you to cite it. Our policy information is available from the repository home page.

# **Photoactivatable Ru(II) polypyridyl complexes as antibacterial agents**

by

Nichola Ann Smith, *M.Chem.*

A thesis submitted for the degree of Doctor of  
Philosophy

University of Warwick  
Department of Chemistry  
September 2015

# Contents

Acknowledgments	i
Declaration	ii
Abstract	iii
Abbreviations	v
Publications	vii
Conferences attended	viii
<b>Chapter 1. Introduction</b>	<b>1</b>
1.1. Bacterial infections	2
1.1.1. Bacterial resistance	3
1.1.2. Tuberculosis	4
1.2. Metals in medicine	7
1.2.1. Ruthenium	8
1.2.1.1. Antibacterial	10
1.2.1.2. Tuberculosis	11
1.2.2. Other metals	12
1.3. Photoactive metal complexes	13
1.3.1. Photochemistry	13
1.3.2. Electronic transitions and deactivation pathways	14
1.3.3. Photochemistry of Ru(II) complexes	18
1.4. Photoactive metal complexes in medicine	20
1.4.1. Photodynamic therapy	20
1.4.1.1. Role of metal complexes n PDT	22
1.4.2. Meal complexes in photochemotherapy	23
1.4.2.1. Photorelease of bioactive ligands	24
1.4.2.2. Imaging	27
1.4.2.3. Interaction with DNA	27
1.4.3. Importance of wavelength of activation	29
1.4.3.1. Ligand modification	30
1.4.3.2. Two-photon activation	31
1.4.3.3. Upconverting nanoparticles	32
1.5. Aims	33

1.6. References	33
<b>Chapter 2. Experimental methods and materials</b>	44
2.1. NMR spectroscopy	45
2.2. X-ray crystallography	45
2.3. Elemental analysis	46
2.4. Light sources	46
2.4.1. KiloArc <sup>TM</sup> lamp	46
2.4.2. Blue LED	48
2.4.3. 96-array blue LED	49
2.4.4. 32-array multi-coloured LED	49
2.4.5. Laser set-up	50
2.4.5.1. One-photon transient absorption spectroscopy	51
2.4.5.2. Two-photon transient absorption spectroscopy	51
2.4.5.3. Two-photon absorption spectroscopy	52
2.5. Electrospray ionisation mass spectrometry (ESI-MS)	52
2.6. High resolution electrospray mass spectrometry (HR-MS)	53
2.7. Liquid chromatography-high resolution mass spectrometry (LC-HRMS)	53
2.8. Liquid chromatography-mass spectrometry (LC-MS)	54
2.9. High performance liquid chromatography (HPLC)	54
2.10. UV-visible absorption spectroscopy	55
2.11. Microplate reader	55
2.12. Synthesis of starting materials	56
2.13. References	58
<b>Chapter 3. Synthesis, characterisation and dark solution chemistry of Ru(II) polypyridyl complexes</b>	60
3.1. Introduction	61
3.2. Experimental	62
3.2.1. Materials	62
3.2.2. Preparation of Ru(II) polypyridyl halide complexes	63
3.2.3. Preparation of Ru(II) polypyridyl bis-substituted complexes	65



3.2.4. X-ray crystallography	68
3.2.5. Dark stability in aqueous solution	68
3.2.5.1. Hydrolysis of Ru(II) polypyridyl halide complexes	68
3.2.5.2. Stability of Ru(II) polypyridyl bis-substituted complexes	68
3.2.6. Dynamic behaviour in solution	69
3.2.6.1. Dynamic behaviour studied by variable temperature <sup>1</sup> H-NMR	69
3.2.6.2. Solvent effect on dynamic behaviour studied by <sup>1</sup> H-NMR	70
3.2.6.3. Dynamic behaviour studied by DFT	70
3.3 Results	71
3.3.1. Synthesis and characterisation	71
3.3.2. X-Ray crystal structures	74
3.3.3. Dark stability in aqueous solution	81
3.3.3.1. Hydrolysis of Ru(II) polypyridyl halide complexes	81
3.3.3.2. Stability of Ru(II) polypyridyl bis-substituted complexes	84
3.3.4. Dynamic behaviour in solution	85
3.3.4.1. Dynamic behaviour studied by variable temperature <sup>1</sup> H-NMR	86
3.3.4.2. Solvent effect on dynamic behaviour studied by <sup>1</sup> H-NMR	93
3.3.4.3. Dynamic behaviour studied by DFT	95
3.4. Discussion	99
3.4.1. Synthesis and characterisation	99
3.4.2. X-Ray crystal structures	101
3.4.3. Dark stability in aqueous solution	102
3.4.4. Dynamic behaviour in solution	104
3.5. Summary	108
3.6. References	109
 <b>Chapter 4. Photochemical and photophysical properties of Ru(II) polypyridyl complexes</b>	 114
4.1. Introduction	115
4.2. Experimental	116
4.2.1. Materials	116

4.2.2. Photoirradiation followed by UV-visible absorption spectroscopy	117
4.2.2.1. Wavelength dependence	117
4.2.2.2. Stability of photoproducts	117
4.2.3. Photoirradiation followed by LC-HRMS	118
4.2.4. Power dependence followed by LC-MS	118
4.2.5. Photoirradiation using 96-array blue LED followed by HPLC	118
4.2.6. Photoirradiation followed by <sup>1</sup> H-NMR spectroscopy	119
4.2.7. Emission properties	119
4.2.8. Computation analysis	119
4.2.9. Transient-absorption spectroscopy	120
4.3. Results	120
4.3.1. Photoirradiation followed by UV-visible spectroscopy	120
4.3.1.1. Wavelength dependence	124
4.3.1.2. Stability of photoproducts	125
4.3.2. Photoirradiation followed by LC-HRMS	126
4.3.3. Power dependence followed by LC-MS	129
4.3.4. Photoirradiation using 96-array blue LED followed by HPLC	133
4.3.5. Photoirradiation followed by <sup>1</sup> H-NMR	134
4.3.6. Emission properties	137
4.3.7. Computational analysis	138
4.3.7.1. Ground state (S <sub>0</sub> ) geometry	138
4.3.7.2. Ground state (S <sub>0</sub> ) molecular orbitals	140
4.3.7.3. Lowest-lying triplet state (T <sub>1</sub> ) geometry	143
4.3.7.4. Lowest-lying triplet state (T <sub>1</sub> ) molecular orbitals	144
4.3.7.5. Absorption spectra and singlet excited states	146
4.3.7.6. Triplet excited states	150
4.3.8. Transient-absorption spectroscopy	152
4.4. Discussion	156
4.4.1. Effect of solvent on the photorelease	156
4.4.2. Assessment of structure-active relationships	156
4.4.2.1. Qualitative assessment by DFT/TD-DFT	158
4.4.3. Wavelength dependence	161
4.4.4. Photochemical pathways	161

4.4.5. Ultrafast studies	163
4.5. Summary	163
4.6. References	164
<b>Chapter 5. Photobiological properties of Ru(II) polypyridyl complexes</b>	168
5.1. Introduction	169
5.2. Experimental	170
5.2.1. Materials	170
5.2.3. Photoirradiation in the presence of 9-ethylguanine and L-cysteine	171
5.2.4. Photoactivity against <i>B. subtilis</i> and <i>E. coli</i>	171
5.2.5. Photoactivity against <i>M. smegmatis</i>	172
5.2.5.1. Photoirradiation using the 96-array blue LED	172
5.2.5.2. Photoirradiation using the 32-array multi-coloured LED	173
5.2.6. BacLight™ assay with <i>M. smegmatis</i>	173
5.3. Results	174
5.3.1. Design of 96-array blue LED	174
5.3.2. Photoirradiation in the presence of 9-ethylguanine and L-cysteine	177
5.3.3. Photoactivity against <i>B. subtilis</i> and <i>E. coli</i>	181
5.3.4. Photoactivity against <i>M. smegmatis</i>	182
5.3.4.1. Photoirradiation using the 96-array blue LED	182
5.3.4.2. Photoirradiation using the 32-array multi-coloured LED	185
5.3.5. BacLight™ assay with <i>M. smegmatis</i>	187
5.4. Discussion	189
5.4.1. Light sources	189
5.4.2. Photoirradiation in the presence of 9-ethylguanine and L-cysteine	190
5.4.3. Photoactivity against <i>E. coli</i> and <i>B. subtilis</i>	193
5.4.4. Photoactivity against <i>M. smegmatis</i>	194
5.4.4.1. Effect of blue light alone on survival of <i>M. smegmatis</i>	194
5.4.4.2. Photoactivity of complexes against <i>M. smegmatis</i>	195
5.4.4.3. BacLight™ assay	197
5.5. Summary	198
5.6. References	199

<b>Chapter 6. Extending photoactivation of Ru(II) polypyridyl complexes into the phototherapeutic window</b>	203
6.1. Introduction	204
6.2. Experimental	206
6.2.1. Materials	206
6.2.2. Preparation of MOPEP	206
6.2.3. Preparation of <i>cis</i> -[Ru(bpy) <sub>2</sub> (MOPEP) <sub>2</sub> ][PF <sub>6</sub> ] <sub>2</sub>	207
6.2.4. Preparation of <i>cis</i> -[Ru(bpy) <sub>2</sub> (py) <sub>2</sub> ][PF <sub>6</sub> ] <sub>2</sub>	207
6.2.5. Photoirradiation using non-laser light source	208
6.2.6. Photoirradiation using laser light source	208
6.2.7. Interaction with DNA	209
6.3. Results	210
6.3.1. Photoirradiation using non-laser light source	210
6.3.2. Photoirradiation using laser light source	214
6.3.3. Interaction with DNA	215
6.4. Discussion	216
6.4.1. Two-photon activation	216
6.4.2. Interaction with DNA	219
6.5. Summary	220
6.6. References	220
 <b>Chapter 7. Conclusions and future work</b>	 222
7.1. Conclusions	223
7.2. Future work	226
7.2.1. Addition of an antibacterial scaffold	226
7.2.2. Addition of red-light shifting moieties to the chelating scaffold	227
7.2.3. Further biological testing	229
7.2.4. Affecting the NADH/NAD <sup>+</sup> ratio with photoactive ruthenium(II) complexes	230
7.5. References	232

## **Acknowledgements**

Firstly, I would like to thank Professor Peter J. Sadler for giving me the opportunity to carry out my PhD in his research group, and for his supervision and guidance throughout. It has been a pleasure to work with such brilliant scientists, and I am thankful for all the fantastic opportunities I have had.

For financial support I would like to thank the Engineering and Physical Sciences Research Council (EPSRC).

I would like to thank Dr Ivan Prokes for help with NMR spectroscopy, Dr Lijang Song and Mr Phil Aston for their help with mass spectrometry, Dr Guy Clarkson for X-ray crystallography, Mrs Anne Smith, Mr Daniel McFeely and Professor Christopher Dowson for their help with the bacteria experiments, Dr Luca Salassa and Dr Giovanni Salassa for their help and guidance with calculations, Dr Vas Stavros, Dr Ed Greenough and Mr Mitch Horbury for their transient-absorption work, Mr Nick Barker for the thoroughly enjoyable Outreach opportunities and Mr Rod Wesson for his amazing light source skills!

A special thank you to everyone in the PJS group past and present. It has been a special 4 years to be able to go to work and be around friends that support you, guide you and most of all keep a big smile on your face though the ups and downs of a PhD. Thanks to Jess (and Ziga of course) for the one and only amazing karaoke session, thanks to Evyenia and Joan for your support and for always making me laugh, and thanks to the C409 crew past (Adam, Ziga, Evyenia and Nicolas) and present (Joan, Isolda, Carlos and Russell) for being so fun and awesome. I will miss you all!

Finally, I would like to thank my family, my parents and Chris for their unconditional love and support. Thank you so much for always being there for me, you are the best!

## **Declaration**

I hereby declare that except where specific reference is made to other sources, the work contained in the Thesis is the original work of the author. It has been composed by myself and has not been submitted, in whole or in part, for any other degree, diploma, or other qualification.

Nichola Ann Smith

June 2015

## Abstract

Novel photoactive ruthenium(II) complexes were designed to incorporate existing anti-tuberculosis drugs, isoniazid and nicotinamide, that could be released from the ruthenium(II) cage by photoactivation with visible light.

Two sets of complexes were synthesised based on *cis*-[Ru(*N-N'*)<sub>2</sub>(L)<sub>2</sub>][PF<sub>6</sub>]<sub>2</sub> and *cis*-[Ru(*N-N'*)<sub>2</sub>(L)X][PF<sub>6</sub>], where *N-N'* is 2,2'-bipyridine (bpy) or 1,10-phenanthroline (phen), L is isoniazid (INH) or nicotinamide (NA) and X is either Cl or I. Their dynamic behaviour in solution was explored using NMR to probe the presence of atropisomers. In the case of *cis*-[Ru(bpy)<sub>2</sub>(NA)Cl][PF<sub>6</sub>] (**1**) and *cis*-[Ru(bpy)<sub>2</sub>(NA)I][PF<sub>6</sub>] (**2**), the rotation of NA is hindered on the NMR timescale at room temperature, behaviour that was surprisingly not observed for *cis*-[Ru(bpy)<sub>2</sub>(NA)<sub>2</sub>][PF<sub>6</sub>]<sub>2</sub> (**5**). The hindered rotation was explored by computational methods (DFT) and revealed that hydrogen bonding between the halide and protons of the NA ligand hindered the rotation.

The photochemical properties of the Ru(II) complexes were explored by UV-visible spectroscopy and liquid chromatography. All *cis*-[Ru(*N-N'*)<sub>2</sub>(L)<sub>2</sub>][PF<sub>6</sub>]<sub>2</sub> complexes in aqueous solution release one ligand, L, in under 1 min using a blue LED ( $\lambda_{\text{irr}} = 463$  nm, 50 mW cm<sup>-2</sup>) to form the photoproduct *cis*-[Ru(*N-N'*)<sub>2</sub>(L)(H<sub>2</sub>O)]<sup>2+</sup>. Continued photoirradiation releases a second ligand, L, with the production of various Ru(II) and Ru(III) aqua photoproducts (with both *cis* and *trans* geometry). Interestingly their production was dependent on the power of the light source. Complementary computational studies (DFT/TD-DFT) were utilised to understand structure-activity relationships with respect to photoactivity. The results from the calculations suggest that the number of key electronic transitions (notably <sup>1</sup>MLCT) and the favourable

leaving properties of the ligand, L, influence the rate of photorelease. In the latter case, a stronger  $\pi$ -accepting leaving ligand shifts the dissociative  $^3\text{MC}$  state to lower energy, thus promoting more efficient ligand release.

The photobiological properties of the Ru(II) complexes were explored by investigating binding to biomolecules and screening their antibacterial activity *in vitro*. The complex *cis*-[Ru(bpy)<sub>2</sub>(INH)<sub>2</sub>][PF<sub>6</sub>]<sub>2</sub> (**4**) binds to the nucleobase 9-ethylguanine (9-EtG) after photoirradiation with a blue LED to produce *cis*-[Ru(bpy)<sub>2</sub>(INH)(9-EtG)]<sup>2+</sup>, however reaction with the amino acid L-cysteine was not observed. A 96-array blue LED ( $\lambda_{\text{irr}} = 465 \text{ nm}$ , 20 mW cm<sup>-2</sup>) and 32-array multi-coloured LED ( $\lambda_{\text{irr}} = 465 \text{ nm}$ , 520 nm, 589 nm and 625 nm, 5 mW cm<sup>-2</sup>) were designed in-house to screen the activity of the complexes *in vitro*. Their design and construction is described in detail. When tested against *Mycobacterium smegmatis* (a model for *Mycobacterium tuberculosis*), complexes *cis*-[Ru(bpy)<sub>2</sub>(INH)<sub>2</sub>][PF<sub>6</sub>]<sub>2</sub> (**4**) and *cis*-[Ru(phen)<sub>2</sub>(INH)<sub>2</sub>][PF<sub>6</sub>]<sub>2</sub> (**6**) showed the greatest activity upon photoirradiation for 1 min with a blue LED, with at least a 3x increase in potency when compared to the ligand alone, INH. Most importantly the complexes are inactive in the dark, showing that the antibacterial ligand is selectively released *in vitro* after photoirradiation.

The complex *cis*-[Ru(bpy)<sub>2</sub>(MOPEP)<sub>2</sub>][PF<sub>6</sub>]<sub>2</sub> (**9**), where MOPEP is 4-[2-(4-methoxyphenyl)ethynyl]pyridine, was initially designed to study two-photon activation via a femtosecond-pulsed laser. Surprisingly the complex was one-photon active with 600 nm and 800 nm light, due to the MOPEP ligand extending and increasing the intensity of the one-photon absorption band shoulder in the 600-800 nm region.



## Abbreviations

9-EtG	9-ethylguanine
Abs	Absorbance
Å	Angstrom
ACN	Acetonitrile
APT	Attached proton test
bpy	2,2'-bipyridine
COSY	Correlation spectroscopy
Cys	L-cysteine
DFT	Density functional theory
DMF	Dimethylformamide
DMSO	Dimethylsulfoxide
DNA	Deoxyribonucleic acid
ESI-MS	Electrospray ionisation mass spectrometry
FDA	US Food and Drug Administration
HOMO	Highest occupied molecular orbital
HPLC	High performance liquid chromatography
HR-MS	High-resolution mass spectrometry
HSQC	Heteronuclear single quantum coherence
IC	Internal conversion
INA	Isonicotinamide
INH	Isoniazid
ISC	Intersystem crossing
LC-HRMS	Liquid chromatography-high resolution mass spectrometry
LC-MS	Liquid chromatography-mass spectrometry
LED	Light emitting diode
LUMO	Lowest unoccupied molecular orbital
MC	Metal-centred
MIC	Minimum inhibitory concentration
MLCT	Metal-to-ligand charge transfer
MLLCT	Metal-ligand-to-ligand charge transfer
MOPEP	4-[2-(4-methoxyphenyl)ethynyl]pyridine

MS	Mass spectrometry
m/z	Mass/charge
NA	Nicotinamide
NADH	Reduced nicotinamide adenine dinucleotide
NAD <sup>+</sup>	Oxidised nicotinamide adenine dinucleotide
NMR	Nuclear magnetic resonance
NOSEY	Nuclear Overhauser effect spectroscopy
OD	Optical density
PBS	Phosphate-buffered saline
PDT	Photodynamic therapy
phen	1,10-phenanthroline
ppm	Parts per million
py	Pyridine
SOMO	Singly-occupied molecular orbital
TD-DFT	Time-dependent density functional theory
TFA	Trifluoroacetic acid
TPA	Two-photon activation
UV	Ultraviolet
UVA	Ultraviolet A

## Publications

Greenough, S.E., Roberts, G.M., Smith, N.A., Horbury, M.D., McKinlay, R.G., Zurek, J.M., Paterson, M.J., Sadler, P.J., Stavros, V.G. Ultrafast photo-induced ligand solvolysis of *cis*-[Ru(bipyridine)<sub>2</sub>(nicotinamide)<sub>2</sub>]<sup>2+</sup>: experimental and theoretical insight into its photoactivation mechanism. *Physical Chemistry Chemical Physics*, **2014**, 16, 19141-19155

Smith, N.A., Sadler, P.J. Photoactivatable metal complexes: from theory to applications in biotechnology and medicine. *Philosophical transactions. Series A, Mathematical, physical, and engineering sciences*, **2013**, 371(1995), 20120519, doi:10.1098/rsta.2012.0519

## Conferences attended

### *Metals in Biology: The Inorganic Chemistry of Life*

Gordon Research Conference, Ventura, California, USA, January **2015**.

Smith, N.A., McFeely, D., Dowson, C., Sadler, P.J. Photoactivatable antibiotics. (Poster and 5 min talk)

### *Dalton 2014*

University of Warwick, UK, April **2014**.

Smith, N.A., Sadler, P.J. Dynamic behaviour of photoactive ruthenium(II) polypyridyl complexes. (Poster)

### *Metallodrugs I: Design and mechanism of action*

Olomouc, Czech Republic, December **2012**.

Smith, N.A., Photoactivatable ruthenium(II) complexes. (25 min talk)

### *Photoactivatable metal complexes: exciting potential in biotechnology and medicine?*

The Royal Society at Chicheley Hall, Milton Keynes, UK, June **2012**.

### *Photoactivatable metal complexes: from theory to therapy*

The Royal Society, London, UK, June **2012**.

### *Inorganic Chemistry 2012: A joint meeting of Dalton Division Interests*

University of Warwick, UK, April **2012**.

### *Drug discovery: a job too complex for academia or industry alone?*

University of Oxford, UK, January **2012**.

# **Chapter 1**

## **Introduction**

---

## Chapter 1

### Introduction

The aim of this chapter is to introduce the issue of bacterial infections and particularly focus on the application of metals in medicine. Subsequent sections refer to photoactivation of metal complexes for biological applications and their clinical relevance. Throughout this chapter particular emphasis is placed on the applications of ruthenium complexes.

#### 1.1. Bacterial infections

Pathogenic bacteria can cause a variety of illnesses, for example *Mycobacterium tuberculosis* is responsible for tuberculosis (TB), *Escherichia coli* and *Staphylococcus aureus* can cause infections, while *Streptococcus pneumonia* can cause pneumonia. If the disease is not treated with antibiotics / antibacterial agents it can be fatal.

An antibiotic can be described as an antibacterial agent that is produced by a microorganism, while an antibacterial agent is any agent (either natural or synthetic) that is harmful to bacteria. The first antibiotic was discovered in 1928 by Alexander Fleming when he noticed that an agent, which he called penicillin, was produced by the fungus *Penicillium* and was able to inhibit the growth of *Staphylococcus* bacteria. Between the 1940's and 1960's many new classes of antibiotics were discovered by screening natural products for bacterial growth inhibition.<sup>1</sup> However, only two new major classes of antibiotics / antibacterials discovered in past 30 years are on the market (discovery of lipopeptides in 1986 and diarylquinolines in 1997), resulting in a large time gap in the discovery of new antibiotics / antibacterials.<sup>1-2</sup> This is a problem as the occurrence of bacterial resistance is increasing, which will be discussed in more detail in Section 1.1.1. The most recent finding was made in early 2015 when a new

class of antibiotic, Teixobactin, was discovered from a screen of uncultured bacteria from soil samples (provisionally called *Eleftheria terrae*); Teixobactin showed activity against *S. aureus* (including methicillin-resistant *S. aureus*, MRSA) and *M. tuberculosis*.<sup>3</sup>

### 1.1.1. Bacterial resistance

Bacterial resistance has been a growing threat for several decades, with national data showing that the proportion of *E. coli*, *K. pneumoniae* and *S. aureus* resistant to commonly used antibacterial agents is > 50 % in many cases.<sup>4</sup>

There are four major mechanisms of action for antibacterial agents; 1) cell wall / cytoplasmic membrane synthesis inhibition, 2) protein synthesis inhibition, 3) nucleic acid synthesis inhibition, and 4) inhibition of metabolic pathways.<sup>5-6</sup> Resistance to such antibacterial agents is either intrinsic / natural (for example where a microorganism does not naturally have a specific target for the drug) or acquired (where the microorganism develops mechanisms in order to circumvent the action of the drug).<sup>7</sup> The major clinically-relevant mechanisms of resistance are modification of the target, decreased penetration of the drug, efflux of the drug, overproduction of the target, enzymatic inactivation or modification of the drug and bypass pathways.<sup>2</sup>

One approach that may help to overcome resistance is by developing a therapeutic agent that can inhibit or affect multiple targets.<sup>8</sup> Furthermore metal-containing antibacterial drugs could help overcome resistance by providing a metal-specific mechanism of action, which cannot be attained by organic-based molecules.<sup>9</sup>

---

### 1.1.2. Tuberculosis

Tuberculosis (TB) is a disease caused by the bacteria *Mycobacterium tuberculosis*. It is still one of the world's most deadly infectious diseases; *c.a.* 9 million people in 2013 developed TB globally (56% of the cases were in South-East Asia and Western Pacific) with 1.5 million people dying from the disease.<sup>10</sup>

The bacteria are initially inhaled into the lung from droplets that have been expelled from an infected person. Macrophages (cells forming part of the immune response that destroys foreign microorganisms) engulf the bacteria containing it in a compartment called a phagosome. In order to destroy the bacteria a lysosome fuses to the phagosome to expose the bacteria to a destructive environment (for example low pH, reactive oxygen species and lysosomal enzymes).<sup>11</sup> If the macrophage fails to eradicate the bacteria, the immune system tries to contain the bacteria by forming a granuloma around the infected macrophages (known as the primary lesion) consisting of other macrophages and immune cells. If the growth of the bacteria is inhibited by this process it is known as latent TB, as it may be activated if the immune system becomes weakened.<sup>12</sup> The centre of the granuloma can become necrotic, causing cavities and damaging the function of the lung. If the bacteria continually replicate and escape from the primary lesion, they will spread to other parts of the lung to form secondary lesions and extensive damage, see Figure 1.1.



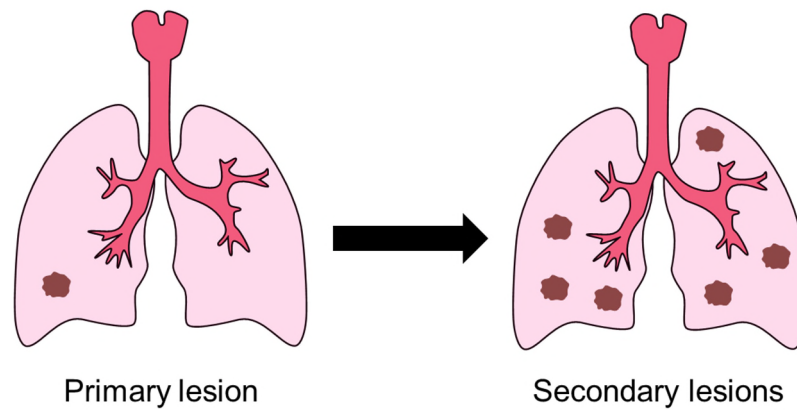


**Figure 1.1.** Primary and secondary lesions in tuberculosis (TB).

The main problem with *Mycobacterium tuberculosis* is that it is virulent. It has evolved several survival strategies to survive in the hostile environment of a macrophage by inhibiting phagosome-lysosome fusion, adapting to the limited nutritional environment of the macrophage and increasing the resistance to toxic agents produced by the host cell.<sup>13-14</sup>

Current treatment of TB involves a chemotherapy regime that lasts for > 6 months. The first-line drugs isoniazid, pyrazinamide, ethambutol and rifampicin (Figure 1.2) are given together for the first 2 months of treatment, then a combination of 2, 3 or 4 of these drugs is given for a further 4 to 5 months.<sup>15</sup> Problems with this long treatment include the development of resistance due to errors in the treatment regime and patient failure to adhere to the regime, both of which make it difficult to control TB.<sup>16</sup> Multi-drug resistant tuberculosis (MDR-TB) occurs when *M. tuberculosis* is resistant to at least isoniazid and rifampicin (i.e. first line drugs) and extensively-drug resistant tuberculosis (XDR-TB) occurs when resistant to any of the second line drugs (capreomycin, kanamycin and amikacin).<sup>17</sup>

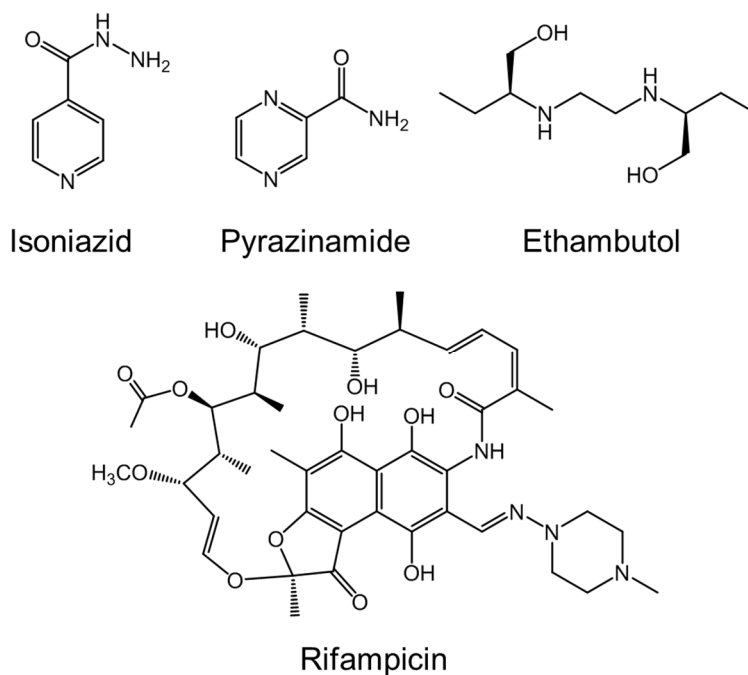


**Figure 1.2.** First line anti-tuberculosis drugs.

The target of isoniazid is an enoyl-acyl carrier protein reductase enzyme known as InhA. InhA utilizes NADH (reduced nicotinamide adenine dinucleotide) to reduce the *trans* double bond of a fatty acid chain that is attached to the protein.<sup>18</sup> This is an integral part of mycolic acid synthesis, which is required for the cell wall of *M. tuberculosis*. Isoniazid is a prodrug that is activated by a catalase-peroxidase enzyme called KatG to produce an isonicotinic acyl radical, see Figure 1.3. This radical is coupled to NAD<sup>+</sup> (oxidised nicotinamide adenine dinucleotide) to produce an INH-NAD adduct.<sup>19</sup> It has been postulated that the isonicotinic acyl radical may be coupled to either NAD<sup>+</sup> or NAD<sup>•</sup> within the active site of InhA.<sup>20</sup> The resulting INH-NAD adduct inhibits the function of InhA, thus disrupting the synthesis of mycolic acids, and results in bacterial cell death.<sup>21</sup> Resistance mechanisms of *M. tuberculosis* against isoniazid include mutations in *katG* and InhA enzymes.<sup>21</sup>

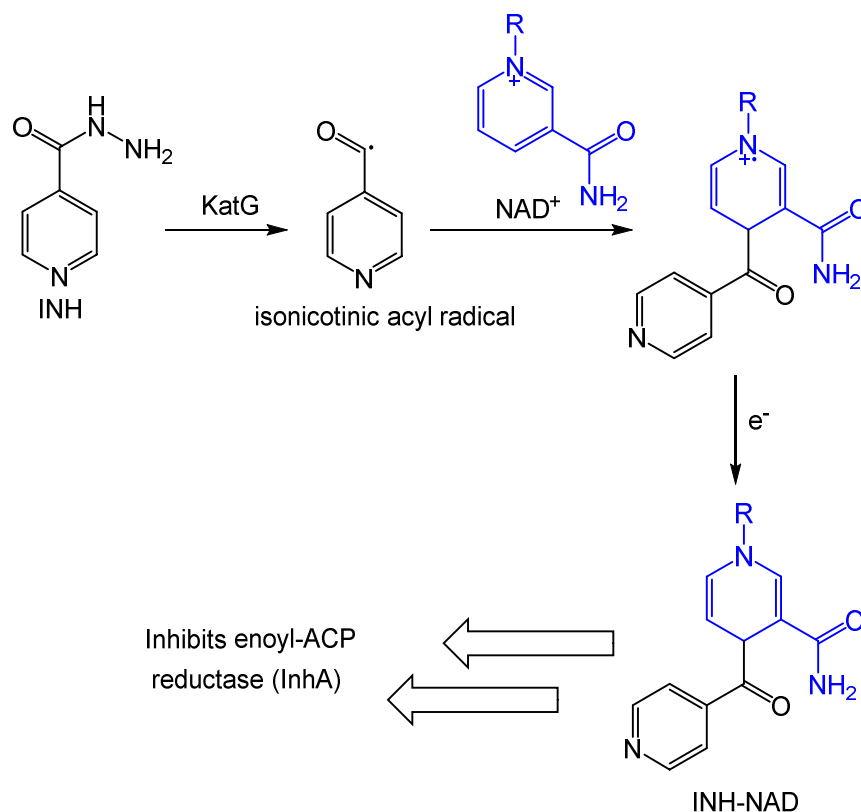


**Figure 1.3.** Activation and mechanism of action of isoniazid, where R is adenine dinucleotide.<sup>19, 21</sup>

Interestingly structurally-related nicotinamide has been shown to be active against *M. tuberculosis* and human immunodeficiency virus (HIV), however studies need to be conducted to investigate if it is effective in treating HIV-*M. tuberculosis* coinfection.<sup>22</sup>

## 1.2. Metals in medicine

Metals are important for many functions in the human body, for example iron is involved in dioxygen storage and transport (e.g. haemoglobin), zinc is involved in carbon dioxide transport (e.g. carbonic anhydrase) while cobalt is found in vitamin B<sub>12</sub>.<sup>23</sup> However all metals whether they are essential (e.g. iron and zinc) or nonessential (e.g. mercury and lead) are toxic in excess.<sup>24</sup>

Metals have been used for medical applications for thousands of years. Copper sulfate was used by Egyptians to sterilise their potions, gold was used in China in medical preparations in *c.a.* 2500 BC, and mercury was used to treat syphilis in the 16<sup>th</sup> century.<sup>23</sup> It was not until the early 1900's when the term chemotherapy was first invented by Paul Ehrlich, with the meaning of using chemicals to treat diseases.<sup>25</sup> The first modern chemotherapeutic agent discovered and synthesised in Ehrlich's lab was an organoarsenic compound Arsphenamine (also known as Salvarsan), and was used to treat syphilis. His "magic bullet" concept aimed to synthesise drugs that go to its intended cell target, leaving healthy cells unharmed, which has since given way to targeted medicine.<sup>26</sup>

### 1.2.1. Ruthenium

Ruthenium is a rare transition metal that is part of the platinum group metals. It has various properties that make it suitable for medical applications<sup>27</sup>:

- Rate of ligand exchange (similar exchange kinetics to platinum(II) complexes currently used for cancer treatment e.g. cisplatin).
- A range of accessible oxidation states under physiological conditions (Ru(II), Ru(III) and Ru(IV)).
- Ability to mimic iron (thought to be why ruthenium drugs have a low toxicity to healthy cells).

Relatively inert chlorido Ru(III) complexes can be activated by reduction to give active chlorido Ru(II) complexes in diseased tissue, for example a cancer cell has a very reducing environment with high levels of glutathione, low oxygen concentration and low pH.<sup>27</sup> Currently there are three Ru(III) anti-cancer complexes in clinical trials; NAMI-A, KP1019 and NKP-1339, see Figure 1.4.<sup>28</sup> For KP1019 and NKP-1339, it is

proposed that plasma proteins albumin and transferrin act as transporters and delivery systems for the complexes to cancer cells.<sup>28</sup>

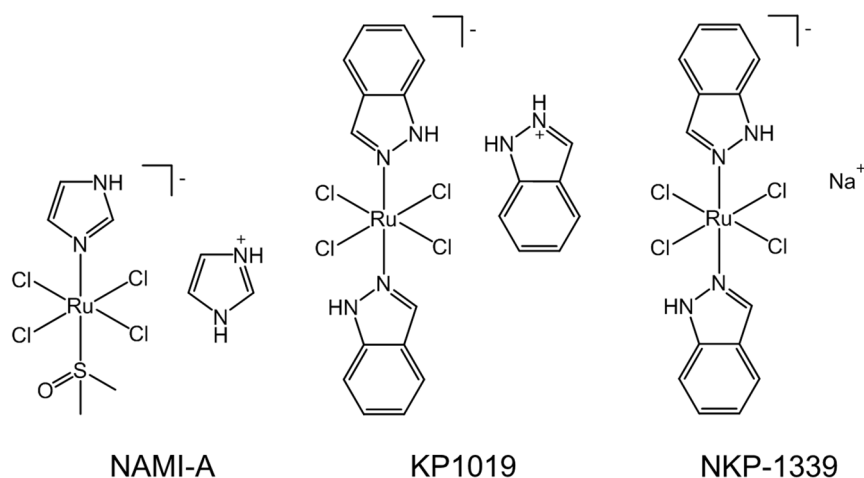


**Figure 1.4.** Ruthenium(III) complexes currently in clinical trials

In the case of Ru(II), many half-sandwich complexes have been investigated for their anticancer activity, some examples are shown in Figure 1.5. RM175,  $[(\eta^6\text{-biphenyl})\text{RuCl}(\text{en})]^+$  where en is ethylenediamine, exhibited a similar potency to the anticancer drug carboplatin against an ovarian cancer cell line (A2780) and were found to bind covalently to DNA via guanine.<sup>29</sup> RAPTA-C,  $[\text{Ru}(\eta^6\text{-}p\text{-cymene})\text{Cl}_2(\text{pta})]$  where pta is 1,3,5-triaza-7-phosphaadamantane, reduced the growth of an ovarian tumour by ~75% and was shown to have an anti-angiogenic effect.<sup>30</sup> Attachment of a bidentate ligand based on a protein kinase inhibitor (indolocarbazole alkaloid) to a Ru(II) centre resulted in a complex, DW12, that is inert towards nucleic acids however exhibits anticancer activity due to its potent inhibition of a protein kinase (GSK-3).<sup>31-</sup>

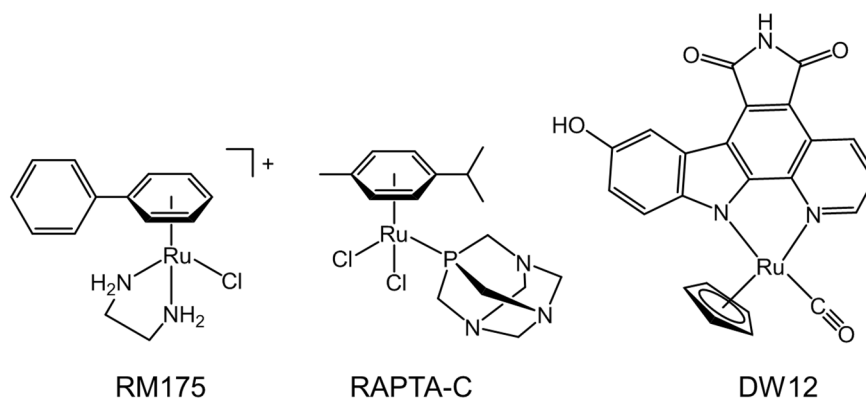


**Figure 1.5.** Anticancer ruthenium(II) arene complexes

#### 1.2.1.1. Antibacterial

Ru(II) complexes have been extensively studied for their antibacterial activity.<sup>33</sup> Ru(II) polypyridyl complexes containing extended aromatic ligands, for example  $[\text{Ru}(\text{2,9-Me}_2\text{phen})_2(\text{DPPZ})]^{2+}$  where 2,9-Me<sub>2</sub>phen is 2,9-dimethyl-1,10-phenanthroline and DPPZ is dipyrido[3,2-a:2',3'-c]phenazine, are able to intercalate into DNA and were found to be active against Gram-positive *B. subtilis* and *S. aureus*, but was inactive against Gram-negative *E. coli*.<sup>34</sup> Interestingly in the case of  $[\text{Ru}(\text{bpy})_2(\text{NPDA})]^{2+}$ , where NPDA is *N*-phenyl-substituted diazofluorene, the complex is active against methicillin resistant *S. aureus* (MRSA) and produced reactive oxygen species (ROS) when incubated with MRSA.<sup>35</sup> Dinuclear complexes have also been studied (see Figure 1.6), where rigid linkers between metal centres showed lower activity (e.g.  $\Delta\Delta\text{-}\{[\text{Ru}(\text{phen})_2]_2(\mu\text{-bpm})\}^{2+}$  where phen is 1,10-phenanthroline and bpm is 2,2'-bipyrimidine) compared to flexible linkers (e.g.  $[\text{Ru}(\text{phen})_2]_2(\mu\text{-bb}_{16})]^{2+}$  where bb<sub>16</sub> is bis[4(4'-methyl-2,2'-bipyridyl)]-1,16-alkane) when tested against *S. aureus* and *E. coli*.<sup>36</sup> The activity was proposed to be linked to lipophilicity, as increased lipophilicity results in increased penetration through the cell membrane and therefore increased uptake.<sup>37</sup>

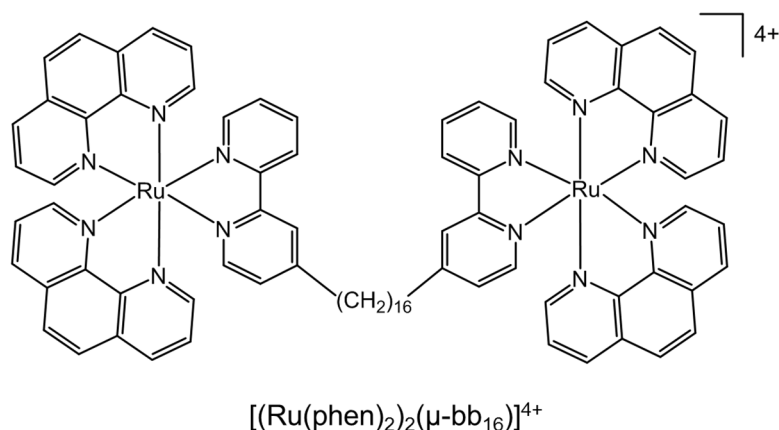


**Figure 1.6.** Dinuclear ruthenium(II) antibacterial complex

Another strategy to design antibacterial agents is to attach an existing organic antibacterial agent to a Ru(II) centre, for example attachment of  $\beta$ -lactam to a cyclopentadiene moiety or using ofloxacin as a chelating ligand.<sup>38-39</sup> This strategy can be used either to try and overcome resistance, or to investigate a potential synergistic effect between the metal and the antibacterial agent.

#### 1.2.1.2. Tuberculosis

Currently there are a few examples of Ru(II) complexes that are being developed for anti-tuberculosis activity. Complexes containing phosphine, diimine and picolinate moieties have shown promising activity against *M. tuberculosis*.<sup>40-42</sup> For example  $\text{cis-}[\text{Ru}(\text{pic})(\text{dppe})_2]^+$ , where pic is 2-pyridinecarboxylate and dppe is 1,2-bis(diphenylphosphino)ethane, had a better activity than isoniazid against *M. tuberculosis* and retained its activity against an isoniazid resistant strain.<sup>41-42</sup>

An interesting strategy to induce dormancy in *mycobacteria* is to block hydrophilic nutrient channels, and Ru(II) quaterpyridinium complexes have been found to bind to MspA (porin A from *M. smegmatis*) which leads to the formation of large MspA aggregates.<sup>43-44</sup>

### 1.2.2. Other metals

Cisplatin, carboplatin and oxaliplatin are platinum(II) anticancer drugs approved for clinical use globally, see Figure 1.7, while nedaplatin, lobaplatin and heptaplatin are approved in Japan, China and Korea respectively.<sup>45</sup> Carboplatin was designed to overcome the side effects of cisplatin by replacing the chloride ligands with 1,1-cyclobutanedicarboxylate which aquates at a slower rate, while oxaliplatin overcomes cisplatin resistance by forming different adducts with DNA.<sup>45</sup>

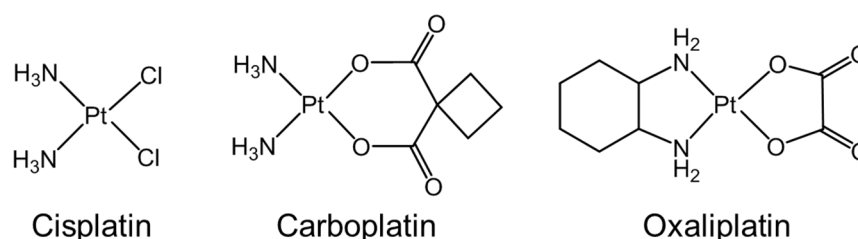


**Figure 1.7.** Globally approved platinum(II) anticancer complexes

Addition of a biologically-active ligand to an iron(II) centre has been investigated for applications in treatment of malaria and tuberculosis, see Figure 1.8. A chloroquine (currently used to treat malaria) mimicking ferrocene complex, known as ferroquine, is 22 times more active than chloroquine against the causative agent of malaria (*Plasmodium falciparum*).<sup>46</sup> Ferroquine is currently in phase II clinical trials.<sup>47</sup> In the case of tuberculosis, the complex  $[\text{Fe}(\text{CN})_5(\text{isoniazid})]^{3-}$  was found to inhibit the isoniazid target InhA (discussed in Section 1.1.2) without being activated by the enzyme KatG; KatG activation is blocked in isoniazid resistant strains of *M. tuberculosis*.<sup>48-50</sup>



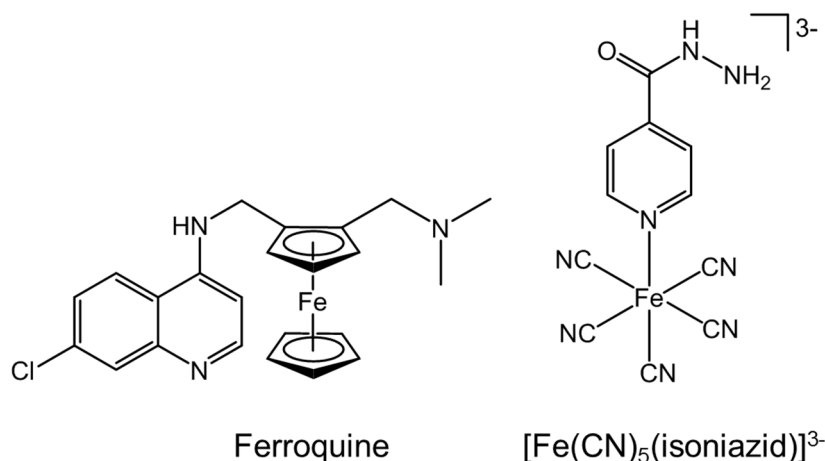
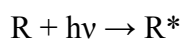


**Figure 1.8.** Iron(II) antimalarial (ferroquine) and anti-tuberculosis ([Fe(CN)<sub>5</sub>(isoniazid)]<sup>3-</sup> complexes.

### 1.3. Photoactive metal complexes

#### 1.3.1. Photochemistry

The absorption of one photon ( $h\nu$ ) by one molecule (R) causes excitation of an electron to promote the molecule into an electronically excited state (R\*):



The energy required to produce this electronically excited state is dictated by the energy gap between ground state ( $E_1$ ) and the excited state ( $E_2$ ).<sup>51</sup> As a result only a photon with that energy can cause photoexcitation, see Equation 1.1.

$$\Delta E = |E_2 - E_1| = h\nu = \frac{hc}{\lambda} \quad \text{Equation 1.1}$$

where  $h$  is Planck's constant,  $\nu$  is the frequency,  $c$  is the speed of light and  $\lambda$  is the wavelength. The theoretical probability of an electronic transition is known as the oscillator strength ( $f$ ) and is related to the transition dipole moment ( $\mu$ ), mass of an electron ( $m_e$ ) and the charge of an electron ( $e$ ), see Equation 1.2.<sup>52</sup> The oscillator

strength is related to the experimentally obtained extinction coefficient ( $\epsilon$ ) and wavenumber ( $\bar{\nu}$ ) by equation, see Equation 1.3.<sup>51</sup> The extinction coefficient ( $\epsilon$ ) is related to the absorbance ( $A$ ) and concentration ( $c$ ) of a compound and the path length of light ( $l$ ) by the Beer-Lambert Law, see Equation 1.4.

$$f \equiv \frac{8\pi^2 m_e \nu |\mu|^2}{3 h e^2} \quad \text{Equation 1.2}$$

$$f \equiv 4.3 \times 10^{-9} \int \epsilon d\bar{\nu} \quad \text{Equation 1.3}$$

$$A = \epsilon c l \quad \text{Equation 1.4}$$

The oscillator strength ( $f$ ) has a value approaching unity for strongly allowed transitions.<sup>53</sup> Selection rules dictate that electronic transitions are forbidden (and thus have a transition dipole moment of zero) if:<sup>52</sup>

- The transition is between states of equal parity ( $g \rightarrow g$  or  $u \rightarrow u$ ). This is known as a Laporte-forbidden transition ( $\Delta l = \pm 1$  for allowed transitions).
- The transition is between states of different multiplicity. This is known as a spin-forbidden transition ( $\Delta S = 0$  for allowed transitions).

Relaxation of these rules can be encountered to make formally forbidden transitions allowed, which will be discussed below.

### 1.3.2. Electronic transitions and deactivation pathways

Excitation of a metal complex into an electronically excited state occurs when an electron is promoted from the highest occupied molecular orbital (HOMO) to the lowest unoccupied molecular orbital (LUMO). In an octahedral transition metal

complex the molecular orbitals can be described according to the predominant atomic orbital contributions see Figure 1.9.

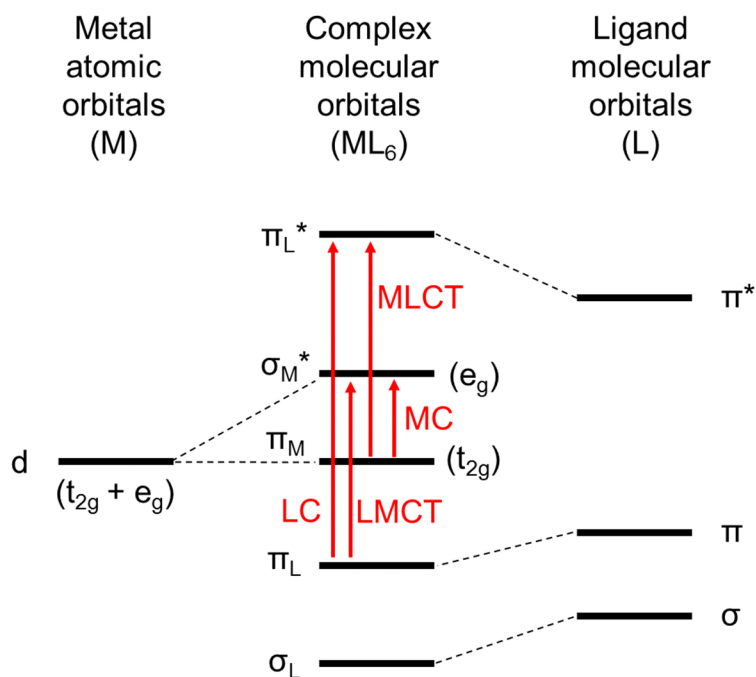


**Figure 1.9.** Molecular orbital diagram and the electronic transitions that can occur in an octahedral transition metal complex.<sup>54-55</sup>

Thus the following electronic transitions can occur in octahedral transition metal complexes:

- d-d transition from  $\pi_M (t_{2g})$  to  $\sigma_M^* (e_g)$  known as metal-centred transition (MC)
- transition from  $\pi_M (t_{2g})$  to  $\pi_L^*$  known as metal-to-ligand charge transfer (MLCT)
- transition from  $\pi_L$  to  $\sigma_M^* (e_g)$  known as ligand-to-metal charge transfer (LMCT)
- transition from  $\pi_L$  to  $\pi_L^*$  known as ligand-centred transition (LC)

As discussed previously, the selection rules govern the probability of an electronic transition. However the Laporte selection rule can be relaxed if a molecule departs from a centrosymmetric structure, as is the case for many d-d transitions. For example a molecule may be distorted and the inversion centre removed either partially (by an asymmetric vibration caused by vibronic coupling) or permanently (e.g. by Jahn-Teller distortion), and d and p orbital mixing results in a “mixed” character d-d transition.<sup>56</sup> As a result the intensity of absorption bands, and thus extinction coefficients  $\epsilon_{\max}$ , vary depending if a transition is allowed or forbidden by the selection rules, see Table 1.1.

**Table 1.1.** Typical extinction coefficients ( $\epsilon_{\max}$ ) observed for metal complexes.<sup>57</sup>

Type of transition	Selection rules		$\epsilon_{\max}$ ( $\text{M}^{-1} \text{cm}^{-1}$ )
	Spin	Laporte	
$\Delta S \neq 0$	Forbidden	Forbidden	$<1$
MC (with centre of symmetry)	Allowed	Forbidden	$1 - 10^2$
MC (without centre of symmetry)	Allowed	Forbidden	$10^2 - 10^3$
MLCT / LMCT	Allowed	Allowed	$10^3 - 10^5$

Once the electronically excited state has been formed, there are various deactivation pathways that can occur, see Figure 1.10. Initial photoexcitation results in a vertical electronic transition to populate a vibrational level of the excited state which has same multiplicity (i.e.  $S_{0(v=0)} \rightarrow S_{1(v>0)}$ ). This is known as the Franck-Condon principle, and as a result the excited level is called the Franck-Condon state. From this state vibrational relaxation occurs rapidly whereby energy is dissipated to the surrounding environment, for example by colliding with a solvent molecule. Radiationless processes can occur whereby another excited state of the same multiplicity ( $\Delta S = 0$ ) is

populated, known as internal conversion (IC), or an excited state of a different multiplicity ( $\Delta S \neq 0$ ) is populated, known as intersystem crossing (ISC). Similarly radiative processes can occur from the lowest vibrational level of the lowest excited state to the ground state that results in no change in multiplicity ( $\Delta S = 0$ ), known as fluorescence, or a change in multiplicity ( $\Delta S \neq 0$ ), known as phosphorescence.

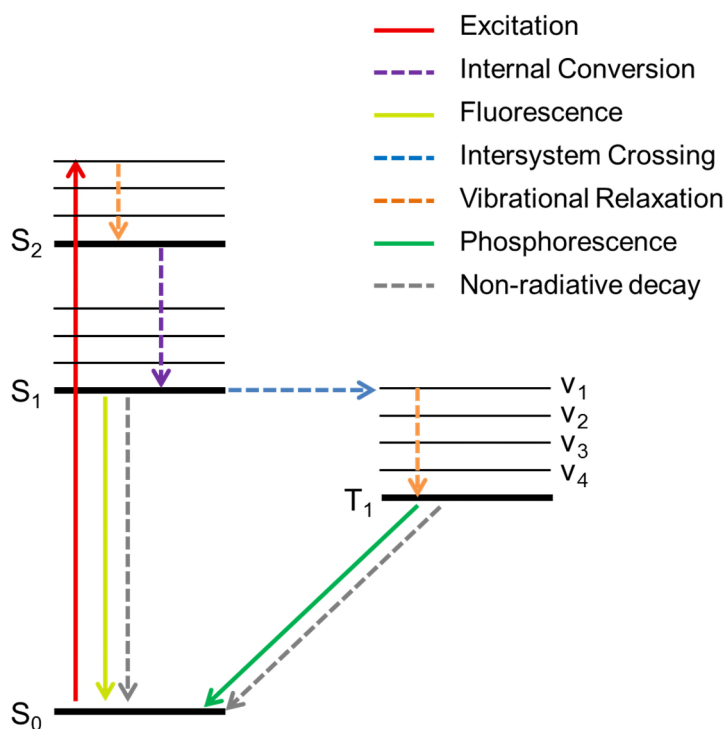


**Figure 1.10.** Jablonski diagram of deactivation pathways.

Typical timescales for the deactivation processes are listed in Table 1.2. Kasha's rule states that radiative processes (fluorescence and phosphorescence) or chemical reactions can occur only from the lowest vibrational level of the lowest excited state ( $S_1$  or  $T_1$ ). This can be rationalised due to the fast timescale of internal conversion / vibrational relaxation (femtoseconds to picoseconds) when compared to other decay processes such as fluorescence and phosphorescence (picoseconds to milliseconds). Processes involving a change in multiplicity (e.g. phosphorescence) are much longer

lived than those involving no change in multiplicity (e.g. fluorescence) as these are spin-forbidden processes.

**Table 1.2.** Typical timescales of deactivation processes.<sup>58</sup>

Process	Example transition	Timescale (s)
Vibrational relaxation	$S_{n(v>0)} \rightarrow S_{n(v=0)}$	$10^{-13} - 10^{-9}$
Internal conversion	$S_n \rightarrow S_1$	$10^{-14} - 10^{-11}$
Internal conversion	$S_1 \rightarrow S_0$	$10^{-9} - 10^{-7}$
Intersystem crossing	$S_1 \rightarrow T_1$	$10^{-11} - 10^{-8}$
Fluorescence	$S_1 \rightarrow S_0 + h\nu$	$10^{-12} - 10^{-6}$
Phosphorescence	$T_1 \rightarrow S_0 + h\nu$	$10^{-3} - 10^{-2}$

### 1.3.3. Photochemistry of Ru(II) complexes

Due to the increased energy difference between  $t_{2g}$  and  $e_g$  orbitals in Ru(II) complexes  $[\text{Ru}(N-N')_3]^{2+}$ , where  $N-N'$  is a bidentate polypyridyl ligand, the lowest excited state is MLCT in character followed by MC and LC states, see Figure 1.11.<sup>55</sup>

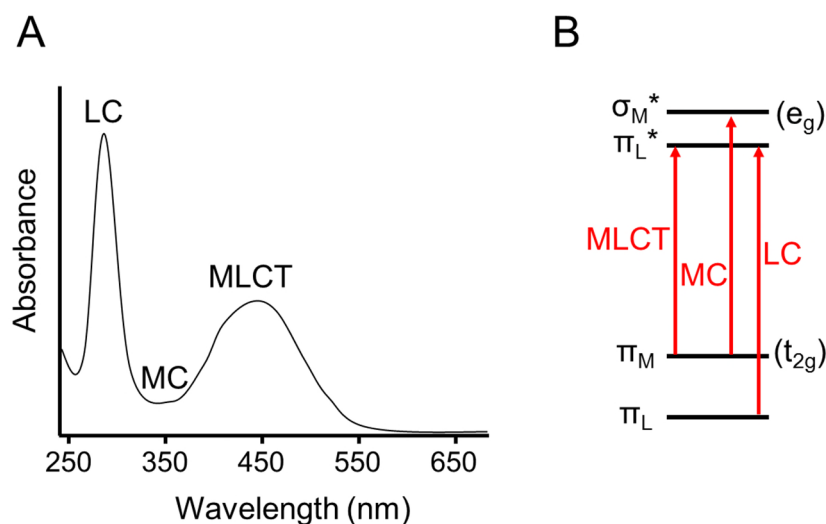


**Figure 1.11.** Typical UV-visible absorption spectrum of  $[\text{Ru}(N-N')_3]^{2+}$  complexes (A) with molecular orbitals and possible electronic transitions (B), where subscripted M/L is a metal/ligand based orbital respectively.<sup>55</sup>

After photoexcitation of  $[\text{Ru}(\text{N-N}')_3]^{2+}$  complexes in their MLCT band, different photochemical/photophysical events may occur. Intersystem crossing is very efficient in ruthenium complexes due to spin-orbit coupling, therefore population of the  $^3\text{MLCT}$  state occurs rapidly.<sup>59</sup> Interestingly if this is the lowest lying triplet state phosphorescence is observed, however if the  $^3\text{MC}$  state is accessible from the  $^3\text{MLCT}$  state, ligand dissociation occurs, see Figure 1.12.<sup>60</sup>

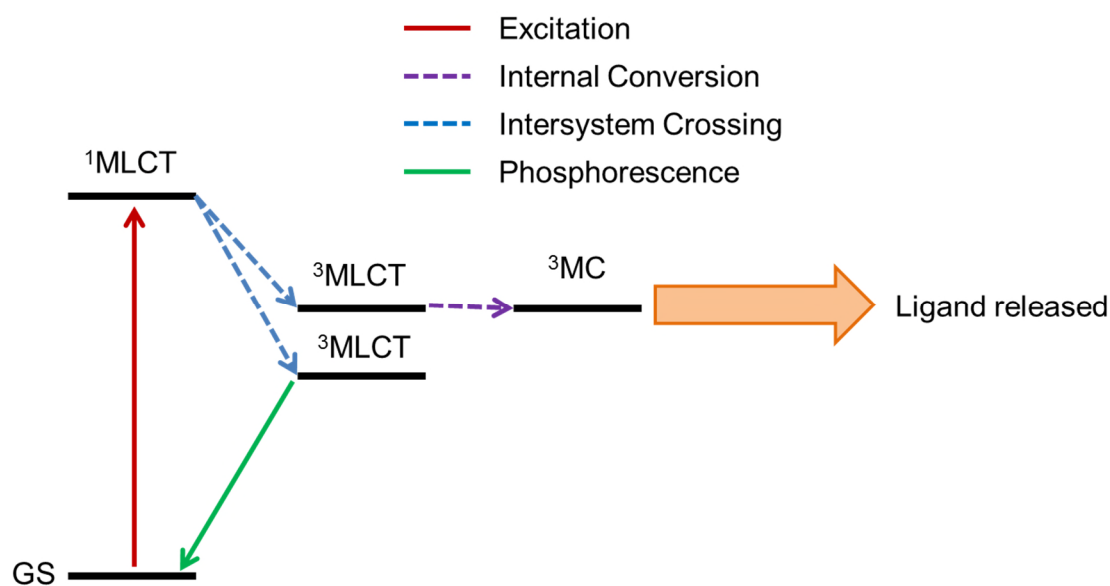
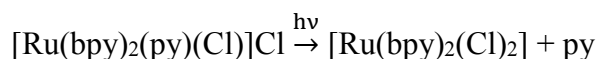
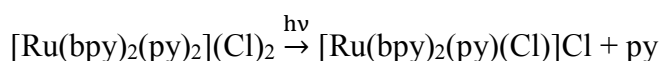


**Figure 1.12.** Photochemical/photophysical pathways observed in  $[\text{Ru}(\text{N-N}')_3]^{2+}$  complexes.

For example, photolysis of *cis*- $[\text{Ru}(\text{bpy})_2(\text{py})_2](\text{Cl})_2$ , where bpy is 2,2'-bipyridine and py is pyridine, in low polarity solvents such as dichloromethane results in the photorelease of py ligands and the binding of the coordinating counter ion<sup>61</sup>:



However in water or acetonitrile the solvent binds instead of the counter ion.<sup>61</sup>

## 1.4. Photoactive metal complexes in medicine

The various treatments that involve the use of light to treat a disease can be categorized as follows<sup>62</sup>:

- Phototherapy – the general term to describe the use of ultraviolet, visible and near-infrared light to treat a disease. Thus a specific area of the body is photoirradiated.
- Photochemotherapy – involves the administration of a photosensitizer that is activated once photoirradiated (discussed in Section 1.4.2.).
- Photodynamic therapy – involves the administration of a photosensitizer which once photoirradiated produces reactive oxygen species (discussed in Section 1.4.1.).
- Photopheresis – an extracorporeal procedure where the blood is removed from the body, treated with a photosensitizer and photoirradiated. Once complete, the blood is flowed back into the body.

Phototherapy and photochemotherapy have been used for thousands of years (for example ancient Egypt and Greece), while photodynamic therapy has been used over the past 100 years.<sup>63</sup> Photopheresis is a relatively modern technique, with the first clinical trial for the treatment of cutaneous T-cell lymphoma using photopheresis with 8-methoxypsoralen reported in 1987.<sup>64</sup> Subsequently in 1988 the food and drug administration (FDA) agency approved photopheresis for the treatment of cutaneous T-cell lymphoma.<sup>65</sup>

### 1.4.1. Photodynamic therapy

Photodynamic therapy (PDT) is a type of treatment whereby a non-toxic sensitizer (commonly based on a porphyrin or phthalocyanine type structure) is administered to



the patient and a light source is used to photoirradiate the sensitizer in a specific area of the body, for example a cancerous tumour. The main advantage of this technique is that only a certain area is affected, leaving surrounding healthy tissue unharmed. The first PDT agent to be approved by a health agency was Photofrin® (see Figure 1.13) in 1993 for the treatment of bladder cancer in Canada, and since then has been approved for the treatment of lung cancer and oesophageal cancer in parts of Europe, Japan and US.<sup>66</sup>

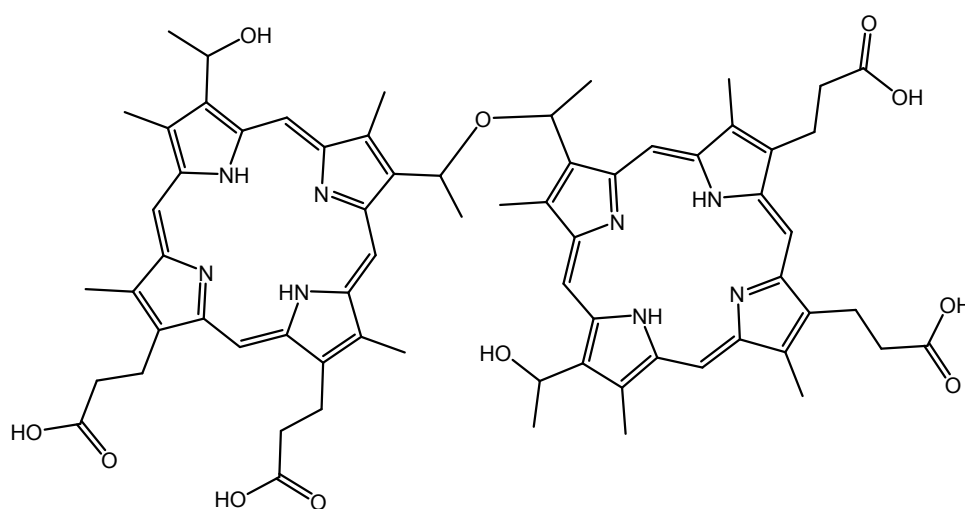


**Figure 1.13.** Structure of Photofrin®.<sup>67</sup>

The photosensitizer requires oxygen to produce toxic species by either a Type I or Type II mechanism, see Figure 1.14. The Type I mechanism involves promoting the photosensitizer to its triplet excited state ( $^3P^*$ ) via light and subsequent interaction with a substrate molecule (S) involving either an electron or hydrogen transfer. As a result the Type I mechanism involves the production of radicals and, in the presence of oxygen, superoxide radical anion ( $O_2^{\cdot-}$ ) that can produce reactive oxygen species (ROS) such as hydroxyl radical ( $\cdot OH$ ) and hydrogen peroxide ( $H_2O_2$ ). The Type II mechanism involves the production of singlet oxygen ( $^1O_2$ ) by energy transfer from

the photosensitizer in its triplet excited state ( $^3P^*$ , via light) to molecular oxygen ( $O_2$ ). Reactive oxygen species (including singlet oxygen  $^1O_2$ ) are very reactive and can efficiently oxidize biomolecules to cause biological damage.<sup>68</sup>

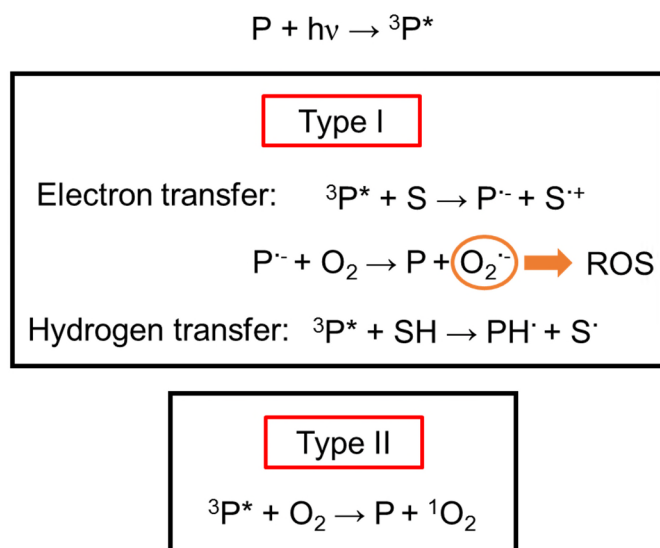


**Figure 1.14.** Mechanisms of photodynamic therapy (PDT), Type I and Type II, where P is the photosensitizer,  $^3P^*$  is the triplet excited state of the photosensitizer, S is the substrate and ROS is reactive oxygen species.<sup>69</sup>

#### 1.4.1.1. Role of metal complexes in PDT

The chelation of diamagnetic transition metals and lanthanide ions to photosensitizers produces complexes with promising PDT properties due to the enhanced rate of intersystem crossing (ISC) as a result of the heavy metal effect.<sup>70</sup> For example, chelating diamagnetic ions such as  $Zn^{2+}$ ,  $Al^{3+}$  and  $Ga^{3+}$  to phthalocyanine results in high singlet oxygen quantum yields and long lifetimes of the triplet excited state.<sup>71</sup>

Ruthenium(II) polypyridyl complexes, for example  $[(Ph_2phen)_2Ru(dpp)]^{2+}$  where  $Ph_2phen$  is 4,7-diphenyl-1,10-phenanthroline and dpp is 2,3-bis(2-pyridyl)pyrazine, produce singlet oxygen and photocleave DNA due to the quenching of the  $^3MLCT$  state by molecular oxygen, however the efficiency of quenching was only *c.a.* 5%.<sup>72</sup>

Another approach is to attach a Ru(II) arene complex to the peripheral of 5,10,15,20-tetra(4-pyridyl)porphyrin (TPP), for example  $[\text{Ru}_4(\eta^6\text{-hmb})_4(\text{TPP})\text{Cl}_8]$  where hmb is hexamethylbenzene, in order to obtain a dual activity complex where Cl is photorelease of from the Ru(II) centre and the PDT effect comes from the porphyrin system, see Figure 1.15.<sup>73</sup>

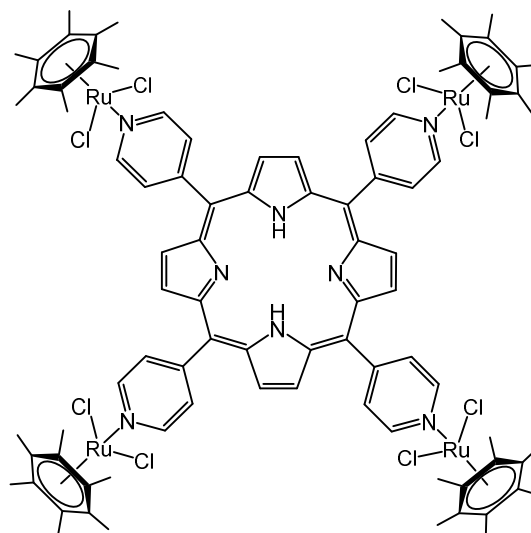


**Figure 1.15.** Dual activity ruthenium(II) porphyrin complex,  $[\text{Ru}_4(\eta^6\text{-hmb})_4(\text{TPP})\text{Cl}_8]$ .

Curcumin was found to be a PDT agent however it is relatively unstable in phosphate buffer and in cell culture media.<sup>74-75</sup> Interestingly binding curcumin to an oxovanadium(IV) complex,  $[\text{VO}(\text{cur})(\text{DPPZ})\text{Cl}]$  where cur is deprotonated curcumin and DPPZ is dipyrido[3,2-a:2',3'-c]phenazine, stabilises curcumin and results in a PDT agent that is more potent than curcumin alone and Photofrin® against HeLa cancer cells.<sup>76</sup>

#### 1.4.2. Metal complexes in photochemotherapy

One disadvantage of PDT is that it requires the presence of oxygen and hypoxia (low levels of oxygen) is a common problem for certain diseases, for example cancer.<sup>77</sup>

Thus it is important to develop prodrugs that have a different mechanism of action to PDT (i.e. do not rely on the presence of oxygen).<sup>78</sup> This section describes metal complexes developed for that purpose.

#### **1.4.2.1. Photorelease of bioactive molecules**

Nitric oxide (NO) is endogenously produced in the human body and is an important bioregulator inducing vasodilation, regulating programmed cell death and acting as a neurotransmitter.<sup>79</sup> However the physiological effect of NO depends on the local concentration, for example at low NO concentrations tumour growth and cancer cell proliferation are promoted, whereas high NO concentrations can either induce cancer cell apoptosis or inhibit cancer cell growth.<sup>80</sup> As a result, the controlled delivery and release of NO have been extensively investigated by the use of photoactivation. The enzyme nitrile hydratase has an iron in the active site bound to a carboxamide frame and NO, and upon light exposure NO is released. This inspired the synthesis of Fe(III), Mn(II) and Ru(III) nitrosyl complexes containing the pentadentate PaPy<sub>3</sub> ligand,  $[M^{n+}(\text{PaPy}_3)\text{NO}]^{n-1+}$ , where PaPy<sub>3</sub> is deprotonated N,N-bis(2-pyridylmethyl)amine-N-ethyl-2-pyridine-2-carboxamide, able to release NO upon photoactivation.<sup>81-84</sup> Increasing the conjugation of the pentadentate ligand increases the quantum yield of photorelease and shifts the activation to a longer wavelength.<sup>82-83</sup> In the case of  $[\text{Mn}(\text{PaPy}_2\text{Q})(\text{NO})]^+$ , where PaPy<sub>2</sub>Q is deprotonated N,N-bis(2-pyridylmethyl)amine-N-ethyl-2-quinoline-2-carboxamide, the activation is shifted to near IR (810 nm), see Figure 1.16.<sup>82</sup>

Interestingly for a Cr(III) nitrito complex, *trans*- $[\text{Cr}(\text{cyclam})(\text{ONO})_2]^+$  where cyclam is 1,4,8,11-tetraazacyclotetradecane, photoaquation of NO<sub>2</sub> occurs in deaerated aqueous solution. However in an aerated aqueous solution,  $\beta$ -cleavage of the CrO-NO

bond occurs upon photoactivation to produce a Cr(IV) intermediate *trans*-[Cr(cyclam)(O)(ONO)]<sup>+</sup>.<sup>85</sup>

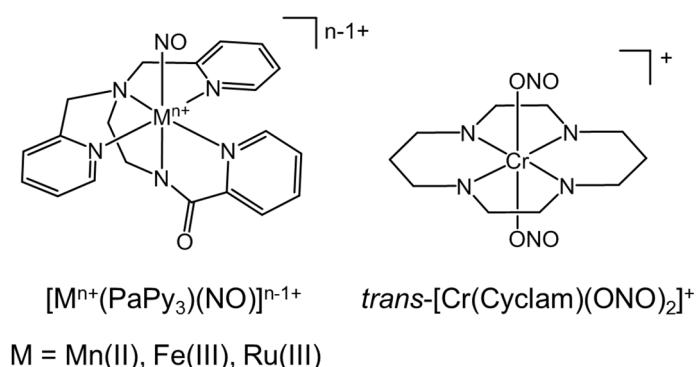


**Figure 1.16.** Photoactive nitrosyl and nitrito complexes

Carbon monoxide (CO) is also endogenously produced in the human body. It has been implicated in neuron and vascular signalling, and has therapeutic effects such as anti-apoptosis, anti-proliferative and anti-inflammatory.<sup>86</sup> However high concentrations of exogenous CO can cause tissue hypoxia, due to the increased affinity of haemoglobin for CO when compared to O<sub>2</sub> (210 times greater).<sup>87</sup> Similarly to NO, the controlled delivery and release of CO has been investigated by the use of metal complexes that photorelease CO. A Mn(I) carbonyl complex, *fac*-[Mn(pqa)(CO)<sub>3</sub>]<sup>+</sup> where pqa is (2-pyridylmethyl)(2-quinolylmethyl)amine, was found to release CO upon exposure to visible light.<sup>88</sup> Interestingly a Re(I) complex, *fac*-[Re(bpy)(CO)<sub>3</sub>(thp)]<sup>+</sup> where bpy is 2,2'-bipyridine and thp is tris(hydroxymethyl)phosphine, photoreleased CO with visible light and the differing luminescence of the starting material ( $\lambda_{\text{em}} = 515 \text{ nm}$ ) and photoproduct ( $\lambda_{\text{em}} = 585 \text{ nm}$ ) allowed the transformation to be followed by confocal fluorescence microscopy in a prostate cancer cell line, see Figure 1.17.<sup>89</sup>

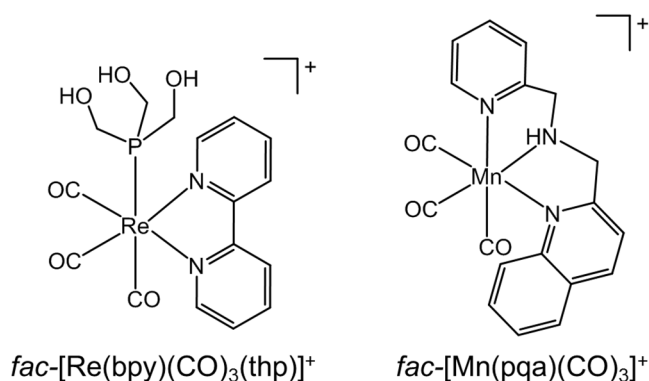


**Figure 1.17.** Photoreleasing CO complexes.

The photorelease of biologically active organic moieties from a Ru(II) polypyridyl scaffold has been explored, for example the release of anti-cancer agents and neurocompounds / neurotransmitters.<sup>90-93</sup> The complex  $cis-[Ru(bpy)_2(5-CU)_2]^{2+}$ , where bpy is 2,2'-bipyridine and 5-CU is 5-cyanouracil (an anti-cancer compound), releases two equivalents of 5-CU upon exposure to visible light and forms  $cis-[Ru(bpy)_2(H_2O)_2]^{2+}$  (see Figure 1.18) which is able to bind covalently to DNA.<sup>90</sup>

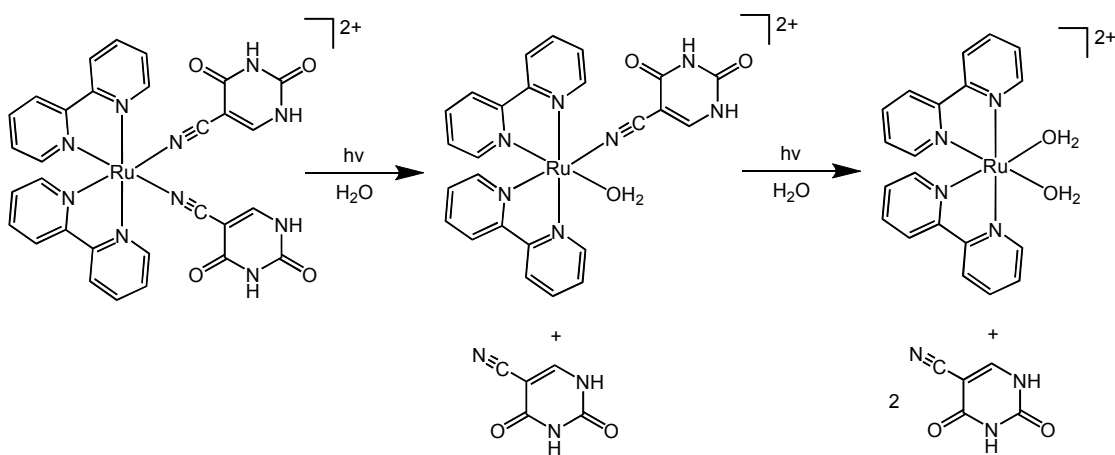


**Figure 1.18.** Photorelease of 5-cyanouracil (5-CU) from  $[Ru(bpy)_2(5-CU)_2]^{2+}$  with visible light.

### 1.4.2.2. *Imaging*

Cyclometallated iridium(III) complexes have gained significant interest for their high phosphorescent quantum yields and ability to “colour-tune” by changing the structure of the cyclometallating ligand.<sup>94</sup> There are many examples of Ir(III) complexes with groups attached to the periphery of the complex that bind to biomolecules and thus allow the complex to act as a chemical / biological probe.<sup>95</sup> For example  $[\text{Ir}(\text{ppy})_2(\text{phen-DPA})]^+$ , where ppy is deprotonated 2-phenylpyridine and phen-DPA is 5-(di-2-picolylamino)-1,10-phenanthroline, binds  $\text{Zn}^{2+}$  ions via the phen-DPA moiety which subsequently enhances the emission of the complex by *c.a.* 5 fold.<sup>96</sup> Similarly for  $[\text{Ir}(\text{pq})_2(\text{bpy-ind})]^+$ , where pq is deprotonated 2-phenylquinoline and bpy-ind is 4-((2-(indol-3-yl)ethyl)aminocarbonyl)-4'-methyl-2,2'-bipyridine, the indole moiety (bpy-ind) binds to bovine serum albumin and the emission of the Ir(III) complex increases.<sup>97</sup>

Imaging has also been extended to Ru(II) complexes. A dinuclear Ru(II) polypyridyl complex,  $[(\text{phen})_2\text{Ru}(\text{tpphz})\text{Ru}(\text{phen})_2]^{4+}$  where phen is 1,10-phenanthroline and tpphz is tetrapyrido[3,2-a:2',3'-c:3'',2''-h:2''',3'''-j]phenazine, binds to DNA and luminesces to act as a DNA stain in both eukaryotic and prokaryotic cells.<sup>98</sup>

### 1.4.2.3. *Interaction with DNA*

Simple metal complexes such as  $[\text{Ru}(\text{bpy})_3]^{2+}$ , where bpy is 2,2'-bipyridine, interact with DNA via electrostatic interactions, however complexes containing extended planar aromatic ligands intercalate between adjacent base pairs in double helical DNA.<sup>99</sup>

Light switch complexes have been developed, such as  $[\text{Ru}(\text{bpy})_2(\text{DPPZ})_2]^{2+}$  where bpy is 2,2'-bipyridine and DPPZ is dipyrdo[3,2-a:2',3'-c]phenazine), that only

luminesce in the presence of double-helical DNA due to intercalative binding.<sup>100</sup> The absence of luminescence in aqueous solution is due to deactivation of the excited state by hydrogen bonding with DPPZ ligand, however once the complex is intercalated into DNA it is shielded from the solvent and thus luminescence is restored.<sup>101-102</sup> Interestingly the complex  $[\text{Rh}(\text{bpy})_2(\text{chrysi})]^{3+}$  (see Figure 1.19), where chrysi is 5,6-chrysenequinone diimine, intercalates into mismatched sites of DNA and is able to photocleave the adjacent DNA backbone.<sup>103-104</sup>

In contrast  $[\text{Ru}(\text{TAP})_2(\text{bpy})]^{2+}$  (see Figure 1.19), where TAP is 1,4,5,8-tetraazaphenanthrene, is able to form covalent adducts with a nucleotide (guanosine monophosphate, GMP) via the TAP ligand after photoirradiation and is a result of an electron transfer process.<sup>105</sup>

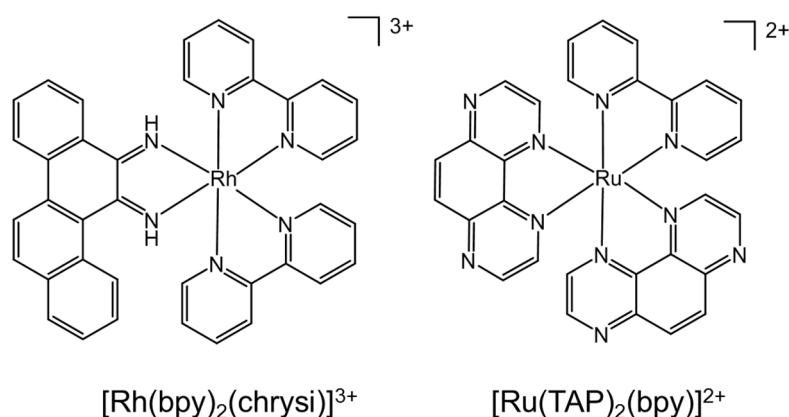


**Figure 1.19.** Complexes that interact with DNA.

Ru(II) arene complexes are able to covalently bind to DNA after photoirradiation. For example the complex  $[(\eta^6\text{-}p\text{-cymene})\text{Ru}(\text{bpm})(\text{RBP})]^{2+}$ , where bpm is 2,2'-bipyrimidine and RBP is a receptor binding peptide, releases RBP upon photoirradiation and the resulting aqua complex binds to DNA via guanine.<sup>106</sup>



### 1.4.3. Importance of wavelength of activation

Longer wavelength light ( $> 600$  nm) penetrates deeper into human tissue than shorter wavelength light ( $< 600$  nm), as shown in Figure 1.20. As a result the optimum wavelength of light used to activate a photoactive therapeutic agent (from a clinical perspective) is known as the phototherapeutic window, and is typically between 600 nm – 1000 nm.

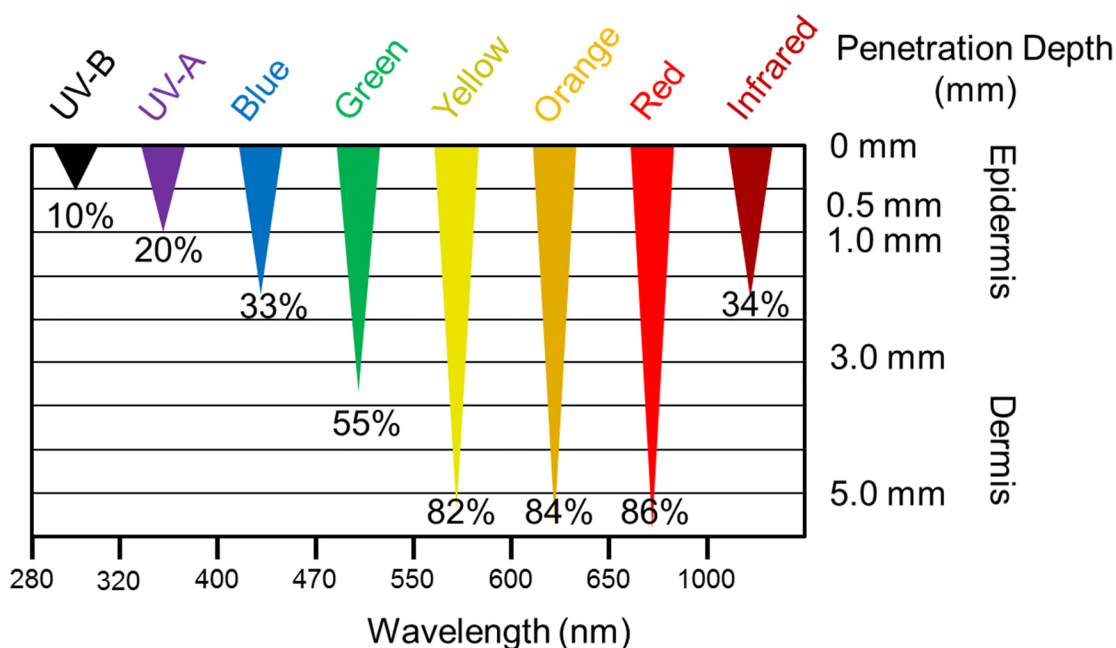


**Figure 1.20.** Depth of penetration of various wavelengths of light.<sup>107</sup>

This range is selected for the following reasons: a) tissues absorb lower wavelengths light ( $< 600$  nm) due to endogenous chromophores such as deoxyhemoglobin, b) tissues scatter lower wavelengths of light, and c) water absorbs significantly at wavelengths  $> 1,300$  nm.<sup>67</sup> Thus a clinically applicable photosensitizer should have a strong absorption band in this phototherapeutic window. However for some metal

complexes this is not possible, and several methods have been adopted to overcome this problem.

#### ***1.4.3.1. Ligand modification***

Modifying the ligands surrounding a metal can change the photochemical and photophysical properties of a metal complex. The complex  $[\text{Ru}(\text{biq})_2(\text{phen})]^{2+}$ , where phen is 1,10-phenanthroline and biq 2,2'-biquinoline, photoreleased one biq ligand in aqueous solution with  $>600$  nm light, with photoactivation aided by the increase in aromaticity (causing a red shift in the MLCT band) and increased distortion due to the bulky biq ligand (distortion from octahedral geometry lowers the energy of the dissociative  $^3\text{MC}$  state).<sup>108</sup>

Interestingly the cyclometallated analogue containing deprotonated 2-phenylpyridin (phpy),  $[\text{Ru}(\text{biq})_2(\text{phpy})]^+$ , had a comparatively red-shifted MLCT band (shifted by  $\sim 100$  nm) however photorelease of the biq ligand did not occur.<sup>109</sup> Cyclometallating ligands destabilise metal-based orbitals and have little effect on the  $\pi^*$  orbitals of the other ligands, thus lowering the energy of the MLCT band.<sup>110</sup> However in the previous example, it was found that the lack of photorelease was due to the significant destabilisation of the  $e_g$  orbitals, thus increasing the energy of the dissociative  $^3\text{MC}$  state.<sup>109</sup>

The complex  $[\text{Ru}(\text{Rterpy})(\text{bpy})(\text{Hmte})]^{3+}$ , where Rterpy is a rhodamine B functionalised 2,2';6',2''-terpyridine moiety and Hmte is 2-(methylthio)ethanol, was synthesised in order to exploit the favourable properties of rhodamine B (an efficient fluorophore with a large extinction coefficient at  $\sim 550$  nm).<sup>111</sup> The complex was able to release Hmte upon exposure to yellow light ( $\sim 570$  nm) due to the overlap of the Rterpy emission band (centred at 586 nm) with the absorption band of the

$[\text{Ru}(\text{terpy})(\text{bpy})\text{Hmte}]^{2+}$  (centred at  $\sim 450$  nm), via an energy transfer process that is known as reverse-FRET (Förster energy transfer), see Figure 1.21.<sup>111</sup>

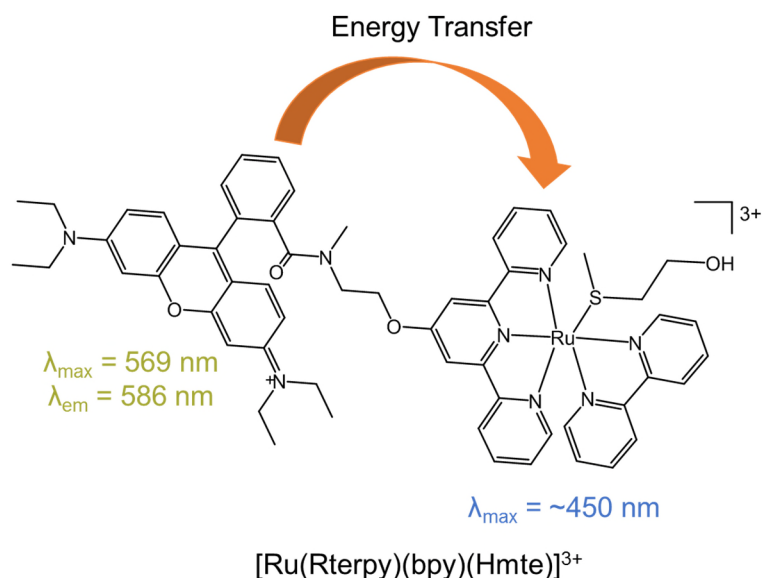


**Figure 1.21.** Energy transfer by addition of a fluorophore to a ruthenium(II) complex.

#### 1.4.3.2. Two-photon activation

Two-photon activation occurs when a molecule simultaneously absorbs two photons of low energy (from an intense femtosecond pulsed laser) to achieve the equivalent of a higher energy transition, see Figure 1.22.<sup>112</sup>

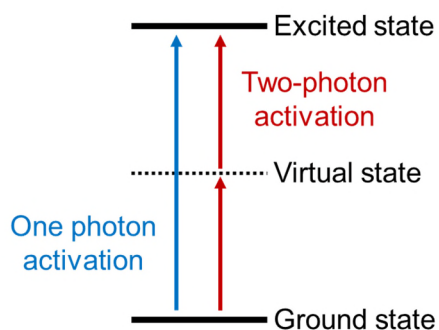


**Figure 1.22.** Schematic of one-photon and two-photon activation.

The probability of absorbing two-photons is directly related to the transition dipole moment and efficient two-photon activation occurs in molecules with a) terminal donor (D) and acceptor (A) groups (for example in a conjugated molecule D- $\pi$ -A) as this increases the displacement of charge during the transition from donor to acceptor and b) long  $\pi$ -conjugated planar chains as transition moments are related to the distance that the charge is displaced by during the transition.<sup>113</sup>

Ru(II) polypyridyl complexes  $[\text{Ru}(\text{bpy})_3]^{2+}$  and  $[\text{Ru}(\text{bpy})_2(\text{dcb})]^{2+}$ , where bpy is 2,2'-bipyridine and dcb is 2,2'-bipyridine-4,4'-dicarboxylic acid, luminesce from the  $^3\text{MLCT}$  state in a one-photon regime with 440 nm excitation and in a two-photon regime at 880 nm excitation.<sup>114</sup> However the efficiency of two-photon absorption was increased by adding highly conjugated fluorene units to the peripheral of the complex.<sup>115</sup> Additionally  $[\text{Ru}(\text{L1TEG})_3]^{2+}$ , where L1TEG is triethylene glycol functionalised 5-fluorene-1,10-phenanthroline, not only showed relatively efficient two-photon activation with 740 nm excitation but also showed improved solubility in biological media to the triethylene glycol units.<sup>116</sup>

#### ***1.4.3.3. Upconverting nanoparticles***

Upconverting nanoparticles work on the principle of energy-transfer upconversion, whereby one-photon is absorbed by an ion and energy transfer results in a neighbouring ion populating a higher excited emitting state.<sup>117</sup> For example 980 nm light has been used to excite  $\text{NaYF}_4$  nanoparticles doped with  $\text{Yb}^{3+}/\text{Er}^{3+}$  that emit green light at  $\sim 540$  nm which was quenched by the photoreleasing Ru(II) complex  $[\text{Ru}(\text{bpy})_2(\text{py})_2]^{2+}$  adsorbed onto the nanoparticle, where bpy is 2,2'-bipyridine and py is pyridine, to release py into solution.<sup>118</sup>

## 1.5. Aims

The general theme of this thesis is to explore the synthesis, design, photochemical and photobiological properties of ruthenium(II) polypyridyl complexes designed as antibacterial agents. The photoactive complexes of choice are based on *cis*-[Ru(*N-N'*)<sub>2</sub>(L)<sub>2</sub>]<sup>2+</sup> and *cis*-[Ru(*N-N'*)<sub>2</sub>(L)X]<sup>+</sup>, where *N-N'* is a bidentate polypyridyl ligand, X is a halide and L is either isoniazid or nicotinamide (anti-tuberculosis compounds). The aim is to release the biologically active ligand by photoactivation, and form reactive ruthenium(II) aqua species. The individual aims of the thesis are:

- a) To investigate the solution chemistry of the ruthenium(II) polypyridyl complexes in the dark.
- b) To explore the photochemical and photophysical behaviour of the ruthenium(II) polypyridyl complexes by photoirradiating with visible light.
- c) To assess the antibacterial activity of the ruthenium(II) polypyridyl complexes against a *M. tuberculosis* model, *M. smegmatis*, in the dark and once exposed to various wavelengths of visible light.
- d) To investigate extending the photoactivation of the ruthenium(II) polypyridyl complexes from the visible region to the phototherapeutic window (600 nm – 1000 nm) by modifying ligands surrounding the metal.

## 1.6. References

1. Silver, L. L. *Clin. Microbiol. Rev.*, **2011**, 24 (1), 71-109.
2. Lewis, K. *Nat. Rev. Drug Discov.*, **2013**, 12 (5), 371-387.
3. Ling, L. L.; Schneider, T.; Peoples, A. J.; Spoering, A. L.; Engels, I.; Conlon, B. P.; Mueller, A.; Schaberle, T. F.; Hughes, D. E.; Epstein, S.; Jones, M.; Lazarides,

- 
- L.; Steadman, V. A.; Cohen, D. R.; Felix, C. R.; Fetterman, K. A.; Millett, W. P.; Nitti, A. G.; Zullo, A. M.; Chen, C.; Lewis, K. *Nature*, **2015**, 517 (7535), 455-459.
4. WHO, *Antimicrobial resistance: global report on surveillance 2014*. 2014.
  5. Neu, H. C. *Science*, **1992**, 257 (5073), 1064-1073.
  6. Tenover, F. C. *Am. J. Med.*, **2006**, 119 (6), S3-S10.
  7. Byarugaba, D., Mechanisms of Antimicrobial Resistance. In *Antimicrobial Resistance in Developing Countries*, Sosa, A. d. J.; Byarugaba, D. K.; Amábile-Cuevas, C. F.; Hsueh, P.-R.; Kariuki, S.; Okeke, I. N., Eds. Springer New York: 2010; pp 15-26.
  8. Oldfield, E.; Feng, X. *Trends Pharmacol. Sci.*, **2014**, 35 (12), 664-674.
  9. Patra, M.; Gasser, G.; Metzler-Nolte, N. *Dalton Trans.*, **2012**, 41 (21), 6350-6358.
  10. WHO, *Global tuberculosis report 2014*. 2014.
  11. Smith, I. *Clin. Microbiol. Rev.*, **2003**, 16 (3), 463-496.
  12. Manabe, Y. C.; Bishai, W. R. *Nat. Med.*, **2000**, 6 (12), 1327-1329.
  13. Forrellad, M. A.; Klepp, L. I.; Gioffré, A.; Sabio y García, J.; Morbidoni, H. R.; Santangelo, M. d. l. P.; Cataldi, A. A.; Bigi, F. *Virulence*, **2012**, 4 (1), 3-66.
  14. Meena, L. S.; Rajni *FEBS J.*, **2010**, 277 (11), 2416-2427.
  15. Dilvani O. Santos; Selma M.A. Sias; Antas, P. R. Z., Natural History of Tuberculosis in the Human Host: Infection, Latency and Active Disease. Are these Treatable? In *Current Diagnosis of Infant Tuberculosis Infection*, Antas, P. R. Z., Ed. Bentham Science: United Arab Emirates, 2012.
  16. Spiegelburg, D. D., *New Topics in Tuberculosis Research*. Nova Science Publishers: New York, 2007.

17. Gandhi, N. R.; Nunn, P.; Dheda, K.; Schaaf, H. S.; Zignol, M.; van Soolingen, D.; Jensen, P.; Bayona, J. *Lancet*, **2010**, 375 (9728), 1830-1843.
18. Rozwarski, D. A.; Vilchèze, C.; Sugantino, M.; Bittman, R.; Sacchettini, J. C. *J. Biol. Chem.*, **1999**, 274 (22), 15582-15589.
19. Timmins, G. S.; Deretic, V. *Mol. Microbiol.*, **2006**, 62 (5), 1220-1227.
20. Rozwarski, D. A.; Grant, G. A.; Barton, D. H. R.; Jacobs, W. R.; Sacchettini, J. C. *Science*, **1998**, 279 (5347), 98-102.
21. Vilchèze, C.; Jacobs, J., William R. *Annu. Rev. Microbiol.*, **2007**, 61 (1), 35-50.
22. Murray, M. F. *Clin. Infect. Dis.*, **2003**, 36 (4), 453-460.
23. Jones, C. J.; Thornback, J. R., *Medicinal Applications of Coordination Chemistry*. The Royal Society of Chemistry: Cambridge, UK, 2007.
24. Lippard, S. J., Metals in medicine. In *Bioinorganic chemistry*, University Science Books: Mill Valley, California, 1994; pp 505-584.
25. DeVita, V. T.; Chu, E. *Cancer Res.*, **2008**, 68 (21), 8643-8653.
26. Strebhardt, K.; Ullrich, A. *Nat. Rev. Cancer*, **2008**, 8 (6), 473-480.
27. Allardyce, C. S.; Dyson, P. J. *Platinum Metals Review*, **2001**, 45 (2), 62-69.
28. Trondl, R.; Heffeter, P.; Kowol, C. R.; Jakupec, M. A.; Berger, W.; Keppler, B. K. *Chem. Sci.*, **2014**, 5 (8), 2925-2932.
29. Morris, R. E.; Aird, R. E.; del Socorro Murdoch, P.; Chen, H.; Cummings, J.; Hughes, N. D.; Parsons, S.; Parkin, A.; Boyd, G.; Jodrell, D. I.; Sadler, P. J. *J. Med. Chem.*, **2001**, 44 (22), 3616-3621.
30. Weiss, A.; Berndsen, R. H.; Dubois, M.; Muller, C.; Schibli, R.; Griffioen, A. W.; Dyson, P. J.; Nowak-Sliwinska, P. *Chem. Sci.*, **2014**, 5 (12), 4742-4748.

- 
31. Williams, D. S.; Atilla, G. E.; Bregman, H.; Arzoumanian, A.; Klein, P. S.; Meggers, E. *Angew. Chem. Int. Ed.*, **2005**, *44* (13), 1984-1987.
32. Meggers, E.; Atilla-Gokcumen, G. E.; Grundler, K.; Frias, C.; Prokop, A. *Dalton Trans.*, **2009**, (48), 10882-10888.
33. Li, F.; Collins, J. G.; Keene, F. R. *Chem. Soc. Rev.*, **2015**, *44* (8), 2529-2542.
34. Bolhuis, A.; Hand, L.; Marshall, J. E.; Richards, A. D.; Rodger, A.; Aldrich-Wright, J. *Eur. J. Pharm. Sci.*, **2011**, *42* (4), 313-317.
35. Lam, P. L.; Lu, G. L.; Hon, K. M.; Lee, K. W.; Ho, C. L.; Wang, X.; Tang, J. C. O.; Lam, K. H.; Wong, R. S. M.; Kok, S. H. L.; Bian, Z. X.; Li, H.; Lee, K. K. H.; Gambari, R.; Chui, C. H.; Wong, W. Y. *Dalton Trans.*, **2014**, *43* (10), 3949-3957.
36. Li, F.; Mulyana, Y.; Feterl, M.; Warner, J. M.; Collins, J. G.; Keene, F. R. *Dalton Trans.*, **2011**, *40* (18), 5032-5038.
37. Li, F.; Feterl, M.; Mulyana, Y.; Warner, J. M.; Collins, J. G.; Keene, F. R. *J. Antimicrob. Chemother.*, **2012**, *67* (11), 2686-2695.
38. Turel, I.; Kljun, J.; Perdih, F.; Morozova, E.; Bakulev, V.; Kasyanenko, N.; Byl, J. A. W.; Osheroff, N. *Inorg. Chem.*, **2010**, *49* (23), 10750-10752.
39. Lewandowski, E. M.; Skiba, J.; Torelli, N. J.; Rajnisz, A.; Solecka, J.; Kowalski, K.; Chen, Y. *Chem. Commun.*, **2015**, *51* (28), 6186-6189.
40. Pavan, F. R.; Poelhsitz, G. V.; Barbosa, M. I. F.; Leite, S. R. A.; Batista, A. A.; Ellena, J.; Sato, L. S.; Franzblau, S. G.; Moreno, V.; Gambino, D.; Leite, C. Q. F. *Eur. J. Med. Chem.*, **2011**, *46* (10), 5099-5107.
41. Pavan, F. R.; Poelhsitz, G. V.; da Cunha, L. V.; Barbosa, M. I.; Leite, S. R.; Batista, A. A.; Cho, S. H.; Franzblau, S. G.; de Camargo, M. S.; Resende, F. A.; Varanda, E. A.; Leite, C. Q. *PloS one*, **2013**, *8* (5), e64242.



- 
42. Pavan, F. R.; Poelhsitz, G. V.; do Nascimento, F. B.; Leite, S. R. A.; Batista, A. A.; Deflon, V. M.; Sato, D. N.; Franzblau, S. G.; Leite, C. Q. F. *Eur. J. Med. Chem.*, **2010**, *45* (2), 598-601.
43. Perera, A. S.; Wang, H.; Basel, M. T.; Pokhrel, M. R.; Gamage, P. S.; Kalita, M.; Wendel, S.; Sears, B.; Welideniya, D.; Liu, Y.; Turro, C.; Troyer, D. L.; Bossmann, S. H. *Langmuir*, **2013**, *29* (1), 308-315.
44. Pokhrel, M. R.; Gamage, P.; Kalita, M.; Shi, A.; Bossmann, S. H. *JNCS*, **2009**, *23*, 2-10.
45. Wheate, N. J.; Walker, S.; Craig, G. E.; Oun, R. *Dalton Trans.*, **2010**, *39* (35), 8113-8127.
46. Biot, C.; Glorian, G.; Maciejewski, L. A.; Brocard, J. S.; Domarle, O.; Blampain, G.; Millet, P.; Georges, A. J.; Abessolo, H.; Dive, D.; Lebibi, J. *J. Med. Chem.*, **1997**, *40* (23), 3715-3718.
47. Biot, C.; Nosten, F.; Fraisse, L.; Ter-Minassian, D.; Khalife, J.; Dive, D. *Parasite*, **2011**, *18* (3), 207-14.
48. Sousa, E. H. S.; de Mesquita Vieira, F. G.; Butler, J. S.; Basso, L. A.; Santiago, D. S.; Diógenes, I. C. N.; Lopes, L. G. d. F.; Sadler, P. J. *J. Inorg. Biochem.*, **2014**, *140*, 236-244.
49. Sousa, E. H. S.; Basso, L. A.; Santos, D. S.; Diógenes, I. C. N.; Longhinotti, E.; de França Lopes, L. G.; de Sousa Moreira, Í. *J. Biol. Inorg. Chem.*, **2012**, *17* (2), 275-283.
50. Oliveira, J. S.; Sousa, E. H. S.; Basso, L. A.; Palaci, M.; Dietze, R.; Santos, D. S.; Moreira, I. S. *Chem. Commun.*, **2004**, (3), 312-313.
51. N. J. Turro; V. Ramamurthy; Scaiano, J. C., *Principles of Molecular Photochemistry: An Introduction*. University Science Books: USA, 2009.

- 
52. Sýkora, J.; Šima, J. *Coord. Chem. Rev.*, **1990**, *107* (0), 1-212.
53. Sole, J. G.; Bausa, L. E.; Jaque, D., *An Introduction to the Optical Spectroscopy of Inorganic Solids*. John Wiley & Sons: 2005.
54. Balzani, V.; Bergamini, G.; Campagna, S.; Puntoriero, F., Photochemistry and Photophysics of Coordination Compounds: Overview and General Concepts. In *Photochemistry and Photophysics of Coordination Compounds I*, Balzani, V.; Campagna, S., Eds. Springer Berlin Heidelberg: 2007; Vol. 280, pp 1-36.
55. Kalyanasundaram, K., *Photochemistry of Polypyridine and Porphyrin Complexes*. Academic Press: San Diego, CA, 1992.
56. Reddy, K. V., *Symmetry and Spectroscopy of Molecules*. New Age International: New Delhi, 1998.
57. Dabrowiak, J. C., *Metals in Medicine*. Wiley: West Sussex, UK, 2009.
58. Wardle, B., *Principles and Applications of Photochemistry*. Wiley: West Sussex, UK, 2009.
59. Lytle, F. E.; Hercules, D. M. *J. Am. Chem. Soc.*, **1969**, *91* (2), 253-257.
60. Campagna, S.; Puntoriero, F.; Nastasi, F.; Bergamini, G.; Balzani, V., Photochemistry and Photophysics of Coordination Compounds: Ruthenium. In *Photochemistry and Photophysics of Coordination Compounds I*, Balzani, V.; Campagna, S., Eds. Springer Berlin Heidelberg: 2007; Vol. 280, pp 117-214.
61. Durham, B.; Walsh, J. L.; Carter, C. L.; Meyer, T. J. *Inorg. Chem.*, **1980**, *19* (4), 860-865.
62. Bonnett, R., *Chemical Aspects of Photodynamic Therapy*. Gordon and Breach Science Publishers: The Netherlands, 2000.
63. Ackroyd, R.; Kelty, C.; Brown, N.; Reed, M. *Photochem. Photobiol.*, **2001**, *74* (5), 656-669.

- 
64. Edelson, R.; Berger, C.; Gasparro, F.; Jegasothy, B.; Heald, P.; Wintroub, B.; Vonderheid, E.; Knobler, R.; Wolff, K.; Plewig, G.; McKiernan, G.; Christiansen, I.; Oster, M.; Honigsmann, H.; Wilford, H.; Kokoschka, E.; Rehle, T.; Perez, M.; Stingl, G.; Laroche, L. *N. Engl. J. Med.*, **1987**, *316* (6), 297-303.
65. Zic, J. A.; Miller, J. L.; Stricklin, G. P.; King Jr, L. E. *Ther. Apher.*, **1999**, *3* (1), 50-62.
66. Usuda, J.; Kato, H.; Okunaka, T.; Furukawa, K.; Tsutsui, H.; Yamada, K.; Suga, Y.; Honda, H.; Nagatsuka, Y.; Ohira, T.; Tsuboi, M.; Hirano, T. *J. Thorac. Oncol.*, **2006**, *1* (5), 489-493.
67. Castano, A. P.; Demidova, T. N.; Hamblin, M. R. *Photodiagnosis Photodyn. Ther.*, **2004**, *1* (4), 279-293.
68. Toyokuni, S. *Pathol. Int.*, **1999**, *49* (2), 91-102.
69. Aveline, B. M., Chapter 2 Primary processes in photosensitization mechanisms. In *Comprehensive Series in Photosciences*, Piergiacomo Calzavara-Pinton, R.-M. S.; Bernhard, O., Eds. Elsevier: 2001; Vol. Volume 2, pp 17-37.
70. Leanne B, J.; Ross W, B. *Met. Based Drugs*, **2008**, *2008*, 276109.
71. Ali, H.; van Lier, J. E. *Chem. Rev.*, **1999**, *99* (9), 2379-2450.
72. Mongelli, M. T.; Heinecke, J.; Mayfield, S.; Okyere, B.; Winkel, B. S. J.; Brewer, K. J. *J. Inorg. Biochem.*, **2006**, *100* (12), 1983-1987.
73. Schmitt, F.; Govindaswamy, P.; Süß-Fink, G.; Ang, W. H.; Dyson, P. J.; Juillerat-Jeanneret, L.; Therrien, B. *J. Med. Chem.*, **2008**, *51* (6), 1811-1816.
74. Park, K.; Lee, J. H. *Oncol. Rep.*, **2007**, *17* (3), 537-40.
75. Wang, Y.-J.; Pan, M.-H.; Cheng, A.-L.; Lin, L.-I.; Ho, Y.-S.; Hsieh, C.-Y.; Lin, J.-K. *J. Pharm. Biomed. Anal.*, **1997**, *15* (12), 1867-1876.

- 
76. Banerjee, S.; Prasad, P.; Hussain, A.; Khan, I.; Kondaiah, P.; Chakravarty, A. R. *Chem. Commun.*, **2012**, 48 (62), 7702-7704.
77. Vaupel, P.; Mayer, A. *Cancer Metastasis Rev.*, **2007**, 26 (2), 225-239.
78. Ruggiero, E.; Alonso-de Castro, S.; Habtemariam, A.; Salassa, L., *The Photochemistry of Transition Metal Complexes and Its Application in Biology and Medicine*. Springer: Berlin, 2014; pp 1-39.
79. Rosselli, M.; Keller, R.; Dubey, R. *Hum. Reprod. Update*, **1998**, 4 (1), 3-24.
80. Xu, W.; Liu, L. Z.; Loizidou, M.; Ahmed, M.; Charles, I. G. *Cell Res.*, **2002**, 12 (5-6), 311-320.
81. Patra, A. K.; Rowland, J. M.; Marlin, D. S.; Bill, E.; Olmstead, M. M.; Mascharak, P. K. *Inorg. Chem.*, **2003**, 42 (21), 6812-6823.
82. Eroy-Reveles, A. A.; Leung, Y.; Beavers, C. M.; Olmstead, M. M.; Mascharak, P. K. *J. Am. Chem. Soc.*, **2008**, 130 (13), 4447-4458.
83. Rose, M. J.; Olmstead, M. M.; Mascharak, P. K. *Polyhedron*, **2007**, 26 (16), 4713-4718.
84. Patra, A. K.; Mascharak, P. K. *Inorg. Chem.*, **2003**, 42 (23), 7363-7365.
85. De Leo, M.; Ford, P. C. *J. Am. Chem. Soc.*, **1999**, 121 (9), 1980-1981.
86. Ryter, S. W.; Otterbein, L. E. *BioEssays*, **2004**, 26 (3), 270-280.
87. Prockop, L. D.; Chichkova, R. I. *J. Neurol. Sci.*, **2007**, 262 (1-2), 122-130.
88. Gonzalez, M. A.; Yim, M. A.; Cheng, S.; Moyes, A.; Hobbs, A. J.; Mascharak, P. K. *Inorg. Chem.*, **2012**, 51 (1), 601-608.
89. Pierri, A. E.; Pallaoro, A.; Wu, G.; Ford, P. C. *J. Am. Chem. Soc.*, **2012**, 134 (44), 18197-18200.
90. Garner, R. N.; Gallucci, J. C.; Dunbar, K. R.; Turro, C. *Inorg. Chem.*, **2011**, 50 (19), 9213-9215.

- 
91. Respondek, T.; Garner, R. N.; Herroon, M. K.; Podgorski, I.; Turro, C.; Kodanko, J. J. *J. Am. Chem. Soc.*, **2011**, *133* (43), 17164-17167.
92. Zayat, L.; Calero, C.; Alborés, P.; Baraldo, L.; Etchenique, R. *J. Am. Chem. Soc.*, **2003**, *125* (4), 882-883.
93. Zayat, L.; Salierno, M.; Etchenique, R. *Inorg. Chem.*, **2006**, *45* (4), 1728-1731.
94. You, Y.; Park, S. Y. *Dalton Trans.*, **2009**, (8), 1267-1282.
95. Lo, K. K.-W.; Li, S. P.-Y.; Zhang, K. Y. *New J. Chem.*, **2011**, *35* (2), 265-287.
96. Lee, P.-K.; Law, W. H.-T.; Liu, H.-W.; Lo, K. K.-W. *Inorg. Chem.*, **2011**, *50* (17), 8570-8579.
97. Lau, J. S.-Y.; Lee, P.-K.; Tsang, K. H.-K.; Ng, C. H.-C.; Lam, Y.-W.; Cheng, S.-H.; Lo, K. K.-W. *Inorg. Chem.*, **2009**, *48* (2), 708-718.
98. Gill, M. R.; Garcia-Lara, J.; Foster, S. J.; Smythe, C.; Battaglia, G.; Thomas, J. A. *Nature Chem.*, **2009**, *1* (8), 662-667.
99. Gill, M. R.; Thomas, J. A. *Chem. Soc. Rev.*, **2012**, *41* (8), 3179-3192.
100. Friedman, A. E.; Chambron, J. C.; Sauvage, J. P.; Turro, N. J.; Barton, J. K. *J. Am. Chem. Soc.*, **1990**, *112* (12), 4960-4962.
101. Erkkila, K. E.; Odom, D. T.; Barton, J. K. *Chem. Rev.*, **1999**, *99* (9), 2777-2796.
102. Olson, E. J. C.; Hu, D.; Hörmann, A.; Jonkman, A. M.; Arkin, M. R.; Stemp, E. D. A.; Barton, J. K.; Barbara, P. F. *J. Am. Chem. Soc.*, **1997**, *119* (47), 11458-11467.
103. Jackson, B. A.; Barton, J. K. *J. Am. Chem. Soc.*, **1997**, *119* (52), 12986-12987.
104. Pierre, V. C.; Kaiser, J. T.; Barton, J. K. *Proc. Natl. Acad. Sci.*, **2007**, *104* (2), 429-434.
105. Jacquet, L.; Davies, R. J. H.; Kirsch-De Mesmaeker, A.; Kelly, J. M. *J. Am. Chem. Soc.*, **1997**, *119* (49), 11763-11768.

- 
106. Barragán, F.; López-Senín, P.; Salassa, L.; Betanzos-Lara, S.; Habtemariam, A.; Moreno, V.; Sadler, P. J.; Marchán, V. *J. Am. Chem. Soc.*, **2011**, *133* (35), 14098-14108.
107. Q. Products AG, Q.Light Phototherapy Beauty & Skin Care. [http://www.colourlight.ch/images/downloads/Brochure\\_Cosmetic\\_E.PDF](http://www.colourlight.ch/images/downloads/Brochure_Cosmetic_E.PDF) (accessed 1st Oct 2013).
108. Wachter, E.; Heidary, D. K.; Howerton, B. S.; Parkin, S.; Glazer, E. C. *Chem. Commun.*, **2012**, *48* (77), 9649-9651.
109. Albani, B. A.; Pena, B.; Dunbar, K. R.; Turro, C. *Photochem. Photobiol. Sci.*, **2014**, *13* (2), 272-280.
110. Medlycott, E. A.; Hanan, G. S. *Chem. Soc. Rev.*, **2005**, *34* (2), 133-142.
111. Bahreman, A.; Cuello-Garibo, J.-A.; Bonnet, S. *Dalton Trans.*, **2014**, *43* (11), 4494-4505.
112. Bonnet, S. *Comments Inorg. Chem.*, **2014**, 1-35.
113. Pawlicki, M.; Collins, H. A.; Denning, R. G.; Anderson, H. L. *Angew. Chem. Int. Ed.*, **2009**, *48* (18), 3244-3266.
114. Castellano, F. N.; Malak, H.; Gryczynski, I.; Lakowicz, J. R. *Inorg. Chem.*, **1997**, *36* (24), 5548-5551.
115. Four, M.; Riehl, D.; Mongin, O.; Blanchard-Desce, M.; Lawson-Daku, L. M.; Moreau, J.; Chauvin, J.; Delaire, J. A.; Lemerrier, G. *Phys. Chem. Chem. Phys.*, **2011**, *13* (38), 17304-17312.
116. Boca, S. C.; Four, M.; Bonne, A.; van der Sanden, B.; Astilean, S.; Baldeck, P. L.; Lemerrier, G. *Chem. Commun.*, **2009**, (30), 4590-4592.
117. Haase, M.; Schäfer, H. *Angew. Chem. Int. Ed.*, **2011**, *50* (26), 5808-5829.

- 
118. Ruggiero, E.; Habtemariam, A.; Yate, L.; Mareque-Rivas, J. C.; Salassa, L. *Chem. Commun.*, **2014**, 50 (14), 1715-1718.

# **Chapter 2**

## **Experimental methods and materials**



---

## Chapter 2

### Experimental methods and materials

This chapter describes the general techniques and instrumentation that are used in this thesis. Additional detail will be given in the appropriate Chapter where the technique / instrument is used.

#### 2.1. NMR spectroscopy

$^1\text{H}$  and  $^{13}\text{C}$  NMR spectra were recorded on either a Bruker DPX-300 ( $^1\text{H}$ : 300.13 MHz), Bruker AV-400 ( $^1\text{H}$ : 399.10 MHz) or Bruker AV III-500 HD ( $^1\text{H}$ : 500.13 MHz) spectrometer. Amber NMR tubes (5 mm diameter) were used for characterisation of complexes while 5 mm clear NMR tubes were used for photoirradiation studies.  $^1\text{H}$ -NMR,  $^{13}\text{C}$ -APT,  $^1\text{H}$ - $^1\text{H}$  COSY and  $^1\text{H}$ - $^{13}\text{C}$  HSQC spectra were recorded using standard pulse sequences. Typically the data were acquired with 16-128 transients into 2048-33,000 data points over a spectral width of 21-25 ppm. The  $^1\text{H}$  and  $^{13}\text{C}$  resonances were calibrated with the residual solvent peak ( $\delta_{\text{H}}$  DMSO- $d_6$  = 2.50 ppm,  $\delta_{\text{H}}$  acetone- $d_6$  = 2.05 ppm,  $\delta_{\text{C}}$  acetone- $d_6$  = 29.84 and 206.26 ppm, and  $\delta_{\text{H}}$  acetonitrile- $d_3$  = 1.94 ppm) or by the addition of 1,4-dioxane ( $\delta_{\text{H}}$  = 3.75 ppm) in  $\text{D}_2\text{O}$ .<sup>1</sup>

#### 2.2. X-ray crystallography

Data collection and solution of the structures were performed by Dr Guy Clarkson from Department of Chemistry at University of Warwick. Diffraction data were collected on an Oxford Diffraction Gemini four-circle system with Ruby CCD area detector and an Oxford Cryosystem Cryostream Cobra cooler. The structure was solved by direct methods using SHELXS<sup>2</sup> (TREF) with additional light atoms found by Fourier methods. Hydrogen atoms were added at calculated positions and refined

using a riding model with freely rotating methyl groups. Anisotropic displacement parameters were used for all non-H atoms; H-atoms were given isotropic displacement parameters equal to 1.2 (or 1.5 for OH and NH hydrogen atoms) times the equivalent isotropic displacement parameter of the atom to which the H-atom is attached. Refinement used SHELXL 97.<sup>3</sup> The solved structures were analysed by Mercury 3.3.

### 2.3. Elemental analysis

Elemental analysis was performed by Exeter Analytical using a CHN/O/S Elemental Analyser (CE440).

### 2.4. Light sources

Power measurements for the KiloArc<sup>TM</sup> and blue LED setup were recorded using International Light Technologies Powermeter (ILT1400-A) equipped with SEL 033 detector and flat response visible filter F/W (400-1064 nm). The output spectrum of each light source was measured using an Ocean Optics USB4000-UV-Vis spectrophotometer equipped with a fibre optic cable. The data were processed using Ocean Optics SpectraSuite software.

#### 2.4.1. KiloArc<sup>TM</sup> lamp

The KiloArc<sup>TM</sup> broadband arc lamp was fitted with a liquid filter, monochromator and sample compartment in order to photoirradiate samples with various wavelengths of light, see Figure 2.1. The power and output spectrum of each wavelength used was recorded with the appropriate high-pass cut off filter placed in the path of the beam, see Table 2.1 and Figure 2.2.

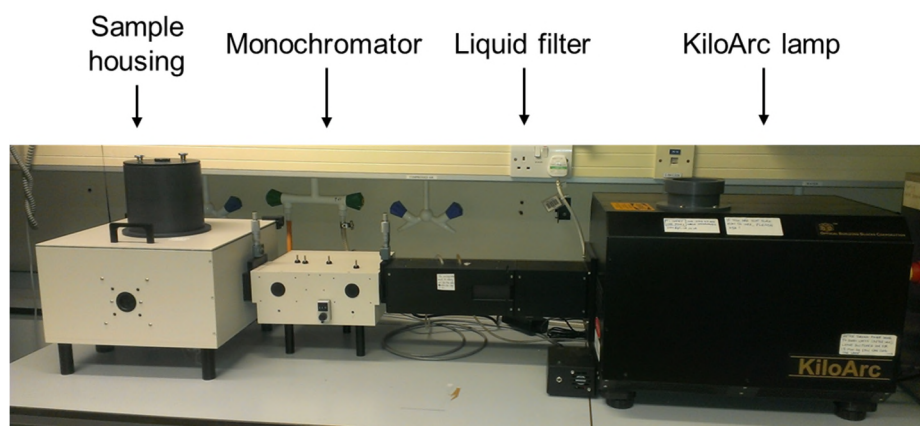


**Figure 2.1.** Image of KiloArc™ lamp setup.

**Table 2.1.** Wavelengths used with KiloArc™ lamp.

Wavelength (nm)	High-pass filter (nm)	Power (mW cm <sup>-2</sup> )
440	UV	16
465	UV	16
500	475	10
560	530	9
600	570	6
610	590	6
800	610	3

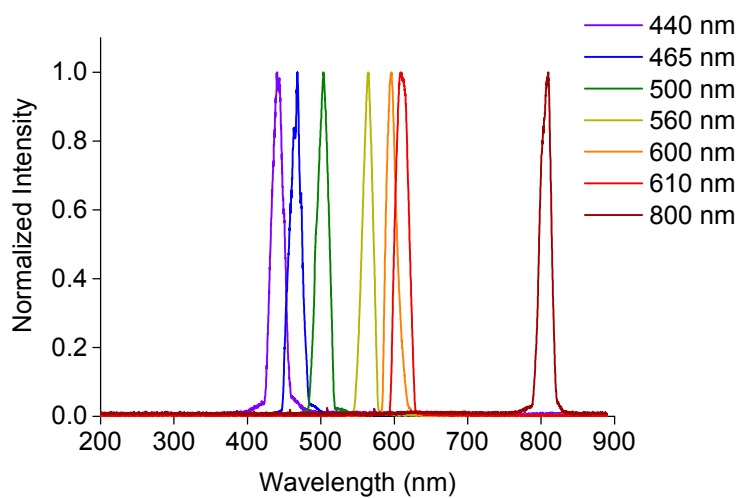


**Figure 2.2.** Output spectrum for each wavelength used from the KiloArc™ lamp.

### 2.4.2. Blue LED

The blue LED was used to either photoirradiate a sample in a cuvette or an NMR tube, see Figure 2.3. The blue LED was placed 4 cm away from the sample in both cases. The output spectrum was measured and was found to be centred at 463 nm with a power of  $50 \text{ mW cm}^{-2}$ , see Figure 2.4.

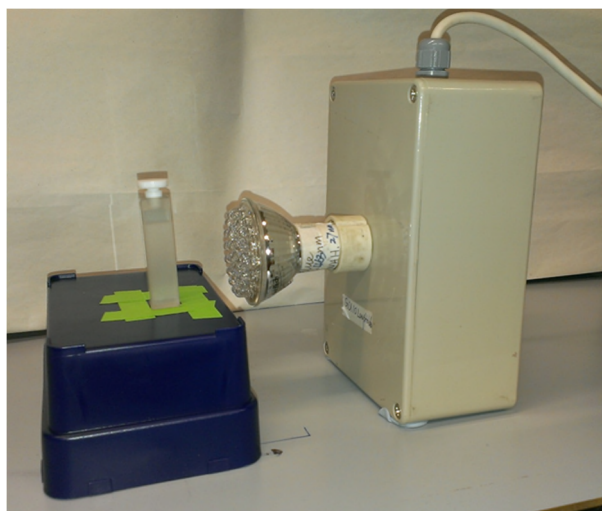


**Figure 2.3.** Image of blue LED used with a sample in a cuvette.

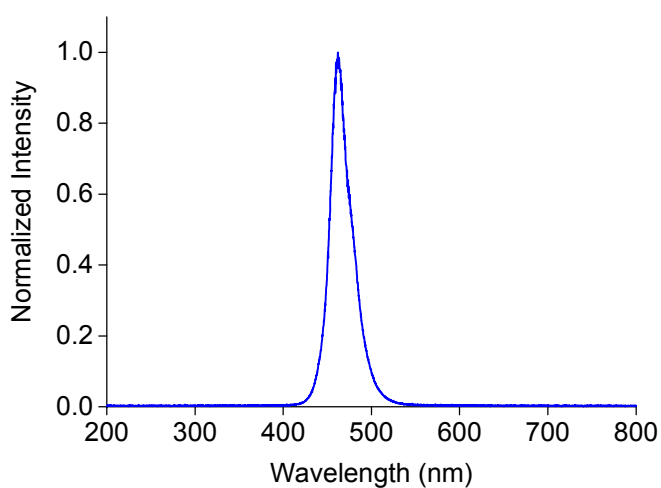


**Figure 2.4.** Output spectrum of blue LED.

### 2.4.3. 96-array blue LED

A 96-array of blue LED's (see Figure 2.5) was constructed by Mr Rod Wesson, Electrical and Electronics Workshop, Department of Chemistry from University of Warwick. The LED's used were Multicomp OVL-5523 5 mm LED's with a dominant wavelength of 465 nm and a power of  $20 \text{ mW cm}^{-2}$  once constructed into the array. The design will be discussed in more detail in Chapter 5.

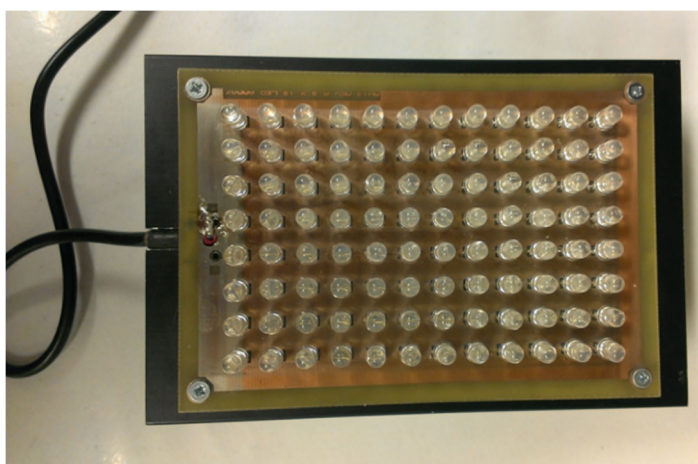


**Figure 2.5.** Image of 96-array blue LED.

### 2.4.4. 32-array multi-coloured LED

A 32-array of blue LED's with individual switches (see Figure 2.6) was constructed by Mr Rod Wesson, Electrical and Electronics Workshop, Department of Chemistry from University of Warwick. The LED's used were Multicomp OVL-5523 5 mm (dominant wavelength of 465 nm), Multicomp OVL-5524 5 mm (dominant wavelength of 520 nm), Multicomp OVL-5526 5 mm (dominant wavelength of 589 nm) and Multicomp OVL-5528 5 mm (dominant wavelength of 625 nm) with a power of  $5 \text{ mW cm}^{-2}$  once constructed into the array. The design will be discussed in more detail in Chapter 5.

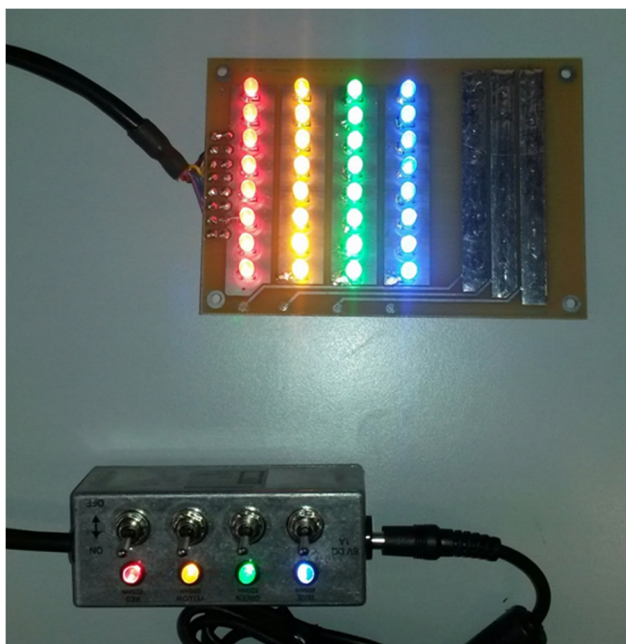


**Figure 2.6.** Image of 32-array multi-coloured LED (625 nm, 589 nm, 520 nm and 465 nm).

#### 2.4.5. Laser set-up

The general set-up of the laser system is described below, with any changes stated in the appropriate section. The equipment was maintained by Dr Simon E. Greenough from Department of Chemistry at University of Warwick and has been described previously.<sup>4-5</sup>

The sample was recirculated using a peristaltic pump (Masterflex) with PTFE tubing throughout, at a flow speed sufficient to ensure fresh solution was sampled with each laser shot. Pump and probe pulses were generated from a commercially available femtosecond Ti-sapphire regenerative amplified laser system (SpectraPhysics, Spitfire XP) operating at 1 kHz. The output of the laser system is split to give two 800 nm beams: (i) 950 mW (pump) and (ii) 5 mW (probe). Broadband white light continuum (340 to 675 nm) probe pulses were generated by focusing an attenuated probe beam into a vertically translated CaF<sub>2</sub> window and detected using a fibre couple UV/Vis

spectrometer (Avantes, AvaSpec Ultrafast). The use of a 500 Hz mechanical chopper (Thorlabs) in the pump beam creates an alternating pumped and non-pumped sample from which a difference spectrum was calculated after probing. Pump–probe delays (up to 2 ns) were created using a motorized optical delay line in the probe beam path. The pump beam was focused behind the sample to ensure a beam waist  $\sim 3$  times that of the probe. A purpose built LabVIEW code controlled the system and acquired data.

#### ***2.4.5.1. One-photon transient absorption spectroscopy***

This method was used in Chapter 4. The sample was delivered using a 1 mm path length flow through quartz cuvette (Starna UK). The pump beam was used to pump an optical parametric amplifier (OPA) (Light Conversion, TOPAS-C (UV-VIS)). The OPA provides the pump source with tuneable wavelengths in the range 240–1160 nm, here sample was excited using 340 nm (3.65 eV), 640  $\mu$ W,  $\sim 50$  fs pump pulses. The pump beam was focused 10 mm behind the sample.

#### ***2.4.5.2. Two-photon transient absorption spectroscopy***

This method was used in Chapter 6. The sample was delivered using a steel flow-through cell (Harrick Scientific), comprising two  $\text{CaF}_2$  windows and a 950  $\mu$ m thick Teflon spacer, which defines the optical path length. The pump beam was attenuated to provide a pump power of 24 mW (this maximum power limit prevented white light generation in the sample) using a neutral density filter. Sample was excited using 800 nm (1.55 eV),  $\sim 50$  fs pump pulses. This power was further attenuated, as required for power dependence studies, with a second, variable neutral density filter to give excitation energies in the range of 0.5–1 mW. The pump beam was focused  $\sim 20$  mm behind the sample to ensure a beam waist at the sample of 150  $\mu$ m.

#### 2.4.5.3. Two-photon absorption spectroscopy

This method was used in Chapter 6. The sample (350  $\mu\text{L}$ ) was placed in a 5 mm path length quartz cuvette and stirred using a micro-stirrer bar and magnetic stirring plate. The pump beam was used to pump an optical parametric amplifier (OPA) (Light Conversion, TOPAS-C) to generate tuneable wavelength fs laser pulses - here 800 nm (1.55 eV) and 600 nm  $\sim$ 35 fs pump pulses were used. A fused silica lens ( $f = 75$  mm) was used to focus the beam in the centre of the cuvette, see Figure 2.7. Power was attenuated using a neutral density filter to avoid undesired white light generation in the quartz or solution. This power was further attenuated, as required for power dependence studies, with a second, variable neutral density filter to give excitation energies in the range of 12-24 mW. The probe beam was not necessary due to the use of Ocean Optics USB4000-UV-Vis spectrophotometer equipped with a fibre optic cable and Miniature Deuterium Tungsten Halogen UV-Vis-NIR Light Source (DT-MINI-2-GS). The data were processed using Ocean Optics SpectraSuite software.

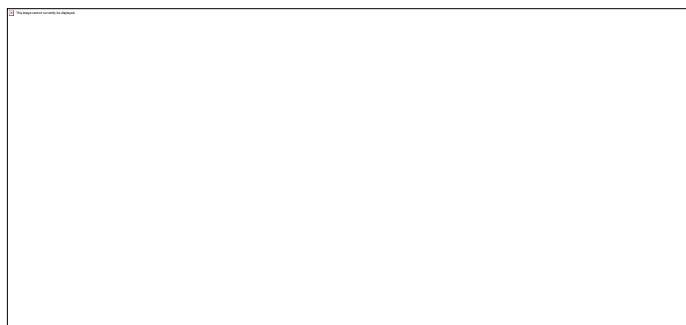


**Figure 2.7.** Schematic of the laser setup for two-photon activation.

### 2.5. Electrospray ionisation mass spectrometry (ESI-MS)

Positive ion ESI-MS spectra were obtained using an Agilent 6130B single quad coupled to an automated sample delivery system (isocratic Agilent 1100 HPLC



without column) with 80% methanol: 20% H<sub>2</sub>O as the mobile phase. Samples were diluted with either double deionised water (ddH<sub>2</sub>O) or acetonitrile. The detection of ruthenium species was aided by its isotope pattern with natural abundance of <sup>96</sup>Ru (5.54%), <sup>98</sup>Ru (1.87%), <sup>99</sup>Ru (12.76), <sup>100</sup>Ru (12.60), <sup>101</sup>Ru (17.06%), <sup>102</sup>Ru (31.55%) and <sup>104</sup>Ru (18.62%).

## 2.6. High resolution electrospray mass spectrometry (HR-MS)

Data collection was performed by Dr Lijiang Song and Mr. Phil Aston from the Department of Chemistry at University of Warwick. Positive ion HR-MS spectra were obtained on a Bruker MicroTOF. Samples were diluted with either double deionised water (ddH<sub>2</sub>O) or acetonitrile. The data were processed using Bruker Daltonics DataAnalysis version 4.1. The error was calculated using the equation below:

$$\text{Error (ppm)} = \left( \frac{\text{Experimental (m/z)} - \text{Calculated (m/z)}}{\text{Calculated (m/z)}} \right) \times (1 \times 10^{-6})$$

## 2.7. Liquid chromatography-high resolution mass spectrometry (LC-HRMS)

Data collection was performed by Dr Lijiang Song from the Chemistry Department at University of Warwick. LC-MS analysis was carried out with Dionex 3000RS UHPLC coupled with Bruker MaXis Q-TOF mass spectrometer. An Agilent Zorbax Eclipse plus column (C18, 100 x 2.1 mm, 1.8 μm) was used. Mobile phases consisted of A (water with 0.1% formic acid) and B (ACN with 0.1% formic acid). A gradient of 5% B to 100% B in 15 minutes was employed with a flow rate at 0.2 ml min<sup>-1</sup>. The UV detector was set to detect at 254 nm. The mass spectrometer was operated in electrospray positive mode with a scan range 50-2,000 m/z. Source conditions were: end plate offset at -500 V; capillary at -4500 V; nebulizer gas (N<sub>2</sub>) at 1.6 bar, dry gas

(N<sub>2</sub>) at 8 L min<sup>-1</sup>; dry temperature at 180 °C. Ion transfer conditions were: ion funnel RF at 200 V pp; multiple RF at 200 V pp; quadrupole low set at 55 m/z; collision energy at 5.0 eV; collision RF at 600 V pp; ion cooler RF at 50-350 V pp; transfer time set at 121 µs; pre-pulse storage time set at 1 µs. Calibration was made with sodium formate (10 mM) through a loop injection of 20 µL of standard solution at beginning of each run. Samples were diluted with either double deionised water (ddH<sub>2</sub>O) or acetonitrile. The data were processed using Bruker Daltonics DataAnalysis version 4.1. The error (ppm) was calculated as in Section 2.6.

## **2.8. Liquid chromatography-mass spectrometry (LC-MS)**

Data collection was performed by Mr. Phil Aston from the Department of Chemistry at University of Warwick. The LC-MS spectra were obtained on an Agilent 1200 series liquid chromatography system coupled to a HCT-Ultra-ETD-PTR PTM Discovery. An Agilent Zorbax Eclipse plus column (C18, 250 x 4.6 mm, 5 µm) was used. Mobile phases consisted of A (water with 0.1% trifluoroacetic acid) and B (ACN with 0.1% trifluoroacetic acid). A gradient of 10% B (0 min), 80% B (30 min), 80% B (40 min), 10% B (41 min) and 10% B (55 min) was employed with a flow rate at 1 ml min<sup>-1</sup> and UV detector was set to detect at 254 nm. Samples were diluted with either double deionised water (ddH<sub>2</sub>O) or acetonitrile. The data were processed using Bruker Daltonics DataAnalysis version 4.1.

## **2.9. High performance liquid chromatography (HPLC)**

Data collection was performed by Mr. Adam Millett from the Department of Chemistry at University of Warwick. HPLC was performed on an Agilent 1200 system. The column, mobile phase, gradient and detection were performed as in

Section 2.8. Samples were diluted with either double deionised water (ddH<sub>2</sub>O) or acetonitrile. The sample was injected (50  $\mu$ L) into a 100  $\mu$ L loop.

### **2.10. UV-visible absorption spectroscopy**

UV-visible absorption spectra were recorded on a Varian Cary 300 UV-vis spectrophotometer fitted with an external Varian Cary temperature controller. Spectra were recorded at 298 K from 800 nm to 200 nm with a scan rate of 600 nm min<sup>-1</sup>. The spectra were processed using UV-Winlab software.

### **2.11. Microplate reader**

The change in optical density (OD) of a bacterial suspension at 600 nm was monitored using Thermo Labsystems IEMS MF microplate reader with a 96-well plate. The conditions of each experiment was a shake function before taking an OD<sub>600 nm</sub> reading with a speed of 1020 rpm for 1 min, a background shake with speed of 360 rpm for on time of 30 s and off time of 30 s, while maintaining the temperature throughout at 310 K. The OD<sub>600 nm</sub> was monitored over a 72 h period taking OD<sub>600 nm</sub> measurements every 1h. The data were processed using Ascent software version 2.6. A typical OD<sub>600 nm</sub> curve can be found in Figure 2.8.

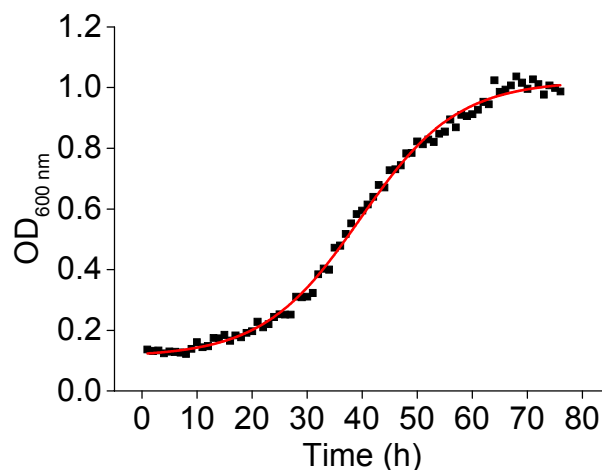


**Figure 2.8.** Typical OD<sub>600 nm</sub> curve observed for a bacterial suspension over a 72 h period fitted to a Boltzmann sigmoidal curve (red line).

The corrected final OD<sub>600 nm</sub> was calculated by taking the final OD<sub>600 nm</sub> measurement at 72 h and subtracting the starting OD<sub>600 nm</sub> at 0 h. In a typical experiment each sample well contained the bacteria and the drug, while the control contained bacteria with no drug. Any changes are specified in the appropriate section. The percentage survival was then calculated using the following:

$$\text{Percentage survival (\%)} = \left( \frac{\text{Corrected final OD}_{600 \text{ nm}} \text{ sample}}{\text{Corrected final OD}_{600 \text{ nm}} \text{ control}} \right) \times 100$$

## 2.12. Synthesis of starting materials

RuCl<sub>3</sub>·3H<sub>2</sub>O was purchased from Precious Metals Online. 2,2'-Bipyridine, 1,10-phenanthroline, lithium chloride (LiCl), sodium iodide (NaI), dimethylformamide (DMF) and acetone were purchased from Sigma Aldrich. The NMR spectroscopy solvents acetone-*d*<sub>6</sub> and DMSO-*d*<sub>6</sub> were purchased from Cambridge Isotope Laboratories Inc.

***cis*-[Ru(bpy)<sub>2</sub>(Cl)<sub>2</sub>]**

The complex was synthesised using a similar procedure as previously described.<sup>6</sup> RuCl<sub>3</sub>·3H<sub>2</sub>O (1 g, 3.8 mmol), 2,2'-bipyridine (1.2 g, 7.7 mmol) and LiCl (1 g, 25 mmol) were refluxed in DMF (30 mL) under nitrogen while stirring in the dark for 8 h. The solution turned to red/violet in colour and was allowed to cool to room temperature. Acetone (110 mL) was added and solution was stored in the freezer at 253 K for 18 h. The solution was filtered and the black precipitate washed with cold water and diethyl ether. Yield 43% (800 mg, 1.7 mmol). Elemental analysis calculated for C<sub>20</sub>H<sub>16</sub>Cl<sub>2</sub>N<sub>4</sub>Ru %C: 49.60, %H: 3.33, %N: 11.57; found %C: 49.44, %H: 3.25, %N: 11.49. <sup>1</sup>H-NMR (DMSO-*d*<sub>6</sub>, 300 MHz) δ<sub>H</sub>: 7.1 (2H, t, *J* = 6.7 Hz), 7.5 (2H, d, *J* = 5.5 Hz), 7.7 (2H, t, *J* = 7.6 Hz), 7.8 (2H, t, *J* = 6.6 Hz), 8.1 (2H, t, *J* = 7.8 Hz), 8.5 (2H, t, *J* = 8.1 Hz), 8.6 (2H, d, *J* = 8.1 Hz), 10.0 (2H, d, *J* = 5.5 Hz).

***cis*-[Ru(bpy)<sub>2</sub>(I)<sub>2</sub>]**

The complex was synthesised using a similar procedure as previously described.<sup>7</sup> Water (10 mL) was degassed by bubbling nitrogen through it for 15 min. *Cis*-[Ru(bpy)<sub>2</sub>(Cl)<sub>2</sub>] was added (100 mg, 200 μmol) and solution heated at 353 K under nitrogen while stirring in the dark for 2 h. The solution turned brown and was cooled to room temperature. The solution was filtered to remove any unreacted starting material. NaI (864 mg, 5.8 mmol) was added and the solution heated at 353 K for a further 2 h. The solution was placed in fridge at 277 K overnight, and then filtered to isolate the black precipitate. Yield 100% (140 mg, 200 μmol). <sup>1</sup>H-NMR (DMSO-*d*<sub>6</sub>, 300 MHz) δ<sub>H</sub>: 7.2 (2H, t, *J* = 6.5 Hz), 7.5 (2H, d, *J* = 5.5 Hz), 7.7 (4H, m), 8.1 (2H, t, *J* = 7.5 Hz), 8.5 (2H, d, *J* = 8.0 Hz), 8.7 (2H, d, *J* = 8.1 Hz), 10.4 (2H, d, *J* = 5.7 Hz).

***cis*-[Ru(phen)<sub>2</sub>(Cl)<sub>2</sub>]**

The complex was synthesised using the procedure described for *cis*-[Ru(bpy)<sub>2</sub>(Cl)<sub>2</sub>] above.<sup>8</sup> RuCl<sub>3</sub>·3H<sub>2</sub>O (100 mg, 380 μmol), LiCl (110 mg, 2.6 mmol) and 1,10-phenanthroline (138 mg, 760 μmol) added to DMF (5 mL). Acetone (25 mL) was added and solution was red/purple. A black precipitate was obtained. Yield 51% (104 mg, 200 μmol). Elemental analysis calculated for C<sub>24</sub>H<sub>16</sub>Cl<sub>2</sub>N<sub>4</sub>Ru %C: 54.15, %H: 3.03, %N: 10.52, found %C: 53.68, %H: 3.30, %N: 10.54. <sup>1</sup>H-NMR (DMSO-d<sub>6</sub>, 400 MHz) δH: 7.3 (2H, dd, *J* = 8.2 and 5.4 Hz), 7.8 (2H, d, *J* = 5.4 Hz), 8.1 (2H, d, *J* = 8.8 Hz), 8.2 (4H, m), 8.3 (2H, d, *J* = 8.9 Hz), 8.7 (2H, d, *J* = 8.1 Hz), 10.3 (2H, d, *J* = 5.2 Hz).

**2.13. References**

1. Fulmer, G. R.; Miller, A. J. M.; Sherden, N. H.; Gottlieb, H. E.; Nudelman, A.; Stoltz, B. M.; Bercaw, J. E.; Goldberg, K. I. *Organometallics*, **2010**, 29 (9), 2176-2179.
2. Sheldrick, G. *Acta Crystallogr. Sect. A*, **1990**, 46 (6), 467-473.
3. Sheldrick, G. M.; Schneider, T. R. *Methods Enzymol.*, **1997**, 277, 319-343.
4. Greenough, S. E.; Roberts, G. M.; Smith, N. A.; Horbury, M. D.; McKinlay, R. G.; Zurek, J. M.; Paterson, M. J.; Sadler, P. J.; Stavros, V. G. *Phys. Chem. Chem. Phys.*, **2014**, 16 (36), 19141-19155.
5. Greenough, S. E.; Horbury, M. D.; Thompson, J. O. F.; Roberts, G. M.; Karsili, T. N. V.; Marchetti, B.; Townsend, D.; Stavros, V. G. *Phys. Chem. Chem. Phys.*, **2014**, 16 (30), 16187-16195.
6. Sullivan, B. P.; Salmon, D. J.; Meyer, T. J. *Inorg. Chem.*, **1978**, 17 (12), 3334-3341.

- 
7. Dwyer, F.; Goodwin, H.; Gyarfas, E. *Aust. J. Chem.*, **1963**, *16* (4), 544-548.
  8. Nakabayashi, Y.; Watanabe, Y.; Nakao, T.; Yamauchi, O. *Inorg. Chim. Acta*, **2004**, *357* (9), 2553-2560.

# **Chapter 3**

## **Synthesis, characterisation and dark solution chemistry of Ru(II) polypyridyl complexes**



---

## Chapter 3

# Synthesis, characterisation and dark solution chemistry of Ru(II) polypyridyl complexes

### 3.1. Introduction

Photoactivation of metal complexes has been widely studied for its use in oncology<sup>1-5</sup> and bacterial infections.<sup>6-8</sup> The technique relies on the sensitizer reaching the target unharmed, allowing selective activation by shining light on the target site. Systematic administration of drugs encounters the issue that the drug has to pass through many organs and cells before it can reach the target site, being exposed to different cell components and enzymes that can deactivate the drug before it reaches its target.<sup>9</sup> In some cases, before a drug can interact with a biomolecule it needs to undergo a chemical reaction. For example, the anticancer agent cisplatin hydrolyses to provide binding sites available for binding to biomolecules such as DNA.<sup>10</sup> Thus before investigating the photoactivation of any potential photoactive drug, it is important to understand its behaviour in aqueous solution in the dark.

The most common targets for drugs are either proteins (e.g. enzymes, receptors) or nucleic acids (e.g. DNA), and a drug can bind to such targets either by a direct reaction and thus covalent bonding, or by intermolecular bonds (e.g. hydrogen bonding, hydrophobic interactions).<sup>11</sup> It is well known that cisplatin binds to DNA, and its binding properties have been extensively studied.<sup>12</sup> Ru(II) octahedral compounds, such as  $[\text{Ru}(\text{azpy})_2\text{Cl}_2]$ , where azpy is 2-(phenylazo)pyridine, have been shown to be cytotoxic to breast cancer cell lines.<sup>13</sup> Since DNA is an important target, the addition of benzimidazole ligands (to simulate the binding of nucleic acids) to form *cis*-

$[\text{Ru}(\text{azpy})_2(\text{MeBim})_2]^{2+}$ , where MeBim is methylbenzimidazole, was investigated and the rotation behaviour of MeBim was explored.<sup>14</sup> Similar analysis was also carried out with *cis*- $[\text{Ru}(\text{bpy})_2(\text{MeBim})_2]^{2+}$ , concluding that more sterically-demanding ligands rotate more slowly.<sup>15</sup> Atropisomers occur in compounds in which rotation about a single bond is hindered. Is it an important area of drug design, as different atropisomers can have different binding affinities to targets and thus different activities.<sup>16-19</sup>

This chapter concentrates on two sets of photoactive antibacterial compounds:

- Ru(II) polypyridyl bis-substituted complexes of the type *cis*- $[\text{Ru}(N-N')_2(\text{L})_2]^{2+}$ , where *N-N'* is 2,2'-bipyridine or 1,10-phenanthroline, and L is nicotinamide or isoniazid (existing antibacterial organic ligands).
- Ru(II) polypyridyl halide complexes of the type *cis*- $[\text{Ru}(\text{bpy})_2(\text{L})\text{X}]^+$ , where bpy is 2,2'-bipyridine, L is either nicotinamide or isonicotinamide and X is Cl or I.

Their dark solution chemistry has been explored, both in terms of their stability in aqueous solution and with respect to any intramolecular interactions that may occur in solution. Intermolecular interactions for Ru(II) polypyridyl bis-substituted complexes have been explored in the solid state by investigating their crystal structures.

## 3.2. Experimental

### 3.2.1. Materials

Nicotinamide (NA), isonicotinamide (INA), isoniazid (INH) and  $\text{NH}_4\text{PF}_6$  were purchased from Sigma-Aldrich and used without further purification. The *cis*- $[\text{Ru}(N-N')_2(\text{X})_2]$  starting materials, where *N-N'* is 2,2'-bipyridine (bpy) or 1,10-phenanthroline

(phen), and X is Cl or I, were synthesised as described in Chapter 2. The solvents used for UV-visible absorption spectroscopy were reagent grade acetone, DMSO and DMF, and deionised water. The NMR spectroscopy solvents acetone-*d*<sub>6</sub>, DMSO-*d*<sub>6</sub> and methanol-*d*<sub>4</sub> were purchased from Cambridge Isotope Laboratories Inc, and D<sub>2</sub>O was purchased from Sigma-Aldrich. All solutions of complexes were kept in the dark.

### 3.2.2. Preparation of Ru(II) polypyridyl halide complexes

Complexes of the type *cis*-[Ru(bpy)<sub>2</sub>(L)X][PF<sub>6</sub>], where bpy is 2,2'-bipyridine; L is nicotinamide or isonicotinamide; and X is Cl or I, were synthesised using a similar procedure as previously described.<sup>20</sup> Typically 1.2 mol equivalent of ligand L was added to a solution of the appropriate *cis*-[Ru(bpy)<sub>2</sub>(X)<sub>2</sub>] starting material in 10 mL of 1:4 v/v water:ethanol mixture. The solution was refluxed under nitrogen while stirring for 5 h, with the reaction vessel covered in foil to avoid light exposure. The resulting solution was cooled to room temperature and filtered to remove any unreacted starting material. The solvent was evaporated under reduced pressure and the resulting residue re-dissolved in 7 mL water. To this, 5 mol equivalent of NH<sub>4</sub>PF<sub>6</sub> was added to give a precipitate and suspension was placed in the fridge at 277 K overnight to encourage further precipitation. The precipitate was collected by filtration and washed with cold water and diethyl ether. If necessary the precipitate was dried overnight under vacuum. Any variation in synthetic procedure is detailed below, including weights of reactants and volume of solvents. <sup>13</sup>C-NMR spectroscopy data was obtained for samples where elemental analysis data is not supplied.

***cis*-[Ru(bpy)<sub>2</sub>(NA)Cl][PF<sub>6</sub>] (1).** A solution of *cis*-[Ru(bpy)<sub>2</sub>(Cl)<sub>2</sub>] (104 mg, 0.2 mmol) and nicotinamide (NA) (30 mg, 0.24 mmol) in 1:4 v/v water:ethanol turned from light red to dark red and NH<sub>4</sub>PF<sub>6</sub> (163 mg, 1 mmol) was added. A dark red precipitate was obtained. Yield 82 % (118 mg, 0.16 mmol). Elemental analysis

calculated for  $C_{26}H_{22}ClF_6N_6OPRu \cdot H_2O$  %C: 42.55, %H: 3.30, %N: 11.45; found %C: 42.26, %H: 2.86, %N: 11.34. ESI-MS calculated for  $C_{26}H_{22}ClN_6ORu [M]^+$   $m/z$  571.1, found  $m/z$  570.9.  $^1H$ -NMR (acetone- $d_6$ , 500 MHz)  $\delta_H$ : 6.9 (1H, NH), 7.3 (1H, ddd,  $J = 7.6, 5.5$  and  $1.2$  Hz), 7.4 (1H, ddd,  $J = 7.6, 5.6$  and  $1.2$  Hz), 7.5 (1H, t,  $J = 7.0$ ), 7.6 (1H, NH), 7.7 (1H, ddd,  $J = 7.7, 5.5$  and  $1.2$  Hz), 7.8 (1H, d,  $J = 5.7$  Hz), 7.9 (1H, ddd,  $J = 7.6, 5.5$  and  $1.1$  Hz), 7.9 (2H, m), 8.1 (1H, d,  $J = 5.7$  Hz), 8.2 (2H, m), 8.3 (1H, dt,  $J = 7.9$  and  $1.5$  Hz), 8.6 (1H, d,  $J = 8.1$  Hz), 8.6 (1H, d,  $J = 8.2$  Hz), 8.6 (1H, d,  $J = 8.1$  Hz), 8.7 (1H, d,  $J = 5.6$  Hz), 8.7 (1H, d,  $J = 8.1$  Hz), 9.1 (2H, br s), 10.1 (1H, d,  $J = 5.6$  Hz).

***cis*-[Ru(bpy) $_2$ (NA)I][PF $_6$ ] (2).** A solution of *cis*-[Ru(bpy) $_2$ (I) $_2$ ] (25 mg, 35  $\mu$ mol) and nicotinamide (NA) (5 mg, 42  $\mu$ mol) in 2.5 mL 1:4 v/v water:ethanol turned from light red to dark red/brown and NH $_4$ PF $_6$  (28 mg, 17  $\mu$ mol) was added. A dark red/brown precipitate was obtained. Yield 35 % (10 mg, 12  $\mu$ mol). ESI-MS calculated for  $C_{26}H_{22}IN_6ORu [M]^+$   $m/z$  663.0, found  $m/z$  662.9.  $^1H$ -NMR (acetone- $d_6$ , 500 MHz)  $\delta_H$ : 6.9 (1H, NH), 7.3 (1H, t,  $J = 6.6$  Hz), 7.4 (2H, m), 7.5 (1H, NH), 7.8 (1H, t,  $J = 6.6$  Hz), 7.9 (2H, m), 8.0 (2H, m), 8.0 (1H, d,  $J = 5.8$  Hz), 8.2 (2H, m), 8.3 (1H, d,  $J = 7.9$  Hz), 8.5 (1H, d,  $J = 8.1$  Hz), 8.6 (1H, d,  $J = 8.0$  Hz), 8.6 (1H, d,  $J = 8.2$  Hz), 8.8 (1H, d,  $J = 8.1$  Hz), 8.9 (1H, d,  $J = 5.4$  Hz), 9.3 (1H, br s), 9.3 (1H, br s), 10.6 (1H, d,  $J = 5.6$ ).  $^{13}C$ -NMR (acetone- $d_6$ , 500 MHz)  $\delta_C$ : 124.1, 124.5, 124.7, 124.8, 125.6, 127.0, 127.7, 128.4, 129.0, 136.2, 137.2, 137.4, 137.4, 137.9, 152.7, 153.7, 154.1, 158.6, 158.9, 159.2, 159.5, 160.1.

***cis*-[Ru(bpy) $_2$ (INA)Cl][PF $_6$ ] (3).** A solution of *cis*-[Ru(bpy) $_2$ (Cl) $_2$ ] (104 mg, 0.2 mmol) and isonicotinamide (INA) (32 mg, 0.26 mmol) in 12 mL 1:5 v/v water:ethanol turned from light red to dark red and NH $_4$ PF $_6$  (163 mg, 0.1 mmol) was added. A dark red was obtained. Yield 92 % (132 mg, 0.18 mmol). Elemental analysis calculated for

$C_{26}H_{22}ClF_6N_6OPRu \cdot H_2O$  %C: 42.55, %H: 3.30, %N: 11.45; found %C: 42.05, %H: 2.88, %N: 11.28. ESI-MS calculated for  $C_{26}H_{22}ClN_6ORu [M]^+$   $m/z$  571.1, found  $m/z$  571.1.  $^1H$ -NMR (acetone- $d_6$ , 400 MHz)  $\delta_H$ : 7.1 (1H, NH), 7.3 (1H, ddd,  $J = 7.7, 5.6$  and 1.2 Hz), 7.4 (1H, ddd,  $J = 7.6, 5.7$  and 1.3 Hz), 7.7 (3H, m), 7.8 (1H, d, 5.6 Hz), 7.9 (1H, ddd,  $J = 7.6, 5.6, 1.2$  Hz), 7.9 (2H, m), 8.1 (1H, d,  $J = 5.6$  Hz), 8.2 (2H, m), 8.6 (1H, d,  $J = 8.2$  Hz), 8.6 (1H, d,  $J = 8.2$  Hz), 8.6 (1H, d,  $J = 8.2$  Hz), 8.7 (1H, d, 5.5 Hz), 8.7 (1H, d,  $J = 8.2$  Hz), 8.9 (1H, br s), 10.1 (1H, d,  $J = 5.6$  Hz).

**Nicotinamide (NA).**  $^1H$ -NMR (acetone- $d_6$ , 400 MHz)  $\delta_H$ : 6.9 (1H, NH), 7.5 (1H, dd,  $J = 8.0$  and 4.9 Hz), 7.7 (1H, NH), 8.3 (1H, dt,  $J = 8.0$  and 1.9 Hz), 8.7 (1H, dd,  $J = 4.9$  and 1.5 Hz), 9.1 (1H, d,  $J = 1.8$  Hz).

**Isonicotinamide (INA).**  $^1H$ -NMR (acetone- $d_6$ , 400 MHz)  $\delta_H$ : 7.0 (1H, NH), 7.7 (1H, NH), 7.8 (2H, dd,  $J = 4.1$  and 1.5 Hz), 8.7 (2H, dd,  $J = 4.0$  and 1.4 Hz).

### 3.2.3. Preparation of Ru(II) polypyridyl bis-substitued complexes

Complexes of the type  $cis-[Ru(N-N')_2(L)_2][PF_6]_2$ , where  $N-N'$  is 2,2'-bipyridine or 1,10-phenanthroline and L is nicotinamide or isoniazid, were synthesised using a similar procedure as previously described.<sup>21</sup> Typically 10 mL water was degassed by bubbling nitrogen through the solution for 15 min. Subsequently, 1 mol equivalent of the appropriate  $cis-[Ru(N-N')_2(Cl)_2]$  starting material was added. The solution was heated at 353 K under nitrogen while stirring for 15 min, with the reaction vessel covered in foil to avoid light exposure. To this, 5 mol equivalent of ligand L was added and solution heated at 353 K for 6 h. Solution was allowed to cool to room temperature and filtered to remove any unreacted starting material. To this, 5 mol equivalent of  $NH_4PF_6$  was added to give a precipitate and suspension was placed in the fridge at 277 K overnight to encourage further precipitation. The precipitate was collected by

filtration and washed with cold water and diethyl ether. If necessary the precipitate was dried overnight under vacuum. Any variation in synthetic procedure is detailed below, including the weights of reactants and volume of solvents.

***cis*-[Ru(bpy)<sub>2</sub>(INH)<sub>2</sub>][PF<sub>6</sub>]<sub>2</sub> (4).** The suspension of *cis*-[Ru(bpy)<sub>2</sub>(Cl)<sub>2</sub>] (104 mg, 0.2 mmol) in water turned to a red solution after heating. Isoniazid (INH) (137 mg, 1 mmol) was added and solution turned from red to deep red. NH<sub>4</sub>PF<sub>6</sub> (163 mg, 1 mmol) was added and a dark red precipitate was obtained. Yield 66 % (130 mg, 0.1 mmol). Suitable crystals for X-ray crystallography were obtained from slow diffusion of 1,4-dioxane into a saturated acetonitrile solution at room temperature (298 K). Elemental analysis calculated for C<sub>32</sub>H<sub>30</sub>F<sub>12</sub>N<sub>10</sub>O<sub>2</sub>P<sub>2</sub>Ru.2H<sub>2</sub>O %C: 37.92, %H: 3.38, %N: 13.82; found %C: 37.99, %H: 3.07, %N: 13.35. ESI-MS calculated for C<sub>32</sub>H<sub>30</sub>N<sub>10</sub>O<sub>2</sub>Ru [M]<sup>2+</sup> *m/z* 344.1, found *m/z* 343.9. <sup>1</sup>H-NMR (DMSO-*d*<sub>6</sub>, 400 MHz) δ<sub>H</sub>: 4.7 (4H, NH<sub>2</sub>), 7.5 (2H, t, *J* = 6.4 Hz), 7.6 (4H, d, *J* = 6.7 Hz), 7.9 (2H, t, *J* = 6.5 Hz), 7.9 (2H, d, *J* = 5.1 Hz), 8.0 (2H, t, *J* = 7.5 Hz), 8.2 (2H, t, *J* = 7.3), 8.5 (4H, d, *J* = 6.4 Hz), 8.6 (2H, d, *J* = 8.3 Hz), 8.7 (2H, d, *J* = 7.8 Hz), 9.0 (2H, d, *J* = 5.4 Hz), 10.2 (2H, NH).

***cis*-[Ru(bpy)<sub>2</sub>(NA)<sub>2</sub>][PF<sub>6</sub>]<sub>2</sub> (5).** The suspension of *cis*-[Ru(bpy)<sub>2</sub>(Cl)<sub>2</sub>] (104 mg, 0.2 mmol) in water turned to a red solution after heating. Nicotinamide (NA) (122 mg, 1 mmol) was added and solution heated to 2.5 h. Solution turned from red to deep red and NH<sub>4</sub>PF<sub>6</sub> (163 mg, 1 mmol) added. An orange precipitate was isolated. Yield 49 % (92 mg, 97 μmol). Suitable crystals for X-ray crystallography were obtained from a saturated water solution at 277 K. Elemental analysis calculated for C<sub>32</sub>H<sub>28</sub>F<sub>12</sub>N<sub>8</sub>O<sub>2</sub>P<sub>2</sub>Ru %C: 40.56, %H: 2.98, %N: 11.82; found %C: 40.25, %H: 2.91, %N: 11.48. ESI-MS calculated for C<sub>32</sub>H<sub>28</sub>N<sub>8</sub>O<sub>2</sub>Ru [M]<sup>2+</sup> *m/z* 329.1, found *m/z* 328.9. <sup>1</sup>H-NMR (acetone-*d*<sub>6</sub>, 500 MHz) δ<sub>H</sub>: 7.0 (2H, NH), 7.6 (6H, m), 8.0 (2H, ddd, *J* = 7.8, 5.6 and 1.3 Hz), 8.1 (2H, td, *J* = 7.9 and 1.4 Hz), 8.3 (4H, m), 8.4 (2H, dt, *J* = 8.0 and

1.5 Hz), 8.6 (2H, d,  $J = 8.1$  Hz), 8.7 (2H, d,  $J = 8.0$  Hz), 8.9 (2H, d,  $J = 5.6$  Hz), 9.0 (2H, s), 9.4 (2H, d,  $J = 5.7$  Hz).

***cis*-[Ru(phen)<sub>2</sub>(INH)<sub>2</sub>][PF<sub>6</sub>]<sub>2</sub> (6).** The suspension of *cis*-[Ru(phen)<sub>2</sub>(Cl)<sub>2</sub>] (25 mg, 47 μmol) in water turned to a red solution after heating. Isoniazid (INH) (32 mg, 0.23 mmol) added and solution turned from red to deep red. NH<sub>4</sub>PF<sub>6</sub> (38 mg, 0.23 mmol) was added and an orange precipitate was obtained. Yield 52% (25 mg, 24 μmol). Suitable crystals for X-ray crystallography were obtained from a saturated water solution with a drop of diethyl ether at 277 K. Elemental analysis calculated for C<sub>36</sub>H<sub>30</sub>F<sub>12</sub>N<sub>10</sub>O<sub>2</sub>P<sub>2</sub>Ru.6H<sub>2</sub>O %C: 38.14, %H: 3.73, %N: 12.35; found %C: 38.50, %H: 3.20, %N: 11.00. ESI-MS calculated for C<sub>36</sub>H<sub>30</sub>N<sub>10</sub>O<sub>2</sub>Ru [M]<sup>2+</sup>  $m/z$  368.1, found  $m/z$  368.2. <sup>1</sup>H-NMR (DMSO-*d*<sub>6</sub>, 400 MHz)  $\delta_{\text{H}}$ : 4.6 (4H, NH<sub>2</sub>), 7.6 (4H, d,  $J = 6.6$  Hz), 7.7 (2H, dd,  $J = 8.5, 5.3$  Hz), 8.1 (2H, d,  $J = 5.1$  Hz), 8.2 (2H, d,  $J = 8.9$  Hz), 8.3 (2H, dd,  $J = 8.4, 5.3$  Hz), 8.3 (2H, d,  $J = 8.9$  Hz), 8.6 (2H, d,  $J = 8.3$  Hz), 8.7 (4H, d,  $J = 5.8$  Hz), 8.9 (2H, d,  $J = 8.3$  Hz), 9.6 (2H, d,  $J = 5.2$  Hz), 10.1 (2H, NH).

***cis*-[Ru(phen)<sub>2</sub>(NA)<sub>2</sub>][PF<sub>6</sub>]<sub>2</sub> (7).** The suspension of *cis*-[Ru(phen)<sub>2</sub>(Cl)<sub>2</sub>] (25 mg, 47 μmol) in water turned to a red solution after heating. Nicotinamide (NA) (29 mg, 0.23 mmol) was added and solution turned from red to deep red. NH<sub>4</sub>PF<sub>6</sub> (38 mg, 0.23 mmol) was added and a yellow precipitate was obtained. Yield 51% (24 mg, 24 μmol). Elemental analysis calculated for C<sub>36</sub>H<sub>28</sub>F<sub>12</sub>N<sub>8</sub>O<sub>2</sub>P<sub>2</sub>Ru.2H<sub>2</sub>O %C: 41.91, %H: 3.13, %N: 10.86; found %C: 41.73, %H: 2.65, %N: 10.56. ESI-MS calculated for C<sub>36</sub>H<sub>28</sub>N<sub>8</sub>O<sub>2</sub>Ru [M]<sup>2+</sup>  $m/z$  353.1, found  $m/z$  352.9. <sup>1</sup>H-NMR (DMSO-*d*<sub>6</sub>, 400 MHz)  $\delta_{\text{H}}$ : 7.4 (2H, ds,  $J = 8.2, 5.8$  Hz), 7.7 (2H, dd,  $J = 8.5, 5.3$  Hz), 7.7 (2H, NH), 8.2 (4H, m), 8.2 (2H, d,  $J = 8.9$  Hz), 8.3 (6H, m), 8.6 (2H, d,  $J = 8.3$  Hz), 8.7 (2H, d,  $J = 5.6$  Hz), 8.8 (2H, s), 8.9 (2H, d,  $J = 8.1$  Hz), 9.6 (2H, d,  $J = 5.2$  Hz).

### 3.2.4. X-ray crystallography

The details of the instrumentation, data collection, and solution of the structures are described in Chapter 2. The crystal structures of *cis*-[Ru(bpy)<sub>2</sub>(INH)<sub>2</sub>][PF<sub>6</sub>]<sub>2</sub> (**4**), *cis*-[Ru(bpy)<sub>2</sub>(NA)<sub>2</sub>][PF<sub>6</sub>]<sub>2</sub> (**5**) and *cis*-[Ru(phen)<sub>2</sub>(INH)<sub>2</sub>][PF<sub>6</sub>]<sub>2</sub> (**6**) discussed in this chapter were determined by Dr Guy Clarkson from the Department of Chemistry at University of Warwick.

### 3.2.5. Dark stability in aqueous solution

#### 3.2.5.1. Hydrolysis of Ru(II) polypyridyl halide complexes

The hydrolysis of the Ru(II) polypyridyl halide complex *cis*-[Ru(bpy)<sub>2</sub>(NA)Cl][PF<sub>6</sub>] (**1**) was monitored by UV-visible absorption spectroscopy. The identity of the hydrolysis products was verified by ESI-MS. The complex was dissolved in either deionised water or 5% (v/v) DMSO, acetone or DMF to give a complex concentration of 40 µM. The absorbance over the range 200 – 800 nm was recorded at several time intervals over 18 – 24 h at 298 K. Where applicable plots of change in absorbance versus time were fitted to the exponential equation  $A = A_0 + Ce^{Rt}$  (where A is absorbance, t is time and A<sub>0</sub>, C and R are calculated parameters) using OriginPro 9.1 to give the half-life (t<sub>1/2</sub>).

#### 3.2.5.2. Stability of Ru(II) polypyridyl bis-substituted complexes

The stability of Ru(II) polypyridyl bis-substituted complexes *cis*-[Ru(bpy)<sub>2</sub>(INH)<sub>2</sub>][PF<sub>6</sub>]<sub>2</sub> (**4**), complexes *cis*-[Ru(bpy)<sub>2</sub>(NA)<sub>2</sub>][PF<sub>6</sub>]<sub>2</sub> (**5**), *cis*-[Ru(phen)<sub>2</sub>(INH)<sub>2</sub>][PF<sub>6</sub>]<sub>2</sub> (**6**) and *cis*-[Ru(phen)<sub>2</sub>(NA)<sub>2</sub>][PF<sub>6</sub>]<sub>2</sub> (**7**) was monitored by UV-visible absorption spectroscopy. The complexes were dissolved in deionised water to give a complex concentration of 40 µM. The absorbance over the range 200 – 800 nm was recorded at several time intervals over 6 h at 298 K.



### 3.2.6. Dynamic behaviour in solution

#### 3.2.6.1. Dynamic behaviour studied by variable temperature $^1\text{H}$ -NMR

Data collection was performed by Dr Ivan Provkes from Department of Chemistry at University of Warwick.  $^1\text{H}$ -NMR spectra of Ru(II) polypyridyl complexes *cis*-[Ru(bpy)<sub>2</sub>(NA)Cl][PF<sub>6</sub>] (**1**), *cis*-[Ru(bpy)<sub>2</sub>(NA)I][PF<sub>6</sub>] (**2**) and *cis*-[Ru(bpy)<sub>2</sub>(NA)<sub>2</sub>][PF<sub>6</sub>]<sub>2</sub> (**5**) in acetone-*d*<sub>6</sub> were obtained initially at 10-30 K intervals from 185-323 K on a Bruker AV-500 spectrometer ( $^1\text{H}$  = 500 MHz) using 5 o.d. NMR tubes. The concentration of each sample was 2.5 mg in 600  $\mu\text{L}$  of NMR solvent (c.a. 6 mM). To obtain an accurate coalescent temperature ( $T_c$ ) for **1** and **2** the intervals were lowered to 2 K around the coalescence point. All data processing was carried out using Bruker Topspin 2.1. By using Equation 3.1 the rate constant at coalescence ( $k_c$ ) of an unequally populated two-site system can be found, where  $X$  is a value taken from tabulated values for various population ( $P$ ) differences ( $\Delta P = (P_1 - P_2)$ ) and  $\delta\nu$  is the difference in resonance frequency of the exchange protons.<sup>22-24</sup> The free energy of activation ( $\Delta G_c^\ddagger$ ) was calculated using Equation 3.2, where  $a$  is a constant with a value of  $1.914 \times 10^{-2} \text{ kJ/mol}$ .<sup>22</sup>

$$k_c = \frac{\pi\delta\nu}{X} \quad \text{Equation 3.1.}$$

$$\Delta G_c^\ddagger = aT_c \left[ 10.319 + \log \left( \frac{T_c}{k_c} \right) \right] \quad \text{Equation 3.2.}$$

NOESY spectra were obtained at 185 K using mixing time of 0.8 s.

### 3.2.6.2. Solvent effect on dynamic behaviour studied by $^1\text{H}$ -NMR

The effect of solvent on the dynamic behaviour of Ru(II) polypyridyl halide complexes *cis*-[Ru(bpy)<sub>2</sub>(NA)Cl][PF<sub>6</sub>] (**1**) and *cis*-[Ru(bpy)<sub>2</sub>(NA)I][PF<sub>6</sub>] (**2**) was studied by investigating the  $^1\text{H}$ -NMR spectra at 298 K in acetone-*d*<sub>6</sub> and DMSO-*d*<sub>6</sub> on a Bruker DPX-400 spectrometer ( $^1\text{H}$  = 400 MHz) using 5 o.d. NMR tubes. The concentration of each sample was 2.5 mg in 600  $\mu\text{L}$  of deuterated solvent (c.a. 6 mM).

### 3.2.6.3. Dynamic behaviour studied by DFT

The starting geometry of the Ru(II) polypyridyl halide complexes *cis*-[Ru(bpy)<sub>2</sub>(NA)Cl][PF<sub>6</sub>] (**1**) and *cis*-[Ru(bpy)<sub>2</sub>(NA)I][PF<sub>6</sub>] (**2**) was adapted from the crystal structure of **5** using the  $\Lambda$  enantiomer, and the DFT geometry optimisation was performed using Gaussian 03 in the gas phase.<sup>25</sup> Becke's three-parameter hybrid functional<sup>26</sup> with Lee-Yang-Parr's gradient-corrected correlation functional (B3LYP)<sup>27</sup> was used. The LanL2DZ basis set<sup>28</sup> and effective core potential were used for the ruthenium atom, and the split valence 3-21G basis set<sup>29</sup> was used for all other atoms. The nature of all stationary points were confirmed by normal mode analysis. A relaxed potential energy surface scan was performed using the B3LYP/LanL2DZ/3-21G optimised geometry to find a potential transition state using the same functional / basis set. The dihedral angle between the monodentate ligand (L) and the ruthenium atom was adjusted by intervals of 20 degrees to simulate the rotation of nicotinamide (NA) in complexes of the type [Ru(bpy)<sub>2</sub>(NA)X]<sup>+</sup>, where X is either Cl or I. Geometry optimisation of the transition states were performed using B3LYP/LanL2DZ/3-21G as above. All B3LYP/LanL2DZ/3-21G geometries were then re-optimised using B3LPY/LanL2DZ/6-31G\*\*+ and PB1PBE<sup>30</sup>/LanL2DZ/6-31G\*\*+; the LanL2DZ basis set and effective core potential was used for the ruthenium and halide atom, and the split valence 6-31G\*\*+ basis set<sup>31</sup> used for all other atoms.

The DFT free energy of activation ( $\Delta G_{\text{DFT}}^\ddagger$ ), i.e. energy of the rotational barrier, was calculated by taking the difference between total energy of the starting geometry ( $E_S$ ) and total energy of the transition state ( $E_T$ ), see Equation 3.3.

$$\Delta G_{\text{DFT}}^\ddagger = E_T - E_S \quad \text{Equation 3.3.}$$

### 3.3. Results

#### 3.3.1. Synthesis and characterisation

The Ru(II) polypyridyl complexes studied in this chapter are listed in Table 3.1 with the general structure shown in Figure 3.1.

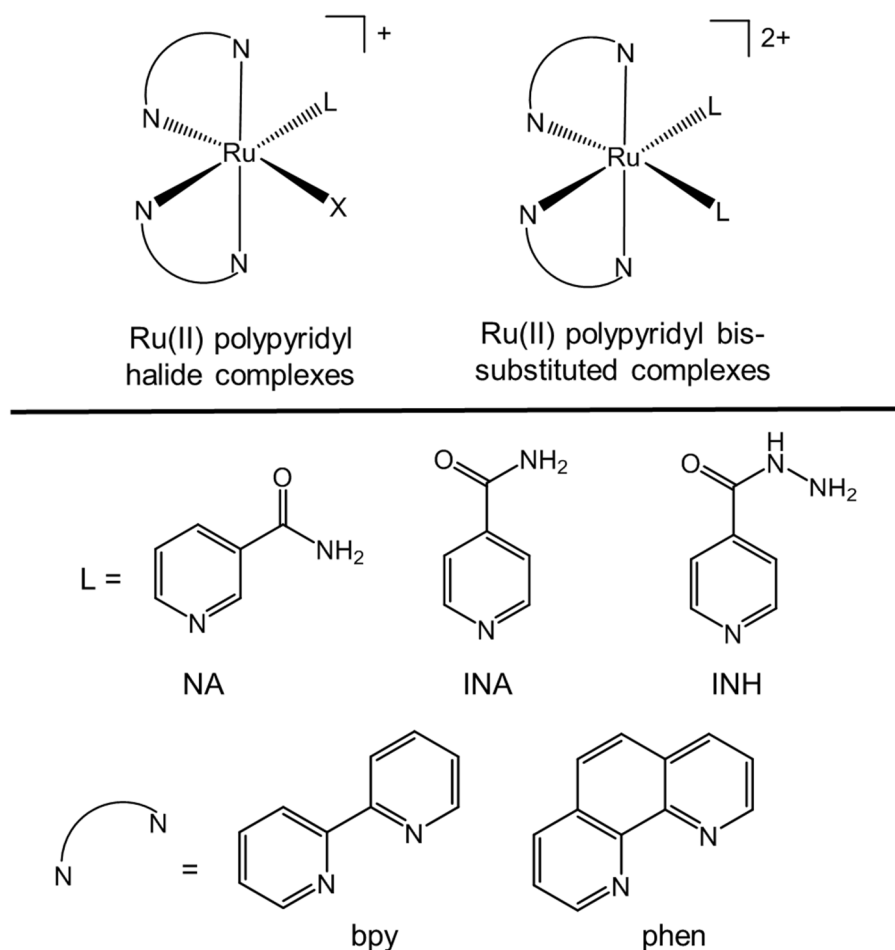


**Figure 3.1.** General structures of the complexes studied in this work.

**Table 3.1.** *Cis*-[Ru(*N-N'*)<sub>2</sub>(L)X][PF<sub>6</sub>] and *cis*-[Ru(*N-N'*)<sub>2</sub>(L)<sub>2</sub>][PF<sub>6</sub>]<sub>2</sub> complexes studied in this work.

Complex		<i>N-N'</i>	L	X
	<b>1</b>	bpy	NA	Cl
<i>cis</i> -[Ru( <i>N-N'</i> ) <sub>2</sub> (L)X][PF <sub>6</sub> ]	<b>2</b>	bpy	NA	I
	<b>3</b>	bpy	INA	Cl
<i>cis</i> -[Ru( <i>N-N'</i> ) <sub>2</sub> (L) <sub>2</sub> ][PF <sub>6</sub> ] <sub>2</sub>	<b>4</b>	bpy	INH	
	<b>5</b>	bpy	NA	
	<b>6</b>	phen	INH	
	<b>7</b>	phen	NA	

The monocationic Ru(II) polypyridyl halide complexes, *cis*-[Ru(bpy)<sub>2</sub>(L)X][PF<sub>6</sub>] (**1** – **3**), were synthesised by the reaction of the appropriate *cis*-[Ru(bpy)<sub>2</sub>(X)<sub>2</sub>] starting material with 1.2-1.3 mol equivalents of pyridine based ligand L in a mixture of 1:4 v/v water:ethanol. The complexes were fully characterised by 1D and 2D <sup>1</sup>H-NMR in acetone-*d*<sub>6</sub>. For the chlorido complexes *cis*-[Ru(bpy)<sub>2</sub>(NA)Cl][PF<sub>6</sub>] (**1**) and *cis*-[Ru(bpy)<sub>2</sub>(INA)Cl][PF<sub>6</sub>] (**3**) there is one doublet located at ~10.1 ppm, which is low-field-shifted to 10.62 ppm for the iodido complex *cis*-[Ru(bpy)<sub>2</sub>(NA)I][PF<sub>6</sub>] (**2**). The spectrum of *cis*-[Ru(bpy)<sub>2</sub>(NA)Cl][PF<sub>6</sub>] (**1**) is shown in Figure 3.2.

An interesting feature at approximately 9-9.5 ppm for complexes **1** – **3** is a broad peak that can be attributed to protons H<sub>9</sub> and H<sub>10</sub> on the monodentate ligand L that are closest to the nitrogen of the pyridine ring. Both protons appear to be exchanging at room temperature (298 K), attributed to the lack of COSY and NOE cross peaks in the <sup>1</sup>H-<sup>1</sup>H NOESY spectrum of **1** at room temperature (298 K), see Figure 3.3. This intermediate conformational exchange can be attributed to the hindered rotation of the NA ligand.

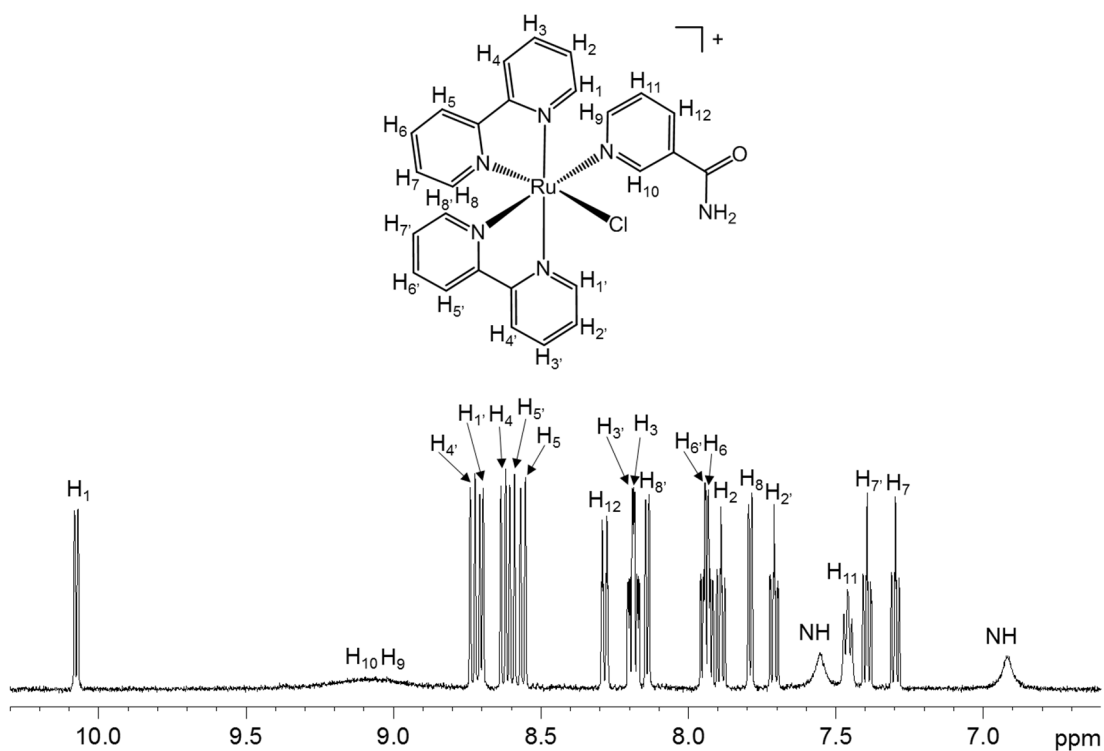


**Figure 3.2.**  $^1H$ -NMR spectrum (500 MHz) of complex  $cis-[Ru(bpy)_2(NA)Cl][PF_6]$  (1) in  $acetone-d_6$  at 298 K.

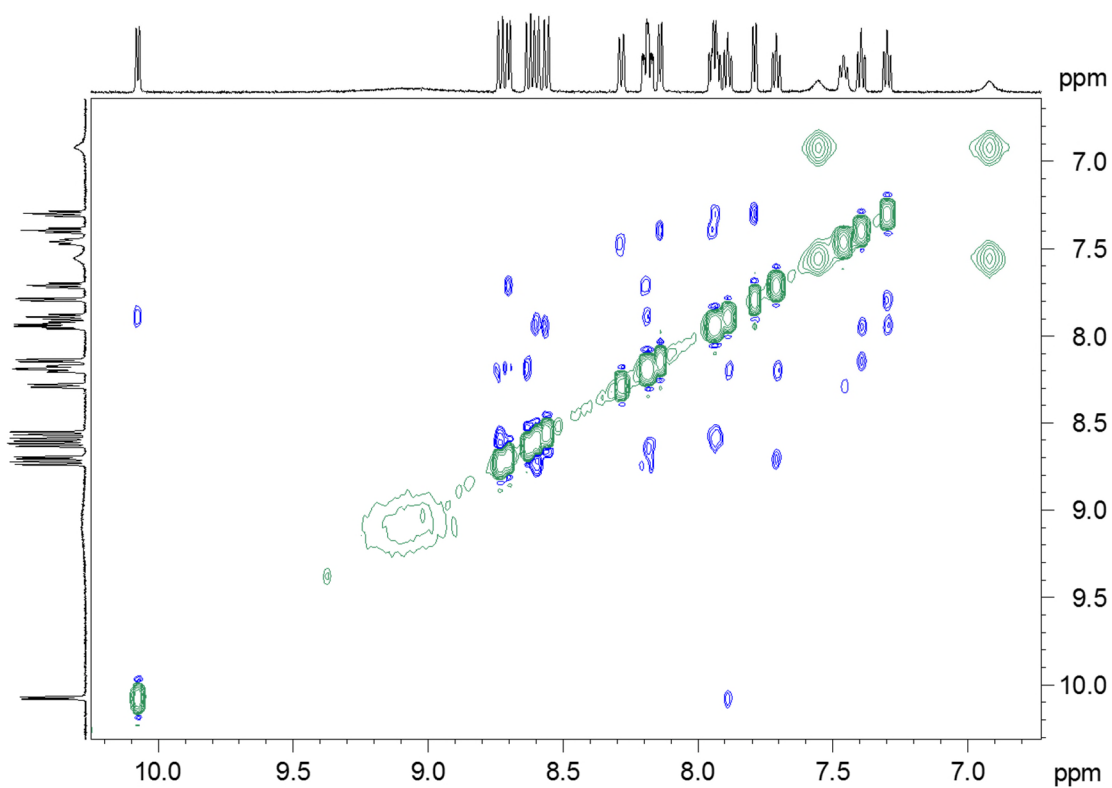


**Figure 3.3.**  $^1H$ - $^1H$  NOESY spectrum (500 MHz) of  $cis-[Ru(bpy)_2(NA)Cl][PF_6]$  (1) in  $acetone-d_6$  at 298 K.

The dicationic Ru(II) polypyridyl bis-substituted complexes, *cis*-[Ru(bpy)<sub>2</sub>(L)<sub>2</sub>][PF<sub>6</sub>]<sub>2</sub> (**4** – **6**), were synthesised by the reaction of the appropriate *cis*-[Ru(*N-N'*)<sub>2</sub>(Cl)<sub>2</sub>] starting material with a 5 mol equivalent excess of pyridine based ligand L in water. The complexes were fully characterised by 1D and 2D <sup>1</sup>H-NMR. Unlike complexes **1** – **3**, the <sup>1</sup>H-NMR peaks for **4** – **7** are sharp and the number of proton peaks observed is reduced by half, see Figure 3.4.

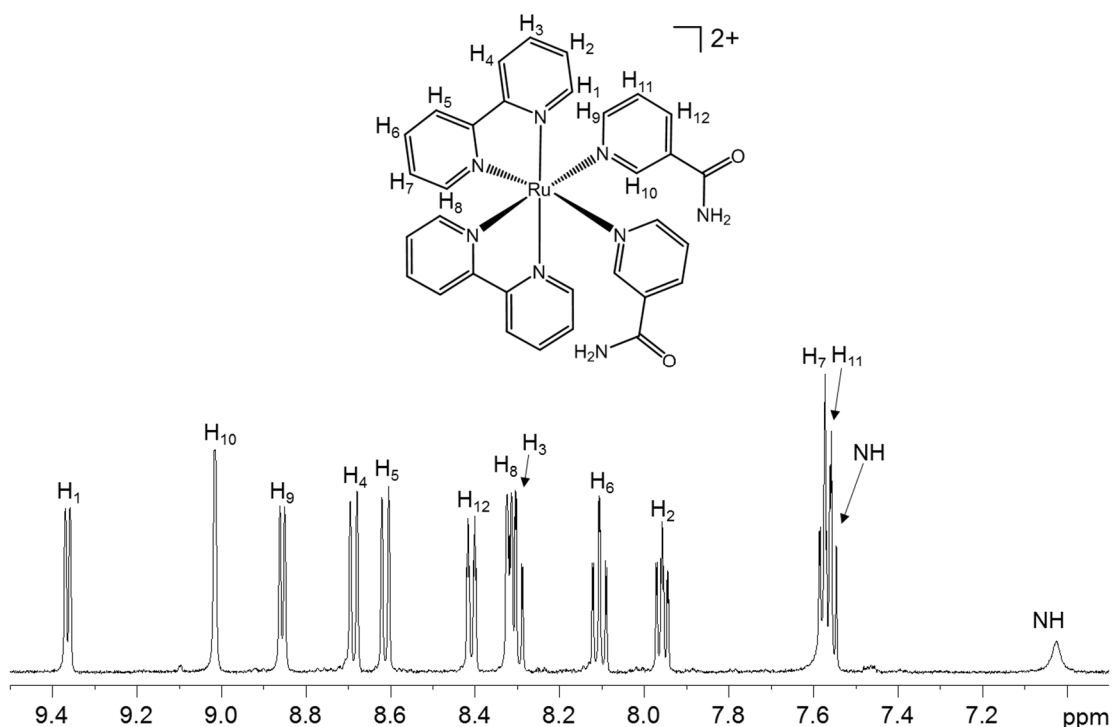


**Figure 3.4.** <sup>1</sup>H-NMR spectrum (500 MHz) of *cis*-[Ru(bpy)<sub>2</sub>(NA)<sub>2</sub>][PF<sub>6</sub>]<sub>2</sub> (**5**) in acetone-*d*<sub>6</sub> at 298 K.

### 3.3.2. X-Ray crystal structures

The molecular structures of bis-substituted complexes *cis*-[Ru(bpy)<sub>2</sub>(INH)<sub>2</sub>][PF<sub>6</sub>]<sub>2</sub> (**4**), *cis*-[Ru(bpy)<sub>2</sub>(NA)<sub>2</sub>][PF<sub>6</sub>]<sub>2</sub> (**5**), and *cis*-[Ru(phen)<sub>2</sub>(INH)<sub>2</sub>][PF<sub>6</sub>]<sub>2</sub> (**6**) were determined by single crystal X-ray diffraction. The complexes are chiral and their crystal structures show the presence of both enantiomers (Δ and Λ) in the unit cell. For **4** and

**5** the asymmetric unit contains half a complex (i.e. half a Ru atom, one bpy ligand, one monodentate ligand, one PF<sub>6</sub> counter ion) and solvent molecules. In contrast, for **6** the asymmetric unit contains one and a half Ru complexes (i.e. three phen ligands, three monodentate ligands and three PF<sub>6</sub> counter ions). Due to the complexity of the crystal structure for **6**, both enantiomers ( $\Lambda$  and  $\Delta$ ) are highlighted. The structures are shown in Figure 3.5, with selected bond lengths given in Table 3.3 for complexes **4** and **5**, and Table 3.4 for **6**. The crystallographic data are shown in Table 3.2.

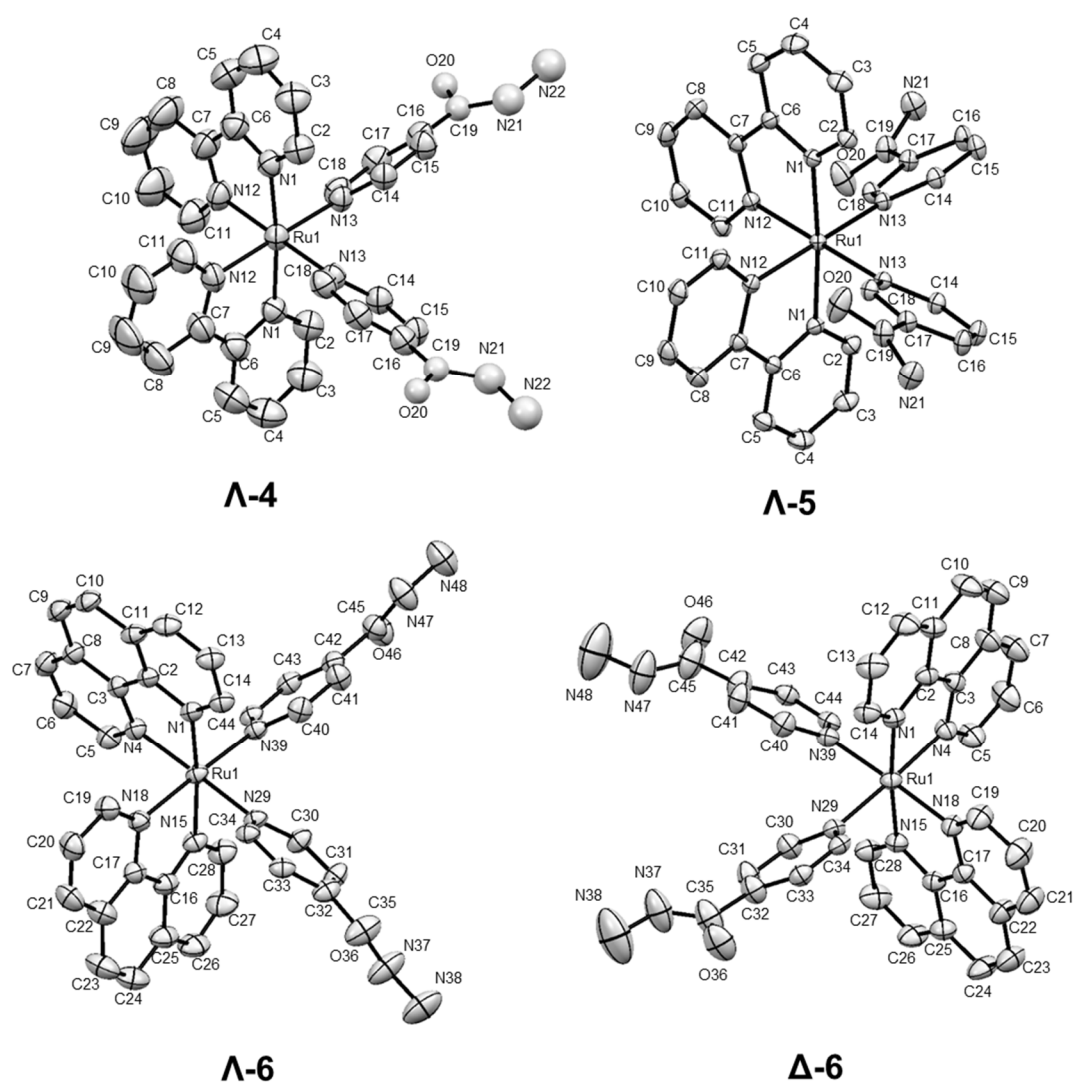


**Figure 3.5.** X-ray structures of the cations *cis*-[Ru(bpy)<sub>2</sub>(INH)<sub>2</sub>][PF<sub>6</sub>]<sub>2</sub> (**4**), *cis*-[Ru(bpy)<sub>2</sub>(NA)<sub>2</sub>][PF<sub>6</sub>]<sub>2</sub> (**5**) and *cis*-[Ru(phen)<sub>2</sub>(INH)<sub>2</sub>][PF<sub>6</sub>]<sub>2</sub> (**6**) with thermal ellipsoids showing 50% probability. The PF<sub>6</sub> anions and hydrogen atoms have been omitted for clarity.

**Table 3.2.** Crystallographic data for complexes *cis*-[Ru(bpy)<sub>2</sub>(INH)<sub>2</sub>][PF<sub>6</sub>]<sub>2</sub> (**4**), *cis*-[Ru(bpy)<sub>2</sub>(NA)<sub>2</sub>][PF<sub>6</sub>]<sub>2</sub> (**5**) and *cis*-[Ru(phen)<sub>2</sub>(INH)<sub>2</sub>][PF<sub>6</sub>]<sub>2</sub> (**6**).

	<b>4</b>	<b>5</b>	<b>6</b>
Formula	C <sub>42</sub> H <sub>48</sub> F <sub>12</sub> N <sub>10</sub> O <sub>7</sub> P <sub>2</sub> Ru	C <sub>32</sub> H <sub>40</sub> F <sub>12</sub> N <sub>8</sub> O <sub>8</sub> P <sub>2</sub> Ru	C <sub>36.88888</sub> H <sub>35.888867</sub> F <sub>12</sub> N <sub>10</sub> O <sub>4.055553</sub> P <sub>2</sub> Ru
Molar mass	1195.91	1055.73	1075.21
Crystal system	Monoclinic	Monoclinic	Monoclinic
Space group	C2/c	C2/c	C2/c
Crystal size (mm)	0.20 x 0.08 x 0.04	0.20 x 0.18 x 0.16	-
Crystal character	Orange block	Orange block	-
<i>a</i> (Å)	21.9093(7)	26.6886(10)	38.4124(5)
<i>b</i> (Å)	15.8193(3)	10.1669(2)	20.4076(3)
<i>c</i> (Å)	19.1282(12)	22.3265(7)	19.0496(2)
<i>α</i> (°)	90	90	90
<i>β</i> (°)	130.884(2)	136.981(2)	114.6440(10)
<i>γ</i> (°)	90	90	90
T (K)	293(2)	150(2)	150(2) K
Z	4	4	12
R1 [I>2σ(I)]	0.0798	0.0405	0.0700

**Table 3.3.** Selected bond lengths (Å) and angles (°) for *cis*-[Ru(bpy)<sub>2</sub>(INH)<sub>2</sub>][PF<sub>6</sub>]<sub>2</sub> (**4**) and *cis*-[Ru(bpy)<sub>2</sub>(NA)<sub>2</sub>][PF<sub>6</sub>]<sub>2</sub> (**5**).

Bond length (Å) / angle (°)	<b>4</b>	<b>5</b>
Ru1-N1	2.066(5)	2.0683(17)
Ru1-N12	2.057(4)	2.0524(17)
Ru1-N13	2.101(4)	2.1084(17)
N1-Ru-N12	78.62(18)	79.34(7)
N12-Ru1-N13	90.26(18)	88.92(7)
N13-Ru1-N13	91.3(2)	94.36(9)



**Table 3.4.** Selected bond lengths (Å) and angles (°) for *cis*-[Ru(phen)<sub>2</sub>(INH)<sub>2</sub>][PF<sub>6</sub>]<sub>2</sub> (**6**).

Bond length, Å / angle, °	<b>6</b>	
	$\Lambda$	$\Delta$
Ru1-N1	2.090(3)	2.080(3)
Ru1-N4	2.058(3)	2.056(3)
Ru1-N15	2.071(3)	2.080(3)
Ru1-N18	2.058(3)	2.056(3)
Ru1-N29	2.088(3)	2.081(3)
Ru1-N39	2.094(3)	2.081(3)
N1-Ru1-N4	79.52(14)	79.77(13)
N15-Ru1-N18	79.94(13)	79.77(13)
N4-Ru1-N39	87.21(13)	89.04(13)
N18-Ru1-N29	91.06(13)	89.04(13)
N39-Ru1-N29	92.68(13)	89.87(18)

The bond lengths for **4** and **5** are very similar, and the bite angle for the bpy (N1-Ru1-N12) is very similar in each case. The angle between both monodentate ligands (N13-Ru1-N13) is bigger in the case of **5** and thus there is a smaller bpy to monodentate ligand angle (N12-Ru1-N13) when compared to **4**.

The bite angle for phen in **6** (N1-Ru1-N4 and N15-Ru1-N18) is very similar to that of bpy in **4** and **5**. Additionally for **6** the angle between the monodentate ligands (N39-Ru1-N29) and the angle between phen and monodentate ligand (N18-Ru1-N29 and N4-Ru1-N39) is very similar to **4**. Interestingly Ru-N1 is slightly longer and the monodentate ligand length (Ru1-N29 and Ru1-N39) is slightly smaller for **6** when compared to both **4** and **5**.

It is worth noting that for **4** there is disorder over the hydrazide group, which is not exhibited for **6**.

For *cis*-[Ru(bpy)<sub>2</sub>(INH)<sub>2</sub>][PF<sub>6</sub>]<sub>2</sub> (**4**) the unit cell comprises of pairs of enantiomers connected via a CH- $\pi$  interaction between CH of bpy from  $\Delta$ -complex and the  $\pi$  system of INH from  $\Lambda$ -complex, see Figure 3.6. The CH<sub>(bpy)</sub>-centroid<sub>(INH)</sub> distance is 3.176 Å and the angle between the ring planes is 81.76°. The hydrazide group on the INH ligand forms a hydrogen-bonded dimer that links enantiomers from different unit cells, see Figure 3.7, with a bond distance of N-H-N 2.199 Å. The bpy ligand deviates from a linear arrangement, with a twist angle between each ring plane of 3.29°.

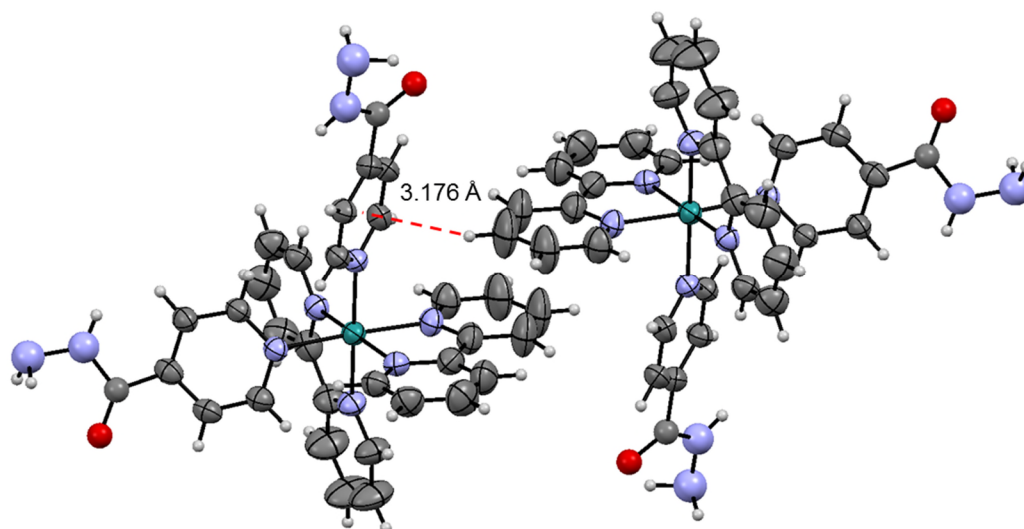


**Figure 3.6.** X-ray crystal structure of *cis*-[Ru(bpy)<sub>2</sub>(INH)<sub>2</sub>][PF<sub>6</sub>]<sub>2</sub> (**4**) showing CH<sub>(bpy)</sub>- $\pi$ <sub>(INH)</sub> interactions connecting two enantiomers in the unit cell. The PF<sub>6</sub> anions have been omitted for clarity.

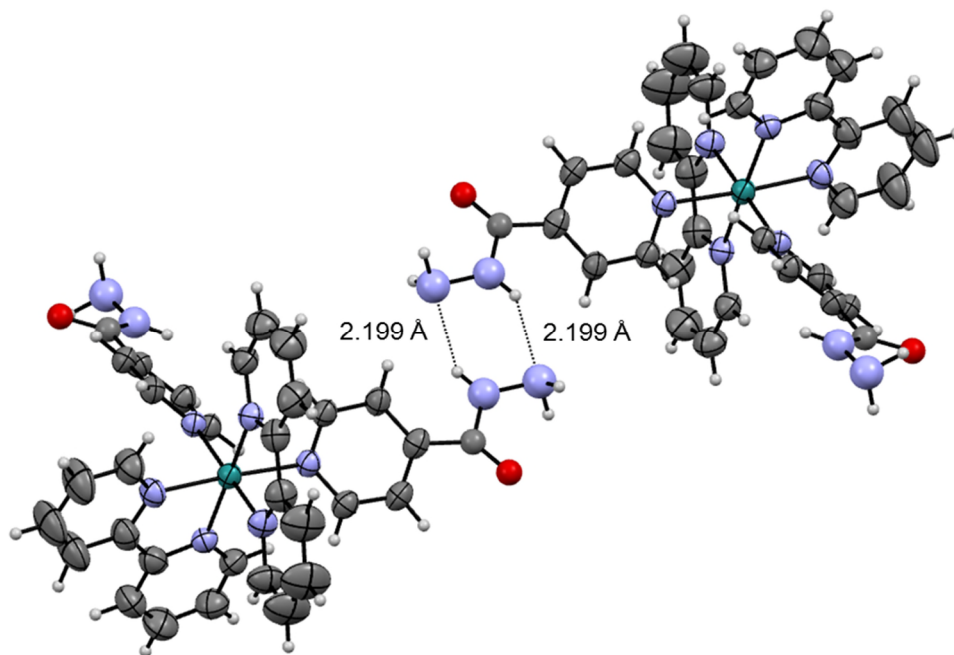


**Figure 3.7.** X-ray crystal structure of *cis*-[Ru(bpy)<sub>2</sub>(INH)<sub>2</sub>][PF<sub>6</sub>]<sub>2</sub> (**4**) showing hydrogen bonding between the hydrazide group of two neighbouring enantiomers from different unit cells.

The unit cell of *cis*-[Ru(bpy)<sub>2</sub>(NA)<sub>2</sub>][PF<sub>6</sub>]<sub>2</sub> (**5**) comprises of pairs of enantiomers connected via both CH- $\pi$  interactions and  $\pi$ - $\pi$  interactions. The CH- $\pi$  interaction involves a CH of bpy from  $\Delta$  complex and the  $\pi$  system of NA from  $\Lambda$ -complex. The CH<sub>(bpy)</sub>-centroid<sub>(NA)</sub> distance is 2.733 Å and the angle between the ring planes is 83.26°. The aforementioned bpy of the  $\Delta$ -complex is involved in  $\pi$ - $\pi$  interaction with bpy of the  $\Lambda$ -complex, see Figure 3.8. The centroid-centroid distance is 4.019 Å with a ring plane angle of 0°. The bpy ligand deviates from a linear arrangement, with a twist angle between each ring plane of 6.57°. Hydrogen bonding occurs between the amide group of NA and adjacent water molecules, with N-H<sub>(NA)</sub>-OH<sub>2</sub> distance of 2.068 Å and O<sub>(NA)</sub>-HOH distance of 1.921 Å. Additional hydrogen bonding occurs between a fluorine from PF<sub>6</sub> and two hydrogens from bpy, see Figure 3.9, with H<sub>(bpy)</sub>-F bond distances of 2.288 Å and 2.565 Å.

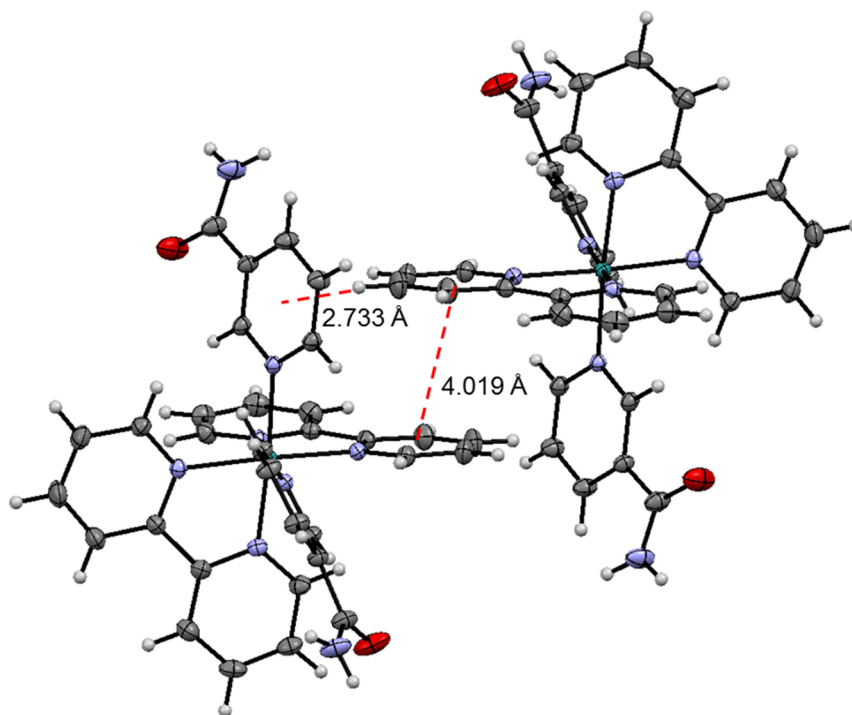


**Figure 3.8.** X-ray crystal structure of *cis*-[Ru(bpy)<sub>2</sub>(NA)<sub>2</sub>][PF<sub>6</sub>]<sub>2</sub> (**5**) showing CH<sub>(bpy)</sub>–π<sub>(NA)</sub> and π<sub>(bpy)</sub>–π<sub>(bpy)</sub> interactions connecting two enantiomers in the unit cell. The PF<sub>6</sub> anions have been omitted for clarity.

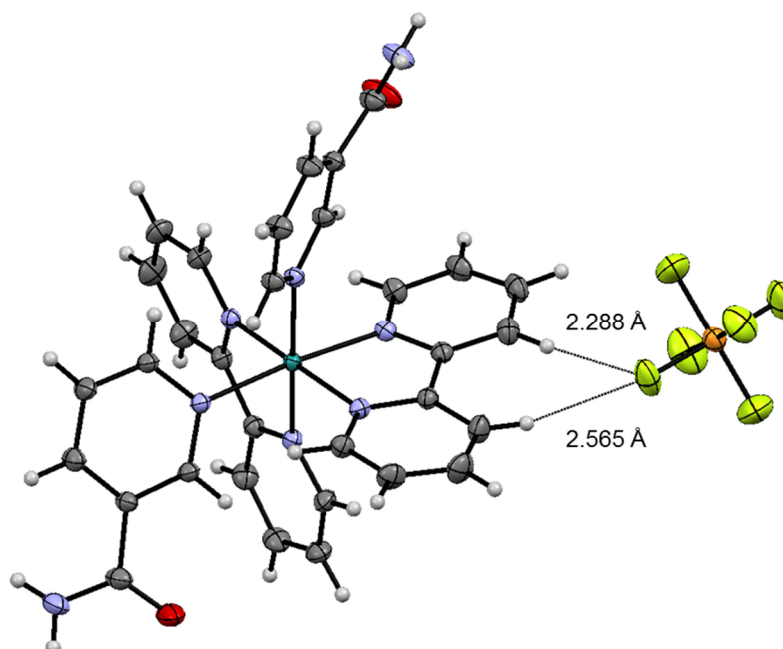


**Figure 3.9.** X-ray crystal structure of *cis*-[Ru(bpy)<sub>2</sub>(NA)<sub>2</sub>][PF<sub>6</sub>]<sub>2</sub> (**5**) showing hydrogen bonding between PF<sub>6</sub> and hydrogens of bpy.

CH- $\pi$  and  $\pi$ - $\pi$  interactions also govern the connection of enantiomers in the unit cell of *cis*-[Ru(phen)<sub>2</sub>(INH)<sub>2</sub>][PF<sub>6</sub>]<sub>2</sub> (**6**). The  $\pi$ - $\pi$  interaction involves the centre ring of the phen, with a centroid-centroid distance of 3.909 Å and an angle between ring planes of 0°, see Figure 3.10. The CH- $\pi$  interaction involves CH of phen and  $\pi$  system of INH, with CH<sub>(phen)</sub>-centroid<sub>(INH)</sub> distance of 2.697 Å and the angle between the ring planes is 86.09°. Throughout the unit cell there is extensive hydrogen bonding between water molecules and the hydrazide group of INH.

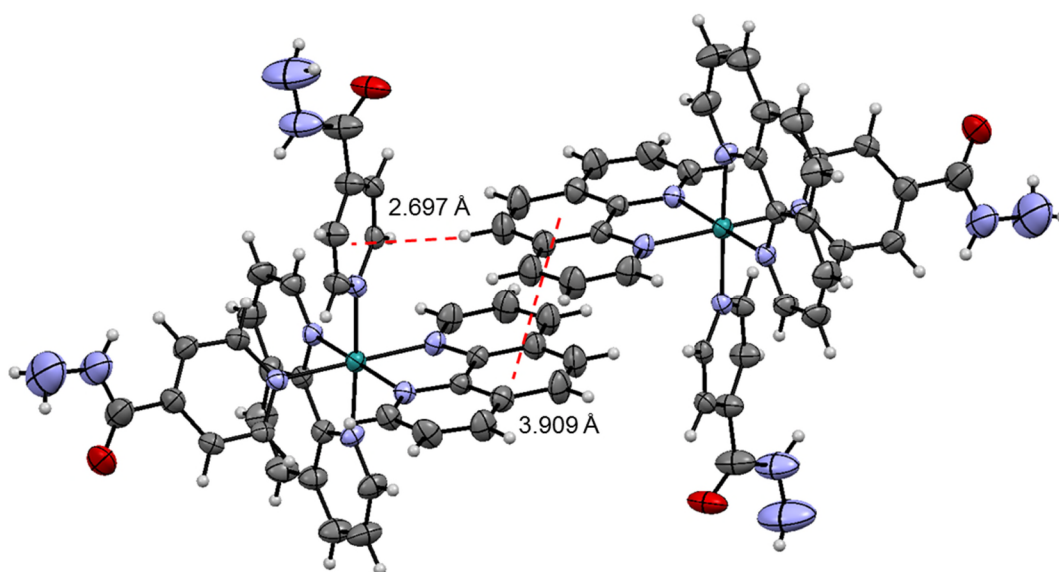


**Figure 3.10.** X-ray crystal structure of *cis*-[Ru(phen)<sub>2</sub>(INH)<sub>2</sub>][PF<sub>6</sub>]<sub>2</sub> (**6**) showing CH<sub>(phen)</sub>- $\pi$ (INH) and  $\pi$ <sub>(phen)</sub>- $\pi$ <sub>(phen)</sub> interactions connecting two enantiomers in the unit cell. The PF<sub>6</sub> anions have been omitted for clarity.

### 3.3.3. Dark stability in aqueous solution

#### 3.3.3.1. Hydrolysis of Ru(II) polypyridyl halide complexes

The hydrolysis of *cis*-[Ru(bpy)<sub>2</sub>(NA)Cl][PF<sub>6</sub>] (**1**) in a) deionised water and b) a 5% (v/v) solution of common organic solvents used to dissolve water-insoluble

compounds (e.g. DMSO, acetone and DMF) was studied by UV-visible spectroscopy over an 18 – 24 h period.

An aqueous solution of **1** (40  $\mu\text{M}$ ) exhibits a band with a maximum at 473 nm that decreased over time, giving rise to a new band with a maximum at 466 nm, see Figure 3.11. No further changes in the spectrum were seen after 6 h. There are isosbestic points at 470 nm and 338 nm, consistent with the stoichiometric formation of *cis*-[Ru(bpy)<sub>2</sub>(NA)(H<sub>2</sub>O)]<sup>2+</sup> with no other side products. The identity of the hydrolysis product was confirmed by ESI-MS, see Table 3.5. The change in absorbance of the band at 466 nm was fitted to a single exponential equation to give  $t_{1/2}$  of 2712 s.

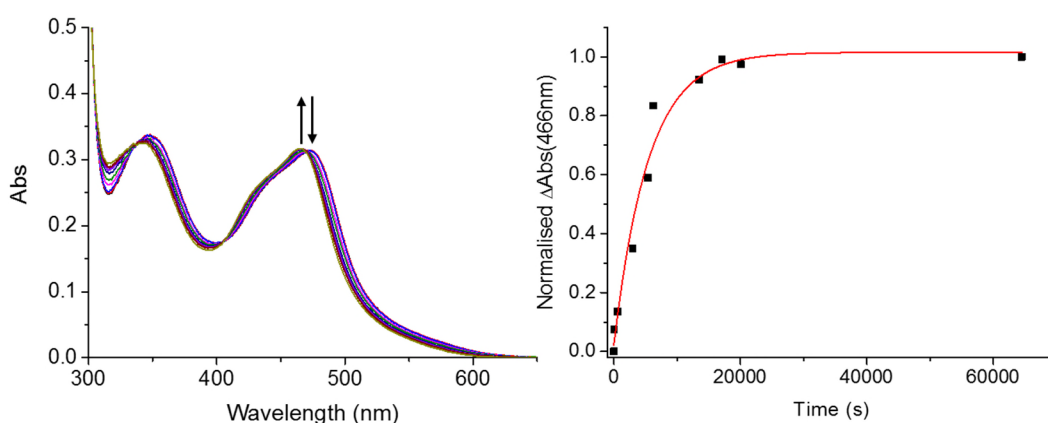


**Figure 3.11.** Hydrolysis of *cis*-[Ru(bpy)<sub>2</sub>(NA)Cl][PF<sub>6</sub>] (**1**) in aqueous solution followed by UV-visible spectroscopy (left) and increase of *cis*-[Ru(bpy)<sub>2</sub>(NA)(H<sub>2</sub>O)]<sup>2+</sup> peak at 466 nm followed over time (right).

When 5% DMSO, acetone or DMF was used, this relationship was not observed. In all cases the band at 475 nm decreases over time, and never reaches an end point, see Figure 3.12. The isosbestic point at 327 nm shifts over time, inferring that more than one process is occurring. The decrease in the band at 475 nm could not be fitted to a single exponential equation, confirming the added complexity.

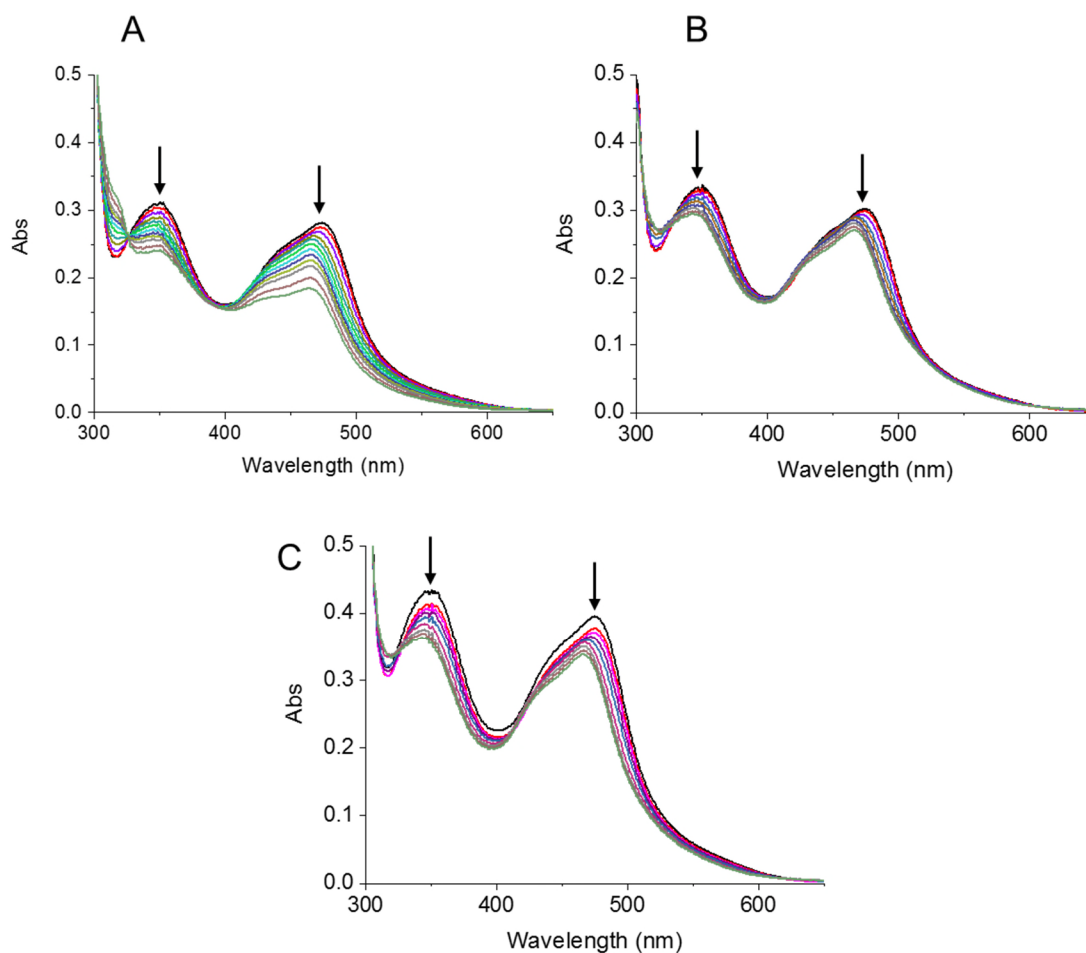


**Figure 3.12.** Hydrolysis of *cis*-[Ru(bpy)<sub>2</sub>(NA)Cl][PF<sub>6</sub>] (**1**) in 5% DMSO (A) 5% acetone (B) and 5% DMF (C) followed by UV-visible spectroscopy over 24 h .

The hydrolysis products were confirmed by ESI-MS, see Table 3.5. In all cases the mass-to-charge ratio and isotopic models obtained were consistent with the formation of *cis*-[Ru(bpy)<sub>2</sub>(NA)(H<sub>2</sub>O)]<sup>2+</sup>. For 5% DMSO another product mass was observed consistent with the formation of *cis*-[Ru(bpy)<sub>2</sub>(NA)(DMSO)]<sup>2+</sup>.

**Table 3.5.** Hydrolysis products of *cis*-[Ru(bpy)<sub>2</sub>(NA)Cl][PF<sub>6</sub>] (**1**) detected by ESI-MS when hydrolysis was performed in various solvents

Hydrolysis solvent	ESI-MS product mass, <i>m/z</i>	Calculated formula and mass of product, <i>m/z</i>
Water	553.2	[[Ru(bpy) <sub>2</sub> (NA)(H <sub>2</sub> O)] <sup>2+</sup> -H] <sup>+</sup> C <sub>26</sub> H <sub>23</sub> N <sub>6</sub> O <sub>2</sub> Ru: 553.1
5% DMSO	758.9	[[Ru(bpy) <sub>2</sub> (NA)(DMSO)] <sup>2+</sup> +PF <sub>6</sub> ] <sup>+</sup> C <sub>28</sub> H <sub>28</sub> F <sub>6</sub> N <sub>6</sub> O <sub>2</sub> PRuS: 759.1
	553.0	[[Ru(bpy) <sub>2</sub> (NA)(H <sub>2</sub> O)] <sup>2+</sup> -H] <sup>+</sup> C <sub>26</sub> H <sub>23</sub> N <sub>6</sub> O <sub>2</sub> Ru: 553.1
5% Acetone	553.0	[[Ru(bpy) <sub>2</sub> (NA)(H <sub>2</sub> O)] <sup>2+</sup> -H] <sup>+</sup> C <sub>26</sub> H <sub>23</sub> N <sub>6</sub> O <sub>2</sub> Ru: 553.1
5% DMF	553.0	[[Ru(bpy) <sub>2</sub> (NA)(H <sub>2</sub> O)] <sup>2+</sup> -H] <sup>+</sup> C <sub>26</sub> H <sub>23</sub> N <sub>6</sub> O <sub>2</sub> Ru: 553.1

**3.3.3.2. Stability of Ru(II) polypyridyl bis-substituted complexes**

The dark stability of *cis*-[Ru(*N-N'*)<sub>2</sub>(L)<sub>2</sub>][PF<sub>6</sub>]<sub>2</sub> complexes **4**, **5**, **6**, and **7** in deionised water was investigated using a 40 μM solution at room temperature, 298 K. Over 6 hours the UV-visible absorption spectra did not change, see Figure 3.13.



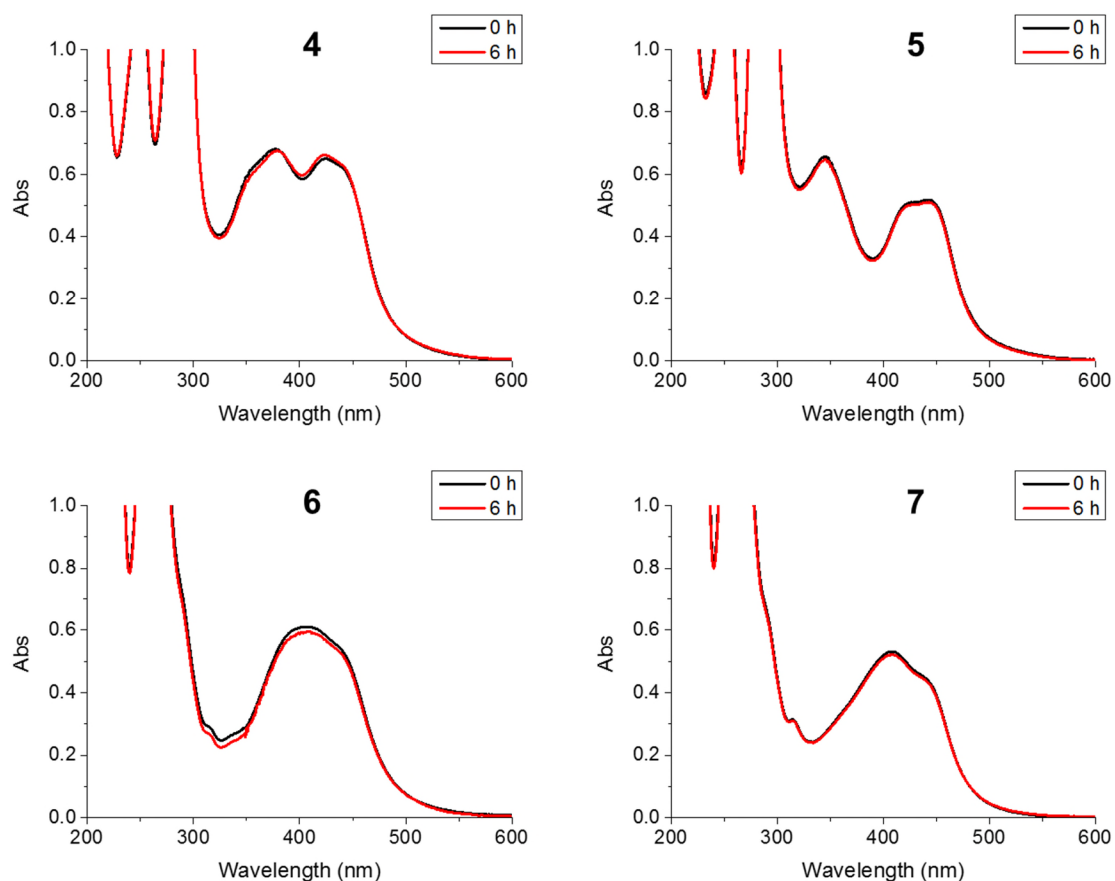


**Figure 3.13.** Dark stability of  $cis-[Ru(bpy)_2(INH)_2][PF_6]_2$  (**4**),  $cis-[Ru(bpy)_2(NA)_2][PF_6]_2$  (**5**),  $cis-[Ru(phen)_2(INH)_2][PF_6]_2$  (**6**) and  $cis-[Ru(phen)_2(NA)_2][PF_6]_2$  (**7**) for 6 h in water followed by UV-visible spectroscopy.

### 3.3.4. Dynamic behaviour in solution

The nomenclature and proton labelling for the complexes (**1**, **2**, **3** and **5**) described in this section are shown in Figure 3.14.

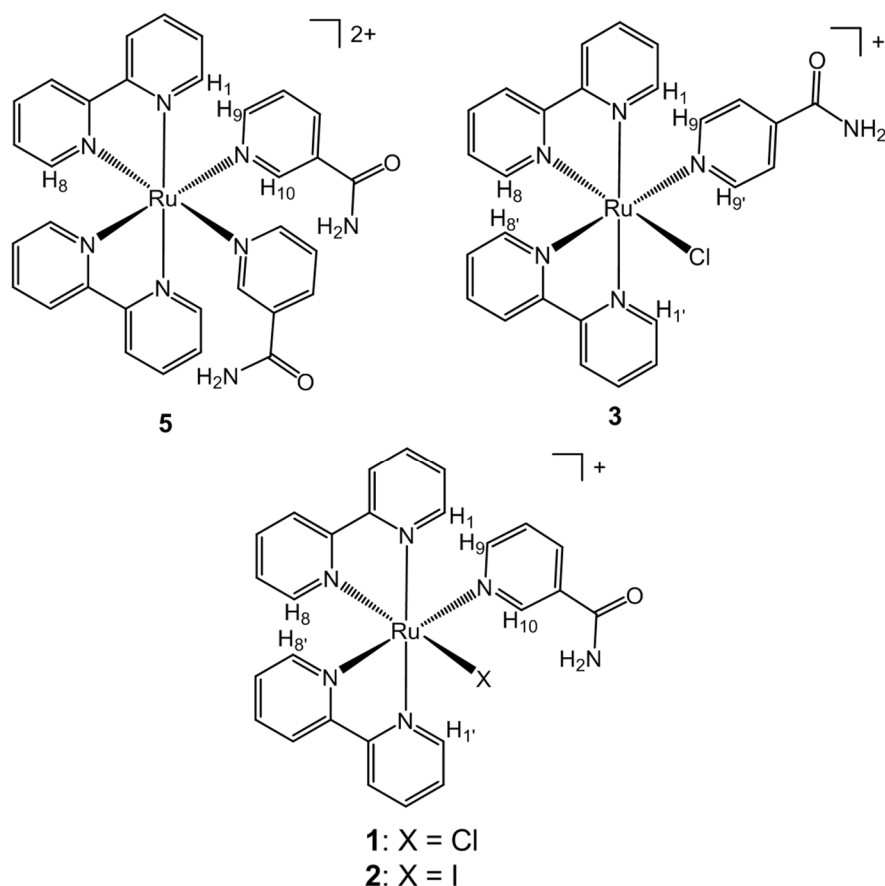


**Figure 3.14.** General structure and labelling of complexes studied in this work.

#### 3.3.4.1. Dynamic behaviour studied by variable temperature $^1\text{H}$ -NMR

Variable temperature  $^1\text{H}$ -NMR was utilised to gain further information about the room temperature (298 K) exchange behaviour observed for **1**, **2**, and **3** described in Section 3.3.1. For the Ru(II) polypyridyl bis-substituted complex *cis*-[Ru(bpy)<sub>2</sub>(NA)<sub>2</sub>][PF<sub>6</sub>]<sub>2</sub> (**5**), the resonances of the NA ligand protons do not shift with increasing temperature (up to 323 K). However upon lowering the temperature to 185 K, a complex spectrum appears owing to the presence of 3 atropisomers (denoted A, B and C), see Figure 3.15. At such low temperature the NA ligand is held in one place for each atropisomer, and its orientation can be described by assigning H<sub>10</sub> as the “head group”, or **H**, and H<sub>9</sub> as the “tail”, or **T**.

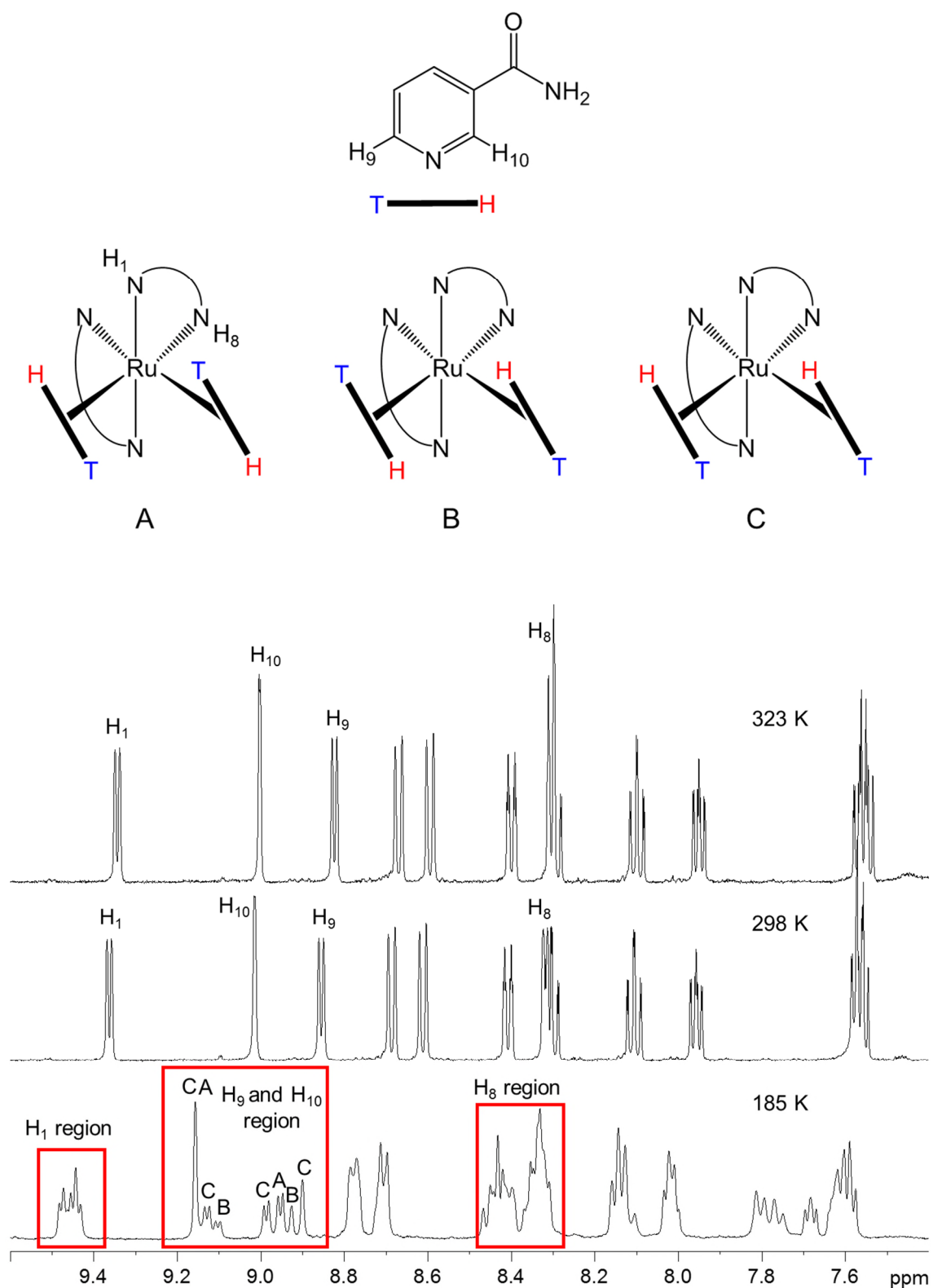


**Figure 3.15.** Variable temperature  $^1\text{H}$ -NMR spectra (500 MHz) of *cis*-[Ru(bpy) $_2$ (NA) $_2$ ][PF $_6$ ] $_2$  (5) in acetone- $d_6$  at 323 K, 298 K and 185 K with nomenclature to describe the atropisomers (top).

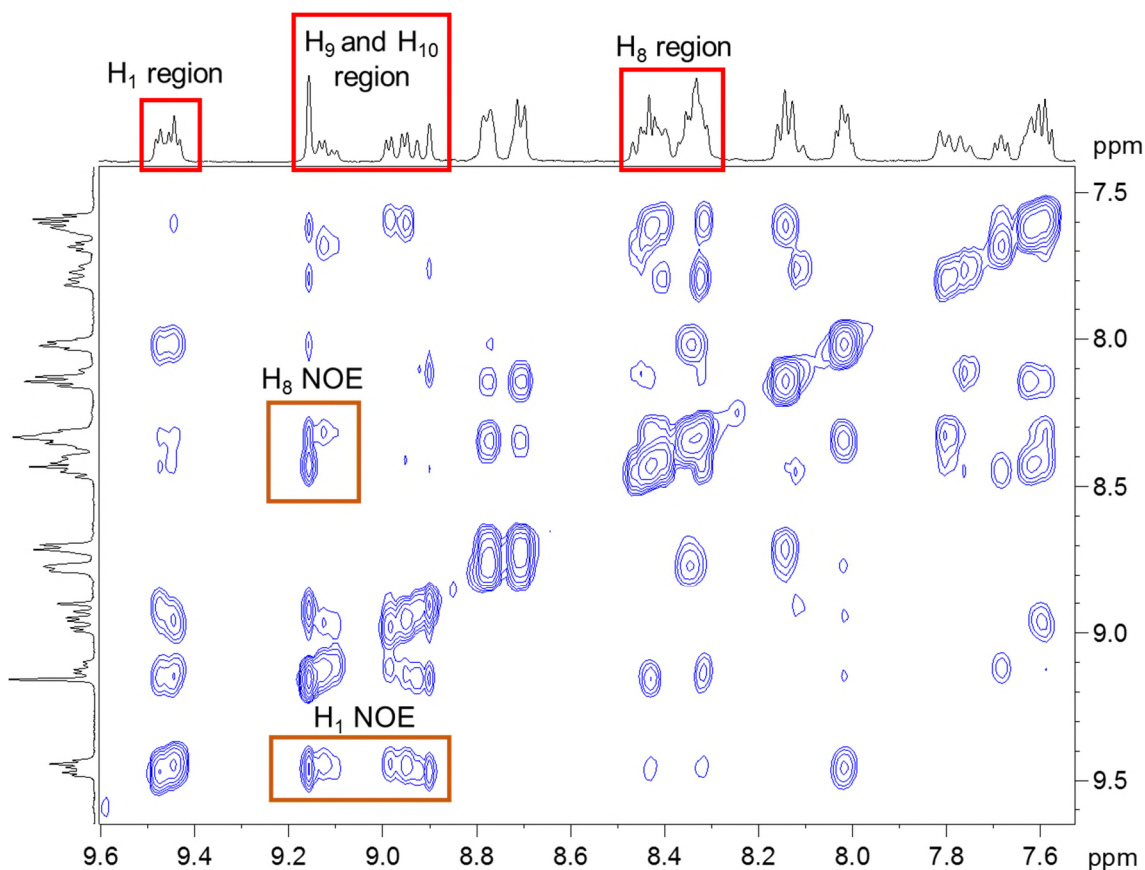


**Figure 3.16.**  $^1\text{H}$ - $^1\text{H}$  NOESY spectrum (500 MHz) of *cis*-[Ru(bpy) $_2$ (NA) $_2$ ][PF $_6$ ] $_2$  (**5**) in acetone- $d_6$  at 185 K.

The atropisomers were assigned by analysing the NOE interaction between H $_{10}$ /H $_9$  with H $_1$ /H $_8$ , see Figure 3.16. For atropisomers A and B, there is only one environment for each H $_{10}$  and H $_9$ , thus there is one peak for each. For atropisomer A, H $_{10}$  shows an NOE interaction with H $_1$  and H $_8$ , and H $_9$  shows an NOE interaction with H $_1$ . For atropisomer B, H $_9$  shows an NOE interaction with H $_1$  and H $_8$ , and H $_{10}$  shows an NOE interaction with H $_1$ . In the case of atropisomer C, there are two environments for H $_{10}$  and two for H $_9$ , thus four peaks are exhibited for these protons. The ratio and chemical shift of selected peaks for each atropisomer is given in Table 3.6.

**Table 3.6.** Comparison of chemical shift data for atropisomers of *cis*-[Ru(bpy)<sub>2</sub>(NA)<sub>2</sub>][PF<sub>6</sub>]<sub>2</sub> (**5**) in acetone-d<sub>6</sub> at 185 K and 298 K

Atropisomer	Chemical shift (ppm)		Ratio in solution
	H <sub>10</sub>	H <sub>9</sub>	
A	9.16	8.95	0.65
B	8.93	9.10	0.3
C	8.90, 9.16	8.99, 9.13	1
<b>5</b> at 298 K	9.02	8.86	-

The chemical shift difference between H<sub>10</sub> and H<sub>9</sub> does not change significantly between each atropisomer (~0.2 ppm). Whether H<sub>10</sub> or H<sub>9</sub> is shifted downfield is dependent on the orientation of the NA ligand. Atropisomer C is the most stable in solution, whereas atropisomer B is the least stable in solution.

For the Ru(II) polypyridyl halide complexes *cis*-[Ru(bpy)<sub>2</sub>(L)X][PF<sub>6</sub>] **1**, **2** and **3**, heating the sample to 323 K results in the broad peak at 9-9.5 ppm becoming sharper, and in the case of **1** and **2**, the peak begins to split into two, see Figure 3.17. Interestingly for **2** the broad peak at 9-9.5 ppm is weakly split into two at 298 K, whereas for **1** it is a single broad peak. When the samples of **1** and **2** are cooled to 185 K, two atropisomers are isolated (denoted as Conf. 1 and Conf. 2), see Figure 3.18. Again the atropisomers were assigned by investigating the NOE interaction between H<sub>10</sub>/H<sub>9</sub> with H<sub>1</sub>/H<sub>8</sub>, see Figure 3.19.

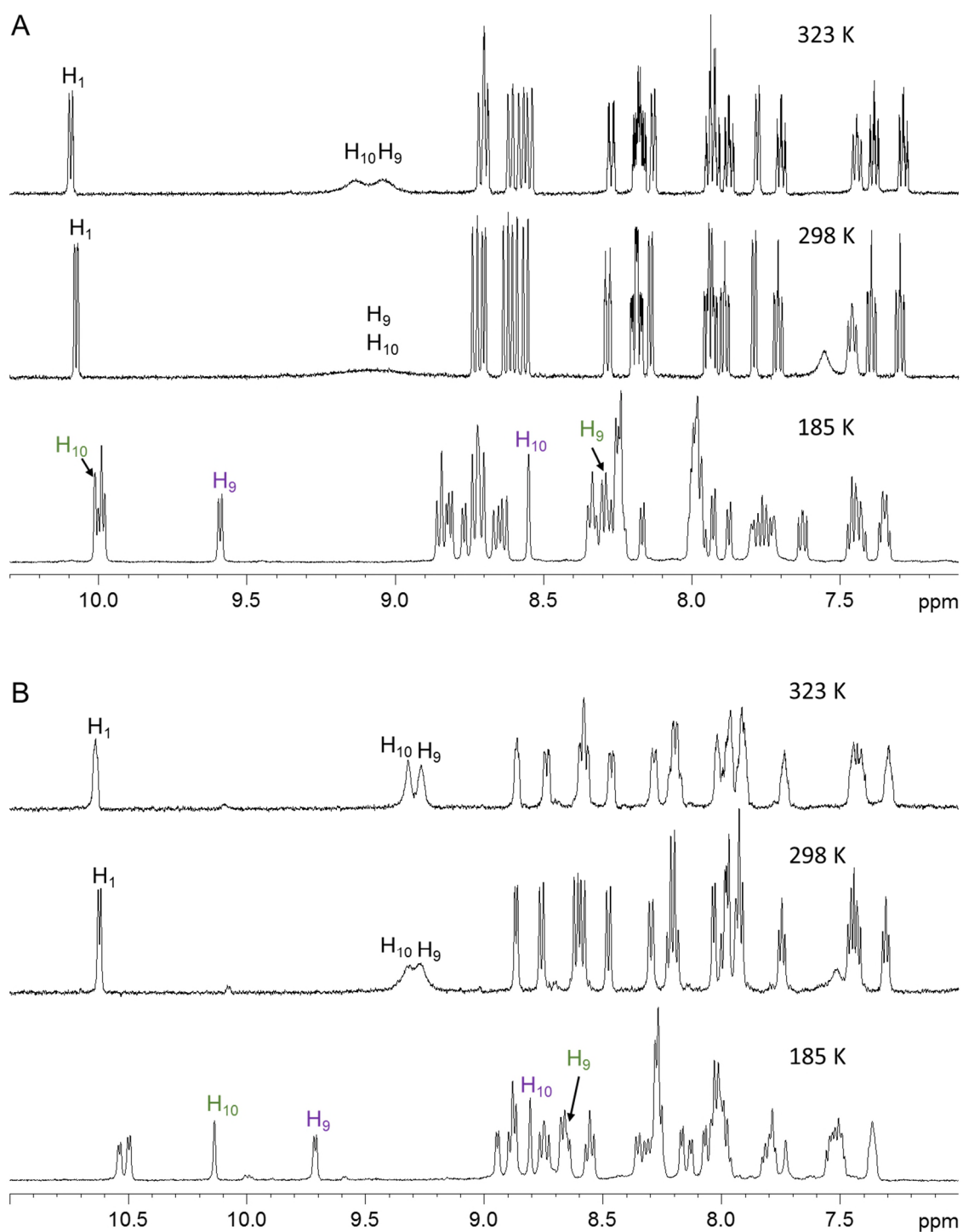


**Figure 3.17.** Variable temperature  $^1\text{H}$ -NMR spectra (500 MHz) of *cis*- $[\text{Ru}(\text{bpy})_2(\text{NA})\text{Cl}][\text{PF}_6]$  (**1**) (A) and *cis*- $[\text{Ru}(\text{bpy})_2(\text{NA})\text{I}][\text{PF}_6]$  (**2**) (B) in  $\text{acetone-}d_6$  at 323 K, 298 K and 185 K.

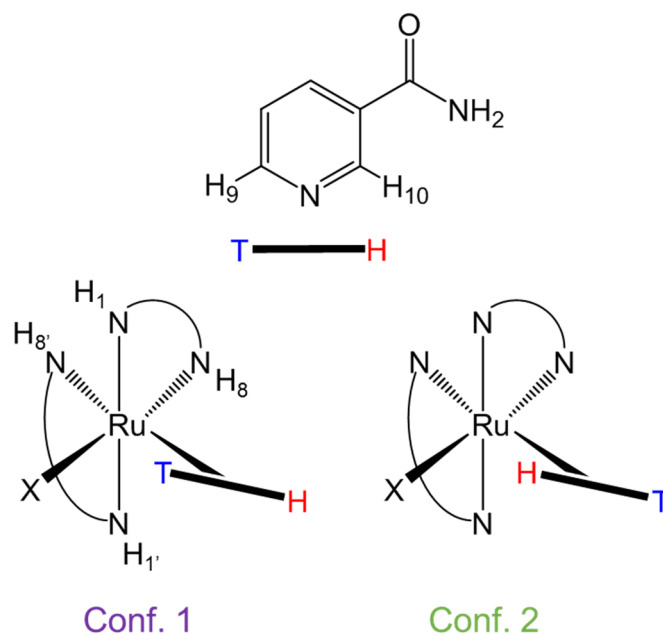


**Figure 3.18.** Structure and nomenclature of the atropisomers of  $cis$ -[Ru(bpy)<sub>2</sub>(NA)X]<sup>+</sup> isolated at 185 K.

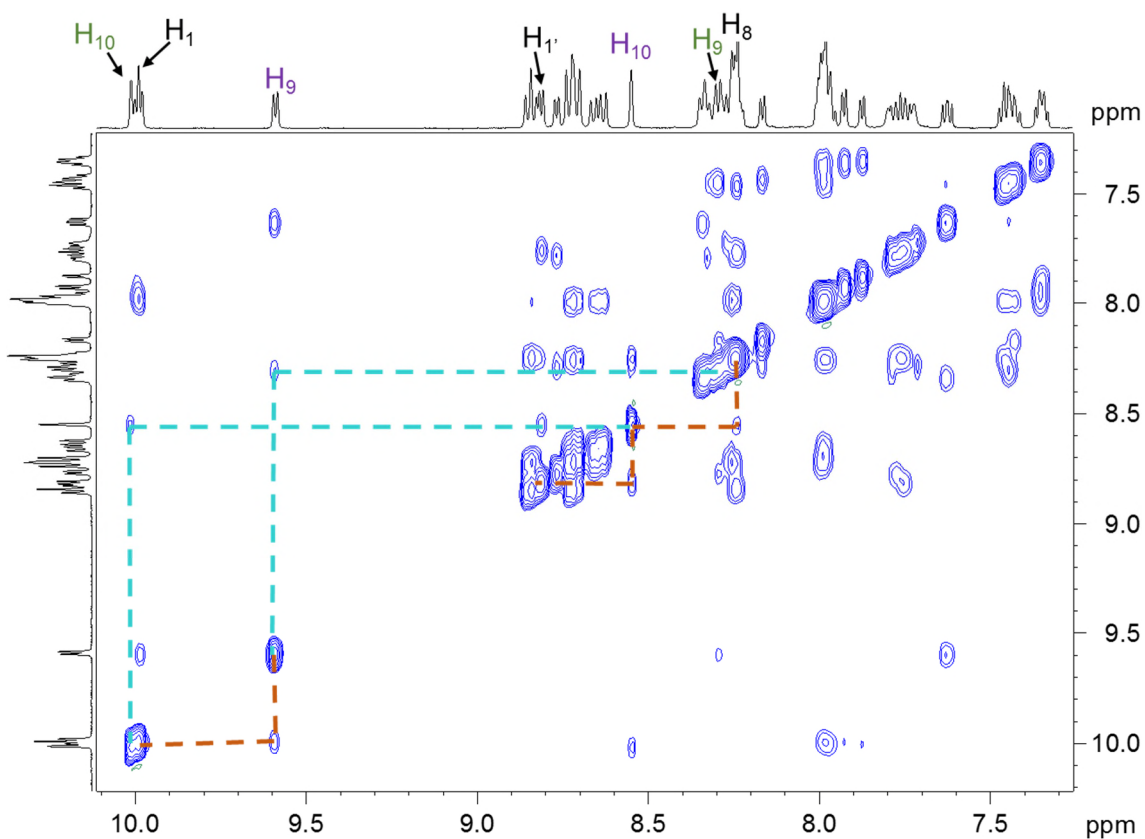


**Figure 3.19.**  $^1\text{H}$ - $^1\text{H}$  NOESY spectrum (500 MHz) of  $cis$ -[Ru(bpy)<sub>2</sub>(NA)Cl][PF<sub>6</sub>] (**1**) in acetone- $d_6$  at 185 K where blue lines represent exchange cross-peaks and orange lines represent NOE cross-peaks.

Whether  $H_{10}$  or  $H_9$  is shifted downfield is dependent on the orientation of the NA ligand. In the case of **3** only one atropisomer is present (denoted as Conf. 1) with  $H_{10}$  proton shifted downfield and  $H_9$  shifted upfield, see Figure 3.20. The chemical shift of selected peaks for each atropisomer is given in Table 3.7.

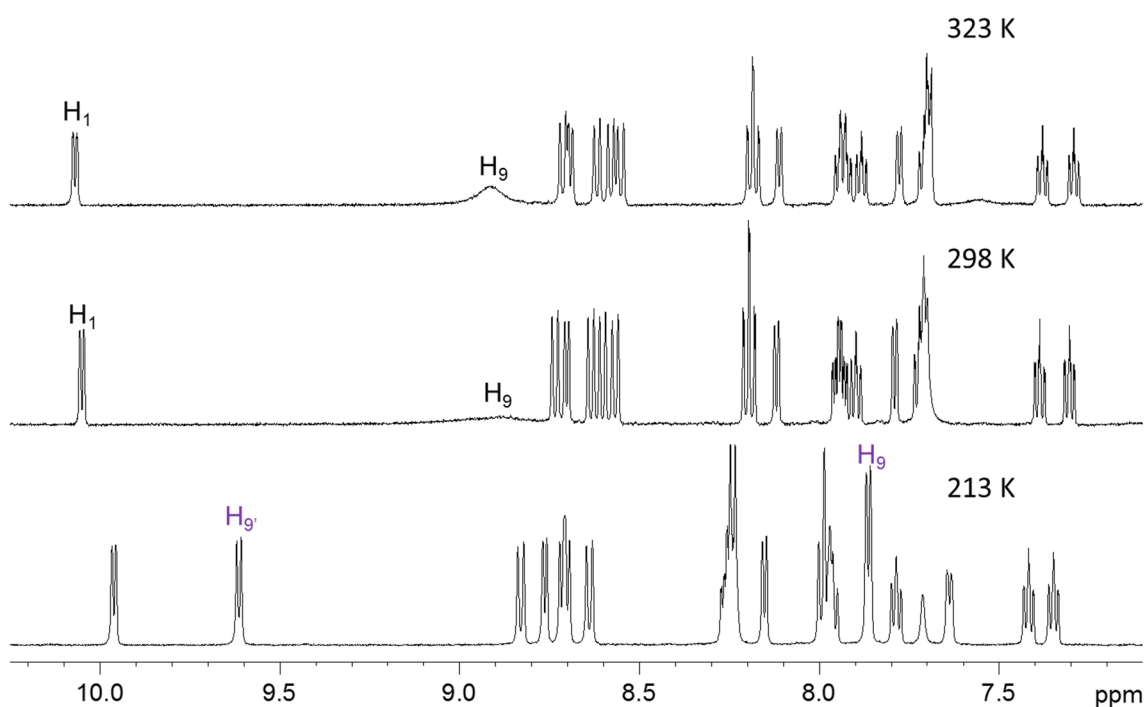


**Figure 3.20.** Variable temperature  $^1\text{H}$ -NMR spectra (500 MHz) of *cis*- $[\text{Ru}(\text{bpy})_2(\text{INA})_2\text{Cl}][\text{PF}_6]$  (**3**) at 213 K, 298 K and 323 K in acetone- $d_6$ .

The chemical shift difference between  $H_{10}$  and  $H_9$  for both atropisomers of **1** (1.04 ppm for Conf. 1 and 1.71 ppm for Conf. 2) is greater than that found for **2** (0.9 ppm for Conf. 1 and 1.49 ppm for Conf. 2). For both **1** and **2** the atropisomer with greatest chemical shift difference for  $H_{10}$  and  $H_9$  is Conf. 2. The chemical shift difference between  $H_{10}$  and  $H_9$  for both **1** and **2** is greater than that found for the free ligand (0.4 ppm for NA).



**Table 3.7.** Chemical shift data for *cis*-[Ru(bpy)<sub>2</sub>(NA)Cl][PF<sub>6</sub>] (**1**), *cis*-[Ru(bpy)<sub>2</sub>(NA)I][PF<sub>6</sub>] (**2**), *cis*-[Ru(bpy)<sub>2</sub>(INA)Cl][PF<sub>6</sub>] (**3**) and the free monodentate ligands in acetone-*d*<sub>6</sub>.

		Chemical shift, ppm			Chemical shift, ppm	
		<b>1</b> <sup>a</sup>	<b>2</b> <sup>a</sup>	<b>3</b> <sup>b</sup>	NA <sup>c</sup>	INA <sup>c</sup>
Conf 1	H <sub>10</sub>	8.55	8.81	(H <sub>9'</sub> ) 9.61	9.11	8.91
	H <sub>9</sub>	9.59	9.71	7.86	8.71	
Conf 2	H <sub>10</sub>	10.01	10.14			
	H <sub>9</sub>	8.30	8.65			

<sup>a</sup> at 185 K, <sup>b</sup> at 213 K and <sup>c</sup> at 298 K.

For **3** the chemical shift difference between H<sub>9'</sub> and H<sub>9</sub> is 1.75 ppm. For both **1** and **2** Conf. 1 is more stable in solution, with the ratio of Conf. 1 to Conf. 2 being 1:0.8.

By using equations stated in Section 3.2.6.1., the experimental free energy of activation ( $\Delta G_c^\ddagger$ ) was calculated, see Table 3.8. The free energy of activation for **1** is 3.9 kJ mol<sup>-1</sup> higher than that found for **2**.

**Table 3.8.** Parameters determined from variable temperature <sup>1</sup>H-NMR experiments in acetone-*d*<sub>6</sub> with *cis*-[Ru(bpy)<sub>2</sub>(NA)Cl][PF<sub>6</sub>] (**1**) and *cis*-[Ru(bpy)<sub>2</sub>(NA)I][PF<sub>6</sub>] (**2**)

Complex	$\delta\nu$ (s <sup>-1</sup> )	$k_c$ (s <sup>-1</sup> )	T <sub>c</sub> (K)	$\Delta G_c^\ddagger$ (kJ mol <sup>-1</sup> )
<b>1</b>	688	1144	278	51.6 ± 0.2
<b>2</b>	598	994	256	47.7 ± 0.3

#### 3.3.4.2. Solvent effect on dynamic behaviour studied by <sup>1</sup>H-NMR

In order to understand the nature of the conformational exchange, *cis*-[Ru(bpy)<sub>2</sub>(NA)Cl][PF<sub>6</sub>] (**1**) and *cis*-[Ru(bpy)<sub>2</sub>(NA)I][PF<sub>6</sub>] (**2**) were dissolved in various deuterated solvents. When **2** is in DMSO-*d*<sub>6</sub>, the broad peaks previously at 9.32 and 9.27 ppm in acetone-*d*<sub>6</sub> begin to separate and shift upfield to 9.09 and 8.97 ppm, see Figure 3.21.

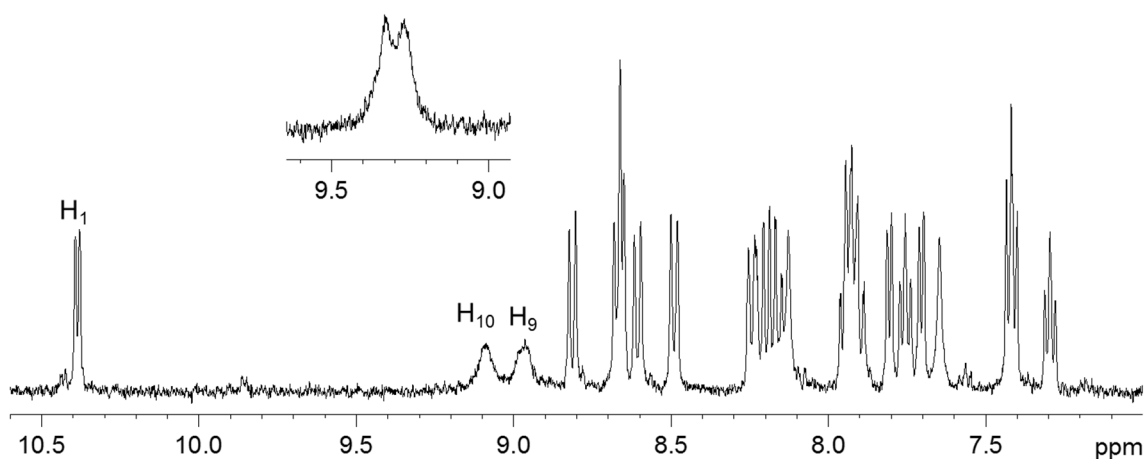


**Figure 3.21.**  $^1\text{H}$ -NMR spectrum (400 MHz) of *cis*-[Ru(bpy) $_2$ (NA)I][PF $_6$ ] (**2**) in DMSO- $d_6$  at 298 K. Inset is  $^1\text{H}$ -NMR spectrum of **2** in acetone- $d_6$  at 298 K.

Similarly the bpy  $\text{H}_1$  peak at 10.62 ppm in acetone- $d_6$  shifts upfield to 10.39 ppm in DMSO- $d_6$ . When **1** is in DMSO- $d_6$ , the broad peak and the bpy  $\text{H}_1$  proton previously at 9.07 and 10.08 ppm, respectively, in acetone- $d_6$  shifts upfield to 8.76 and 9.85 ppm. When a drop of  $\text{D}_2\text{O}$  was added to the DMSO- $d_6$  sample, the broad peak split into two peaks with chemical shifts of 8.92 and 8.64 ppm, and again the bpy  $\text{H}_1$  proton shifted further upfield to 9.78 ppm, see Figure 3.22.

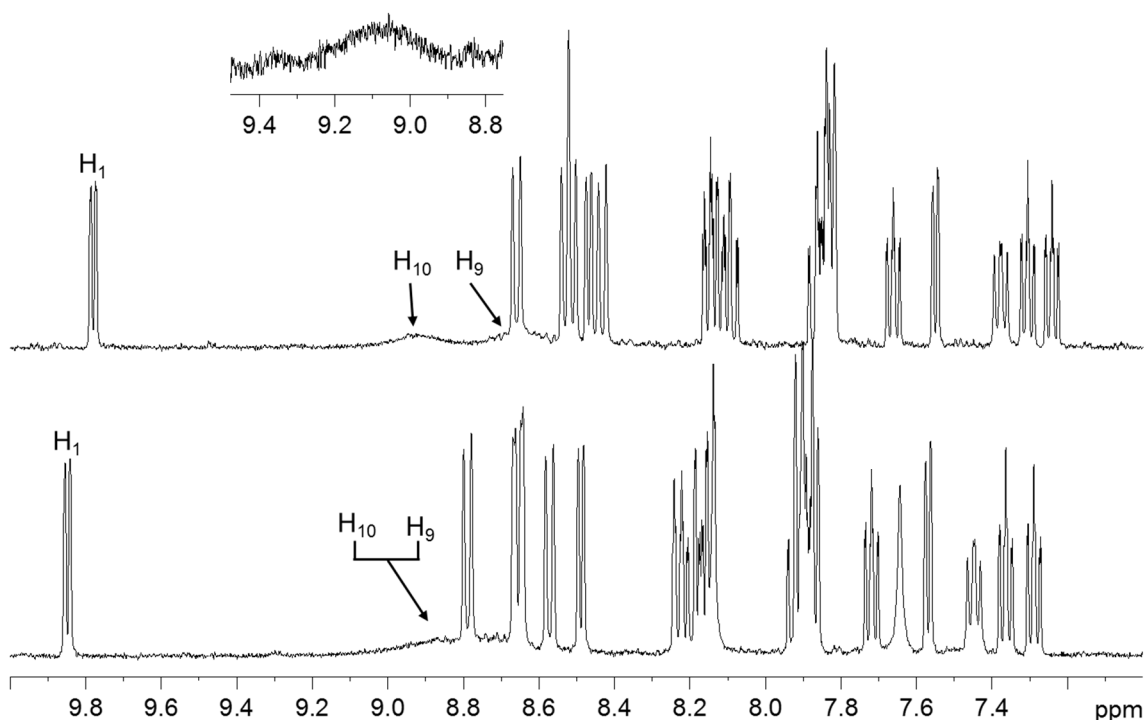


**Figure 3.22.**  $^1\text{H}$ -NMR spectrum (400 MHz) of *cis*-[Ru(bpy) $_2$ (NA)Cl][PF $_6$ ] (**1**) in DMSO- $d_6$  (bottom) and with 20  $\mu\text{L}$  D $_2$ O added (top). Inset is  $^1\text{H}$ -NMR spectrum of **1** in acetone- $d_6$  at 298 K.

#### 3.3.4.3. Dynamic behaviour studied by DFT

DFT was used to investigate whether an intramolecular interaction is the cause for the hindered rotation of the NA ligand at room temperature (298 K) for **1** and **2**. A potential energy scan was performed to investigate the starting geometries and transition states by changing the dihedral angle between the halide and H $_9$ , shown in Figure 3.23.

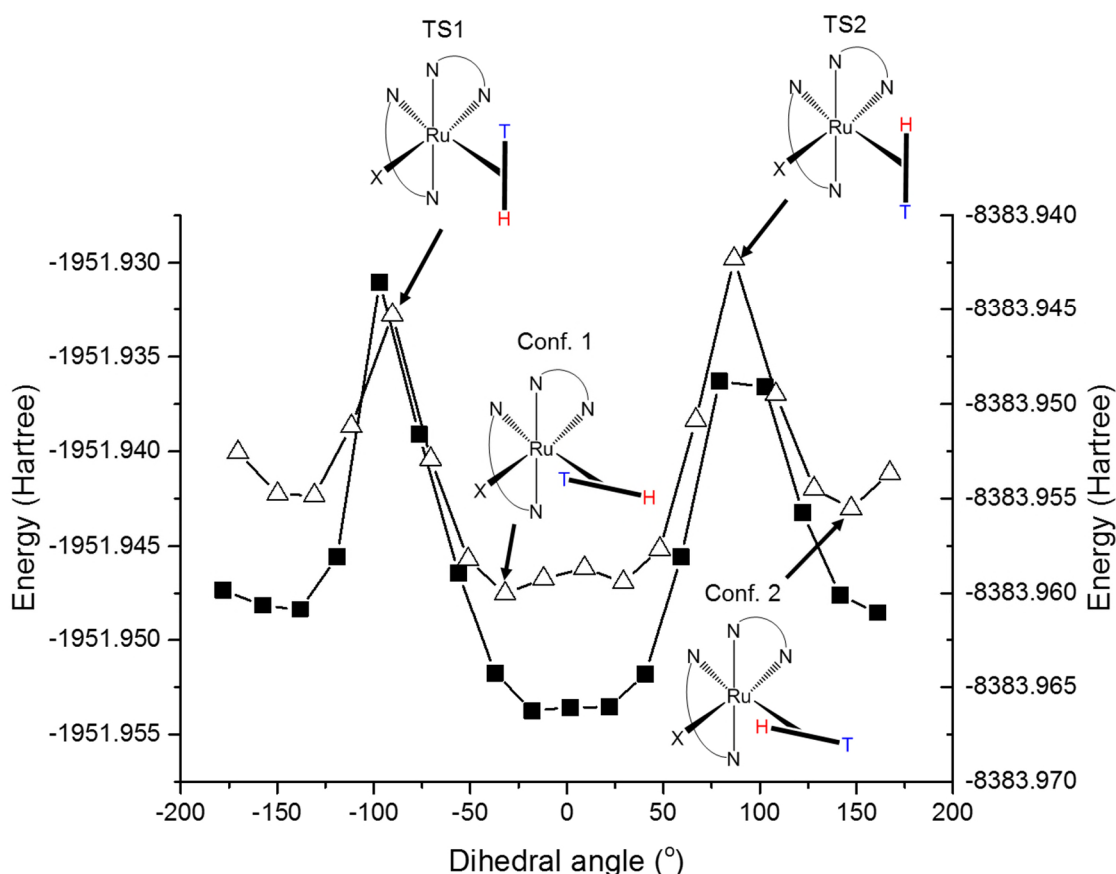


**Figure 3.23.** Potential energy surface scan of *cis*-[Ru(bpy)<sub>2</sub>(NA)Cl]<sup>+</sup> (**1**) (left axis and filled squares) and *cis*-[Ru(bpy)<sub>2</sub>(NA)I]<sup>+</sup> (**2**) (right axis and empty triangles) using B3LYP/LanL2DZ/3-21G as the functional/ basis set.

The lowest energy geometries were found to be Conf. 1 and Conf. 2. The conformation with the lowest energy is Conf. 1. There were two transition states, labelled transition state 1 (TS1) and transition state 2 (TS2), with TS2 having the highest energy. Geometry optimisations were performed to gain accurate energies of the conformations using two different functionals; B3LYP and PBE1PBE. The DFT free energy of activation ( $\Delta G_{\text{DFT}}^\ddagger$ ) was calculated as described in Section 3.2.6.3, see Table 3.9.

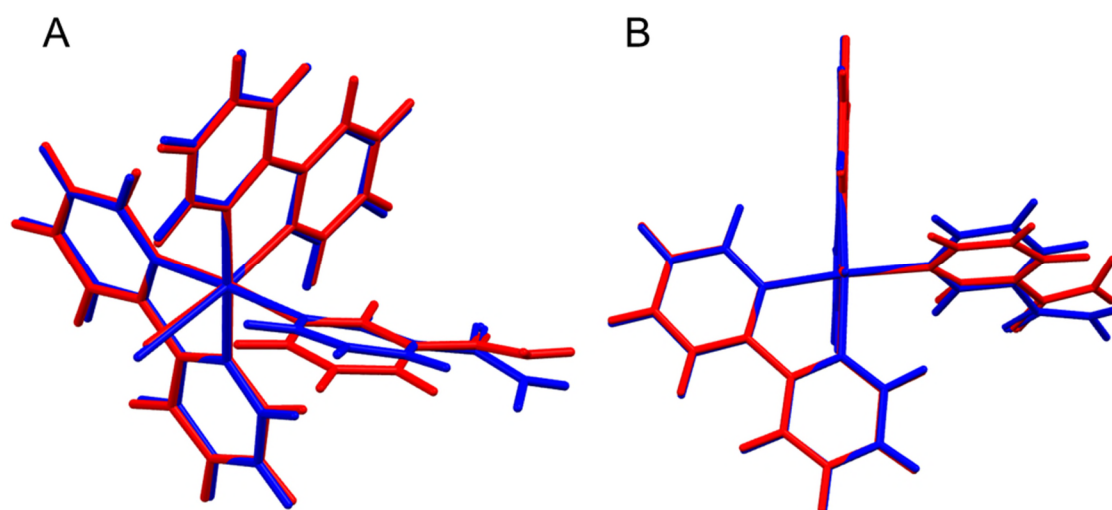
**Table 3.9.** Free energy of activation ( $\Delta G_{DFT}^\ddagger$ ) calculated from geometry optimised DFT structures of *cis*-[Ru(bpy)<sub>2</sub>(NA)Cl]<sup>+</sup> (**1**) and *cis*-[Ru(bpy)<sub>2</sub>(NA)I]<sup>+</sup> (**2**).

		$\Delta G_{DFT}^\ddagger$ (kJ mol <sup>-1</sup> )			
	Functional/ Basis set	Conf 1	Conf 1	Conf 2	Conf 2
		→ TS1	→ TS2	→ TS1	→ TS2
<b>1</b>	B3LYP/LanL2DZ/6-31G**+	46.54	50.02	36.73	40.20
	PBE1PBE/LanL2DZ/6-31G**+	50.17	54.09	40.59	44.50
<b>2</b>	B3LYP/LanL2DZ/6-31G**+	41.08	44.34	32.58	35.83
	PBE1PBE/LanL2DZ/6-31G**+	45.53	49.37	37.45	41.29

Generally the free energies of activation associated with **1** are greater than those for **2**. From exploring the ground state configurations and transitions states, the main geometrical differences between **1** and **2** occur between the ground state configurations. Thus from here onwards only Conf. 1 and Conf. 2 will be discussed. The bond distance between H<sub>10</sub>/H<sub>9</sub> and the halide X was investigated (H $\cdots$ X), see Table 3.10. Both PBE1PBE and B3LYP basis sets show that Conf. 1 has a shorter H<sub>9</sub>/H<sub>10</sub> $\cdots$ X distance than Conf. 2 by  $\sim 0.1$  Å for both **1** and **2**. Additionally both atropisomers of **1** have shorter H<sub>10</sub>/H<sub>9</sub> $\cdots$ X bond distances than both atropisomers of **2**. This can evidently be seen when visualising Conf. 1 of both **1** and **2** as the NA ligand appears to orientate itself closer to the halide for **1**, see Figure 3.24.

**Table 3.10.** Bond distance of  $H_{10}/H_9 \cdots X$  from geometry optimised DFT structures of *cis*-[Ru(bpy)<sub>2</sub>(NA)Cl]<sup>+</sup> (**1**) and *cis*-[Ru(bpy)<sub>2</sub>(NA)I]<sup>+</sup> (**2**)

		H <sub>10</sub> / H <sub>9</sub> ⋯X distance (Å)	
		B3LYP/LanL2DZ/ 6-31G**+	PBE1PBE/LanL2DZ/ 6-31G**+
<b>1</b>	Conf. 1	2.43	2.44
	Conf. 2	2.56	2.53
<b>2</b>	Conf. 1	2.90	2.86
	Conf. 2	3.02	2.97

**Figure 3.24.** Overlay of geometry optimised DFT structures (PBE1PBE/LanL2DZ/6-31G\*\*+) of [Ru(bpy)<sub>2</sub>(NA)Cl]<sup>+</sup> (**1**) (red) and [Ru(bpy)<sub>2</sub>(NA)I]<sup>+</sup> (**2**) (blue) to show orientation of NA ligand from two different angles, with (B) looking down the X-Ru bond.

The Mulliken charges were investigated to see if there is any interaction between  $H_{10}/H_9$  with the halide X, see Table 3.11. The difference in Mulliken charge between  $H_{10}$  and  $H_9$  on the free NA ligand was used as a guide. The difference in charge between  $H_{10}$  and  $H_9$  for free NA ligand is 0.029 with  $H_{10}$  more positive than  $H_9$ . It is worth noting that for Conf. 1  $H_9$  is closest to the halide, whereas for Conf. 2  $H_{10}$  is

closest to the halide. For **1**, Conf. 2 H<sub>10</sub> is more positive than H<sub>9</sub> (with a difference of 0.044), however for Conf. 1 both H<sub>10</sub> and H<sub>9</sub> have the same Mulliken charge. For **2** both conformations show H<sub>10</sub> with a higher positive Mulliken charge than H<sub>9</sub> (with a difference of 0.011 for Conf. 1 and 0.036 for Conf. 2). The halide for **1** and **2** is more negative in Conf. 1 than in Conf. 2.

**Table 3.11.** Mulliken charges for *cis*-[Ru(bpy)<sub>2</sub>(NA)Cl]<sup>+</sup> (**1**), *cis*-[Ru(bpy)<sub>2</sub>(NA)I]<sup>+</sup> (**2**) and ligand alone (NA) from DFT geometry using PBE1PBE/LanL2DZ/6-31G\*\*+.

		Mulliken charge	
	Atom	Conf. 1	Conf. 2
<b>1</b>	H <sub>10</sub>	0.188	0.204 <sup>a</sup>
	H <sub>9</sub>	0.188 <sup>a</sup>	0.160
	X	-0.290	-0.278
<b>2</b>	H <sub>10</sub>	0.186	0.195 <sup>a</sup>
	H <sub>9</sub>	0.175 <sup>a</sup>	0.159
	X	-0.241	-0.227
Nicotinamide (NA)	H <sub>10</sub>	0.172	
	H <sub>9</sub>	0.143	

<sup>a</sup> indicates which atom is closest to the halide.

### 3.4. Discussion

#### 3.4.1. Synthesis and characterisation

In the <sup>1</sup>H-NMR spectra of bis-substituted Ru(II) polypyridyl complexes, *cis*-[Ru(bpy)<sub>2</sub>(INH)<sub>2</sub>][PF<sub>6</sub>]<sub>2</sub> (**4**), *cis*-[Ru(bpy)<sub>2</sub>(NA)<sub>2</sub>][PF<sub>6</sub>]<sub>2</sub> (**5**), *cis*-[Ru(phen)<sub>2</sub>(INH)<sub>2</sub>][PF<sub>6</sub>]<sub>2</sub> (**6**) and *cis*-[Ru(phen)<sub>2</sub>(NA)<sub>2</sub>][PF<sub>6</sub>]<sub>2</sub>, the number of peaks observed is half the amount of protons in the complex. This is due to the presence of a two-fold symmetry axis (C<sub>2</sub> symmetry). For Ru(II) polypyridyl halide complexes, *cis*-[Ru(bpy)<sub>2</sub>(NA)Cl][PF<sub>6</sub>] (**1**), *cis*-[Ru(bpy)<sub>2</sub>(NA)I][PF<sub>6</sub>] (**2**) and *cis*-

$[\text{Ru}(\text{bpy})_2(\text{INA})\text{Cl}][\text{PF}_6]$  (**3**), the asymmetry of the complex results in each proton in the complex having its own unique chemical shift.

Due to the presence of the halide, one doublet from 2,2'-bipyridine is always low-field-shifted for complexes **1** – **3**; for **1** and **3** it is located at 10.1 ppm, and for **2** it is located at 10.62 ppm. This is due to the fact that this proton is in close proximity to the halide, and is thus deshielded. This is confirmed by the fact that the proton in **2** is more low-field-shifted than **1** and **3**; **2** contains an iodide ligand which is bigger than the chloride ligand and therefore the proton comes into closer proximity to it.

For *cis*- $[\text{Ru}(\text{bpy})_2(\text{L})\text{X}][\text{PF}_6]$  complexes **1** – **3** there is a broad peak at 9-9.5 ppm that is due to protons from the monodentate ligand, L, closest to the nitrogen of the pyridine ring. Interestingly, this feature is not present for *cis*- $[\text{Ru}(\text{N-N}')_2(\text{L})_2][\text{PF}_6]_2$  complexes **4** – **7**, and therefore must be due to the presence of the halide.  $^1\text{H}$ - $^1\text{H}$  NOESY spectra confirmed that this broadening is due to conformational exchange, and thus the rotation of the monodentate ligand must be hindered for **1** – **3** at room temperature (298 K) on the NMR timescale (500 MHz), see Section 3.3.1. Previously it has been found that in the complex  $[\text{Ir}(\text{H})_2(\text{PPh}_3)_2(2\text{-AP})\text{F}]$  there is an intramolecular hydrogen bond between the  $\text{NH}_2$  group of 2-AP (2-aminopyridine) and F.<sup>32</sup> It was initially thought that such an interaction could occur in *cis*- $[\text{Ru}(\text{bpy})_2(\text{NA})\text{Cl}][\text{PF}_6]$  (**1**) between the amide group in the 3- position of NA ligand and Cl. However this possibility was rejected as the hindered rotation of the ligand still occurs in *cis*- $[\text{Ru}(\text{bpy})_2(\text{INA})\text{Cl}][\text{PF}_6]$  (**3**), where the amide group is in the 4- position. Thus there must be no interaction between the amide group and the halide in complexes **1** – **3**.



### 3.4.2. X-Ray crystal structures

The bond lengths for *cis*-[Ru(bpy)<sub>2</sub>(INH)<sub>2</sub>][PF<sub>6</sub>]<sub>2</sub> (**4**) and *cis*-[Ru(bpy)<sub>2</sub>(NA)<sub>2</sub>][PF<sub>6</sub>]<sub>2</sub> (**5**) are very similar to each other, and the only difference is the angle between the monodentate ligands (N13-Ru1-N13). For **4** the angle is 91.3 Å and for **5** the angle is 94.36 Å. The angle for **5** could be bigger due to the bulkier nature of the amide in the 3- position of the NA ligand. The bite angle for phen in *cis*-[Ru(phen)<sub>2</sub>(INH)<sub>2</sub>][PF<sub>6</sub>]<sub>2</sub> (**6**) is the same as for bpy in **4** and **5**. This is not surprising as the only difference between bpy and phen is the rigidity of ligand.

CH- $\pi$  interactions are commonly found in crystal structures of metal complexes, with strong interactions showing a CH-centroid distance of < 2.6 Å and weak interactions < 3.0 Å.<sup>33</sup> These interactions were found for **4**, **5** and **6** linking two different enantiomers, involving the chelate ring CH of the  $\Delta$  enantiomer and the aromatic ring of the monodentate ligand of the  $\Lambda$  enantiomer. The CH-centroid distance is 3.176 Å, 2.733 Å and 2.697 Å for **4**, **5** and **6** respectively. The interaction for **4** is a borderline case, however with **5** and **6** the interaction can be classed as weak. Interestingly the complexes with the shortest CH- $\pi$  interactions (**5** and **6**) observed  $\pi$ - $\pi$  stacking between the chelating rings of pairs of enantiomers. The centroid-centroid distance for **5** and **6** is 4.019 Å and 3.909 Å respectively, with the planes of the aromatic rings perfectly parallel. It is thought that the reason for a better  $\pi$ - $\pi$  interaction between the phen ligands of **6** is because there is an extra aromatic ring that extends out further from the ruthenium centre, when compared to bpy, thus allowing for better overlap. For strong  $\pi$ - $\pi$  interactions the centroid-centroid distance is usually ~3.3 Å and for weak interactions is 3.6-3.8 Å.<sup>34</sup> Thus those exhibited for both **5** and **6** can be classed as very weak interactions. Interestingly the bpy twist angle for **5** (6.57°) is bigger than for **4** (3.29°); this could arise from the fact that the bpy in **5** needs to orientate itself

parallel to an adjacent bpy in order for a  $\pi$ - $\pi$  interaction to occur (in **4**  $\pi$ - $\pi$  interactions do not occur).

Throughout the crystal structures of **4**, **5** and **6** there is a wide array of hydrogen bonding. For **4** there is a dimer that forms between two enantiomers of neighbouring unit cells via hydrogen bonding between the hydrazide group of the INH ligand. The bond is strong with a length of 2.199 Å. Interestingly the crystal structure for **4** exhibits disorder over the hydrazide group, which suggest the hydrogen bond is fluxional. For **5** two forms of hydrogen bonding occur: one between the amide group of the NA ligand and water molecules, and one between bpy aromatic protons and PF<sub>6</sub>. In the former, the N-H<sub>(NA)</sub>-OH<sub>2</sub> distance is 2.068 Å and O<sub>(NA)</sub>-HOH distance is 1.921 Å, which again can be classed as strong hydrogen bonding. The bifurcated interaction between PF<sub>6</sub> and aromatic protons of bpy results in bond lengths of 2.565 Å and 2.288 Å, showing that the interaction is reasonably strong. This type of hydrogen bonding is commonly found in PF<sub>6</sub> organometallic salts, and is thought to be assisted by the difference in charge between anion and cation.<sup>35</sup> For **6** there is an extensive network of hydrogen bonds between the hydrazide group of INH and water. The plethora of intermolecular interactions exhibited by complexes **4**, **5** and **6** suggests that such interactions could be important if the complex is recognised by proteins and other target sites.

### 3.4.3. Dark stability in aqueous solution

Before investigating the photoactivity of complexes, it is imperative to understand how the complexes behave in solution in the dark. When stored in aqueous solution over a 6 h period in the dark, bis-substituted *cis*-[Ru(*N-N'*)<sub>2</sub>(L)<sub>2</sub>][PF<sub>6</sub>]<sub>2</sub> complexes **4** – **7** show no appreciable change in the UV-visible spectrum. Thus the complexes are

stable in the dark for the duration of the experiment. Therefore when photoactivation studies are carried out it is certain that any change observed is due to exposure to light.

It is common for ruthenium complexes containing halido ligands to hydrolyse in aqueous solution.<sup>36-38</sup> In some cases, hydrolysis is needed before the complex can be active, for example hydrolysis of the anticancer agent NAMI-A provides binding sites so that the complex can bind to biomolecules such as DNA.<sup>39</sup> It is always ideal for a drug to have good aqueous solubility, however in some cases poor water solubility means that solvents such as 5% DMSO are required to dissolve the drug. Interestingly the use of such solvents can affect the activity of a drug, and in some instances it can reduce the activity *in vitro*.<sup>40</sup> Thus it is important to consider whether the presence of different solvents in the formulation can affect the hydrolysis of a drug.

The UV-visible spectrum of *cis*-[Ru(bpy)<sub>2</sub>(NA)Cl][PF<sub>6</sub>] (**1**) in aqueous solution changes over a period of 6 h with the formation of *cis*-[Ru(bpy)<sub>2</sub>(NA)(H<sub>2</sub>O)]<sup>2+</sup>. There is a decrease in the peak with a maximum at 473 nm, with a rise in a new band with a maximum at 466 nm. The increase in absorbance at 466 nm follows a single exponential curve to give *t*<sub>1/2</sub> of 2712 s. However this behaviour was not seen when using either 5% DMSO, 5% acetone or 5% DMF. Instead the peak with a maximum at 475 nm consistently decreased and never reached an end point over a 24 h period. This decrease did not follow a single exponential relationship. ESI-MS confirmed that hydrolysis was still occurring in these cases by the presence of *cis*-[Ru(bpy)<sub>2</sub>(NA)(H<sub>2</sub>O)]<sup>2+</sup>, but another process must be interfering with the hydrolysis process. For 5% DMSO a product mass was observed consistent with the formation of *cis*-[Ru(bpy)<sub>2</sub>(NA)(DMSO)]<sup>2+</sup>. Thus if an organic solvent is present at a concentration of 5% and can act as a  $\sigma$ -donor ligand, the organic solvent can bind to Ru(II) and interfere with the hydrolysis process. This could have implications for

biological testing, as it may affect the activity of the complex *in vitro*. Additionally the kinetics of the photoreaction are more difficult to measure if more than one process is occurring. Thus for photoirradiation experiments pure water will be used.

#### 3.4.4. Dynamic behaviour in solution

At room temperature (298 K) in acetone-*d*<sub>6</sub>, the rotation of the monodentate ligands (NA) in *cis*-[Ru(bpy)<sub>2</sub>(NA)<sub>2</sub>][PF<sub>6</sub>]<sub>2</sub> (**5**) around the Ru-N axis appears to be fast on the NMR timescale (500 MHz) at 298 K; heating the solution to 323 K does not change the spectrum. However once the solution was cooled to 185 K, the NA ligands rotate much slower on the NMR timescale allowing atropisomers to be viewable in the <sup>1</sup>H-NMR spectrum. The same temperature dependent behaviour was observed for a similar complex *cis*-[Ru(bpy)<sub>2</sub>(4Pic)<sub>2</sub>]<sup>2+</sup>, where 4Pic is 4-picoline.<sup>41</sup> In the case of **5**, 3 atropisomers were in slow exchange at 185 K, termed A, B and C, and were characterised using <sup>1</sup>H-<sup>1</sup>H NOSEY. All regions of the <sup>1</sup>H-NMR spectrum at 185 K were too complicated to analyse completely, apart from the H<sub>9</sub> and H<sub>10</sub> region at ~9 ppm (protons of the NA ligand closest to the nitrogen of the pyridine ring). Either H<sub>10</sub> or H<sub>9</sub> is shifted downfield depending on its environment, and it is characteristic for each atropisomer. The proton of one NA ligand that is located over the centre of the ring of the other NA will be shielded, see Figure 3.25. Thus for atropisomer A, H<sub>9</sub> is high-field-shifted compared to H<sub>10</sub>, for atropisomer B H<sub>10</sub> is high-field-shifted compared for H<sub>9</sub>, and in the case of atropisomer C each proton is consistently in a different environment (the atropisomer is asymmetric).

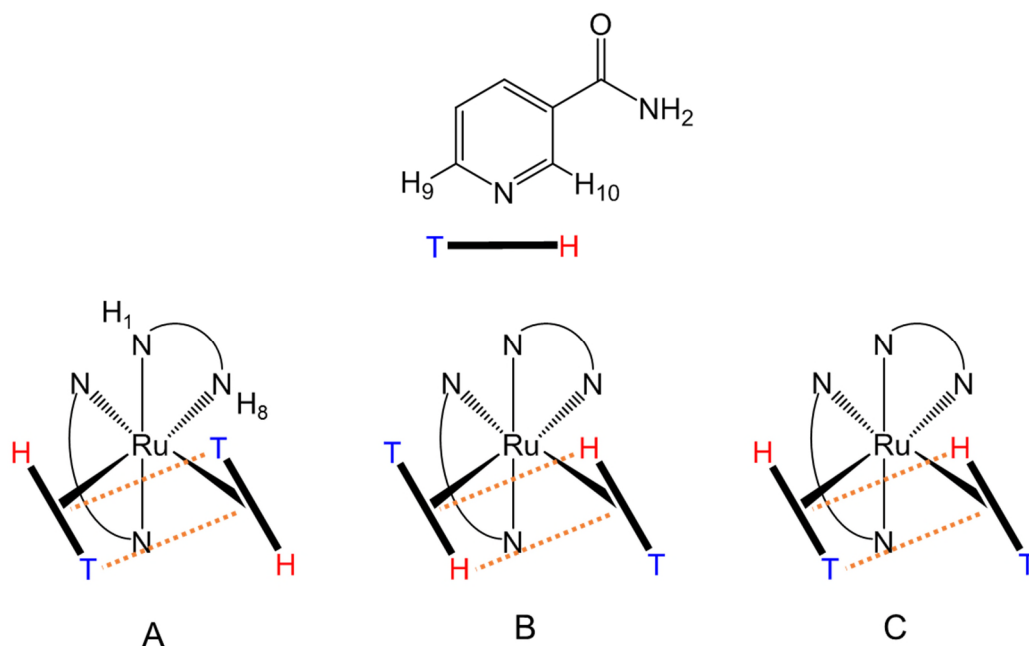


**Figure 3.25.** Structures of the atropisomers of *cis*-[Ru(bpy)<sub>2</sub>(NA)Cl][PF<sub>6</sub>] (**1**) highlighting the position of the NA ligands and the environments of the protons. **H** and **T** refers to the “head” and “tail” orientation of the NA ligand, respectively.

Interestingly for *cis*-[Ru(bpy)<sub>2</sub>(NA)Cl][PF<sub>6</sub>] (**1**), *cis*-[Ru(bpy)<sub>2</sub>(NA)I][PF<sub>6</sub>] (**2**) and *cis*-[Ru(bpy)<sub>2</sub>(INA)Cl][PF<sub>6</sub>] (**3**) the rotation of the monodentate ligand is hindered at room temperature (298 K) in acetone-*d*<sub>6</sub> on the NMR timescale (500 MHz). For **1** and **2** there is a broad peak at 9-9.5 ppm at 298 K which is due to NA protons H<sub>9</sub> and H<sub>10</sub>. Heating an acetone-*d*<sub>6</sub> solution of *cis*-[Ru(bpy)<sub>2</sub>(NA)Cl][PF<sub>6</sub>] (**1**) to 323 K results in this broad peak sharpening and splitting into two peaks. Interestingly an acetone-*d*<sub>6</sub> solution of *cis*-[Ru(bpy)<sub>2</sub>(NA)I][PF<sub>6</sub>] (**2**) at room temperature (298 K) exhibits a broad peak at ~9-9.5 ppm that is sharper and weakly split into two. Heating the solution to 323 K results in the peaks becoming even sharper and two peaks can be clearly observed. All of the above suggests that the rotation of the monodentate ligand in **2** is faster than for **1**. When both **1** and **2** in acetone-*d*<sub>6</sub> are cooled to 185 K, two atropisomers are revealed, termed Conf. 1 and Conf. 2. Again the atropisomers were

characterised by  $^1\text{H}$ - $^1\text{H}$  NOESY. For Conf. 1,  $\text{H}_9$  is low-field-shifted (i.e. deshielded) compared to  $\text{H}_{10}$  because of its close proximity to the halide, and the opposite is true for Conf. 2 (chemical shift of  $\text{H}_{10} > \text{H}_9$ ). The chemical shift difference between  $\text{H}_9$  and  $\text{H}_{10}$  for the free ligand (NA) is 0.4 ppm whereas for **1** and **2** is  $>1$  ppm. This shift suggests that the halide is interacting with the aromatic protons of the monodentate ligand ( $\text{H}_9$  and  $\text{H}_{10}$ ), which could hinder rotation at room temperature. This is proven by the fact that more polar solvents disrupt this interaction (e.g. DMSO- $d_6$  and  $\text{D}_2\text{O}$ ), resulting in more resolved peaks for  $\text{H}_9$  and  $\text{H}_{10}$ . It is hypothesised that the interaction can be classed as hydrogen bonding, which will be discussed in detail later.

The energy barrier to rotation was calculated experimentally by  $^1\text{H}$ -NMR ( $\Delta G_c^\ddagger$ ) and theoretically by DFT ( $\Delta G_{\text{DFT}}^\ddagger$ ). The DFT results correlate well with the experimental results, with the PBE1PBE basis set performing the best, see summary in Table 3.12. The PBE1PBE functional has been shown to predict hydrogen bond energies well.<sup>42</sup>

**Table 3.12.** Summary of the values obtained for the free energy of activation of *cis*- $[\text{Ru}(\text{bpy})_2(\text{NA})\text{Cl}][\text{PF}_6]$  (**1**) and *cis*- $[\text{Ru}(\text{bpy})_2(\text{NA})\text{I}][\text{PF}_6]$  (**2**) from variable temperature  $^1\text{H}$ -NMR experiments ( $\Delta G_c^\ddagger$ ) and DFT ( $\Delta G_{\text{DFT}}^\ddagger$ ).

		$\Delta G_{\text{DFT}}^\ddagger$ (kJ mol <sup>-1</sup> ) <sup>a</sup>	$\Delta G_c^\ddagger$ (kJ mol <sup>-1</sup> )
$[\text{Ru}(\text{bpy})_2(\text{NA})\text{Cl}]^+$ ( <b>1</b> )	Conf. 1	50.17	$51.6 \pm 0.2$
	Conf. 2	40.59	
$[\text{Ru}(\text{bpy})_2(\text{NA})\text{I}]^+$ ( <b>2</b> )	Conf. 1	45.53	$47.7 \pm 0.3$
	Conf. 2	37.45	

<sup>a</sup> only PBE1PBE/LanL2DZ/6-31G\*\*+ and Conf. 1/2 – TS1 values are shown.

Both show that the free energy of activation is greater for **1** when compared to **2**. This can be attributed to the greater acceptor ability of Cl when compared to I, thus for **1**

the rotation of the NA ligand is more hindered. This is supported by the fact that the NA ligand orientates itself closer to the halide in **1**, as shown by the DFT geometry. Similarly the Mulliken charge of the proton that is closest to the halide becomes more positive, and greater positive charges are found in the case of **1**. Interestingly both DFT free energy of activation values and  $^1\text{H}$ -NMR show that Conf. 1 is more stable than Conf. 2, which is shown with the ratio of each in acetone- $d_6$  at 298 K (1 for Conf. 1 and 0.8 for Conf. 2). This can be attributed to the fact that in the free ligand,  $\text{H}_{10}$  has a more positive Mulliken charge than  $\text{H}_9$  due to an intramolecular interaction between  $\text{H}_{10}$  and the oxygen of the amide, see Figure 3.26. The orientation is supported by the DFT geometry. Therefore it will be unfavourable for  $\text{H}_{10}$  to hydrogen bond with the halide, thus rendering Conf. 2 unfavourable (with  $\text{H}_{10}$  in close proximity to the halide).

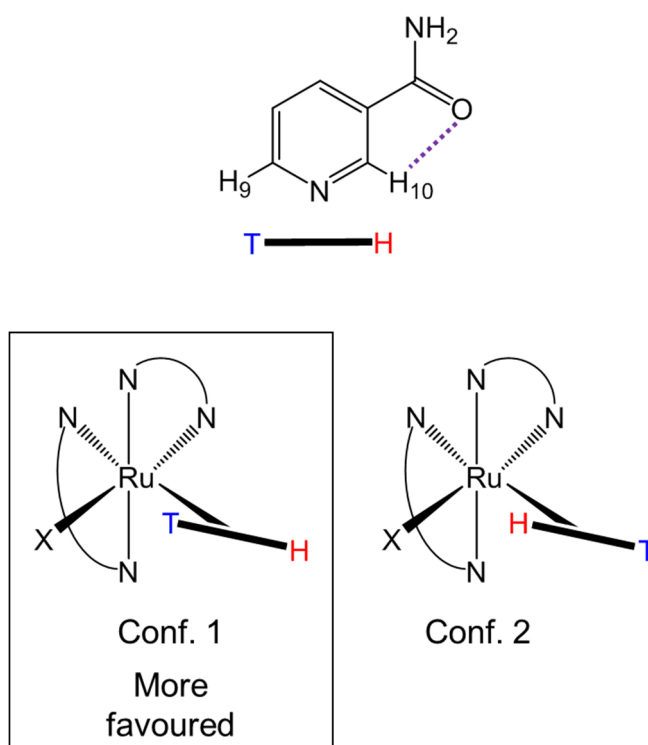


**Figure 3.26.** Structures of the atropisomers of *cis*-[Ru(bpy) $_2$ (NA)Cl][PF $_6$ ] (**1**) and [Ru(bpy) $_2$ (NA)I][PF $_6$ ] (**2**).

To confirm that the interaction can be classed as hydrogen bonding, the bond length of  $\text{CH}\cdots\text{X}$  from the DFT geometries were compared to literature hydrogen bonding values, see Table 3.13.

**Table 3.13.**  $\text{CH}\cdots\text{X}$  bond distances from geometry optimised DFT structures of *cis*- $[\text{Ru}(\text{bpy})_2(\text{NA})\text{Cl}]^+$  (**1**) and *cis*- $[\text{Ru}(\text{bpy})_2(\text{NA})\text{I}]^+$  (**2**) and literature.

CH $\cdots$ X Bond distance (Å)		
$[\text{Ru}(\text{bpy})_2(\text{NA})\text{Cl}]^+$ ( <b>1</b> )	Conf. 1	2.44 <sup>a</sup>
	Conf. 2	2.53 <sup>a</sup>
$[\text{Ru}(\text{bpy})_2(\text{NA})\text{I}]^+$ ( <b>2</b> )	Conf. 1	2.86 <sup>a</sup>
	Conf. 2	2.97 <sup>a</sup>
Literature	C-H $\cdots$ Cl	$2.77 \pm 0.15^b$
	C-H $\cdots$ I	$3.14 \pm 0.16^b$

<sup>a</sup> *PBE1PBE/LanL2DZ/6-31G\*\*+* and <sup>b</sup> values taken from<sup>43</sup>

Interestingly the bond distances found for **1** and **2** are shorter than those found in literature for  $\text{CH}\cdots\text{X}$ , where the CH is part of an aryl moiety, suggesting that the interaction is indeed hydrogen bonding in nature.

### 3.5. Summary

In this Chapter two sets of novel photoactive antibacterial compounds were synthesised; a) Ru(II) polypyridyl bis-substituted complexes *cis*- $[\text{Ru}(\text{bpy})_2(\text{INH})_2][\text{PF}_6]_2$  (**4**), *cis*- $[\text{Ru}(\text{bpy})_2(\text{NA})_2][\text{PF}_6]_2$  (**5**), *cis*- $[\text{Ru}(\text{phen})_2(\text{INH})_2][\text{PF}_6]_2$  (**6**) and *cis*- $[\text{Ru}(\text{phen})_2(\text{NA})_2][\text{PF}_6]_2$  (**7**), and b) Ru(II) polypyridyl halide complexes *cis*- $[\text{Ru}(\text{bpy})_2(\text{NA})\text{Cl}][\text{PF}_6]$  (**1**) and *cis*- $[\text{Ru}(\text{bpy})_2(\text{NA})\text{I}][\text{PF}_6]$  (**2**) where bpy is 2,2'-bipyridine, phen is 1,10-phenanthroline, NA is nicotinamide and INH is isoniazid. In the dark, complexes **4** – **7** are stable in aqueous solution, allowing further photoactive-studies to be carried out. *Cis*- $[\text{Ru}(\text{bpy})_2(\text{NA})\text{Cl}][\text{PF}_6]$  (**1**) was shown to hydrolyse in aqueous solution, forming the



mono-aqua adduct  $cis\text{-}[\text{Ru}(\text{bpy})_2(\text{NA})(\text{H}_2\text{O})]^{2+}$ , which could bind to biomolecules such as proteins or DNA. If **1** is in the presence of either 5% DMSO, 5% DMF or 5% acetone the hydrolysis is complicated by the addition of the organic solvent to the complex; for example in the case of 5% DMSO  $cis\text{-}[\text{Ru}(\text{bpy})_2(\text{NA})(\text{DMSO})]^{2+}$  is formed. The intra- and intermolecular interactions of all complexes have been investigated by the use of X-ray crystallography,  $^1\text{H}$ -NMR spectroscopy and DFT calculations. From X-ray crystallography there was an extensive array of intermolecular interactions for **4**, **5** and **6**, which include CH- $\pi$  interactions,  $\pi$ - $\pi$  interactions and hydrogen bonding. Such interactions may be important in biomolecule recognition and binding.  $^1\text{H}$ -NMR has shown that for  $cis\text{-}[\text{Ru}(\text{bpy})_2(\text{NA})_2][\text{PF}_6]_2$  (**5**) the NA ligand is rotating freely at 298 K on the NMR timescale (500 MHz), however complexes  $cis\text{-}[\text{Ru}(\text{bpy})_2(\text{NA})\text{Cl}][\text{PF}_6]$  (**1**) and  $cis\text{-}[\text{Ru}(\text{bpy})_2(\text{NA})\text{I}][\text{PF}_6]$  (**2**) observe hindered rotation of L at the same temperature. Both  $^1\text{H}$ -NMR spectroscopy and DFT calculations have shown that this hindered rotation is due to hydrogen bonding between the NA protons closest to the nitrogen of the pyridine ring and the halide. Interestingly Cl hinders rotation more than I, which corresponds to hydrogen bonding ability. This has implications that if a biomolecule (BM) binds to form  $cis\text{-}[\text{Ru}(\text{bpy})_2(\text{L})(\text{BM})]^{2+}$  and has a lone pair available for donation, the rotation of ligand L will be hindered, which may potentially affect the way the biomolecule binds.

### 3.6. References

1. Farrer, N. J.; Woods, J. A.; Salassa, L.; Zhao, Y.; Robinson, K. S.; Clarkson, G.; Mackay, F. S.; Sadler, P. J. *Angew. Chem. Int. Ed.*, **2010**, 49 (47), 8905-8908.
2. Howerton, B. S.; Heidary, D. K.; Glazer, E. C. *J. Am. Chem. Soc.*, **2012**, 134 (20), 8324-8327.

3. Garner, R. N.; Gallucci, J. C.; Dunbar, K. R.; Turro, C. *Inorg. Chem.*, **2011**, *50* (19), 9213-9215.
4. Farrer, N. J.; Salassa, L.; Sadler, P. J. *Dalton Trans.*, **2009**, (48), 10690-10701.
5. Ruggiero, E.; Alonso-de Castro, S.; Habtemariam, A.; Salassa, L., *The Photochemistry of Transition Metal Complexes and Its Application in Biology and Medicine*. Springer Berlin Heidelberg: 2014; pp 1-39.
6. Heilman, B. J.; St. John, J.; Oliver, S. R. J.; Mascharak, P. K. *J. Am. Chem. Soc.*, **2012**, *134* (28), 11573-11582.
7. Zoltan, T.; Vargas, F.; López, V.; Chávez, V.; Rivas, C.; Ramírez, Á. H. *Spectrochim. Acta Mol. Biomol. Spectros.*, **2015**, *135*, 747-756.
8. Minnock, A.; Vernon, D. I.; Schofield, J.; Griffiths, J.; Howard Parish, J.; Brown, S. B. *J. Photochem. Photobiol. B*, **1996**, *32* (3), 159-164.
9. Torchilin, V. P. *Eur. J. Pharm. Sci.*, **2000**, *11*, Supplement 2, S81-S91.
10. Reedijk, J. *Proc. Natl. Acad. Sci.*, **2003**, *100* (7), 3611-3616.
11. Patrick, G. L., *An introduction to medicinal chemistry*. 5th Edition ed.; Oxford University Press: Oxford, UK, 2013.
12. Jamieson, E. R.; Lippard, S. J. *Chem. Rev.*, **1999**, *99* (9), 2467-2498.
13. Velders, A. H.; Kooijman, H.; Spek, A. L.; Haasnoot, J. G.; de Vos, D.; Reedijk, J. *Inorg. Chem.*, **2000**, *39* (14), 2966-2967.
14. Velders, A. H.; Quiroga, A. G.; Haasnoot, J. G.; Reedijk, J. *Eur. J. Inorg. Chem.*, **2003**, *2003* (4), 713-719.
15. Velders, A. H.; Hotze, A. C. G.; Albada, G. A. v.; Haasnoot, J. G.; Reedijk, J. *Inorg. Chem.*, **2000**, *39* (18), 4073-4080.
16. Clayden, J.; Moran, W. J.; Edwards, P. J.; LaPlante, S. R. *Angew. Chem. Int. Ed.*, **2009**, *48* (35), 6398-6401.

- 
17. Maple, H. J.; Garlish, R. A.; Whitcombe, I.; Hold, A.; Prosser, C. E.; Ford, D.; Mackenzie, H.; Crosby, J.; Porter, J.; Taylor, R. J.; Crump, M. P. *Anal. Chem.*, **2013**, 85 (12), 5958-5964.
18. LaPlante, S. R.; Forgione, P.; Boucher, C.; Coulombe, R.; Gillard, J.; Hucke, O.; Jakalian, A.; Joly, M.-A.; Kukolj, G.; Lemke, C.; McCollum, R.; Titolo, S.; Beaulieu, P. L.; Stammers, T. *J. Med. Chem.*, **2013**, 57 (5), 1944-1951.
19. Welch, W. M.; Ewing, F. E.; Huang, J.; Menniti, F. S.; Pagnozzi, M. J.; Kelly, K.; Seymour, P. A.; Guanowsky, V.; Guhan, S.; Guinn, M. R.; Critchett, D.; Lazzaro, J.; Ganong, A. H.; DeVries, K. M.; Staigers, T. L.; Chenard, B. L. *Bioorg. Med. Chem. Lett.*, **2001**, 11 (2), 177-181.
20. Sizova, O. V.; Ivanova, N. V.; Ershov, A. Y.; Shashko, A. D. *Russ. J. Gen. Chem.*, **2003**, 73 (12), 1846-1856.
21. Zayat, L.; Salierno, M.; Etchenique, R. *Inorg. Chem.*, **2006**, 45 (4), 1728-1731.
22. Sandstrom, J., *Dynamic NMR Spectroscopy*. First Edition ed.; Academic Press: London, 1982.
23. Gielen, M.; Willem, R.; Wrackmeyer, B., *Fluxional organometallic and coordination compounds*. John Wiley & Sons: West Sussex, UK, 2004.
24. Pons, M.; Millet, O. *Prog. Nucl. Magn. Reson. Spectrosc.*, **2001**, 38 (4), 267-324.
25. Frisch, M. J.; Trucks, G. W.; Schlegel, H. B.; Scuseria, G. E.; Robb, M. A.; Cheeseman, J. R.; Montgomery, J. A.; Vreven Jr., T.; Kudin, K. N.; Burant, J. C.; Millam, J. M.; Iyengar, S. S.; Tomasi, J.; Barone, V.; Mennucci, B.; Cossi, M.; Scalmani, G.; Rega, N.; Petersson, G. A.; Nakatsuji, H.; Hada, M.; Ehara, M.; Toyota, K.; Fukuda, R.; Hasegawa, J.; Ishida, M.; Nakajima, T.; Honda, Y.; Kitao, O.; Nakai, H.; Klene, M.; Li, X.; Knox, J. E.; Hratchian, H. P.; Cross, J. B.; Adamo, C.; Jaramillo,

J.; Gomperts, R.; Stratmann, R. E.; Yazyev, O.; Austin, A. J.; Cammi, R.; Pomelli, C.; Ochterski, J. W.; Ayala, P. Y.; Morokuma, K.; Voth, G. A.; Salvador, P.; Dannenberg, J. J.; Zakrzewski, V. G.; Dapprich, S.; Daniels, A. D.; Strain, M. C.; Farkas, O.; Malick, D. K.; Rabuck, A. D.; Raghavachari, K.; Foresman, J. B.; Ortiz, J. V.; Cui, Q.; Baboul, A. G.; Clifford, S.; Cioslowski, J.; Stefanov, B. B.; Liu, G.; Liashenko, A.; Piskorz, P.; Komaromi, I.; Martin, R. L.; Fox, D. J.; Keith, T.; Al-Laham, M. A.; Peng, C. Y.; Nanayakkara, A.; Challacombe, M.; Gill, P. M. W.; Johnson, B.; Chen, W.; Wong, M. W.; Gonzalez, C.; Pople, J. A. *Gaussian 03*, Gaussian Inc.: Pittsburgh PA, 2003.

26. Becke, A. D. *J. Chem. Phys.*, **1993**, 98 (7), 5648-5652.
27. Lee, C.; Yang, W.; Parr, R. *Phys. Rev. B*, **1988**, 37 (2), 785-789.
28. Hay, P. J.; Wadt, W. R. *J. Chem. Phys.*, **1985**, 82 (1), 270-283.
29. Binkley, J. S.; Pople, J. A.; Hehre, W. J. *J. Am. Chem. Soc.*, **1980**, 102 (3), 939-947.
30. Adamo, C.; Barone, V. *J. Chem. Phys.*, **1999**, 110 (13), 6158-6170.
31. McLean, A. D.; Chandler, G. S. *J. Chem. Phys.*, **1980**, 72 (10), 5639-5648.
32. Peris, E.; Lee, J. C.; Crabtree, R. H. *J. Chem. Soc., Chem. Commun.*, **1994**, (22), 2573-2573.
33. Bogdanović, G. A.; Biré, A. S.-d.; Zarić, S. D. *Eur. J. Inorg. Chem.*, **2002**, 2002 (7), 1599-1602.
34. Janiak, C. *J. Chem. Soc., Dalton Trans.*, **2000**, (21), 3885-3896.
35. Grepioni, F.; Cojazzi, G.; Draper, S. M.; Scully, N.; Braga, D. *Organometallics*, **1998**, 17 (3), 296-307.

- 
36. Sava, G.; Bergamo, A.; Zorzet, S.; Gava, B.; Casarsa, C.; Cocchietto, M.; Furlani, A.; Scarcia, V.; Serli, B.; Iengo, E.; Alessio, E.; Mestroni, G. *Eur. J. Cancer*, **2002**, *38* (3), 427-435.
37. Betanzos-Lara, S.; Novakova, O.; Deeth, R.; Pizarro, A.; Clarkson, G.; Liskova, B.; Brabec, V.; Sadler, P.; Habtemariam, A. *J. Biol. Inorg. Chem.*, **2012**, *17* (7), 1033-1051.
38. Scolaro, C.; Hartinger, C. G.; Allardyce, C. S.; Keppler, B. K.; Dyson, P. J. *J. Inorg. Biochem.*, **2008**, *102* (9), 1743-1748.
39. Bacac, M.; Hotze, A. C. G.; Schilden, K. v. d.; Haasnoot, J. G.; Pacor, S.; Alessio, E.; Sava, G.; Reedijk, J. *J. Inorg. Biochem.*, **2004**, *98* (2), 402-412.
40. Hall, M. D.; Telma, K. A.; Chang, K.-E.; Lee, T. D.; Madigan, J. P.; Lloyd, J. R.; Goldlust, I. S.; Hoeschele, J. D.; Gottesman, M. M. *Cancer Res.*, **2014**, *74* (14), 3913-3922.
41. Velders, A. H.; Massera, C.; Ugozzoli, F.; Biagini-Cingi, M.; Manotti-Lanfredi, A. M.; Haasnoot, J. G.; Reedijk, J. *Eur. J. Inorg. Chem.*, **2002**, *2002* (1), 193-198.
42. Zhao, Y.; Truhlar, D. G. *J. Chem. Theory Comput.*, **2005**, *1* (3), 415-432.
43. Hay, B. P.; Bryantsev, V. S. *Chem. Commun.*, **2008**, (21), 2417-2428.

# **Chapter 4**

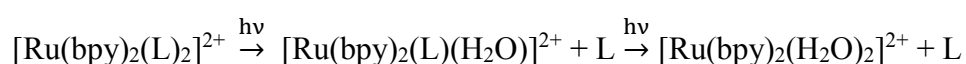
## **Photochemical and photophysical properties of Ru(II) polypyridyl complexes**

## Chapter 4

### Photochemical and photophysical properties of Ru(II) polypyridyl complexes

#### 4.1. Introduction

The photochemistry of complexes of the type  $[\text{Ru}(\text{bpy})_2(\text{L})_2]^{2+}$  and  $[\text{Ru}(\text{bpy})_3]^{2+}$ , where bpy is 2,2'-bipyridine and L is a pyridine / amine / nitrile based ligand, has been widely studied and generally involves the following mechanism: a) initial photoexcitation to form a singlet metal-to-ligand charge transfer state ( $^1\text{MLCT}$ ), b) efficient intersystem crossing (ISC) to the triplet metal-to-ligand charge transfer state ( $^3\text{MLCT}$ ), c) internal conversion (IC) to the triplet metal-centred state ( $^3\text{MC}$ ), if accessible, which is a highly dissociative state that causes bond breakage, or d) if the  $^3\text{MC}$  state is not accessible from the  $^3\text{MLCT}$  state, deactivation to the ground state will occur either with the emission of light (luminescence) or by non-radiative decay.<sup>1-3</sup> If photorelease of ligands occurs in aqueous solution it will do so via the following:



It is important to note that MLCT refers to a transfer of charge from the metal to the chelating ligand, bpy. The accessibility of the  $^3\text{MC}$  state is important, for example, in the design of photoreleasing Ru(II) polypyridyl prodrugs and the efficiency of Ru(II) polypyridyl dye-sensitised solar cells (DSSC).<sup>4-6</sup> In the former it is desirable to have a thermally accessible  $^3\text{MC}$  state in order to aid photorelease of bioactive ligands, whereas in the latter case the  $^3\text{MC}$  state should be thermally inaccessible in order to avoid ligand loss. The energy level of the  $^3\text{MLCT}$  and  $^3\text{MC}$  states can be altered by changing the ligands around the Ru(II) centre. For  $[\text{Ru}(\text{NH}_3)_5(\text{py-X})]^{2+}$ , where py-X

is a substituted pyridine, more electron-withdrawing groups lower the  $^3\text{MLCT}_{(\text{Ru-py-X})}$  state which renders the complex unreactive to photosubstitution, while less electron-withdrawing groups result in an easily accessible  $^3\text{MC}$  state and render the complex reactive to photosubstitution.<sup>7</sup> Similarly in the case of  $[\text{Ru}(N-N')_3]^{2+}$ , where  $N-N'$  is 2,2'-bipyridine or 2,2'-bipyridine-4,4'-dicarboxylic acid, the more electron withdrawing ligands decrease the energy of the  $^3\text{MLCT}$  state.<sup>8</sup>

This chapter focuses on exploring the photophysical/photochemical properties of *cis*- $[\text{Ru}(\text{bpy})_2(\text{INH})_2][\text{PF}_6]_2$  (**4**), *cis*- $[\text{Ru}(\text{bpy})_2(\text{NA})_2][\text{PF}_6]_2$  (**5**), *cis*- $[\text{Ru}(\text{phen})(\text{INH})_2][\text{PF}_6]_2$  (**6**) and *cis*- $[\text{Ru}(\text{phen})_2(\text{NA})_2][\text{PF}_6]_2$  (**7**), where bpy is 2,2'-bipyridine, phen is 1,10-phenanthroline, NA is nicotinamide and INH is isoniazid, by utilising experimental and theoretical techniques. Experimentally their photochemistry was investigated by UV-visible spectroscopy, fluorescence spectroscopy, liquid chromatography, mass spectrometry and transient-absorption spectroscopy. Density functional theory (DFT) and time-dependent density functional theory (TD-DFT) were used to rationalise theoretically how the ligands in a complex affect the photophysical/photochemical processes involved.

## 4.2. Experimental

### 4.2.1. Materials

The synthesis of complexes *cis*- $[\text{Ru}(\text{bpy})_2(\text{NA})\text{Cl}][\text{PF}_6]$  (**1**), *cis*- $[\text{Ru}(\text{bpy})_2(\text{INH})_2][\text{PF}_6]_2$  (**4**), *cis*- $[\text{Ru}(\text{bpy})_2(\text{NA})_2][\text{PF}_6]_2$  (**5**), *cis*- $[\text{Ru}(\text{phen})_2(\text{INH})_2][\text{PF}_6]_2$  (**6**) and *cis*- $[\text{Ru}(\text{phen})_2(\text{NA})_2][\text{PF}_6]_2$  (**7**) studied in this chapter is described in Chapter 3. The solvent used for UV-visible absorption spectroscopy was deionised water. The NMR spectroscopy solvent acetonitrile- $d_3$  was purchased from Cambridge Isotope Laboratories Inc. All solutions of complexes were



kept in the dark. A description of the photoirradiation setups can be found in Chapter 2.

#### 4.2.2. Photoirradiation followed by UV-visible absorption spectroscopy

The general procedure used in this section is detailed below. Any differences are noted in the appropriate section. Ru(II) polypyridyl complexes **1**, **4**, **5**, **6** and **7** were dissolved in deionised water to give a complex concentration of 40  $\mu\text{M}$ . The solution (600  $\mu\text{L}$ ) was placed into a 1 cm path length quartz cuvette and photoirradiated using a blue LED ( $\lambda_{\text{irr}} = 463 \text{ nm}$ , 50  $\text{mW cm}^{-2}$ ) at 298 K for various times. The UV-visible spectrum of each sample was recorded on a Cary 300-Scan spectrophotometer. The absorbance over the range 200 – 800 nm was recorded at 298 K. The data were processed using OriginPro 9.1 and, where applicable, plots of change in absorbance versus time were fitted to the exponential equation  $A = A_0 + Ce^{Rt}$  (where A is absorbance, t is time and C,  $A_0$  and R are calculated parameters) to give the half-life of formation ( $t_{1/2}$ ). The student's *t*-test was performed to determine if the  $t_{1/2}$  values were statistically different ( $p \text{ value} \leq 0.01$ ). The structures of the photoproducts were confirmed by ESI-MS.

##### 4.2.2.1. Wavelength dependence

Aqueous solutions of *cis*-[Ru(bpy)<sub>2</sub>(INH)<sub>2</sub>][PF<sub>6</sub>]<sub>2</sub> (**4**) and *cis*-[Ru(phen)<sub>2</sub>(INH)<sub>2</sub>][PF<sub>6</sub>]<sub>2</sub> (**7**) were photoirradiated using the KiloArc<sup>TM</sup> light source at different wavelengths ( $\lambda_{\text{irr}} = 440 \text{ nm}$ , 465 nm, 500 nm, 560 nm, 610 nm) at 298 K for various times. See Chapter 2 for the power of each wavelength. The half-life of formation ( $t_{1/2}$ ) at each wavelength of photoirradiation was determined.

##### 4.2.2.2. Stability of photoproducts

An aqueous solution of *cis*-[Ru(bpy)<sub>2</sub>(INH)<sub>2</sub>][PF<sub>6</sub>]<sub>2</sub> (**4**) was photoirradiated for various times (50 s, 1 h and 1 h 30 min) and kept in the dark for 1 hour to investigate

the stability of the photoproducts. The UV-visible spectrum of each sample was recorded on a Cary 300-Scan spectrophotometer over the range of 200 – 800 nm at 298 K.

#### 4.2.3. Photoirradiation followed by LC-HRMS

The complex *cis*-[Ru(bpy)<sub>2</sub>(INH)<sub>2</sub>][PF<sub>6</sub>]<sub>2</sub> (**4**) was dissolved in deionised water to give a complex concentration of 40 µM. The solution (600 µL) was placed into a 1 cm path-length quartz cuvette and irradiated using a blue LED ( $\lambda_{\text{irr}} = 463 \text{ nm}$ , 50 mW cm<sup>-2</sup>) at 298 K for various times. The sample was diluted with deionised water and injected into the LC-HRMS instrument. Details of the LC-HRMS setup can be found in Chapter 2.

#### 4.2.4. Power dependence followed by LC-MS

The complex *cis*-[Ru(bpy)<sub>2</sub>(INH)<sub>2</sub>][PF<sub>6</sub>]<sub>2</sub> (**4**) was dissolved in deionised water to give a complex concentration of 40 µM. Two aliquots of the sample were treated using two different methods of photoirradiation; a) 600 µL was added to a 1 cm path length quartz cuvette and photoirradiated using a blue LED ( $\lambda_{\text{irr}} = 463 \text{ nm}$ , 50 mW cm<sup>-2</sup>) at 298 K for 3 hours, and b) 200 µL was added to a black 96-well plate and photoirradiated using the 96-array blue LED ( $\lambda_{\text{irr}} = 465 \text{ nm}$ , 20 mW cm<sup>-2</sup>) at 298 K for 3 hours. Each sample was diluted with deionised water and injected into the LC-MS instrument. Details of the LC-MS setup can be found in Chapter 2.

#### 4.2.5. Photoirradiation using 96-array blue LED followed by HPLC

The complex *cis*-[Ru(bpy)<sub>2</sub>(INH)<sub>2</sub>][PF<sub>6</sub>]<sub>2</sub> (**4**) was dissolved in deionised water to give a complex concentration of 40 µM. An aliquot (200 µL) was added to a black 96-well plate and photoirradiated using the 96-array blue LED ( $\lambda_{\text{irr}} = 465 \text{ nm}$ , 20 mW cm<sup>-2</sup>) at 298 K for various times. After each time point the solution was diluted with deionised

water and injected into the HPLC instrument. Details of the HPLC setup can be found in Chapter 2.

#### 4.2.6. Photoirradiation followed by $^1\text{H}$ -NMR spectroscopy

The chlorido complex *cis*-[Ru(bpy)<sub>2</sub>(NA)Cl][PF<sub>6</sub>] (**1**) was dissolved in acetonitrile-*d*<sub>3</sub> to give a complex concentration of ~ 6 mM and placed in a 5 mm o.d. NMR tube. The sample was photoirradiated using a blue LED ( $\lambda_{\text{irr}} = 463 \text{ nm}$ ,  $50 \text{ mW cm}^{-2}$ ) at 298 K for various times. The  $^1\text{H}$ -NMR spectrum of each sample was recorded on a Bruker AV-400 spectrometer at 298 K. All data processing was carried out using Bruker Topspin 2.1. The sample was diluted with acetonitrile and the structure of the photoirradiation products were confirmed by HR-MS, see Chapter 2 for details of the instrumentation.

#### 4.2.7. Emission properties

Complexes **4**, **5**, **6** and **7** were dissolved in deionised water to give a complex concentration of 40  $\mu\text{M}$ . The solution (3 mL) was placed into a 1 cm path length quartz cuvette and the emission was measured on a Jasco FP-6500 fluorometer at 298 K using an excitation wavelength of 450 nm; the excitation and the emission slit widths were 5 nm; response time was 1 second; sensitivity was high; scan rate was  $200 \text{ nm min}^{-1}$ .

#### 4.2.8. Computational analysis

The starting geometry of complexes **4**, **5** and **6** was adapted from their corresponding crystal structures discussed in Chapter 3, while complex **7** was adapted from the crystal structure of **5**. All calculations were performed using Gaussian 03.<sup>9</sup> Becke's three-parameter hybrid functional<sup>10</sup> with the Lee-Yang-Parr's gradient-corrected correlation functional<sup>11</sup> (B3LYP) was used with LanL2DZ basis set<sup>12</sup> and effective core potential for the ruthenium atom, and the split valence 6-31G\*\* basis set<sup>13-14</sup> for

all other atoms. Geometry optimisations of the ground state ( $S_0$ ) and the lowest-lying triplet state ( $T_1$ ) were performed in the gas phase and the nature of all stationary points was confirmed by normal mode analysis. For the lowest-lying triplet states, the unrestricted Kohn-Sham method (UKS) was utilised with unrestricted B3LYP functional (UB3LYP). The electronic structure and excited states in solution were calculated using the conductor-like polarisable continuum model method<sup>15-17</sup> (CPCM) with water as the solvent. Fifty singlet excited states (with corresponding oscillator strengths) and sixteen triplet excited states (starting from the lowest-lying triplet state geometry) were calculated by time-dependent density functional theory (TD-DFT).<sup>18-19</sup> The electronic distribution and localisation of the excited states were visualised using electron density difference maps (EDDMs).<sup>20</sup> GaussSum1.0<sup>21</sup> was used for the simulation of the electronic absorption spectrum and calculation of the EDMs.

#### 4.2.9. Transient-absorption spectroscopy

Transient-absorption spectroscopy experiments were performed by Dr Simon E. Greenough from Chemistry Department at University of Warwick, and have been published.<sup>22</sup> See Chapter 2 for the set-up of the transient-absorption spectroscopy system. The complex *cis*-[Ru(bpy)<sub>2</sub>(NA)<sub>2</sub>][PF<sub>6</sub>]<sub>2</sub> (**4**) in aqueous solution (890  $\mu$ M) was flowed through a 1 mm path length quartz cuvette and photoirradiated at 340 nm using a 650  $\mu$ W pump laser pulse.

### 4.3. Results

#### 4.3.1. Photoirradiation followed by UV-visible spectroscopy

When aqueous solutions (40  $\mu$ M) of *cis*-[Ru(bpy)<sub>2</sub>(NA)Cl][PF<sub>6</sub>] (**1**), *cis*-[Ru(bpy)<sub>2</sub>(INH)<sub>2</sub>][PF<sub>6</sub>]<sub>2</sub> (**4**), *cis*-[Ru(bpy)<sub>2</sub>(NA)<sub>2</sub>][PF<sub>6</sub>]<sub>2</sub> (**5**), *cis*-[Ru(phen)<sub>2</sub>(INH)<sub>2</sub>][PF<sub>6</sub>]<sub>2</sub> (**6**) and *cis*-[Ru(phen)<sub>2</sub>(NA)<sub>2</sub>][PF<sub>6</sub>]<sub>2</sub> (**7**) were exposed to blue

light ( $\lambda_{\text{irr}} = 463 \text{ nm}$ ,  $50 \text{ mW cm}^{-2}$ ) at 298 K for  $< 1 \text{ min}$ , there were changes in their UV-visible spectra, see Figure 4.1. For **1**, there was a blue shift in the absorption band whereby the peak at 474 nm decreased in intensity and the peak at 466 nm increased, producing isosbestic points at 471 nm, 406 nm and 337 nm. For **4**, **5**, **6** and **7** there was a red shift of the absorption band whereby the peak at  $\sim 420 \text{ nm}$  decreased and the peak at  $\sim 460 \text{ nm}$  increased, producing an isosbestic point at  $\sim 450 \text{ nm}$ . The presence of an isosbestic point suggests that a stoichiometric reaction is occurring. For all complexes, in  $< 1 \text{ min}$  the production of the photoproduct reaches a plateau, see Figure 4.1. The identity of the photoproducts was confirmed by ESI-MS, see Table 4.1.

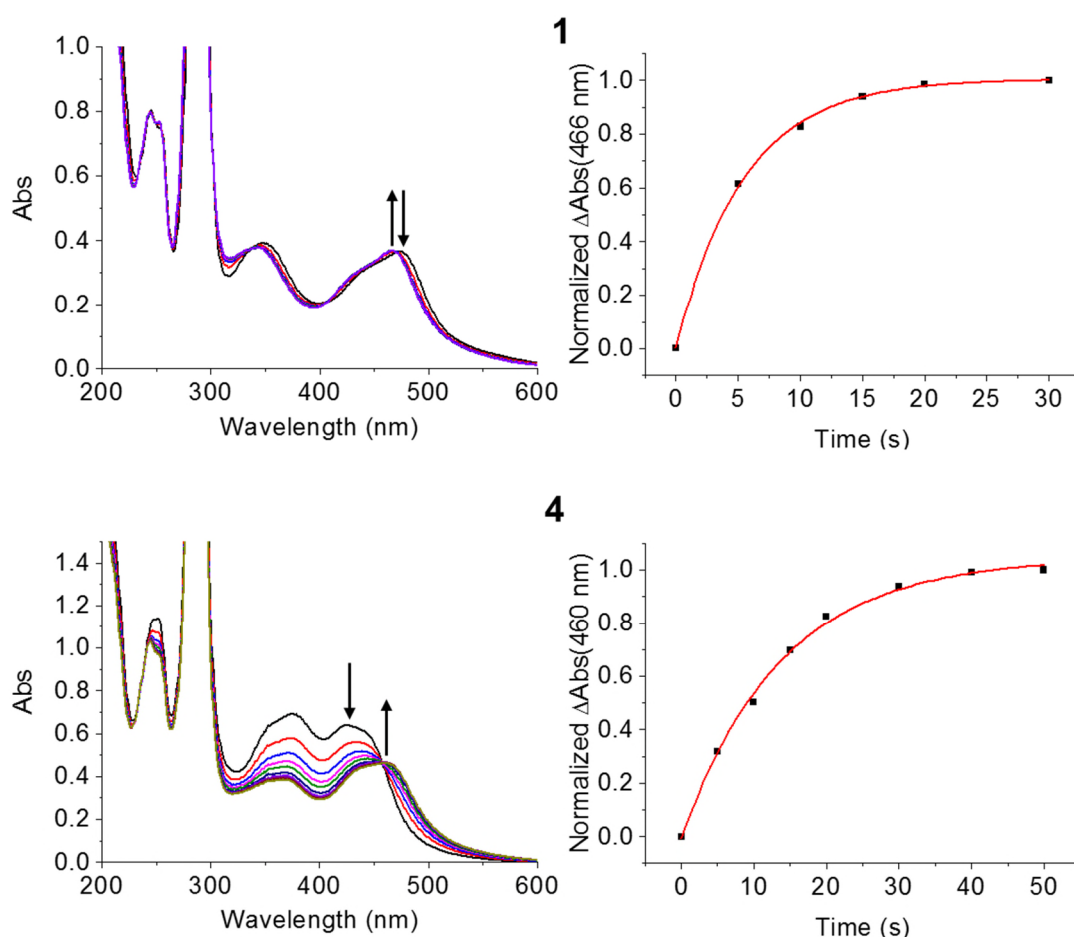


**Figure 4.1.** UV-visible spectra (left) of aqueous solutions ( $40 \mu\text{M}$ ) of *cis*-[Ru(bpy)<sub>2</sub>(NA)Cl][PF<sub>6</sub>] (**1**) and *cis*-[Ru(bpy)<sub>2</sub>(INH)<sub>2</sub>][PF<sub>6</sub>]<sub>2</sub> (**4**) photoirradiated using blue light ( $\lambda_{\text{irr}} = 463 \text{ nm}$ ,  $50 \text{ mW cm}^{-2}$ ) at 298 K with kinetic traces of increase of the photoproduct (right).

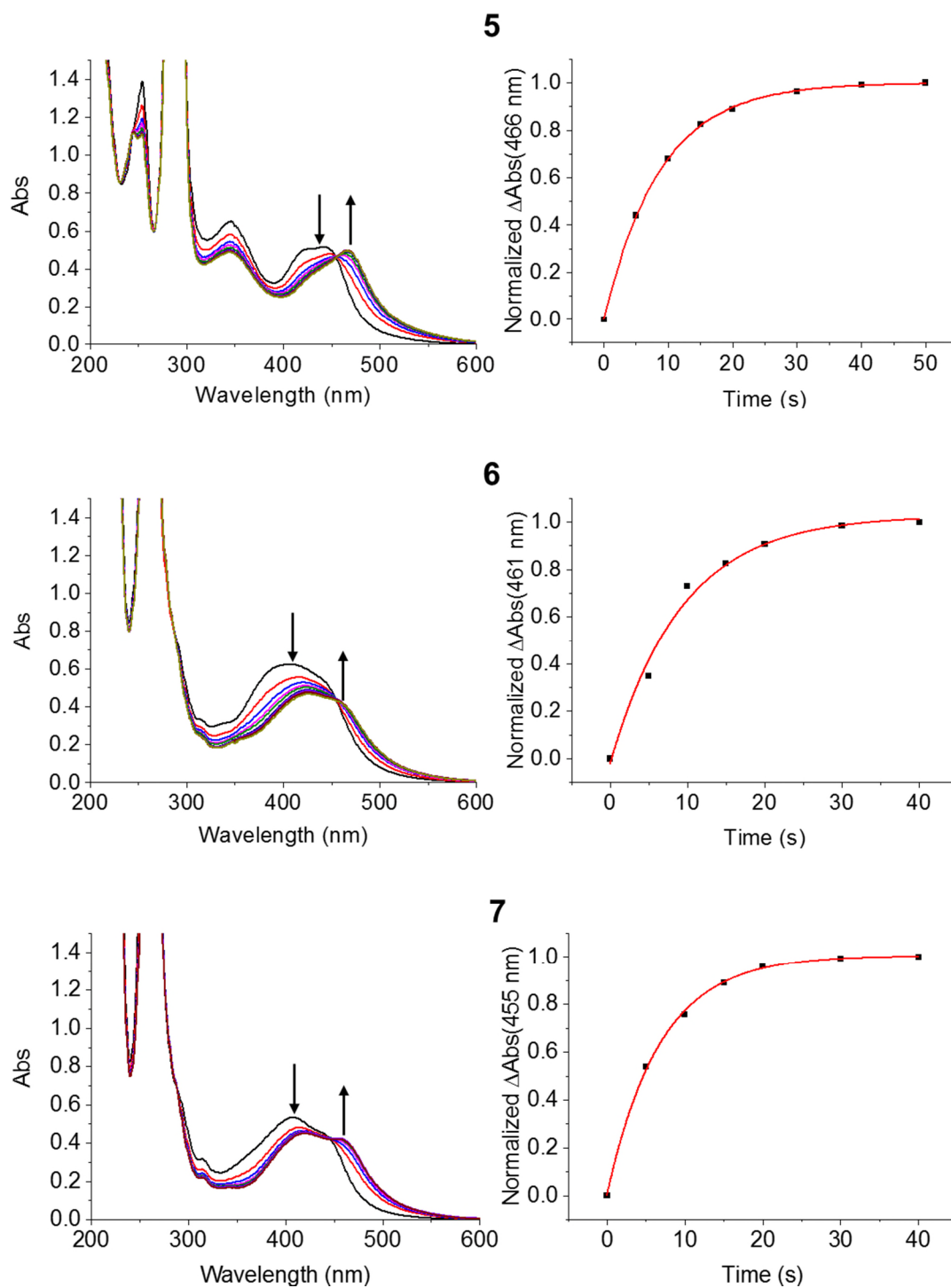


**Figure 4.1. (Continued).** UV-visible spectra (left) of aqueous solutions (40  $\mu$ M) of *cis*-[Ru(bpy)<sub>2</sub>(NA)<sub>2</sub>][PF<sub>6</sub>]<sub>2</sub> (**5**), *cis*-[Ru(phen)<sub>2</sub>(INH)<sub>2</sub>][PF<sub>6</sub>]<sub>2</sub> (**6**) and *cis*-[Ru(phen)<sub>2</sub>(NA)<sub>2</sub>][PF<sub>6</sub>]<sub>2</sub> (**7**) photoirradiated using blue light ( $\lambda_{\text{irr}} = 463$  nm, 50 mW cm<sup>-2</sup>) at 298 K with kinetic traces of increase of the photoproduct (right).

**Table 4.1.** Photoirradiation products detected by ESI-MS when aqueous solutions (40  $\mu\text{M}$ ) of *cis*-[Ru(bpy)<sub>2</sub>(NA)Cl][PF<sub>6</sub>] (**1**), *cis*-[Ru(bpy)<sub>2</sub>(INH)<sub>2</sub>][PF<sub>6</sub>]<sub>2</sub> (**4**), *cis*-[Ru(bpy)<sub>2</sub>(NA)<sub>2</sub>][PF<sub>6</sub>]<sub>2</sub> (**5**), *cis*-[Ru(phen)<sub>2</sub>(INH)<sub>2</sub>][PF<sub>6</sub>]<sub>2</sub> (**6**) and *cis*-[Ru(phen)<sub>2</sub>(NA)<sub>2</sub>][PF<sub>6</sub>]<sub>2</sub> (**7**) were photoirradiated using blue light ( $\lambda_{\text{irr}} = 463 \text{ nm}$ , 50  $\text{mW cm}^{-2}$ ) at 298 K.

Complex	ESI-MS product mass, $m/z$	Calculated formula and mass of product, $m/z$
<b>1</b>	553.2	$[[\text{Ru}(\text{bpy})_2(\text{NA})(\text{H}_2\text{O})]^{2+}-\text{H}]^+$ $\text{C}_{26}\text{H}_{23}\text{N}_6\text{O}_2\text{Ru}$ : 553.1
<b>4</b>	568.0	$[[\text{Ru}(\text{bpy})_2(\text{INH})(\text{H}_2\text{O})]^{2+}-\text{H}]^+$ $\text{C}_{26}\text{H}_{24}\text{N}_7\text{O}_2\text{Ru}$ : 568.1
<b>5</b>	553.0	$[[\text{Ru}(\text{bpy})_2(\text{NA})(\text{H}_2\text{O})]^{2+}-\text{H}]^+$ $\text{C}_{26}\text{H}_{23}\text{N}_6\text{O}_2\text{Ru}$ : 553.1
<b>6</b>	616.2	$[[\text{Ru}(\text{phen})_2(\text{INH})(\text{H}_2\text{O})]^{2+}-\text{H}]^+$ $\text{C}_{30}\text{H}_{24}\text{N}_7\text{O}_2\text{Ru}$ : 616.1
<b>7</b>	601.0	$[[\text{Ru}(\text{phen})_2(\text{NA})(\text{H}_2\text{O})]^{2+}-\text{H}]^+$ $\text{C}_{30}\text{H}_{23}\text{N}_6\text{O}_2\text{Ru}$ : 601.1

**Table 4.2.** Half-life of formation of photoproducts ( $t_{1/2}$ ) obtained when aqueous solutions (40  $\mu\text{M}$ ) of *cis*-[Ru(bpy)<sub>2</sub>(NA)Cl][PF<sub>6</sub>] (**1**), *cis*-[Ru(bpy)<sub>2</sub>(INH)<sub>2</sub>][PF<sub>6</sub>]<sub>2</sub> (**4**), *cis*-[Ru(bpy)<sub>2</sub>(NA)<sub>2</sub>][PF<sub>6</sub>]<sub>2</sub> (**5**), *cis*-[Ru(phen)<sub>2</sub>(INH)<sub>2</sub>][PF<sub>6</sub>]<sub>2</sub> (**6**) and *cis*-[Ru(phen)<sub>2</sub>(NA)<sub>2</sub>][PF<sub>6</sub>]<sub>2</sub> (**7**) were photoirradiated using blue light ( $\lambda_{\text{irr}} = 463 \text{ nm}$ , 50  $\text{mW cm}^{-2}$ ) at 298 K.

Complex	$t_{1/2}$ (s)
<b>1</b>	3.8
<b>4</b>	$8.4 \pm 0.7$
<b>5</b>	$6.4 \pm 0.4$
<b>6</b>	$5.7 \pm 0.6$
<b>7</b>	$4.4 \pm 0.3$

Interestingly in the case of **1** the photoproduct is *cis*-[Ru(bpy)<sub>2</sub>(NA)(H<sub>2</sub>O)]<sup>2+</sup>, confirming the release of the Cl ligand. For **4**, **5**, **6** and **7** the photoproducts were *cis*-[Ru(*N-N'*)<sub>2</sub>(L)(H<sub>2</sub>O)]<sup>2+</sup>, where *N-N'* is 2,2'-bipyridine (bpy) or 1,10-phenanthroline

(phen) and L is isoniazid (INH) or nicotinamide (NA), confirming the release of one ligand (L). The half-lives for formation ( $t_{1/2}$ ) of the photoproduct were compared in order to ascertain a structure-activity relationship, see Table 4.2. When following the increase of the *cis*-[Ru(*N-N'*)<sub>2</sub>(L)(H<sub>2</sub>O)]<sup>2+</sup> peak at ~ 460 nm for all complexes, a single exponential relationship was observed which was fitted in order to obtain the  $t_{1/2}$  value.

Complex **1** photolysed at the fastest rate. Complexes that contain 1,10-phenanthroline (phen) photolysed faster than complexes containing 2,2'-bipyridine (bpy) when they contain the same monodentate ligand, photolysis rate of *cis*-[Ru(phen)<sub>2</sub>(INH)<sub>2</sub>][PF<sub>6</sub>]<sub>2</sub> (**6**) > *cis*-[Ru(bpy)<sub>2</sub>(INH)<sub>2</sub>][PF<sub>6</sub>]<sub>2</sub> (**4**) and *cis*-[Ru(phen)<sub>2</sub>(NA)<sub>2</sub>][PF<sub>6</sub>]<sub>2</sub> (**7**) > *cis*-[Ru(bpy)<sub>2</sub>(NA)<sub>2</sub>][PF<sub>6</sub>]<sub>2</sub> (**5**). Complexes that contain nicotinamide (NA) photolysed faster than complexes that contain isoniazid (INH) when they contain the same chelating ligand, photolysis rate of *cis*-[Ru(bpy)<sub>2</sub>(NA)<sub>2</sub>][PF<sub>6</sub>]<sub>2</sub> (**5**) > *cis*-[Ru(bpy)<sub>2</sub>(INH)<sub>2</sub>][PF<sub>6</sub>]<sub>2</sub> (**4**) and *cis*-[Ru(phen)<sub>2</sub>(NA)<sub>2</sub>][PF<sub>6</sub>]<sub>2</sub> (**7**) > *cis*-[Ru(phen)<sub>2</sub>(INH)<sub>2</sub>][PF<sub>6</sub>]<sub>2</sub> (**6**). Thus the general order of rate of photolysis is **1** > **7** > **6** ~ **5** > **4**.

#### 4.3.1.1. Wavelength dependence

Both complexes *cis*-[Ru(bpy)<sub>2</sub>(INH)<sub>2</sub>][PF<sub>6</sub>]<sub>2</sub> (**4**) and *cis*-[Ru(phen)<sub>2</sub>(INH)<sub>2</sub>][PF<sub>6</sub>]<sub>2</sub> (**7**) exhibited wavelength-dependent behaviour, see Figure 4.2. When both complexes in aqueous solution (40 µM) were exposed to green light ( $\lambda_{\text{irr}} = 500$  nm) at 298 K, the  $t_{1/2}$  value was < 50 s. However upon exposure to near yellow light ( $\lambda_{\text{irr}} = 560$  nm) the  $t_{1/2}$  value increased significantly to 435 s and 476 s for **4** and **7**, respectively. When photoirradiated with red light ( $\lambda_{\text{irr}} = 610$  nm) there is no photoactivity. As a result for both complexes there was an inverse relationship between  $t_{1/2}$  and extinction coefficient in the range of 440 nm - 560 nm; as the wavelength of photoirradiation increased, the extinction coefficient decreased and the photoactivity decreased.



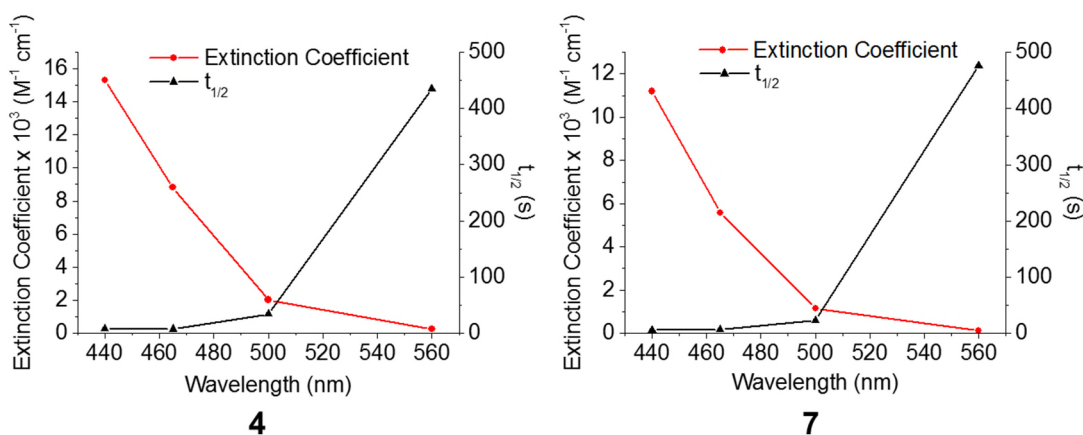


**Figure 4.2.** Relationship between half-life of photoproduct formation ( $t_{1/2}$ ) and extinction coefficient for *cis*-[Ru(bpy)<sub>2</sub>(INH)<sub>2</sub>][PF<sub>6</sub>]<sub>2</sub> (**4**) and *cis*-[Ru(phen)<sub>2</sub>(INH)<sub>2</sub>][PF<sub>6</sub>]<sub>2</sub> (**7**) when photoirradiated using various wavelengths of photoactivation.

#### 4.3.1.2. Stability of photoproducts

The stability of *cis*-[Ru(bpy)<sub>2</sub>(INH)<sub>2</sub>][PF<sub>6</sub>]<sub>2</sub> (**4**) in aqueous solution (40  $\mu\text{M}$ ) at 298 K was investigated by irradiating the sample with blue light ( $\lambda_{\text{irr}} = 463 \text{ nm}$ ,  $50 \text{ mW cm}^{-2}$ ) for various times, and storing the resulting solution in the dark for 1 h. Changes in the UV-visible spectrum were monitored, see Figure 4.3. At all photoirradiation times (50 s, 30 min and 1 h 30 min) the photoproducts appeared to be stable in solution, as there were no changes in the UV- visible spectrum after 1 h of incubation in the dark at 298 K.

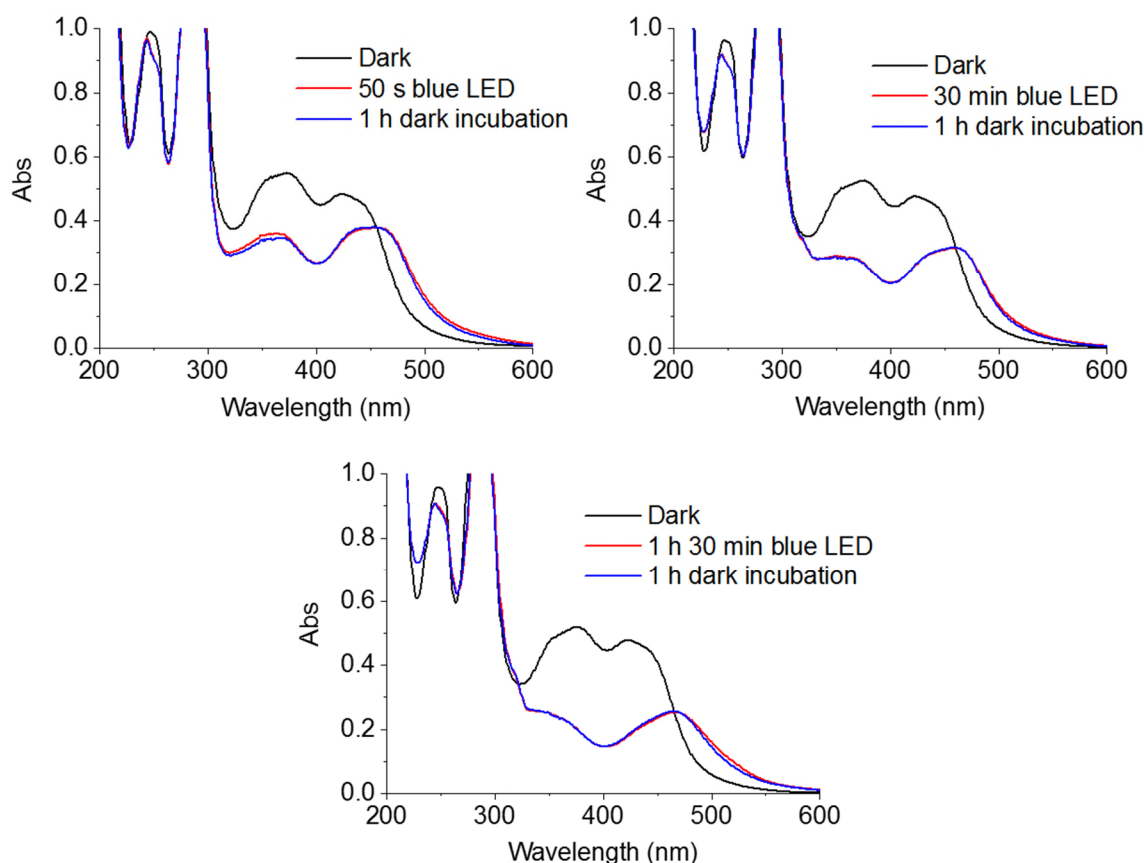


**Figure 4.3.** Change in UV-visible spectrum of *cis*-[Ru(bpy)<sub>2</sub>(INH)<sub>2</sub>][PF<sub>6</sub>]<sub>2</sub> (**4**) when photoirradiated with blue light ( $\lambda_{\text{irr}} = 463 \text{ nm}$ ,  $50 \text{ mW cm}^{-2}$ ) for various times at 298 K and subsequently incubated in the dark for 1 h.

#### 4.3.2. Photoirradiation followed by LC-HRMS

In order to fully characterise the photoirradiation products at photoirradiation times > 1 min, liquid chromatography coupled to a high resolution mass spectrometer (LC-HRMS) was employed. An aqueous solution (40  $\mu\text{M}$ ) of *cis*-[Ru(bpy)<sub>2</sub>(INH)<sub>2</sub>][PF<sub>6</sub>]<sub>2</sub> (**4**) was photoirradiated with blue light ( $\lambda_{\text{irr}} = 463 \text{ nm}$ ,  $50 \text{ mW cm}^{-2}$ ) at 298 K for 50 s and 2 h 20 min. The chromatogram at each time point of photoirradiation and corresponding high resolution mass of each product for each peak can be found in Figure 4.4 and Table 4.3, respectively.

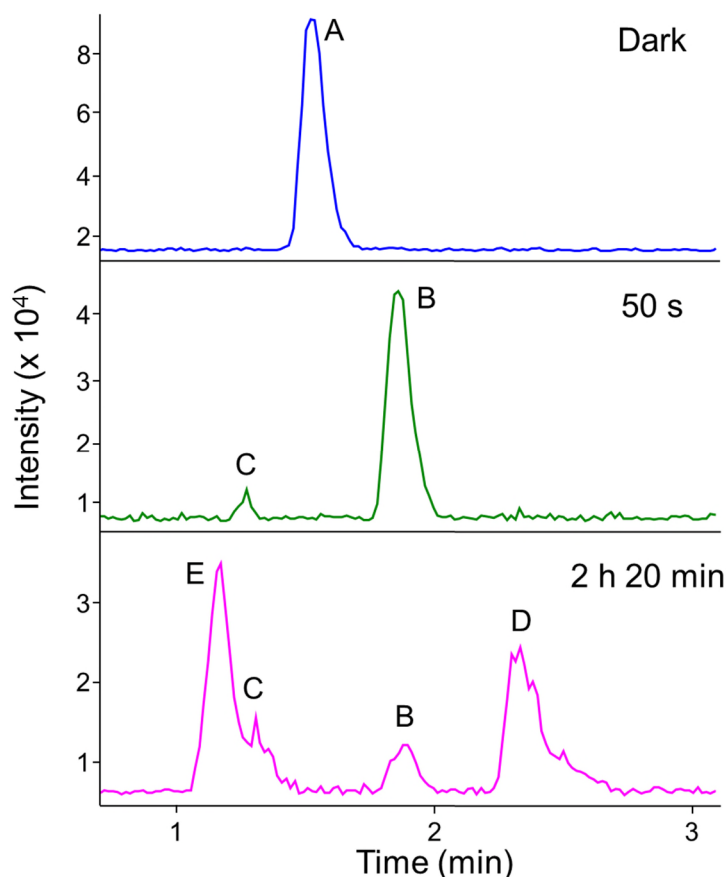


**Figure 4.4.** HR-LCMS chromatograms of *cis*-[Ru(bpy)<sub>2</sub>(INH)<sub>2</sub>][PF<sub>6</sub>]<sub>2</sub> (**4**) when photoirradiated with blue light ( $\lambda_{\text{irr}} = 463 \text{ nm}$ ,  $50 \text{ mW cm}^{-2}$ ) at 298 K for various times. Peak A (*cis*-[Ru(bpy)<sub>2</sub>(INH)<sub>2</sub>]<sup>2+</sup>), B (*cis*-[Ru(bpy)<sub>2</sub>(INH)(H<sub>2</sub>O)]<sup>2+</sup>), C (INH), D ([Ru(bpy)<sub>2</sub>(H<sub>2</sub>O)<sub>2</sub>]<sup>2+</sup>) and E ([Ru(bpy)<sub>2</sub>(H<sub>2</sub>O)(OH)]<sup>2+</sup>) are assigned, see text.

With no photoirradiation, there was only one peak in the chromatogram (peak A) with a retention time of 1.4 min, which corresponds to the starting material *cis*-[Ru(bpy)<sub>2</sub>(INH)<sub>2</sub>]<sup>2+</sup> (**4**). After 50 s of photoirradiation, peak A was no longer present and there were two new peaks at 1.9 min (peak B) and 1.3 min (peak C), which correspond to *cis*-[Ru(bpy)<sub>2</sub>(INH)(H<sub>2</sub>O)]<sup>2+</sup> and INH respectively. After 2 h 20 min of photoirradiation there were two new peaks at 2.3 min (peak D) and 1.2 min (peak E), which correspond to [Ru(bpy)<sub>2</sub>(H<sub>2</sub>O)<sub>2</sub>]<sup>2+</sup> and [Ru(bpy)<sub>2</sub>(H<sub>2</sub>O)(OH)]<sup>2+</sup>, respectively. At this time point of photoirradiation, peak B and peak C were still present, however

peak B decreased in intensity and peak C increased in intensity. For peaks A, B and D the mass-to-charge ratio and isotopic models obtained were consistent with the formation of ruthenium(II) species. However for peak E, the mass-to-charge ratio and isotopic models were consistent with the formation of a ruthenium(III) species, see Figure 4.5.

**Table 4.3.** Photoirradiation products detected by HR-MS for each peak in the LC-HRMS chromatograms in Figure 4.4.

Peak	Retention time (min)	HR-MS product mass (m/z)	Calculated formula and mass of product (m/z)	Error (ppm)
A	1.4	344.0794	$cis\text{-}[\text{Ru}^{\text{II}}(\text{bpy})_2(\text{INH})_2]^{2+}$ $\text{C}_{32}\text{H}_{30}\text{N}_{10}\text{O}_2\text{Ru}$ : 344.0797	0.87
B	1.9	284.5553	$cis\text{-}[\text{Ru}^{\text{II}}(\text{bpy})_2(\text{INH})(\text{H}_2\text{O})]^{2+}$ $\text{C}_{26}\text{H}_{25}\text{N}_7\text{O}_2\text{Ru}$ : 284.5555	0.70
C	1.3	138.0663	$[\text{INH}+\text{H}]^+$ $\text{C}_6\text{H}_7\text{N}_3\text{O}$ : 138.0662	0.72
D	2.3	225.0306	$[\text{Ru}^{\text{II}}(\text{bpy})_2(\text{H}_2\text{O})_2]^{2+}$ $\text{C}_{20}\text{H}_{20}\text{N}_4\text{O}_2\text{Ru}$ : 225.0312	2.67
E	1.2	224.5273	$[[\text{Ru}^{\text{III}}(\text{bpy})_2(\text{H}_2\text{O})_2]^{3+}-\text{H}]^{2+}$ $\text{C}_{20}\text{H}_{19}\text{N}_4\text{O}_2\text{Ru}$ : 224.5273	0

At this point it is worth noting that the starting material,  $cis\text{-}[\text{Ru}(\text{bpy})_2(\text{INH})_2]^{2+}$  has a *cis* geometry, however from the experiments above the geometry of the photoirradiation products  $[\text{Ru}(\text{bpy})_2(\text{H}_2\text{O})_2]^{2+}$  and  $[\text{Ru}(\text{bpy})_2(\text{H}_2\text{O})(\text{OH})]^{2+}$  cannot be confirmed.

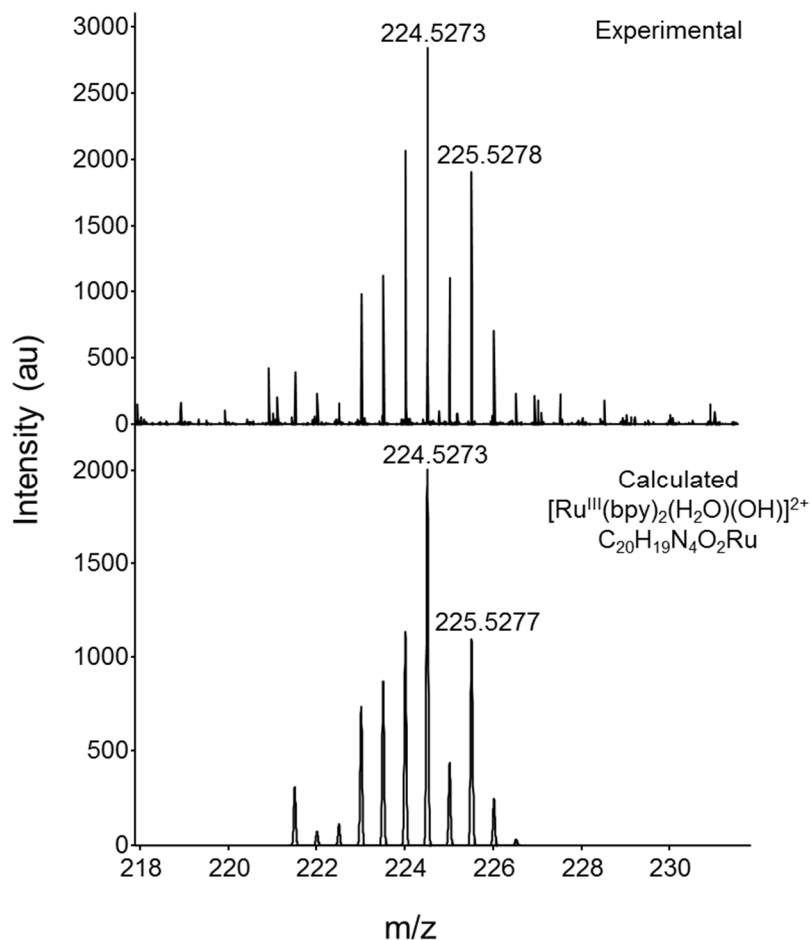


**Figure 4.5.** Experimental and calculated HR-MS peak for the photoproduct *cis*-[Ru(bpy)<sub>2</sub>(H<sub>2</sub>O)(OH)]<sup>2+</sup>.

#### 4.3.3. Power dependence followed by LC-MS

In order to investigate the effect of power on the photochemical pathways for *cis*-[Ru(bpy)<sub>2</sub>(INH)<sub>2</sub>][PF<sub>6</sub>]<sub>2</sub> (**4**), two blue light sources were employed ( $\lambda_{\text{irr}} = 463 \text{ nm}$ , 50 mW cm<sup>-2</sup> and  $\lambda_{\text{irr}} = 465 \text{ nm}$ , 20 mW cm<sup>-2</sup>). Two aliquots of an aqueous solution of **4** (40  $\mu\text{M}$ ) were photoirradiated with each light source for 3 h and the samples were analysed by LC-MS, see Figure 4.6. Interestingly for the sample that was photoirradiated with the 20 mW cm<sup>-2</sup> light source, there was one additional peak (peak F) at a retention time of 6.6 min that was not observed for the sample photoirradiated with the 50 mW cm<sup>-2</sup> light source.

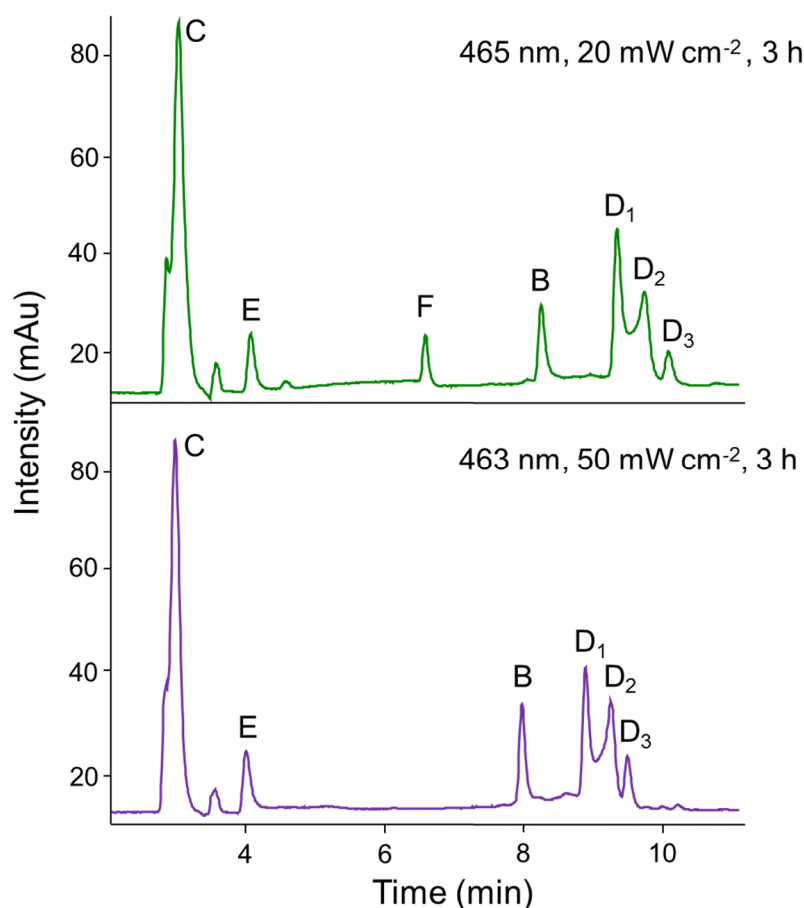


**Figure 4.6.** LC-MS chromatograms of *cis*-[Ru(bpy)<sub>2</sub>(INH)<sub>2</sub>][PF<sub>6</sub>]<sub>2</sub> (**4**) in aqueous solution (40 μM) after photoirradiation with blue light;  $\lambda_{\text{irr}} = 463 \text{ nm}$ , 50 mW cm<sup>-2</sup> (bottom) and  $\lambda_{\text{irr}} = 465 \text{ nm}$ , 20 mW cm<sup>-2</sup> (top) for 3 h at 298 K for various times. Peak B (*cis*-[Ru(bpy)<sub>2</sub>(INH)(H<sub>2</sub>O)]<sup>2+</sup>), C (INH), D<sub>1</sub>, D<sub>2</sub> and D<sub>3</sub> (collectively assigned to originate from *cis*-[Ru(bpy)<sub>2</sub>(H<sub>2</sub>O)<sub>2</sub>]<sup>2+</sup>), E (*trans*-[Ru(bpy)<sub>2</sub>(H<sub>2</sub>O)(OH)]<sup>2+</sup>) and F (*trans*-[Ru(bpy)<sub>2</sub>(H<sub>2</sub>O)<sub>2</sub>]<sup>2+</sup>) are assigned, see text.

The product mass was obtained from mass spectra of each peak to confirm the identity of the photoproducts, see Table 4.4. The characterisation data for peak B, C and E agree with those obtained in Section 4.3.2. There are three peaks close together at a retention time of ~9 min (D<sub>1</sub>, D<sub>2</sub> and D<sub>3</sub>), however the mass spectrum of each only differs by the intensity of the product *m/z* peaks. It is thought that collectively peak D<sub>1</sub>, D<sub>2</sub> and D<sub>3</sub> originates from *cis*-[Ru(bpy)<sub>2</sub>(H<sub>2</sub>O)<sub>2</sub>]<sup>2+</sup> and three chromatographic peaks are present due to the formation of adducts with the HPLC mobile phase (H<sub>2</sub>O/acetonitrile/trifluoroacetic acid).

**Table 4.4.** Photoirradiation products detected by MS for each peak in the LC-MS chromatograms in Figure 4.6.

Peak label	Retention time (min)	ESI-MS product mass (m/z)	Calculated formula and mass of product (m/z)
B	8.2	568.0	<i>cis</i> -[[Ru <sup>II</sup> (bpy) <sub>2</sub> (INH)(H <sub>2</sub> O)] <sup>2+</sup> -H] <sup>+</sup> C <sub>26</sub> H <sub>24</sub> N <sub>7</sub> O <sub>2</sub> Ru: 568.1
C	3.1	137.9	[INH+H] <sup>+</sup> C <sub>6</sub> H <sub>7</sub> N <sub>3</sub> O: 138.1
D <sub>1</sub> , D <sub>2</sub> , D <sub>3</sub>	9-10	448.9	<i>cis</i> -[[Ru <sup>II</sup> (bpy) <sub>2</sub> (H <sub>2</sub> O) <sub>2</sub> ] <sup>2+</sup> -H] <sup>+</sup> C <sub>20</sub> H <sub>19</sub> N <sub>4</sub> O <sub>2</sub> Ru: 449.1
		526.9	<i>cis</i> -[[Ru <sup>II</sup> (bpy) <sub>2</sub> (TFA)] <sup>2+</sup> -H] <sup>+</sup> C <sub>22</sub> H <sub>16</sub> F <sub>3</sub> N <sub>4</sub> O <sub>2</sub> Ru: 527.0
		471.9	<i>cis</i> -[[Ru <sup>II</sup> (bpy) <sub>2</sub> (ACN)(H <sub>2</sub> O)] <sup>2+</sup> -H] <sup>+</sup> C <sub>22</sub> H <sub>20</sub> N <sub>5</sub> ORu: 472.1
E	4.1	447.9	<i>trans</i> -[[Ru <sup>III</sup> (bpy) <sub>2</sub> (H <sub>2</sub> O)(OH)] <sup>2+</sup> -H] <sup>+</sup> C <sub>20</sub> H <sub>18</sub> N <sub>4</sub> O <sub>2</sub> Ru: 448.1
F	6.6	447.9	<i>trans</i> -[[Ru <sup>III</sup> (bpy) <sub>2</sub> (H <sub>2</sub> O)(OH)] <sup>2+</sup> -H] <sup>+</sup> C <sub>20</sub> H <sub>18</sub> N <sub>4</sub> O <sub>2</sub> Ru: 448.1

The UV-spectra of peaks D, E and F were very distinctive; peak D had an absorption band at 474 nm, peak F had an absorption band at 505 nm and peak E had no absorption band in the region of 400-600 nm, see Figure 4.7. These features are characteristic of *cis*-[Ru(bpy)<sub>2</sub>(H<sub>2</sub>O)<sub>2</sub>]<sup>2+</sup>, *trans*-[Ru(bpy)<sub>2</sub>(H<sub>2</sub>O)<sub>2</sub>]<sup>2+</sup> and *trans*-[Ru(bpy)<sub>2</sub>(H<sub>2</sub>O)(OH)]<sup>2+</sup> respectively, and these spectral properties are comparable to those in the literature.<sup>23-24</sup> Thus it is apparent that with a lower power of blue light *trans*-[Ru(bpy)<sub>2</sub>(H<sub>2</sub>O)<sub>2</sub>]<sup>2+</sup> (peak F) was present as a photoproduct, however when using a higher power of light, it was absent. It is worth noting that peak F is assigned to *trans*-[Ru(bpy)<sub>2</sub>(H<sub>2</sub>O)<sub>2</sub>]<sup>2+</sup>, however in the mass spectrum it was found as *trans*-[Ru(bpy)<sub>2</sub>(H<sub>2</sub>O)(OH)]<sup>2+</sup>. This could be due to the higher susceptibility of *trans*-

$[\text{Ru}(\text{bpy})_2(\text{H}_2\text{O})_2]^{2+}$  to air oxidation (which will be discussed later in this chapter) and oxidation may occur during the ESI-MS process.<sup>25-26</sup>

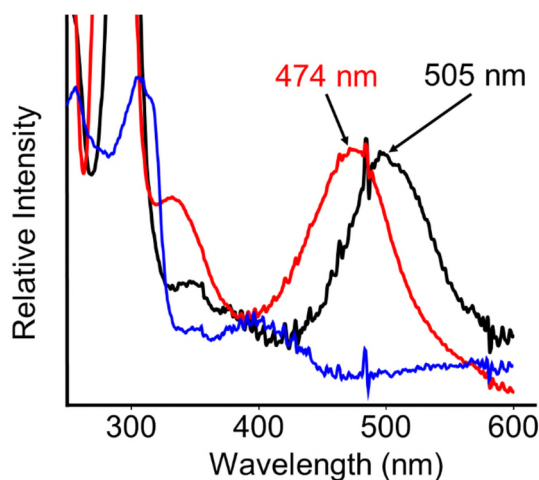


**Figure 4.7.** UV-visible spectra of peaks D (red), E (blue) and F (black) from LC-MS chromatograms in Figure 4.6.

The percentage of each peak was calculated by comparing peak area with sum of all peak areas (ignoring peak C as this is before the solvent front), see Table 4.5. When comparing  $20 \text{ mW cm}^{-2}$  to  $50 \text{ mW cm}^{-2}$ , peak B and E increased in intensity while peak D remained constant.

**Table 4.5.** Percentage (%) area of each peak in the LC-MS chromatograms in Figure 4.6.

Peak	Percentage area (%)	
	$20 \text{ mW cm}^{-2}$	$50 \text{ mW cm}^{-2}$
B	13	17
D <sub>1</sub> , D <sub>2</sub> and D <sub>3</sub>	71	71
E	10	12
F	6	0



#### 4.3.4. Photoirradiation using 96-array blue LED followed by HPLC

It was important to photoirradiate a solution (40  $\mu\text{M}$ ) of *cis*-[Ru(bpy)<sub>2</sub>(INH)<sub>2</sub>][PF<sub>6</sub>]<sub>2</sub> (**4**) using similar conditions as those used for biological cells. The 96-array blue LED ( $\lambda_{\text{irr}} = 465 \text{ nm}$ ,  $20 \text{ mW cm}^{-2}$ ) was used to photoirradiate a sample of **1** (200  $\mu\text{L}$ ) in a black 96 well-plate for various times. Each sample was analysed by HPLC, see Figure 4.8.

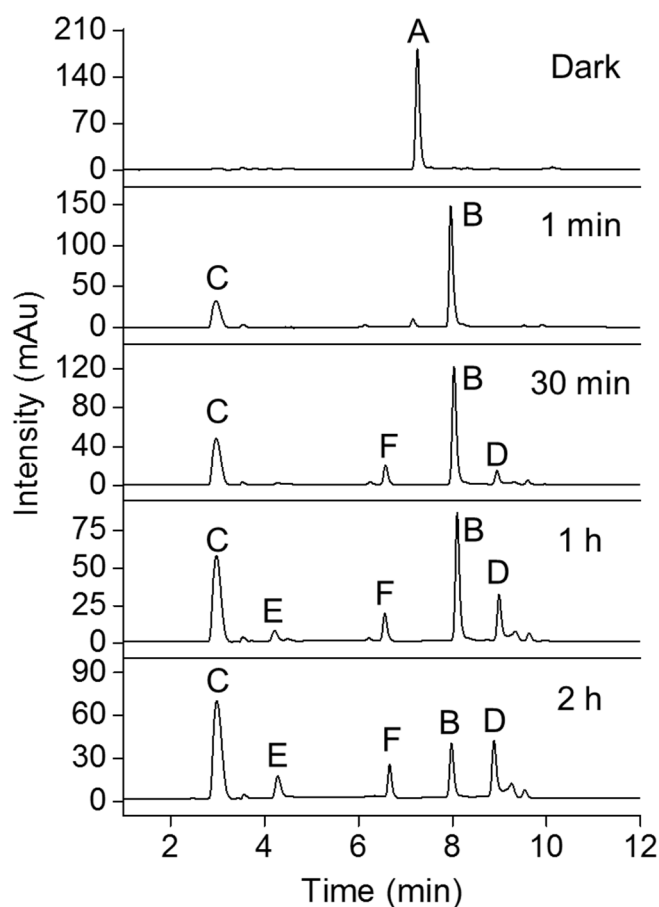


**Figure 4.8.** HPLC chromatograms of *cis*-[Ru(bpy)<sub>2</sub>(INH)<sub>2</sub>][PF<sub>6</sub>]<sub>2</sub> (**4**) in aqueous solution (40  $\mu\text{M}$ ) photoirradiated with 96-array blue LED ( $\lambda_{\text{irr}} = 465 \text{ nm}$ ,  $20 \text{ mW cm}^{-2}$ ) at 298 K for various times. Peak assignments are the same as those in Figure 4.6.

Interestingly even though the power of the light source has been reduced, after 1 min of photoirradiation the starting material (peak A)  $cis\text{-}[\text{Ru}(\text{bpy})_2(\text{INH})_2]^{2+}$  had almost disappeared with the almost exclusive production of  $cis\text{-}[\text{Ru}(\text{bpy})_2(\text{INH})(\text{H}_2\text{O})]^{2+}$  (peak B) and INH (peak C). With increased time of photoirradiation, peak B decreased, however 1-2 h photoirradiation was necessary to gain an appreciable yield of photoproduct  $[\text{Ru}(\text{bpy})_2(\text{H}_2\text{O})_2]^{2+}$  (peak D and F). Interestingly  $trans\text{-}[\text{Ru}(\text{bpy})_2(\text{H}_2\text{O})(\text{OH})]^{2+}$  (peak E) is produced after 1 h photoirradiation.

#### 4.3.5. Photoirradiation followed by $^1\text{H}$ -NMR

An acetonitrile- $d_3$  (ACN- $d_3$ ) solution (6 mM) of  $cis\text{-}[\text{Ru}(\text{bpy})_2(\text{NA})\text{Cl}][\text{PF}_6]$  (**1**) was photoirradiated with blue light ( $\lambda_{\text{irr}} = 463 \text{ nm}$ ,  $50 \text{ mW cm}^{-2}$ ) for 2 h 20 min at 298 K, with the  $^1\text{H}$ -NMR recorded before and after photoirradiation, see Figure 4.9. Prior to photoirradiation, the  $^1\text{H}$ -NMR spectrum exhibited 20 aromatic peaks attributed to the starting material  $cis\text{-}[\text{Ru}(\text{bpy})_2(\text{NA})\text{Cl}]^+$ . After photoirradiating the sample for 2 h 20 min, there were two new sets of peaks. The first set contains 16 aromatic peaks attributed to  $cis\text{-}[\text{Ru}(\text{bpy})_2(\text{ACN-}d_6)(\text{Cl})]^+$ . The second set contains 4 aromatic peaks attributed to free NA in solution. There was a third minor set which consisted of 4 peaks attributed to  $trans\text{-}[\text{Ru}(\text{bpy})_2(\text{ACN-}d_6)(\text{Cl})]^+$ . The identity of the photoirradiation product was confirmed by HR-MS (after diluting the sample with acetonitrile), see Table 4.6.

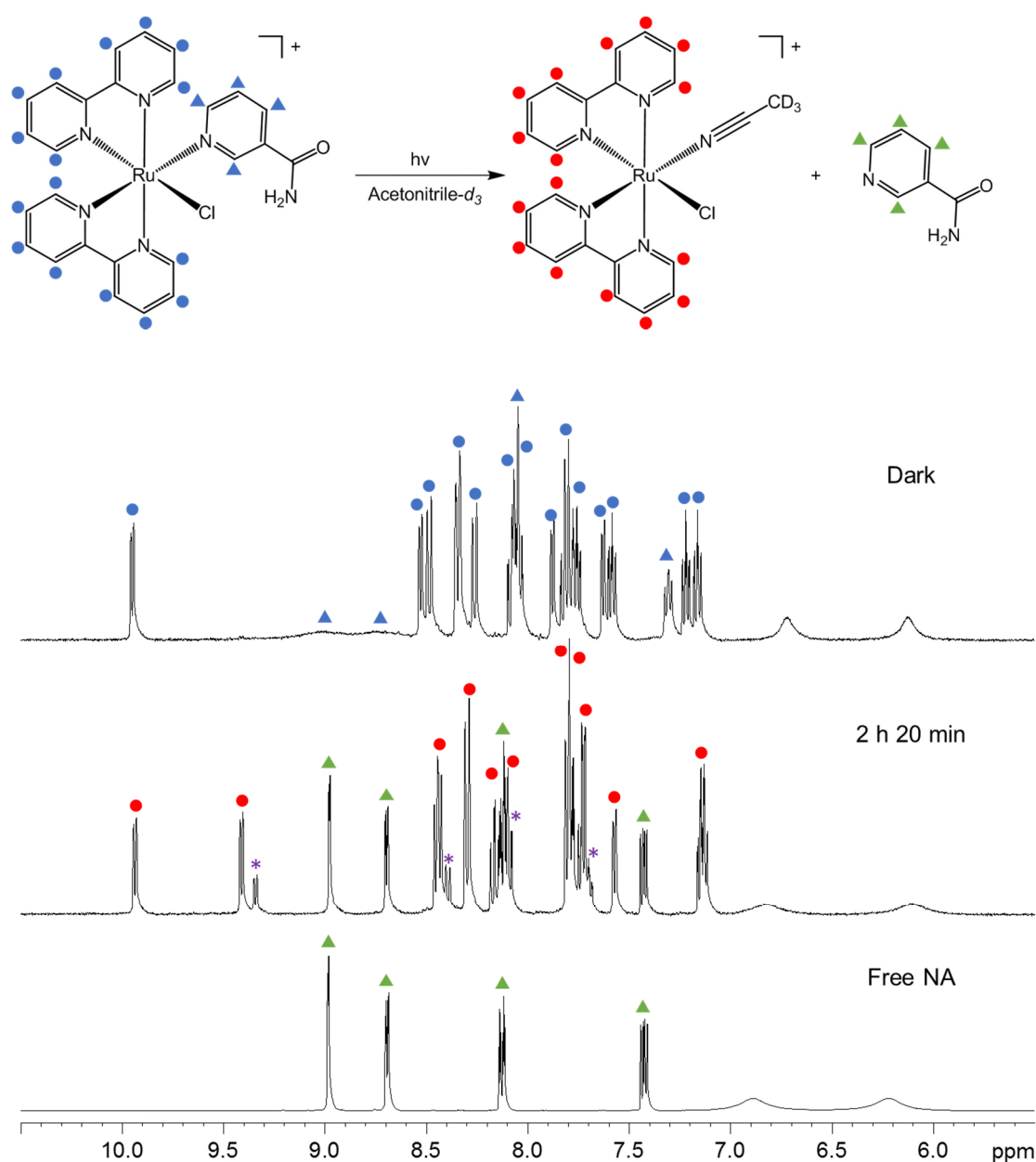


**Figure 4.9.**  $^1\text{H-NMR}$  spectrum of  $\text{cis-[Ru(bpy)}_2\text{(NA)Cl][PF}_6\text{]}^+$  (1) in acetonitrile- $d_3$  photoirradiated with blue light ( $\lambda_{\text{irr}} = 463 \text{ nm}$ ,  $50 \text{ mW cm}^{-2}$ ) at 298 K for various times. A schematic of the photoreaction is also shown (top).

A wide variety of fragment ions were seen by MS that confirm the NA ligand was released leaving the chloride ligand bound to the ruthenium(II) centre. The mass-to-charge ratio and isotopic models obtained were consistent with the formation of  $[\text{Ru(bpy)}_2(\text{ACN-}d_6)\text{Cl}]^+$ , see Figure 4.10.

**Table 4.6.** Photoirradiation products detected by HR-MS for *cis*-[Ru(bpy)<sub>2</sub>(NA)Cl][PF<sub>6</sub>] (**1**) in acetonitrile-*d*<sub>3</sub> photoirradiated with blue light ( $\lambda_{\text{irr}} = 463$  nm, 50 mW cm<sup>-2</sup>) at 298 K for 2 h 20 min.

HR-MS product mass ( <i>m/z</i> )	Calculated formula and mass of product ( <i>m/z</i> )	Error (ppm)
449.0108	[[Ru(bpy) <sub>2</sub> Cl] <sup>+</sup> C <sub>20</sub> H <sub>16</sub> ClN <sub>4</sub> Ru: 449.0103	1.11
467.0205	[[Ru(bpy) <sub>2</sub> (H <sub>2</sub> O)Cl] <sup>+</sup> C <sub>20</sub> H <sub>18</sub> ClN <sub>4</sub> ORu: 467.0209	0.86
490.0393	[[Ru(bpy) <sub>2</sub> (ACN)Cl] <sup>+</sup> C <sub>22</sub> H <sub>19</sub> ClN <sub>5</sub> Ru: 490.0369	4.90
493.0543	[[Ru(bpy) <sub>2</sub> (ACN- <i>d</i> <sub>3</sub> )Cl] <sup>+</sup> C <sub>22</sub> H <sub>16</sub> D <sub>3</sub> ClN <sub>5</sub> Ru: 493.0558	3.04

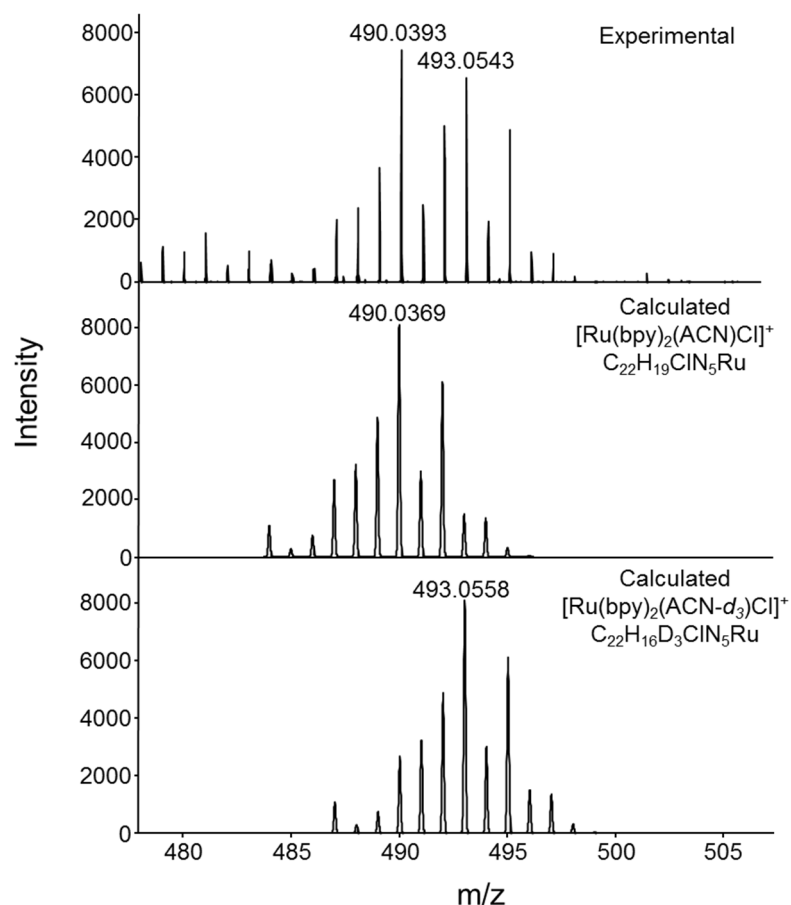


**Figure 4.10.** Experimental and calculated HR-MS peak for the photoproducts [Ru(bpy)<sub>2</sub>(ACN-*d*<sub>3</sub>)Cl]<sup>+</sup> and [Ru(bpy)<sub>2</sub>(ACN)Cl]<sup>+</sup>.

### 4.3.6. Emission properties

The emission properties of *cis*-[Ru(bpy)<sub>2</sub>(INH)<sub>2</sub>][PF<sub>6</sub>]<sub>2</sub> (**4**), *cis*-[Ru(bpy)<sub>2</sub>(NA)<sub>2</sub>][PF<sub>6</sub>]<sub>2</sub> (**5**), *cis*-[Ru(phen)<sub>2</sub>(INH)<sub>2</sub>][PF<sub>6</sub>]<sub>2</sub> (**6**) and *cis*-[Ru(phen)<sub>2</sub>(NA)<sub>2</sub>][PF<sub>6</sub>]<sub>2</sub> (**7**) were investigated by measuring their emission maximum ( $\lambda_{\text{em}}$ ) in aqueous solution (40  $\mu\text{M}$ ) using an excitation wavelength ( $\lambda_{\text{ex}}$ ) of 450 nm, see Figure 4.11

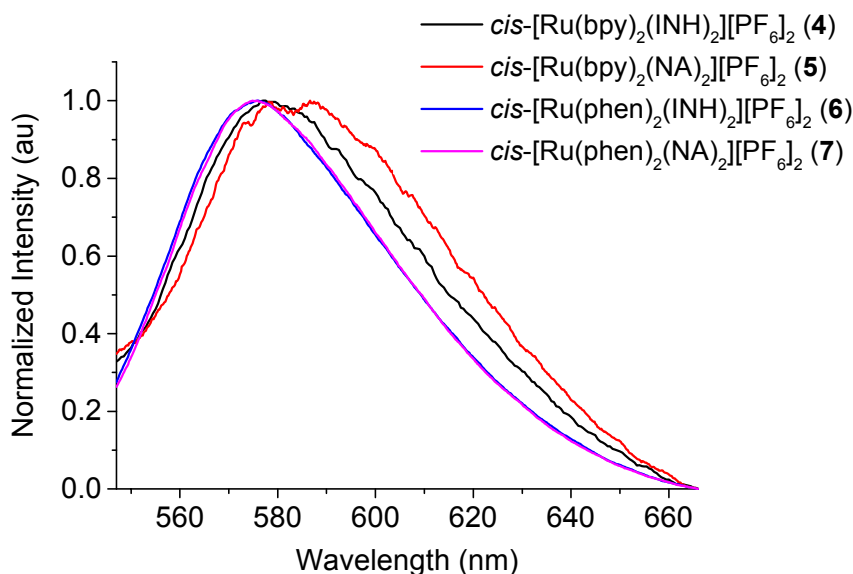


**Figure 4.11.** Emission spectra for *cis*-[Ru(bpy)<sub>2</sub>(INH)<sub>2</sub>][PF<sub>6</sub>]<sub>2</sub> (**4**), *cis*-[Ru(bpy)<sub>2</sub>(NA)<sub>2</sub>][PF<sub>6</sub>]<sub>2</sub> (**5**), *cis*-[Ru(phen)<sub>2</sub>(INH)<sub>2</sub>][PF<sub>6</sub>]<sub>2</sub> (**6**) and *cis*-[Ru(phen)<sub>2</sub>(NA)<sub>2</sub>][PF<sub>6</sub>]<sub>2</sub> (**7**) in aqueous solution (40  $\mu\text{M}$ ) with  $\lambda_{\text{ex}}$  = 450 nm at 298 K.

All complexes exhibit a broad emission band with a maximum centred at ~580 nm, see Table 4.7. The emission maxima for **4** and **5** are very similar, with a difference of 3 nm. Similarly the emission maxima for **6** and **7** only differ by 1 nm. When comparing **4** and **5** with **6** and **7**, the emission maxima differ by only 4-8 nm.

**Table 4.7.** Emission maxima ( $\lambda_{em}$ ) for *cis*-[Ru(bpy)<sub>2</sub>(INH)<sub>2</sub>][PF<sub>6</sub>]<sub>2</sub> (**4**), *cis*-[Ru(bpy)<sub>2</sub>(NA)<sub>2</sub>][PF<sub>6</sub>]<sub>2</sub> (**5**), *cis*-[Ru(phen)<sub>2</sub>(INH)<sub>2</sub>][PF<sub>6</sub>]<sub>2</sub> (**6**) and *cis*-[Ru(phen)<sub>2</sub>(NA)<sub>2</sub>][PF<sub>6</sub>]<sub>2</sub> (**7**) in aqueous solution with  $\lambda_{ex}$  = 450 nm at 298 K.

Complex	Emission maximum, $\lambda_{em}$ (nm)
<b>4</b>	580
<b>5</b>	583
<b>6</b>	576
<b>7</b>	575

#### 4.3.7. Computational analysis

Density functional theory (DFT) was employed to investigate the ground state ( $S_0$ ) and lowest lying triplet state ( $T_1$ ) geometry of *cis*-[Ru(bpy)<sub>2</sub>(INH)<sub>2</sub>]<sup>2+</sup> (**4**), *cis*-[Ru(bpy)<sub>2</sub>(NA)<sub>2</sub>]<sup>2+</sup> (**5**), *cis*-[Ru(phen)<sub>2</sub>(INH)<sub>2</sub>]<sup>2+</sup> (**6**) and *cis*-[Ru(phen)<sub>2</sub>(NA)<sub>2</sub>]<sup>2+</sup> (**7**). Additionally the composition and nature of the molecular orbitals were explored. Time-dependent density functional theory (TD-DFT) was employed to investigate the singlet and triplet excited state transitions.

##### 4.3.7.1. Ground state ( $S_0$ ) geometry

The optimised geometry of the ground state ( $S_0$ ) for **4**, **5**, **6** and **7** was calculated by DFT in the gas phase, with the corresponding bond lengths shown in Table 4.8. Nomenclature for the atoms is in Figure 4.12.

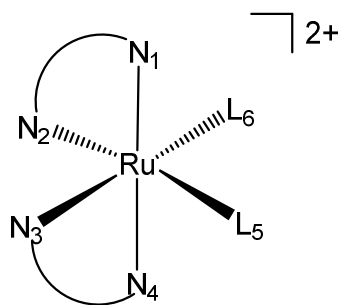


**Figure 4.12.** Atom labels for  $cis-[Ru(N-N')_2(L)_2]^{2+}$ , where  $N_1$ ,  $N_2$ ,  $N_3$  and  $N_4$  belong to the chelating ligand ( $N-N'$ ), and  $L_5$  and  $L_6$  belong to the monodentate ligand ( $L$ ).

**Table 4.8.** Bond distances (Å) for the ground state ( $S_0$ ) geometry of  $cis-[Ru(bpy)_2(INH)_2]^{2+}$  (**4**),  $cis-[Ru(bpy)_2(NA)_2]^{2+}$  (**5**),  $cis-[Ru(phen)_2(INH)_2]^{2+}$  (**6**) and  $cis-[Ru(phen)_2(NA)_2]^{2+}$  (**7**) in comparison to crystal structures determined in Chapter 3.

	Bond distance (Å)							
	<b>4</b>		<b>5</b>		<b>6</b>		<b>7</b>	
	DFT	X-Ray	DFT	X-Ray	DFT	X-Ray	DFT	
Ru- $N_1$	2.127	2.066	2.130	2.068	2.136	2.090	2.141	
Ru- $N_2$	2.109	2.057	2.107	2.052	2.119	2.058	2.116	
Ru- $N_3$	2.109	2.057	2.107	2.052	2.118	2.058	2.115	
Ru- $N_4$	2.127	2.066	2.130	2.068	2.135	2.071	2.140	
Ru- $L_5$	2.177	2.101	2.174	2.108	2.169	2.088	2.167	
Ru- $L_6$	2.177	2.101	2.173	2.108	2.171	2.094	2.168	

The calculated Ru- $N_n$ /Ru- $L_n$  bond distances for **4**, **5** and **6** are very similar to those obtained from the structures determined by X-ray crystallography (see Chapter 3) and differ only by 0.05 Å - 0.08 Å. From the calculated bond distances all complexes have very similar Ru-N / Ru-L bond distances, and only differ by < 0.07 Å.

### 4.3.7.2. Ground state ( $S_0$ ) molecular orbitals

The composition of ground state ( $S_0$ ) molecular orbitals for complexes **4**, **5**, **6** and **7** are found in Figure 4.13, where L is either isoniazid (INH) or nicotinamide (NA) and  $N-N'$  is either 2,2'-bipyridine (bpy) or 1,10-phenanthroline (phen), with images of the frontier orbitals in Figure 4.14.

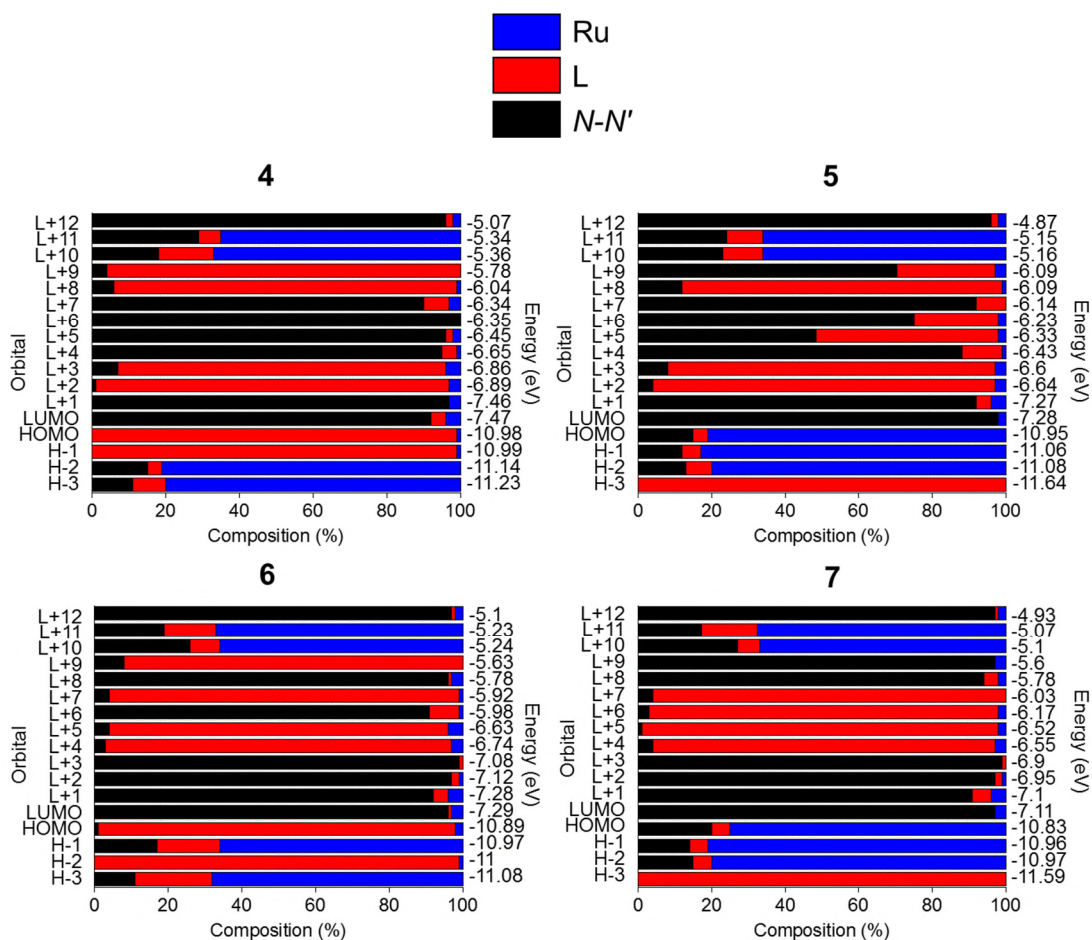


**Figure 4.13.** Molecular orbitals for the ground state ( $S_0$ ) geometry of  $cis-[Ru(bpy)_2(INH)_2]^{2+}$  (**4**),  $cis-[Ru(bpy)_2(NA)_2]^{2+}$  (**5**),  $cis-[Ru(phen)_2(INH)_2]^{2+}$  (**6**) and  $cis-[Ru(phen)_2(NA)_2]^{2+}$  (**7**), where  $N-N'$  is the chelating ligand and L is the monodentate ligand.

Interestingly the HOMO for  $cis-[Ru(bpy)_2(INH)_2]^{2+}$  (**4**) and  $cis-[Ru(phen)_2(INH)_2]^{2+}$  (**6**) is delocalised over the hydrazide group of the monodentate ligand L (INH),



whereas for *cis*-[Ru(bpy)<sub>2</sub>(NA)<sub>2</sub>]<sup>2+</sup> (**5**) and *cis*-[Ru(phen)<sub>2</sub>(NA)<sub>2</sub>]<sup>2+</sup> (**7**) is delocalised predominantly over the ruthenium centre (~ 80 %) with a contribution from the bidentate ligand *N-N'* (~ 20 %). For **5** and **7**, it is HOMO-3 that is delocalised over the amide group of the monodentate ligand L (NA). The occupied L-centred orbitals of **4** and **6** (HOMO-3) are ~ 0.7 eV higher in energy than those for **5** and **7** (HOMO). The energy difference between L-centred HOMO's and metal-centred HOMO's is very small for **4** and **6** (< 0.15 eV), however for **5** and **7** is larger (~ 0.6 eV). The energy of the metal-centred HOMO's is very similar for all complexes, with a difference of < 0.3 eV.

For all complexes, the LUMO is delocalised over the bidentate ligand *N-N'* (> 90 %). Interestingly for **4** and **5** there are two LUMO's delocalised over the bidentate ligand *N-N'* (LUMO and LUMO+1 at -7.5 eV for **4** and -7.3 eV for **5**), whereas for **6** and **7** there are four LUMO's (LUMO, LUMO+1, LUMO+2 and LUMO+3 between -7.1 eV and -7.3 eV for **6** and -6.9 eV and -7.1 eV for **7**). For all complexes, LUMO+10 and LUMO+11 are delocalised predominantly over the metal centre (~ 70 %). Importantly they show  $\sigma^*$ -antibonding character towards the monodentate ligands L and bidentate ligands *N-N'* (with either  $d_{z^2}$  or  $d_{x^2-y^2}$  character), see Figure 4.14.

The energy gap between metal centred HOMO's and LUMO's is very similar for all complexes (~ 5.7 eV for the lowest energy gap). Similarly the energy gap between metal-centred HOMO's and bidentate ligand *N-N'*-centred LUMO's is very similar for all complexes (~ 3.7 eV).

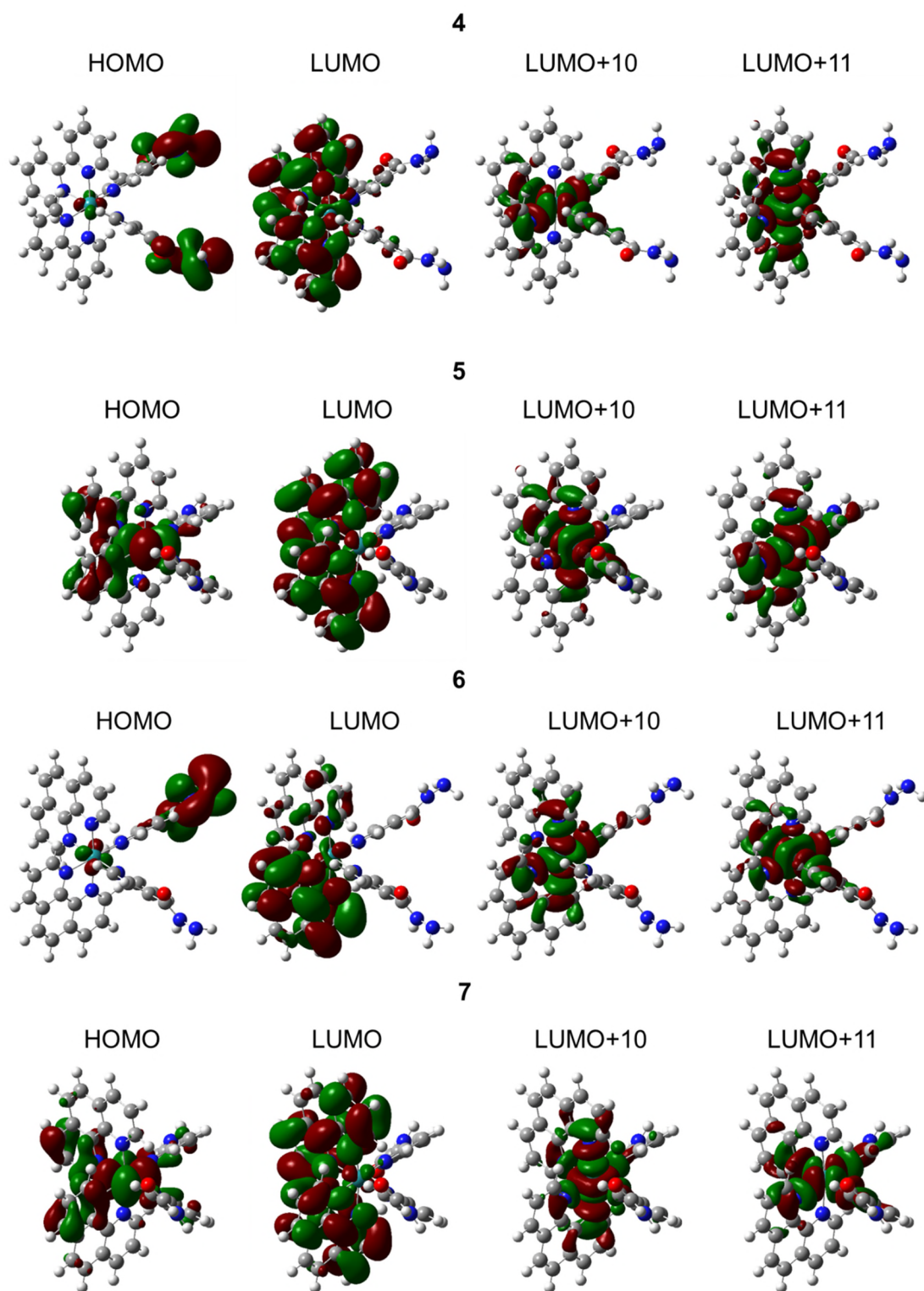


**Figure 4.14.** Frontier orbitals (HOMO and LUMO) and  $\sigma^*$ -antibonding orbitals (LUMO+10 and LUMO+11) for the ground state geometry ( $S_0$ ) of *cis*-[Ru(bpy)<sub>2</sub>(INH)<sub>2</sub>]<sup>2+</sup> (**4**), *cis*-[Ru(bpy)<sub>2</sub>(NA)<sub>2</sub>]<sup>2+</sup> (**5**), *cis*-[Ru(phen)<sub>2</sub>(INH)<sub>2</sub>]<sup>2+</sup> (**6**) and *cis*-[Ru(phen)<sub>2</sub>(NA)<sub>2</sub>]<sup>2+</sup> (**7**). Green and red indicate different phases of the orbitals.

### 4.3.7.3. Lowest-lying triplet state ( $T_1$ ) geometry

The optimised geometry of the lowest lying triplet state ( $T_1$ ) for **4**, **5**, **6** and **7** was calculated by DFT in the gas phase, with the corresponding bond lengths shown in Table 4.9. Nomenclature for the atoms is in Figure 4.15.

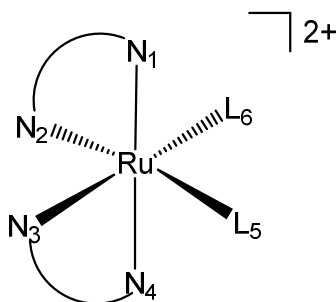


**Figure 4.15.** Atom labels for  $cis\text{-}[\text{Ru}(N\text{-}N')_2(\text{L})_2]^{2+}$ , where  $N_1$ ,  $N_2$ ,  $N_3$  and  $N_4$  belong to the chelating ligand ( $N\text{-}N'$ ), and  $L_5$  and  $L_6$  belong to the monodentate ligand ( $L$ ).

**Table 4.9.** Bond distances (Å) for the lowest-lying triplet state ( $T_1$ ) geometry of  $cis\text{-}[\text{Ru}(\text{bpy})_2(\text{INH})_2]^{2+}$  (**4**),  $cis\text{-}[\text{Ru}(\text{bpy})_2(\text{NA})_2]^{2+}$  (**5**),  $cis\text{-}[\text{Ru}(\text{phen})_2(\text{INH})_2]^{2+}$  (**6**) and  $cis\text{-}[\text{Ru}(\text{phen})_2(\text{NA})_2]^{2+}$  (**7**).

	Bond distance (Å)			
	<b>4</b>	<b>5</b>	<b>6</b>	<b>7</b>
Ru- $N_1$	2.118	2.184	2.128	2.177
Ru- $N_2$	2.062	2.404*	2.007	2.433*
Ru- $N_3$	2.062	2.113	2.111	2.134
Ru- $N_4$	2.118	2.115	2.153	2.123
Ru- $L_5$	2.196	2.964*	2.224	2.925*
Ru- $L_6$	2.196	2.170	2.162	2.161

\* indicates where the  $T_1$  structure has deviated more than 0.3 Å from the  $S_0$  geometry

Interestingly the lowest lying triplet state ( $T_1$ ) geometries for  $cis\text{-}[\text{Ru}(\text{bpy})_2(\text{NA})_2]^{2+}$  (**5**) and  $cis\text{-}[\text{Ru}(\text{phen})_2(\text{NA})_2]^{2+}$  (**7**) show major deviations in bond distances from the ground singlet state ( $S_0$ , see Table 4.8), whereas for  $cis\text{-}[\text{Ru}(\text{bpy})_2(\text{INH})_2]^{2+}$  (**4**) and

*cis*-[Ru(phen)<sub>2</sub>(INH)<sub>2</sub>]<sup>2+</sup> (**6**) the structures are very similar. In the case of **5** and **7**, the bond distances for Ru-N<sub>2</sub> and Ru-L<sub>5</sub> increased by 0.3 Å and 0.8 Å, respectively, to give final bond distances of ~2.4 Å and ~2.9 Å. This can be seen to a great extent when the ground singlet state geometry (S<sub>0</sub>) and the lowest lying triplet state geometry (T<sub>1</sub>) are superimposed, see Figure 4.16. Interestingly, for **5** and **7** the Ru-L<sub>6</sub> monodentate ligand (NA) has rotated out of its plane by 19°, which can be clearly seen in Figure 4.16.

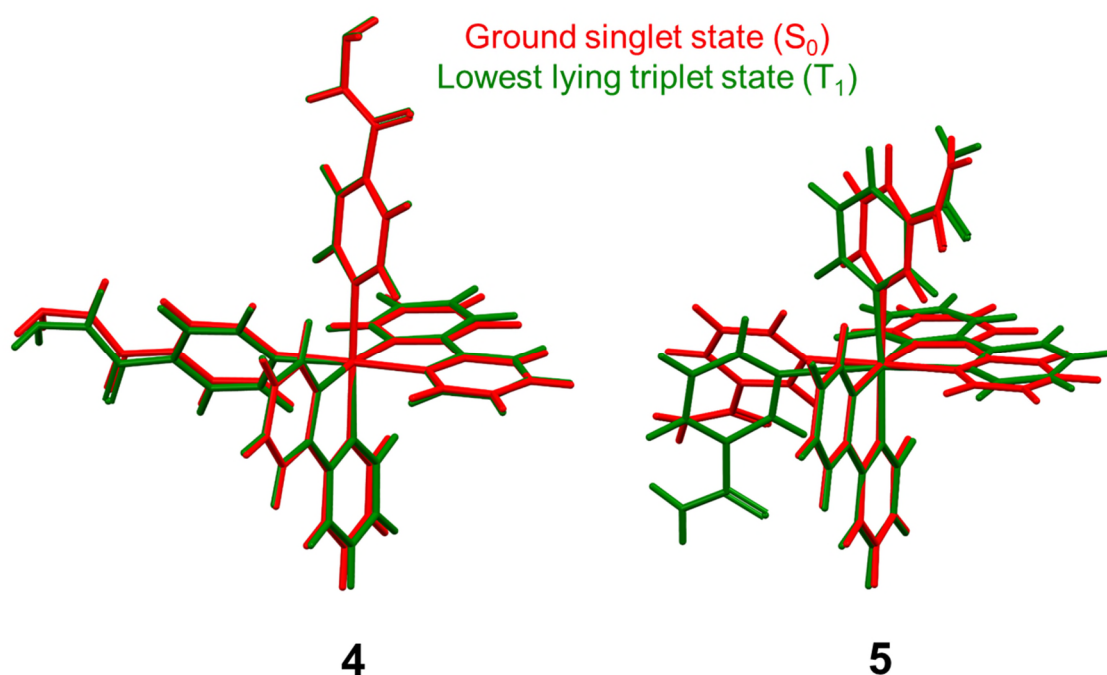


**Figure 4.16.** Superimposition of the ground state (S<sub>0</sub>) geometry (red) and lowest-lying triplet state (T<sub>1</sub>) geometry (green) of *cis*-[Ru(bpy)<sub>2</sub>(INH)<sub>2</sub>]<sup>2+</sup> (**4**) and *cis*-[Ru(bpy)<sub>2</sub>(NA)<sub>2</sub>]<sup>2+</sup> (**5**).

#### 4.3.7.4. Lowest-lying triplet state (T<sub>1</sub>) molecular orbitals

The composition of lowest-lying triplet state (T<sub>1</sub>) molecular orbitals (*l*-SOMO and *h*-SOMO) for complexes **4**, **5**, **6** and **7** as well as the spin density distribution for the state are in Figure 4.17, where *l*-SOMO corresponds to the *lowest* singly-occupied

molecular orbital and *h*-SOMO corresponds to the *highest* singly-occupied molecular orbital.

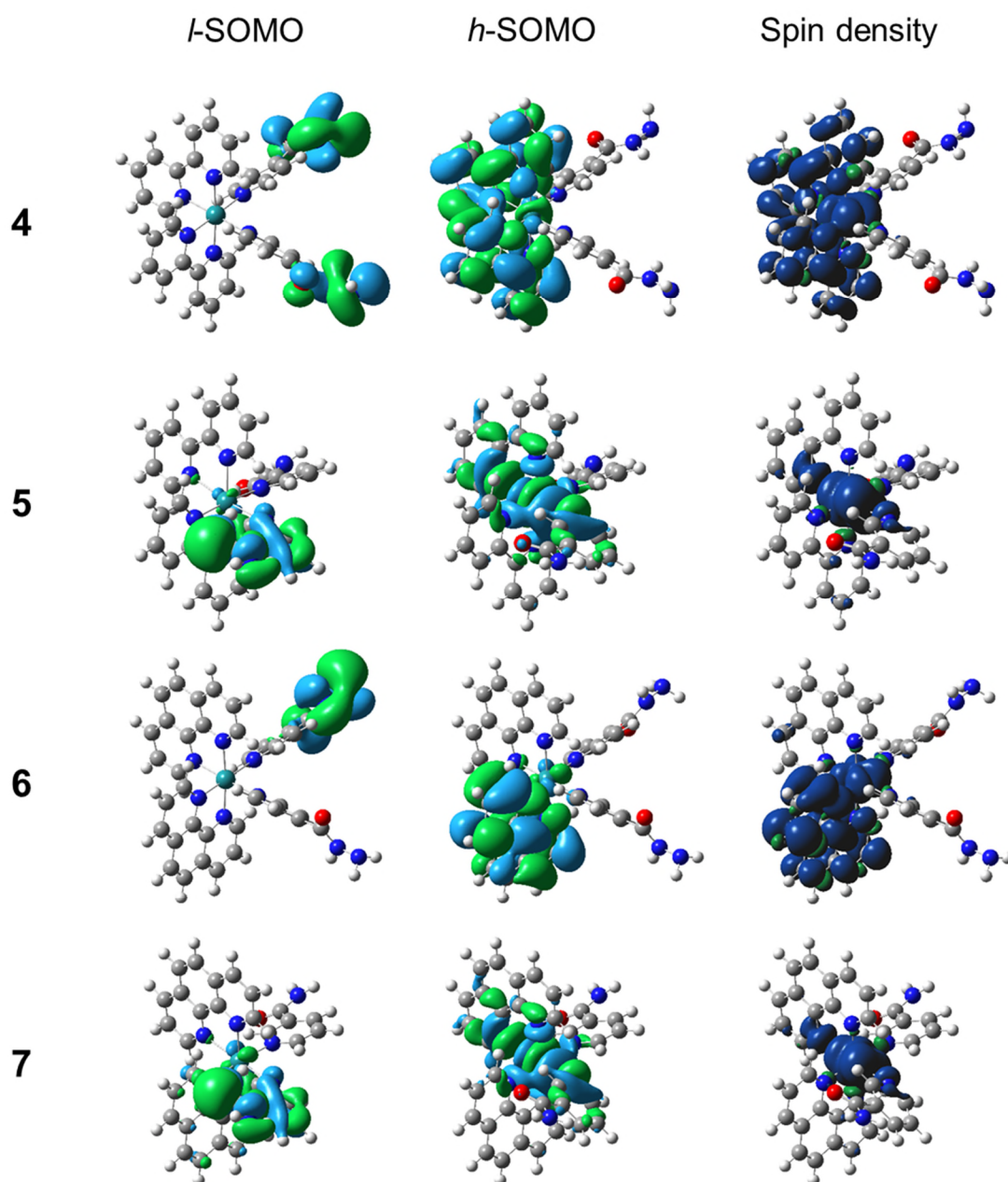


**Figure 4.17.** Lowest-singly occupied orbitals (*l*-SOMO), highest-singly occupied orbitals (*h*-SOMO) and spin density distribution of the lowest-lying triplet state ( $T_1$ ) of *cis*-[Ru(bpy)<sub>2</sub>(INH)<sub>2</sub>]<sup>2+</sup> (4), *cis*-[Ru(bpy)<sub>2</sub>(NA)<sub>2</sub>]<sup>2+</sup> (5), *cis*-[Ru(phen)<sub>2</sub>(INH)<sub>2</sub>]<sup>2+</sup> (6) and *cis*-[Ru(phen)<sub>2</sub>(NA)<sub>2</sub>]<sup>2+</sup> (7). Aqua and green indicate different phases of the orbitals, while dark blue represents spin density.

For all complexes the *l*-SOMO is centred on the monodentate ligand L; in the case of INH it is centred mainly on the hydrazide group. Interestingly for *cis*-[Ru(bpy)<sub>2</sub>(NA)<sub>2</sub>]<sup>2+</sup> (**5**) and *cis*-[Ru(phen)<sub>2</sub>(NA)<sub>2</sub>]<sup>2+</sup> (**7**) the *h*-SOMO is mainly centred on the metal and shows significant  $\sigma^*$ -antibonding character ( $d_{z^2}$  character) towards one of the monodentate ligands L (NA) and one of the pyridine units of the bidentate ligand *N-N'* *trans* to it. For *cis*-[Ru(bpy)<sub>2</sub>(INH)<sub>2</sub>]<sup>2+</sup> (**4**) and *cis*-[Ru(phen)<sub>2</sub>(NA)<sub>2</sub>]<sup>2+</sup> (**6**) the *h*-SOMO is based on the bidentate ligand *N-N'* and the metal centre. The spin density distribution for **4** and **6** is mainly located over the bidentate ligands *N-N'* and the metal centre, whereas for **5** and **7** is located on the metal centre. The spin density distribution confirms that the nature of the lowest-lying triplet state ( $T_1$ ) for *cis*-[Ru(bpy)<sub>2</sub>(INH)<sub>2</sub>]<sup>2+</sup> (**4**) and *cis*-[Ru(phen)<sub>2</sub>(INH)<sub>2</sub>]<sup>2+</sup> (**6**) is <sup>3</sup>MLCT in character and for *cis*-[Ru(bpy)<sub>2</sub>(NA)<sub>2</sub>]<sup>2+</sup> (**5**) and *cis*-[Ru(phen)<sub>2</sub>(NA)<sub>2</sub>]<sup>2+</sup> (**7**) is <sup>3</sup>MC in character.

#### 4.3.7.5. Absorption spectra and singlet excited states

The complexes **4**, **5**, **6** and **7** were dissolved in water and their UV-visible spectra were recorded at 298 K giving the extinction coefficients listed in Table 4.10. The absorption spectrum for each complex was compared to the singlet transitions calculated by TD-DFT, see Figure 4.18 and Table 4.11. Selected electron density distribution maps (EDDMs) for **5** can be found in Figure 4.19. These were utilised in order to characterise each singlet transition.

**Table 4.10.** Experimental extinction coefficients for *cis*-[Ru(bpy)<sub>2</sub>(INH)<sub>2</sub>][PF<sub>6</sub>]<sub>2</sub> (**4**), *cis*-[Ru(bpy)<sub>2</sub>(NA)<sub>2</sub>][PF<sub>6</sub>]<sub>2</sub> (**5**), *cis*-[Ru(phen)<sub>2</sub>(INH)<sub>2</sub>][PF<sub>6</sub>]<sub>2</sub> (**6**) and *cis*-[Ru(phen)<sub>2</sub>(NA)<sub>2</sub>][PF<sub>6</sub>]<sub>2</sub> (**7**) in aqueous solution.

Complex	Wavelength (nm)	Extinction Coefficient (M <sup>-1</sup> cm <sup>-1</sup> )
<b>4</b>	424	15900
	375	17300
	288	42300
<b>5</b>	442	12800
	345	16300
	287	44700
<b>6</b>	438 (sh)	13800
	405	15500
	264	58400
<b>7</b>	439 (sh)	11300
	408	13300
	264	58400

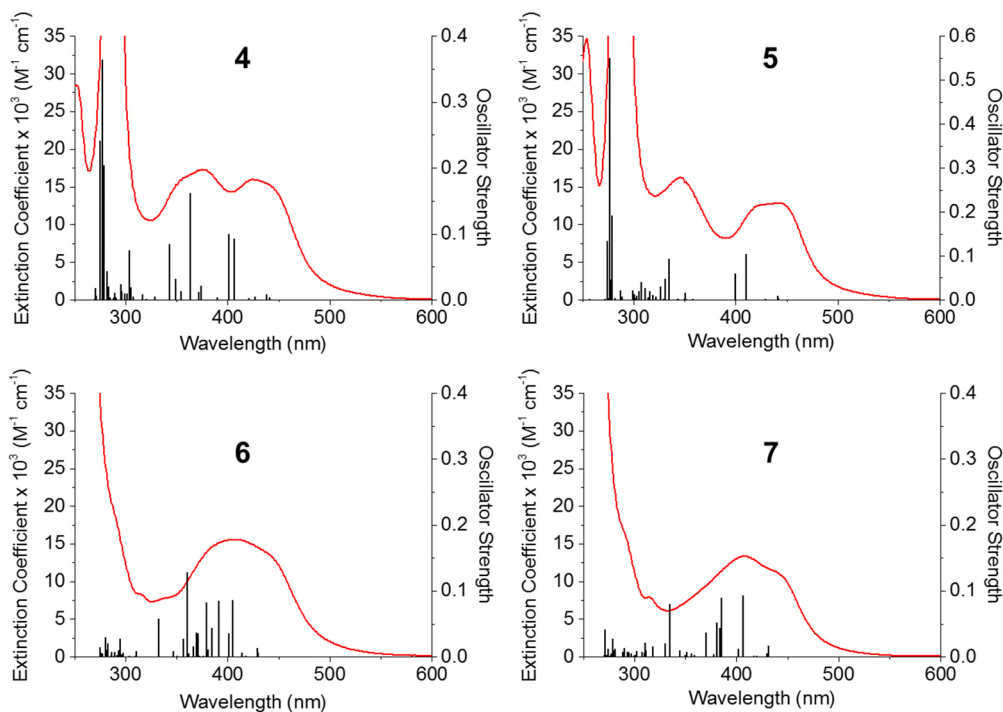


**Figure 4.18.** Experimental absorption spectra (red line, left axis) and TD-DFT calculated vertical singlet transitions (black bars, right axis) for *cis*-[Ru(bpy)<sub>2</sub>(INH)<sub>2</sub>]<sup>2+</sup> (**4**), *cis*-[Ru(bpy)<sub>2</sub>(NA)<sub>2</sub>]<sup>2+</sup> (**5**), *cis*-[Ru(phen)<sub>2</sub>(INH)<sub>2</sub>]<sup>2+</sup> (**6**) and *cis*-[Ru(phen)<sub>2</sub>(NA)<sub>2</sub>]<sup>2+</sup> (**7**) with water as the solvent.

The experimental absorption spectrum and calculated singlet transitions are in reasonable agreement. For all complexes the calculated transitions are blue-shifted compared to the experimental absorption spectrum by 10 nm – 30 nm. For *cis*-[Ru(bpy)<sub>2</sub>(INH)<sub>2</sub>]<sup>2+</sup> (**4**), <sup>1</sup>MLCT<sub>(Ru-bpy)</sub> and <sup>1</sup>MLLCT<sub>(Ru/bpy-INH)</sub> TD-DFT predicted bands were found at 401 nm (3.1 eV) and 364 nm (3.4 eV) respectively, which fits well with the experimental bands at 424 nm and 375 nm, respectively. Similarly for *cis*-[Ru(bpy)<sub>2</sub>(NA)<sub>2</sub>]<sup>2+</sup> (**5**), <sup>1</sup>MLCT<sub>(Ru-bpy)</sub> and <sup>1</sup>MLCT<sub>(Ru-NA)</sub> TD-DFT predicted bands were found at 410 nm (3.0 eV) and 334 nm (3.7 eV) respectively, which fits well with the experimental bands at 442 nm and 334 nm. It is interesting to note that for **4** and **5** S<sub>1</sub> to S<sub>6</sub> have <sup>1</sup>MLCT<sub>(Ru-bpy)</sub> character. For *cis*-[Ru(phen)<sub>2</sub>(INH)<sub>2</sub>]<sup>2+</sup> (**6**) and *cis*-[Ru(phen)<sub>2</sub>(NA)<sub>2</sub>]<sup>2+</sup> (**7**), experimentally there is a broad band that extends over the region of 340 nm – 500 nm (with a small shoulder at ~ 438 nm). This appears to be due to the closely spaced and equal oscillator strength of <sup>1</sup>MLCT<sub>(Ru-phen)</sub> and <sup>1</sup>MLCT<sub>(Ru-INH)</sub> states. For complexes **6** and **7** the TD-DFT predicted <sup>1</sup>MLCT<sub>(Ru-phen)</sub> band has a transition with the largest oscillator strength at 405 nm (3.1 eV) and 407 nm (3.1 eV) respectively, which fits well with the experimental bands at 405 nm and 408 nm, respectively. It is interesting to note that for **6** and **7** S<sub>1</sub> to S<sub>12</sub> have <sup>1</sup>MLCT<sub>(Ru-phen)</sub> character.

For all complexes, the <sup>1</sup>MC state can be found at 350 – 360 nm (3.5 eV). For **4** and **6**, the <sup>1</sup>MC major contribution is from HOMO to LUMO+10 (which is σ\*-antibonding in character), and for **5** and **7** is from HOMO or H-2 to LUMO+11 (which again is σ\*-antibonding in character).



**Table 4.11.** TD-DFT calculated vertical singlet transitions for *cis*-[Ru(bpy)<sub>2</sub>(INH)<sub>2</sub>]<sup>2+</sup> (**4**), *cis*-[Ru(bpy)<sub>2</sub>(NA)<sub>2</sub>]<sup>2+</sup> (**5**), *cis*-[Ru(phen)<sub>2</sub>(INH)<sub>2</sub>]<sup>2+</sup> (**6**) and *cis*-[Ru(phen)<sub>2</sub>(NA)<sub>2</sub>]<sup>2+</sup> (**7**).

	S <sub>n</sub>	Energy (eV)	<i>f</i>	Major contribution	Character
<b>4</b>	1	2.81 (441)	0.003	HOMO→LUMO (81%)	MLCT <sub>(Ru-bpy)</sub>
	3	2.91 (427)	0.004	H-1→LUMO (79%)	MLCT <sub>(Ru-bpy)</sub>
	5	3.05 (407)	0.092	H-2→L+1 (76%)	MLCT <sub>(Ru-bpy)</sub>
	6	3.09 (401)	0.100	H-2→LUMO (53%)	MLCT <sub>(Ru-bpy)</sub>
	11	3.41 (364)	0.161	H-2→L+2 (78%)	MLLCT <sub>(Ru/bpy-INH)</sub>
	12	3.50 (354)	0.013	HOMO→L+10 (55%)	MC
	15	3.62 (343)	0.084	H-2→L+3 (28%)	MC/MLCT <sub>(Ru-INH)</sub>
	45	4.47 (278)	0.364	HOMO→L+9 (37%)	MLCT <sub>(Ru-INH)/LC<sub>(bpy)</sub></sub>
<b>5</b>	1	2.81 (442)	0.003	HOMO→L+1 (70%)	MLCT <sub>(Ru-bpy)</sub>
	3	2.89 (429)	0.002	H-1→L+1 (75%)	MLCT <sub>(Ru-bpy)</sub>
	5	3.02 (410)	0.104	H-2→LUMO (70%)	MLCT <sub>(Ru-bpy)</sub>
	6	3.10 (400)	0.06	H-2→L+1 (51%)	MLCT <sub>(Ru-bpy)</sub>
	10	3.54 (351)	0.016	H-1→L+2 (51%)	MC/MLLCT <sub>(Ru/bpy-NA)</sub>
	11	3.54 (350)	0.001	H-2→L+11 (44%)	MC
	14	3.71 (334)	0.094	H-2→L+3 (82%)	MLCT <sub>(Ru-NA)</sub>
	42	4.48 (277)	0.5488	H-4→LUMO (31%)	MLLCT <sub>(Ru/NA-bpy)/LC<sub>(bpy)</sub></sub>
<b>6</b>	1	2.89 (430)	0.006	HOMO→LUMO (61%)	MLCT <sub>(Ru-phen)</sub>
	3	2.97 (418)	0.001	H-1→LUMO (55%)	MLCT <sub>(Ru-phen)</sub>
	5	3.06 (405)	0.086	H-2→L+1 (44%)	MLCT <sub>(Ru-phen)</sub>
	10	3.27 (379)	0.083	H-1→L+2 (31%)	MLCT <sub>(Ru-phen)/MLCT<sub>(Ru-INH)</sub></sub>
	12	3.33 (373)	0.001	H-1→L+3 (66%)	MLCT <sub>(Ru-phen)/MLCT<sub>(Ru-INH)</sub></sub>
	17	3.44 (360)	0.129	H-2→L+4 (48%)	MLCT <sub>(Ru-INH)</sub>
	18	3.48 (357)	0.027	HOMO→L+10 (43%)	MC
<b>7</b>	1	2.87 (431)	0.017	HOMO→LUMO (84%)	MLCT <sub>(Ru-phen)</sub>
	3	2.95 (420)	0.001	H-1→L+1 (69%)	MLCT <sub>(Ru-phen)</sub>
	5	3.05 (407)	0.093	H-2→LUMO (57%)	MLCT <sub>(Ru-phen)</sub>
	7	3.22 (385)	0.089	HOMO→L+2 (57%)	MLCT <sub>(Ru-phen)</sub>
	12	3.35 (370)	0.037	H-2→L+3 (80%)	MLCT <sub>(Ru-phen)</sub>
	13	3.46 (359)	0.002	HOMO→L+11 (40%)	MC
	20	3.70 (335)	0.080	H-2→L+5 (79%)	MLLCT <sub>(Ru/phen-NA)</sub>

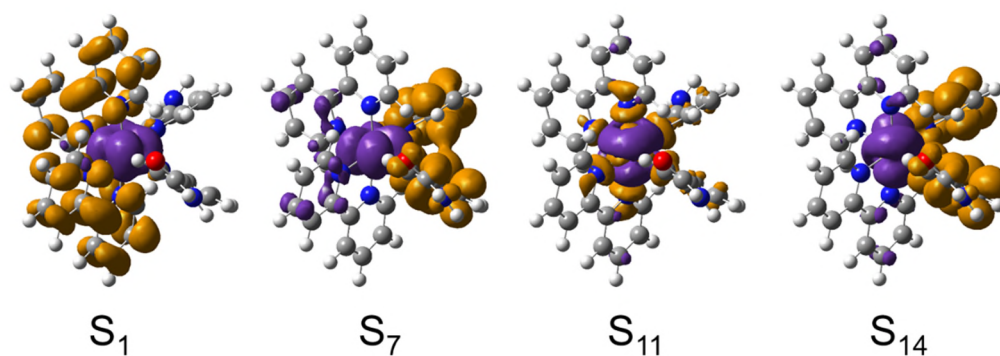


**Figure 4.19.** Selected electron density distribution maps (EDDMs) of singlet excited state transitions for *cis*-[Ru(bpy)<sub>2</sub>(NA)<sub>2</sub>]<sup>2+</sup> (**5**), where orange indicates an increase in electron density while purple indicates a decrease in electron density.

#### 4.3.7.6. Triplet excited states

The triplet transitions were calculated by TD-DFT for **4**, **5** and **6** from the lowest-lying triplet state geometry, see Table 4.12. Selected electron density distribution maps (EDDMs) for **4** can be found in Figure 4.20. These were utilised in order to characterise each triplet transition. The triplet transitions of **7** could not be obtained as the calculation failed to optimise.

For *cis*-[Ru(bpy)<sub>2</sub>(INH)<sub>2</sub>]<sup>2+</sup> (**4**) and *cis*-[Ru(phen)<sub>2</sub>(INH)<sub>2</sub>]<sup>2+</sup> (**6**) T<sub>1</sub> is confirmed to be of <sup>3</sup>MLCT<sub>(Ru-bpy)</sub> and <sup>3</sup>MLCT<sub>(Ru-phen)</sub> in character respectively, with both states at an energy of 2.5 eV. In the case of *cis*-[Ru(bpy)<sub>2</sub>(NA)<sub>2</sub>]<sup>2+</sup> (**5**) T<sub>1</sub> is confirmed to be of <sup>3</sup>MC character at an energy of 2.3 eV. For both **4** and **6** the <sup>3</sup>MC state is much higher in energy (3.4 eV) and the major contribution is HOMO-1 to LUMO+10 (which is σ\*-antibonding in character). Interestingly for **5** there is a mixing of <sup>3</sup>MC/<sup>3</sup>MLCT<sub>(Ru-bpy)</sub> at 3.1 eV, and a <sup>3</sup>MC at higher energy (5 eV) with a major contribution from HOMO-1 to LUMO+11 (σ\*-antibonding in character).

**Table 4.12.** TD-DFT calculated vertical triplet transitions for *cis*-[Ru(bpy)<sub>2</sub>(INH)<sub>2</sub>]<sup>2+</sup> (**4**), *cis*-[Ru(bpy)<sub>2</sub>(NA)<sub>2</sub>]<sup>2+</sup> (**5**), *cis*-[Ru(phen)<sub>2</sub>(INH)<sub>2</sub>]<sup>2+</sup> (**6**) and *cis*-[Ru(phen)<sub>2</sub>(NA)<sub>2</sub>]<sup>2+</sup> (**7**).

	T <sub>n</sub>	Energy (eV)	<i>f</i>	Major contribution	Character
<b>4</b>	1	2.53 (491)	0	HOMO→L+1 (82%)	MLCT <sub>(Ru-bpy)</sub>
	2	2.57 (482)	0	HOMO→LUMO (86%)	MLCT <sub>(Ru-bpy)</sub>
	3	2.83 (438)	0	H-1→LUMO (84%)	MLCT <sub>(Ru-bpy)</sub>
	10	3.30 (375)	0	H-2→L+2 (50%)	MLCT <sub>(Ru-INH)</sub>
	13	3.39 (366)	0	H-1→L+10 (74%)	MC
<b>5</b>	1	2.26 (549)	0	H-2→LUMO (91%)	MC
	2	3.14 (395)	0	H-1→LUMO (46%)	MC / MLCT <sub>(Ru-bpy)</sub>
	3	3.52 (353)	0	HOMO→LUMO (60%)	MC / MLCT <sub>(Ru-bpy)</sub>
	4	4.15 (299)	0	HOMO→L+2 (31%)	MC / MLCT <sub>(Ru-bpy)</sub>
	13	4.99 (248)	0	H-1→L+11 (32%)	MC
<b>6</b>	1	2.47 (501)	0	HOMO→LUMO (87%)	MLCT <sub>(Ru-phen)</sub>
	2	2.87 (432)	0	H-1→LUMO (70%)	MLCT <sub>(Ru-phen)</sub>
	3	2.91 (425)	0	HOMO→L+1 (43%)	MLCT <sub>(Ru-phen)</sub>
	4	3.00 (414)	0	H-2→LUMO (88%)	MLLCT <sub>(Ru/INH-phen)</sub>
	10	3.37 (368)	0	H-1→L+10 (28%)	MC

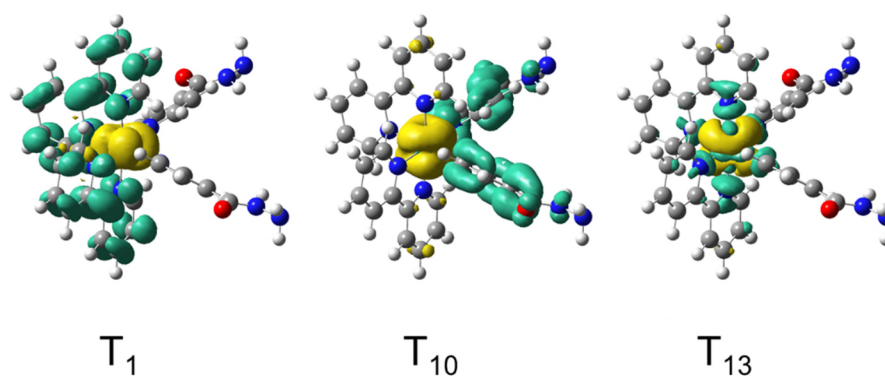


**Figure 4.20.** Selected electron density distribution maps (EDDMs) of triplet excited state transitions for *cis*-[Ru(bpy)<sub>2</sub>(INH)<sub>2</sub>]<sup>2+</sup> (**4**), where turquoise indicates an increase in electron density while yellow indicates a decrease in electron density.

#### 4.3.8. Transient-absorption spectroscopy

The transient-absorption spectrum for *cis*-[Ru(bpy)<sub>2</sub>(NA)<sub>2</sub>][PF<sub>6</sub>]<sub>2</sub> (**5**) in aqueous solution is shown in Figure 4.21. At early pump-probe delays (< 25 ps, see Figure 4.21A) there was a ground state bleach (GSB) signal at 420 nm due to the promotion of *cis*-[Ru(bpy)<sub>2</sub>(NA)<sub>2</sub>]<sup>2+</sup> (**5**) to an excited state after absorption of a photon. At ~ 370 nm there is an absorption band attributed to the bpy<sup>-</sup> state of the <sup>3</sup>MLCT that can be formally represented as [Ru<sup>III</sup>(bpy)(bpy<sup>-</sup>)(NA)<sub>2</sub>]<sup>2+</sup>.<sup>27-28</sup> There should also be an absorption feature at ~ 450 nm – 550 nm attributed to the <sup>3</sup>MLCT state, however this is convoluted with the GSB. The broad absorption feature at > 550 nm can be attributed to the *cis*-[Ru(bpy)<sub>2</sub>(NA)]<sup>2+</sup> penta-coordinate intermediate (PCI).<sup>29</sup> Interestingly this feature is present after only 0.5 ps pump-probe delay. Between 0.5 ps and 25 ps the <sup>3</sup>MLCT absorption decreases and narrows, which can be attributed to vibrational cooling of the <sup>3</sup>MLCT state. This may also account for the decrease in the GSB feature over this time frame, as the GSB feature is overlapped with <sup>3</sup>MLCT features. Additionally the PCI feature decreases over this time frame, attributable to vibrational cooling of the PCI.

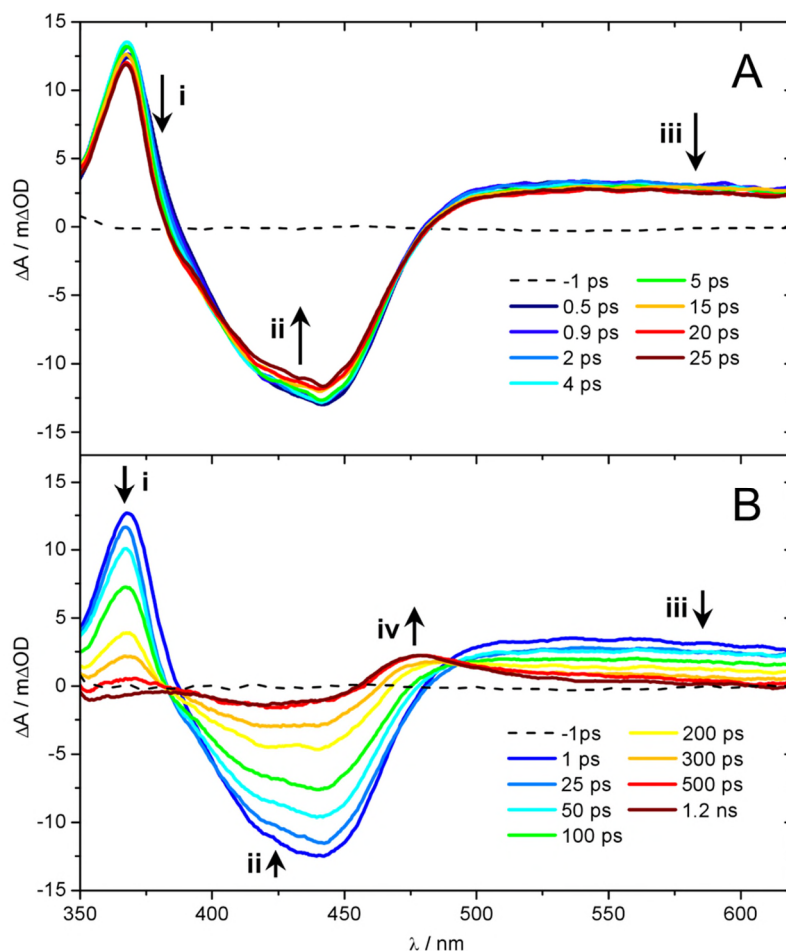


**Figure 4.21.** UV-visible transient-absorption spectra of *cis*-[Ru(bpy)<sub>2</sub>(NA)<sub>2</sub>][PF<sub>6</sub>]<sub>2</sub> (**5**) in aqueous solution after early pump-probe delays, -1 ps to 25 ps (A), and longer pump-probe delays, -1 ps to 1.2 ns (B). Features are <sup>3</sup>MLCT excited state absorption (i), ground state bleach of **5** (ii), absorption of the penta-coordinate intermediate (iii) and absorption of the photoproduct *cis*-[Ru(bpy)<sub>2</sub>(NA)(H<sub>2</sub>O)]<sup>2+</sup> (iv).

At longer pump-probe delays (25 ps to 1.2 ns, see Figure 4.21B), the ground state bleach recovers and the <sup>3</sup>MLCT absorption feature decreases in intensity, with a quasi-isosbestic point at ~ 390 nm. Similarly the absorption of the PCI at > 550 nm decreases and a new absorption feature at 475 nm increases, attributable to the absorption of the photoproduct *cis*-[Ru(bpy)<sub>2</sub>(NA)(H<sub>2</sub>O)]<sup>2+</sup>, with a quasi-isosbestic point at ~ 490 nm. Interestingly over this longer time period the ground state bleach never fully recovers back to  $\Delta A = 0$ , confirming that some of the molecules of **5** that were initially

photoexcited never return to the ground state (i.e. form the photoproduct). In order to calculate the timescales of the various photophysical/photochemical pathways, a “target-analysis” approach was adopted using the KOALA spectral analysis package that can decompose a transient-absorption spectrum into its individual components.<sup>30</sup> The kinetic traces of the integrated area of each individual component over time can be fitted to first/pseudo-first order kinetic equations to afford lifetimes,  $\tau$ . The kinetic traces can be found in Figure 4.22, along with photochemical/photophysical pathways for the photoexcitation of **5** in Figure 4.23 and lifetime values in Table 4.13.

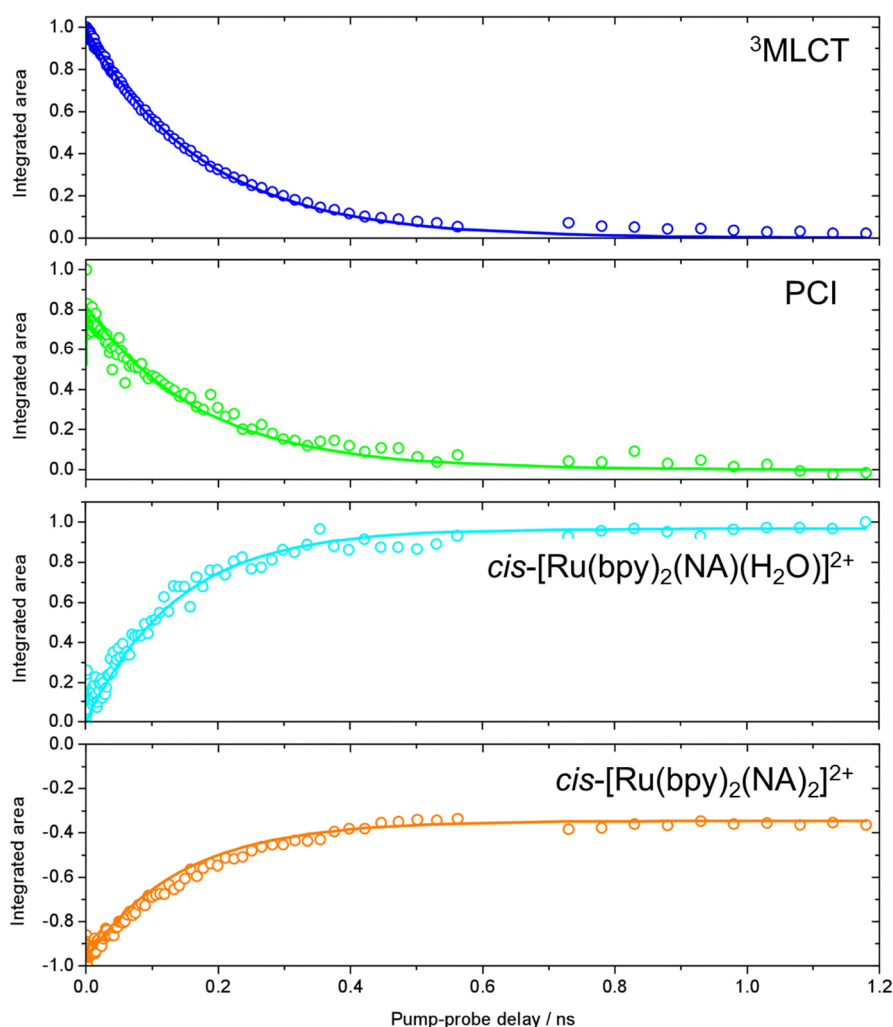


**Figure 4.22.** Kinetic traces labelled from top to bottom: decay of the  $^3\text{MLCT}$  absorption (dark blue), decay of the penta-coordinate intermediate (PCI) absorption (green), growth of the photoproduct  $\text{cis-}[\text{Ru}(\text{bpy})_2(\text{NA})(\text{H}_2\text{O})]^{2+}$  absorption (light blue) and recovery of the ground state bleach (orange).

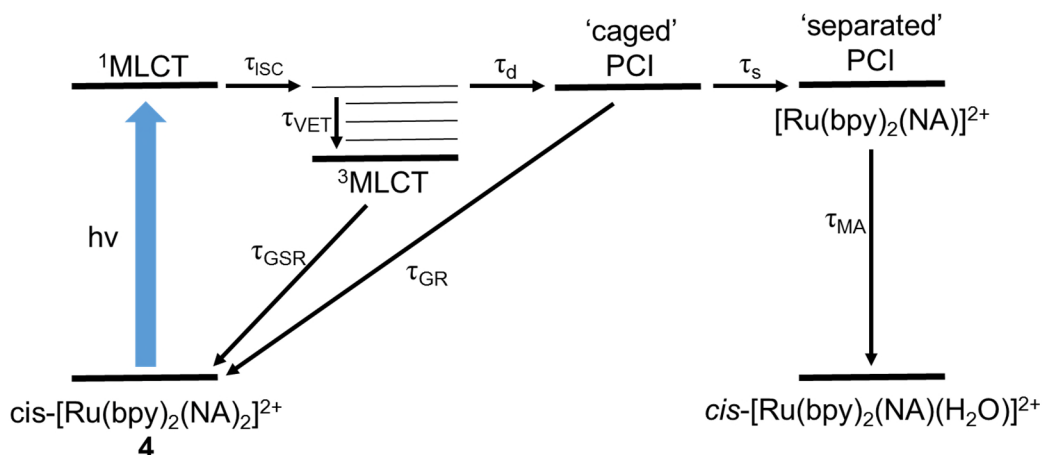


**Figure 4.23.** Photochemical/photophysical pathways following the photoexcitation of *cis*-[Ru(bpy)<sub>2</sub>(NA)<sub>2</sub>]<sup>2+</sup> (**5**).

**Table 4.13.** Lifetimes ( $\tau$ ) of the various photochemical/photophysical pathways of *cis*-[Ru(bpy)<sub>2</sub>(NA)<sub>2</sub>]<sup>2+</sup> (**5**) obtained from the kinetic traces in Figure 4.22.

Process	Lifetime	Time (ps)
Vibrational transfer	$\tau_{\text{VET}}$	3.6
Ground state recovery	$\tau_{\text{GSR}}$	180
Dissociation	$\tau_{\text{d}}$	0.4
Germinate recombination	$\tau_{\text{GR}}$	263
Diffusional separation	$\tau_{\text{s}}$	377
Mono aquation	$\tau_{\text{MA}}$	< 1
Intersystem crossing	$\tau_{\text{ISC}}$	< 0.1

It is worth noting that some assumptions have been made. Firstly, intersystem crossing (ISC) is ultrafast and in the case of [Ru(bpy)<sub>3</sub>]<sup>2+</sup> occurs in < 0.1 ps ( $\tau_{\text{ISC}}$ ).<sup>12, 15</sup> Secondly, after dissociation of NA the PCI is termed to be ‘caged’ as the NA is in close proximity where germinate recombination may occur ( $\tau_{\text{GR}}$ ), however after diffusional separation of the NA and PCI ( $\tau_{\text{s}}$ ) the PCI is termed as ‘separated’ and a H<sub>2</sub>O molecule can bind rapidly ( $\tau_{\text{MA}}$  < 1 ps) to form photoproduct *cis*-[Ru(bpy)<sub>2</sub>(NA)(H<sub>2</sub>O)]<sup>2+</sup>.

## 4.4. Discussion

### 4.4.1. Effect of solvent on the photorelease

This chapter aims to investigate the structure-activity relationship between ligands in Ru(II) polypyridyl complexes and the photoactivity of the complexes. However it is notable that the photorelease was found to be solvent-dependent in the case of *cis*-[Ru(bpy)<sub>2</sub>(NA)Cl][PF<sub>6</sub>] (**1**). When an aqueous solution of **1** (40 μM) was photoirradiated using blue light ( $\lambda_{\text{irr}} = 463 \text{ nm}$ , 50 mW cm<sup>-2</sup>), there were changes in the UV-visible spectrum concurrent with the photorelease of a ligand in < 1 min of photoirradiation, see Figure 4.1. The photoproduct was confirmed to be *cis*-[Ru(bpy)<sub>2</sub>(NA)(H<sub>2</sub>O)]<sup>2+</sup> by ESI-MS. This was unsurprising as the complex hydrolyses (releasing Cl) in the dark (see Chapter 3) but at a much slower rate than the photolysis ( $t_{1/2}$  of 2712 s for hydrolysis and 3.8 s for photolysis). Thus the photorelease of the Cl as opposed to NA must be favoured due to the tendency of water to solvate Cl<sup>-</sup> well. Conversely when **1** was photoirradiated in acetonitrile, changes in the <sup>1</sup>H-NMR spectrum (Figure 4.9) were consistent with the release of NA to produce [Ru(bpy)<sub>2</sub>(Cl)(ACN)]<sup>+</sup>, with the photoproduct confirmed by HR-MS. This can be attributed to poorer solvation of Cl<sup>-</sup> by acetonitrile compared to water, and therefore its photorelease is less favourable. The effect of solvent on the photoactivation of Ru(II) polypyridyl complexes was not investigated further, and the studies discussed below were carried out in aqueous solution.

### 4.4.2. Assessment of structure-activity relationships

When *cis*-[Ru(bpy)<sub>2</sub>(INH)<sub>2</sub>][PF<sub>6</sub>]<sub>2</sub> (**4**), *cis*-[Ru(bpy)<sub>2</sub>(NA)<sub>2</sub>][PF<sub>6</sub>]<sub>2</sub> (**5**), *cis*-[Ru(phen)<sub>2</sub>(INH)<sub>2</sub>][PF<sub>6</sub>]<sub>2</sub> (**6**) and *cis*-[Ru(phen)<sub>2</sub>(NA)<sub>2</sub>][PF<sub>6</sub>]<sub>2</sub> (**7**) in aqueous solution (40 μM) were photoirradiated using blue light ( $\lambda_{\text{irr}} = 463 \text{ nm}$ , 50 mW cm<sup>-2</sup>), there were changes in their UV-visible spectra concurrent with the photorelease of a ligand in <



1 min, see Figure 4.1. The photoproducts were confirmed to be  $cis$ -[Ru( $N$ - $N'$ )<sub>2</sub>(L)(H<sub>2</sub>O)]<sup>2+</sup> by ESI-MS, where  $N$ - $N'$  is 2,2'-bipyridine (bpy) or 1,10-phenanthroline and L is isoniazid (INH) or nicotinamide (NA). It is well known that for complexes of the type [Ru(bpy)<sub>3</sub>]<sup>3+</sup>, the <sup>1</sup>MLCT<sub>(Ru-bpy)</sub> band is commonly found at ~ 450 nm.<sup>2, 31</sup> Interestingly the <sup>1</sup>MLCT<sub>(Ru-bpy)</sub> band for  $cis$ -[Ru(bpy)<sub>2</sub>(NA)Cl]<sup>+</sup> (**1**) is at 474 nm whereas for  $cis$ -[Ru(bpy)<sub>2</sub>(NA)(H<sub>2</sub>O)]<sup>2+</sup> is at 466 nm. Therefore a blue shift was observed by photoirradiating  $cis$ -[Ru(bpy)<sub>2</sub>(NA)Cl]<sup>+</sup> (**1**) in aqueous solution. This is due to H<sub>2</sub>O being a stronger field ligand than Cl, as a result the d-d energy gap ( $\Delta_o$ ) increases and therefore the <sup>1</sup>MLCT<sub>(Ru-bpy)</sub> will increase in energy. The opposite relationship was found in the case of photoirradiating **4**, **5**, **6** and **7**, where the photoproduct was  $cis$ -[Ru( $N$ - $N'$ )<sub>2</sub>(L)(H<sub>2</sub>O)]<sup>2+</sup>. The <sup>1</sup>MLCT<sub>(Ru- $N$ - $N'$ )</sub> band was found at ~ 420 nm for  $cis$ -[Ru( $N$ - $N'$ )<sub>2</sub>(L)<sub>2</sub>]<sup>2+</sup> and ~ 460 nm for  $cis$ -[Ru( $N$ - $N'$ )<sub>2</sub>(L)(H<sub>2</sub>O)]<sup>2+</sup>. This red shift is due to H<sub>2</sub>O being a weaker field ligand than L (which is pyridine based), as a result the d-d energy gap ( $\Delta_o$ ) decreases and therefore <sup>1</sup>MLCT decreases in energy.

The photoactivity of each complex was followed by UV-visible spectroscopy to give the half-life of formation of mono-aqua species ( $t_{1/2}$ ). The order of photoactivity was found to be  $cis$ -[Ru(phen)<sub>2</sub>(NA)<sub>2</sub>]<sup>2+</sup> (**7**) >  $cis$ -[Ru(phen)<sub>2</sub>(INH)<sub>2</sub>]<sup>2+</sup> (**6**) ~  $cis$ -[Ru(bpy)<sub>2</sub>(NA)<sub>2</sub>]<sup>2+</sup> (**5**) >  $cis$ -[Ru(bpy)<sub>2</sub>(INH)<sub>2</sub>]<sup>2+</sup> (**4**). General correlations can be made: complexes containing 1,10-phenanthroline (phen) are more photoactive than complexes containing 2,2'-bipyridine (bpy) (e.g. **7** > **5**), and complexes containing nicotinamide (NA) are more photoactive than complexes containing isoniazid (INH) (e.g. **5** > **4**). However it is notable that all  $t_{1/2}$  values are < 9 s and the greatest difference between  $t_{1/2}$  values is 4 s. Therefore there is only a very minor difference between the photoactivity of each complex.

#### 4.4.2.1. Qualitative assessment by DFT/TD-DFT

DFT and TD-DFT were employed to investigate if computational techniques can be used to qualitatively assess why there is a difference in photoactivity, see Section 4.3.7. Investigating the molecular orbitals in the ground state geometry showed that the energy gap between the metal centred HOMO's and LUMO's for **4**, **5**, **6** and **7** is very similar ( $\sim 5.7$  eV). Again the energy gap between metal centred HOMO's and bidentate ligand *N-N'* LUMO's is similar for all complexes ( $\sim 3.7$  eV). This results in all complexes having similar energies of  $^1\text{MLCT}$  and  $^1\text{MC}$  ( $\sim 3.0$  eV for  $^1\text{MLCT}$  and  $\sim 3.5$  eV for  $^1\text{MC}$ ). It is worth noting that the  $^1\text{MLCT}$  state is non-dissociative, however the  $^1\text{MC}$  state is dissociative and involves either LUMO+11 or LUMO+10 which are  $\sigma^*$ -antibonding in character (due to either  $d_{z^2}$  or  $d_{x^2-y^2}$ ). One major difference is the number of  $^1\text{MLCT}$  states: complexes *cis*-[Ru(bpy)<sub>2</sub>(INH)<sub>2</sub>]<sup>2+</sup> (**4**) and *cis*-[Ru(bpy)<sub>2</sub>(NA)<sub>2</sub>]<sup>2+</sup> (**5**) have 6  $^1\text{MLCT}$  states whereas *cis*-[Ru(phen)<sub>2</sub>(INH)<sub>2</sub>]<sup>2+</sup> (**6**) and *cis*-[Ru(phen)<sub>2</sub>(NA)<sub>2</sub>]<sup>2+</sup> (**7**) have 12. This can be attributed to the fact that for **6** and **7** there are more lower lying 1,10-phenanthroline (phen)-based LUMO's than 2,2'-bipyridine (bpy)-based LUMO's for **4** and **5** (4 *c.f.* 2). This increase in number of available states may confirm why **6** and **7** are more photoactive than **4** and **5**, as there is a greater possibility of occupying the  $^1\text{MLCT}$  state in **6** and **7**.

Another interesting difference can be found in the energy level of the HOMO orbitals that are centred on the monodentate ligand. In complexes *cis*-[Ru(bpy)<sub>2</sub>(INH)<sub>2</sub>]<sup>2+</sup> (**4**) and *cis*-[Ru(phen)<sub>2</sub>(INH)<sub>2</sub>]<sup>2+</sup> (**6**) the HOMO ( $\sim -11$  eV) is located on the hydrazide group of isoniazid (INH), whereas in *cis*-[Ru(bpy)<sub>2</sub>(NA)<sub>2</sub>]<sup>2+</sup> (**5**) and *cis*-[Ru(phen)<sub>2</sub>(NA)<sub>2</sub>]<sup>2+</sup> (**7**) the HOMO-3 ( $\sim -12$  eV) is located on the amide group of the nicotinamide ligand. The reason for the higher energy of the hydrazide HOMO is due to the alpha effect: when two lone pairs are adjacent to each other they interact and

destabilise the HOMO, which subsequently produces a stronger nucleophile.<sup>32</sup> This occurs for isoniazid, resulting in the hydrazide group becoming less electron-withdrawing than the amide group in nicotinamide. It has been previously suggested that in complexes of the type  $cis\text{-}[\text{Ru}(\text{bpy})_2(\text{L})_2]^{2+}$ , where L is an amine-based ligand, ligands (L) with greater  $\pi$ -accepting properties can enhance the photodissociation yield by favouring electron transfer to the leaving ligand.<sup>33</sup> Following this logic, the reason for the increased photoactivity of nicotinamide containing complexes compared to isoniazid containing complexes ( $cis\text{-}[\text{Ru}(\text{bpy})_2(\text{NA})_2]^{2+}$  (**5**) >  $cis\text{-}[\text{Ru}(\text{bpy})_2(\text{INH})_2]^{2+}$  (**4**) and  $cis\text{-}[\text{Ru}(\text{phen})_2(\text{NA})_2]^{2+}$  (**7**) >  $cis\text{-}[\text{Ru}(\text{phen})_2(\text{INH})_2]^{2+}$  (**6**)) may be the greater  $\pi$ -accepting properties of nicotinamide ligand, linked to the presence of the amide group (compared to isoniazid and the hydrazide group). Interestingly triplet state calculations showed dramatic differences between **4**, **5**, and **6** that supports the previous statement.

The lowest-lying triplet state geometry of  $cis\text{-}[\text{Ru}(\text{bpy})_2(\text{NA})_2]^{2+}$  (**5**) and  $cis\text{-}[\text{Ru}(\text{phen})_2(\text{NA})_2]^{2+}$  (**7**) shows large changes in bond distances when compared to the ground state geometry. The Ru-L<sub>5</sub> bond (L<sub>5</sub> is nicotinamide) elongates by 0.8 Å while the Ru-N<sub>2</sub> bond (N<sub>2</sub> is the chelating ligand bpy or phen) *trans* to it elongates by 0.3 Å, resulting in bond distances of ~2.9 Å and ~2.4 Å, respectively. At this bond distance the Ru-nicotinamide bond would be broken, however due to chelation the Ru-bpy/Ru-phen bond remains intact and is therefore shorter in comparison. From inspection of the *h*-SOMO of  $cis\text{-}[\text{Ru}(\text{bpy})_2(\text{NA})_2]^{2+}$  (**5**) and  $cis\text{-}[\text{Ru}(\text{phen})_2(\text{NA})_2]^{2+}$  (**7**) it is clear that the lowest-lying triplet state is <sup>3</sup>MC in character and is  $\sigma^*$ -antibonding towards the Ru-nicotinamide bond and the Ru-bpy/Ru-phen bond *trans* to it (due to the  $d_{z^2}$  character). The spin density maps also confirm this assignment, as the spin density is located on the metal centre. Conversely for  $cis\text{-}[\text{Ru}(\text{bpy})_2(\text{INH})_2]^{2+}$  (**4**) and  $cis\text{-}$

$[\text{Ru}(\text{phen})_2(\text{INH})_2]^{2+}$  (**6**), the *h*-SOMO and spin density maps confirm that the lowest-lying triplet state is  $^3\text{MLCT}$  in character, with no  $\sigma^*$ -antibonding character. Interestingly this difference in character between  $^3\text{MLCT}$  and  $^3\text{MC}$  correlates well with previous literature.<sup>33-34</sup> The triplet excited states were calculated and are shown graphically in Figure 4.24.

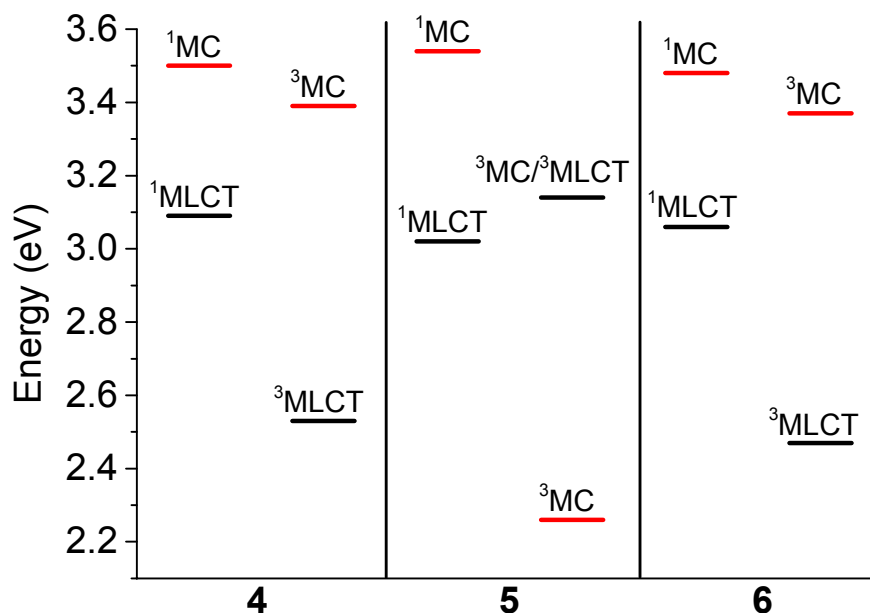


**Figure 4.24.** Singlet and triplet excited states for *cis*- $[\text{Ru}(\text{bpy})_2(\text{INH})_2]^{2+}$  (**4**), *cis*- $[\text{Ru}(\text{bpy})_2(\text{NA})_2]^{2+}$  (**5**) and *cis*- $[\text{Ru}(\text{phen})_2(\text{INH})_2]^{2+}$  (**6**).

For both *cis*- $[\text{Ru}(\text{bpy})_2(\text{INH})_2]^{2+}$  (**4**) and *cis*- $[\text{Ru}(\text{phen})_2(\text{INH})_2]^{2+}$  (**6**), the  $^3\text{MLCT}$  state ( $\sim 2.5$  eV) is found below the  $^3\text{MC}$  state ( $\sim 3.4$  eV). However for *cis*- $[\text{Ru}(\text{bpy})_2(\text{NA})_2]^{2+}$  (**5**) there is mixing of  $^3\text{MC}/^3\text{MLCT}$  (3.1 eV) very close in energy to the  $^1\text{MLCT}$  state (3.0 eV). As a result for complex *cis*- $[\text{Ru}(\text{bpy})_2(\text{NA})_2]^{2+}$  (**5**) after initial photoexcitation to the  $^1\text{MLCT}$  state, efficient ISC may occur through mixing of  $^3\text{MC}/^3\text{MLCT}$  which allows efficient population of the dissociative  $^3\text{MC}$  state.<sup>33</sup> The reason why complexes *cis*- $[\text{Ru}(\text{bpy})_2(\text{NA})_2]^{2+}$  (**5**) and *cis*- $[\text{Ru}(\text{phen})_2(\text{NA})_2]^{2+}$  (**7**) have a lowest-lying triplet state of  $^3\text{MC}$  character is that they contain nicotinamide which is

a stronger  $\pi$ -acceptor than isoniazid, discussed above. Thus favourable leaving properties of the monodentate ligand lowers the energy of the  $^3\text{MC}$  state, resulting in a more photoactive complex, and hence the photoactivity order  $5 > 4$  and  $6 > 7$ .

#### 4.4.3. Wavelength dependence

The photoactivity of *cis*-[Ru(bpy)<sub>2</sub>(INH)<sub>2</sub>][PF<sub>6</sub>]<sub>2</sub> (**4**) and *cis*-[Ru(phen)<sub>2</sub>(INH)<sub>2</sub>][PF<sub>6</sub>]<sub>2</sub> (**7**) was investigated at different wavelengths of photoactivation. There was an inverse relationship between  $t_{1/2}$  and extinction coefficient, see Figure 4.2. Similar results have been reported for a platinum(IV) photoactive complex.<sup>35</sup> This is due to the fact that all photophysical/photochemical processes activated by visible light for Ru(II) polypyridyl complexes arise from the population of the  $^1\text{MLCT}$  state. The  $^1\text{MLCT}$  band for **4** and **7** decreases dramatically over the 440 nm – 560 nm range due to the lack of  $^1\text{MLCT}$  transitions available in that wavelength range. As a result the photoactivity decreases upon increasing wavelength of photoactivation.

#### 4.4.4. Photochemical pathways

The photoirradiation of *cis*-[Ru(bpy)<sub>2</sub>(INH)<sub>2</sub>]<sup>2+</sup> (**4**) in aqueous solution (40  $\mu\text{M}$ ) using blue light ( $\lambda_{\text{irr}} = 463 \text{ nm}$ , 50  $\text{mW cm}^{-2}$ ) at 298 K was followed by HR-LCMS in order to characterise the photoproducts. Interestingly the first step involves release of a ligand (INH) and produces *cis*-[Ru(bpy)<sub>2</sub>(INH)(H<sub>2</sub>O)]<sup>2+</sup> exclusively after 50 s photoirradiation. However continued photoirradiation and release of the second ligand (INH) produces two species, *cis*-[Ru<sup>II</sup>(bpy)<sub>2</sub>(H<sub>2</sub>O)<sub>2</sub>]<sup>2+</sup> and *trans*-[Ru<sup>III</sup>(bpy)<sub>2</sub>(H<sub>2</sub>O)(OH)]<sup>2+</sup>. Interestingly if a lower power light source is used ( $\lambda_{\text{irr}} = 465 \text{ nm}$ , 20  $\text{mW cm}^{-2}$ ) a third species is produced, *trans*-[Ru<sup>II</sup>(bpy)<sub>2</sub>(H<sub>2</sub>O)<sub>2</sub>]<sup>2+</sup>, which is not present when using a higher power light source ( $\lambda_{\text{irr}} = 463 \text{ nm}$ , 50  $\text{mW cm}^{-2}$ ). When *cis*-[Ru(bpy)<sub>2</sub>(H<sub>2</sub>O)<sub>2</sub>]<sup>2+</sup> is photoirradiated in aqueous solution it photoisomerises to *trans*-[Ru(bpy)<sub>2</sub>(H<sub>2</sub>O)<sub>2</sub>]<sup>2+</sup>, however a photostationary state is achieved as the *trans* isomer

can photoisomerise back the *cis* isomer.<sup>23</sup> The *cis* to *trans* photoisomerisation is postulated to be more favourable due to the lower energy of the triplet state of the *trans*-penta-coordinate species when compared to the *cis*-penta-coordinate species.<sup>36</sup> The complex *trans*-[Ru(bpy)<sub>2</sub>(H<sub>2</sub>O)<sub>2</sub>]<sup>2+</sup> is a stronger reducing agent than *cis*-[Ru(bpy)<sub>2</sub>(H<sub>2</sub>O)<sub>2</sub>]<sup>2+</sup> and therefore the *trans* isomer is sensitive to oxidation by molecular oxygen (O<sub>2</sub>) to form *trans*-[Ru(bpy)<sub>2</sub>(H<sub>2</sub>O)<sub>2</sub>]<sup>3+</sup>.<sup>23</sup> Interestingly *trans*-[Ru(bpy)<sub>2</sub>(H<sub>2</sub>O)<sub>2</sub>]<sup>3+</sup> is isolated as *trans*-[Ru(bpy)<sub>2</sub>(H<sub>2</sub>O)(OH)]<sup>2+</sup> in aqueous solution due to the strongly acidic nature of the Ru(III) complex; the pK<sub>a</sub> for [Ru(bpy)<sub>2</sub>(py)(H<sub>2</sub>O)]<sup>3+</sup> is reported to be 0.85 while for [Ru(bpy)<sub>2</sub>(py)(H<sub>2</sub>O)]<sup>2+</sup> was found to be 10.8.<sup>23, 37</sup> It is hypothesised that the results found in this chapter indicate that a higher power light source promotes photochemical oxidation of *trans*-[Ru(bpy)<sub>2</sub>(H<sub>2</sub>O)<sub>2</sub>]<sup>2+</sup> to *trans*-[Ru(bpy)<sub>2</sub>(H<sub>2</sub>O)(OH)]<sup>2+</sup> by molecular oxygen, as a result there is much less *trans*-[Ru(bpy)<sub>2</sub>(H<sub>2</sub>O)<sub>2</sub>]<sup>2+</sup> found when a higher power light source is used.

The complex *cis*-[Ru(bpy)<sub>2</sub>(INH)<sub>2</sub>][PF<sub>6</sub>]<sub>2</sub> (**4**) was photoirradiated using the 96-array blue LED ( $\lambda_{\text{irr}} = 465 \text{ nm}$ , 20 mW cm<sup>-2</sup>) to investigate which photoproducts could be formed in the biological setting. Interestingly even though the light source is half the power than that used in previous experiments, after 1 min photoirradiation *cis*-[Ru(bpy)<sub>2</sub>(INH)(H<sub>2</sub>O)]<sup>2+</sup> is formed almost exclusively. Continued photoirradiation for 2 h again produced *cis*-[Ru(bpy)<sub>2</sub>(H<sub>2</sub>O)<sub>2</sub>]<sup>2+</sup>, *trans*-[Ru(bpy)<sub>2</sub>(H<sub>2</sub>O)<sub>2</sub>]<sup>2+</sup> and *trans*-[Ru(bpy)<sub>2</sub>(H<sub>2</sub>O)(OH)]<sup>2+</sup>, however there is still some *cis*-[Ru(bpy)<sub>2</sub>(H<sub>2</sub>O)(INH)]<sup>2+</sup> present. It is worth noting that all the photoproducts formed were stable in solution for 1 h when incubated in the dark at 298 K, as shown by lack of changes in their UV-visible spectra.

#### 4.4.5. Ultrafast studies

Once *cis*-[Ru(bpy)<sub>2</sub>(NA)<sub>2</sub>][PF<sub>6</sub>]<sub>2</sub> (**5**) is photoirradiated, the <sup>1</sup>MLCT state is populated and efficient intersystem crossing ( $\tau_{\text{ISC}} < 0.1$  ps) populates the <sup>3</sup>MLCT state. Two pathways are possible from this point; either vibrational relaxation to the  $v=0$  <sup>3</sup>MLCT state ( $\tau_{\text{VET}} = 3.6$  ps) or dissociation of a NA ligand ( $\tau_{\text{d}} = 0.4$ ) to form the ‘caged’ penta-coordinate intermediate (PCI) via the <sup>3</sup>MC state. In the former pathway, vibrational relaxation will be followed by ground state recovery ( $\tau_{\text{GSR}} = 180$  ps) with the emission of a photon (luminescence). Due to the fact that the lifetime of the <sup>3</sup>MLCT state is not dependent only on the dissociation of the NA ligand (i.e.  $\tau_{\text{GSR}} \gg \tau_{\text{d}}$ ), there must be a barrier to coupling of the <sup>3</sup>MLCT state with the <sup>3</sup>MC state. Interestingly, from TD-DFT calculations in Section 4.3.7.6., this barrier was found to be relatively small at  $\sim 0.1$  eV. Furthermore, **5** was found to be emissive at room temperature in water, supporting the barrier hypothesis. After formation of the ‘caged’ PCI, the PCI and NA may geminately recombine to form **5** ( $\tau_{\text{GR}} = 263$  ps) or the PCI and NA may diffusively separate to form ‘separated’ PCI ( $\tau_{\text{s}} = 377$  ps), allowing a water molecule to bind ( $\tau_{\text{MA}} < 1$  ps) to form the photoproduct *cis*-[Ru(bpy)<sub>2</sub>(NA)(H<sub>2</sub>O)]<sup>2+</sup>. The analysis above shows that diffusional separation (i.e.  $\tau_{\text{s}}$ ) is the rate-limiting step in the formation of the photoproduct *cis*-[Ru(bpy)<sub>2</sub>(NA)(H<sub>2</sub>O)]<sup>2+</sup>. Interestingly this may open up the possibility of altering the time of this separation by using smaller or larger ligands.

#### 4.5. Summary

Density functional theory (DFT) and time-dependent functional theory (TD-DFT) was used to qualitatively assess how changing the ligands around the ruthenium(II) centre can affect the photoactivity of complexes of the type *cis*-[Ru(*N-N'*)<sub>2</sub>(L)<sub>2</sub>]<sup>2+</sup>. Firstly, it showed that for *cis*-[Ru(phen)<sub>2</sub>(INH)<sub>2</sub>]<sup>2+</sup> (**6**) and *cis*-[Ru(phen)<sub>2</sub>(NA)<sub>2</sub>]<sup>2+</sup> (**7**), there are more <sup>1</sup>MLCT transitions than *cis*-[Ru(bpy)<sub>2</sub>(INH)<sub>2</sub>]<sup>2+</sup> (**4**) and *cis*-[Ru(bpy)<sub>2</sub>(NA)<sub>2</sub>]<sup>2+</sup>

(5). As a result **6** and **7** are more photoactive than **4** and **5**, as the photorelease pathway depends on the population of  $^1\text{MLCT}$  states. Secondly, the calculations suggest that nicotinamide (NA) is a better  $\pi$ -acceptor than isoniazid (INH) and as a result complexes **5** and **7** are more photoactive than **4** and **6**. This was further emphasized by the fact that in the case of *cis*-[Ru(bpy)<sub>2</sub>(NA)<sub>2</sub>]<sup>2+</sup> (**5**), the lowest-lying triplet state ( $T_1$ ) was found to be  $^3\text{MC}$  in character and had considerable  $\sigma^*$ -antibonding character towards the NA ligand. Conversely for complexes containing isoniazid (INH), *cis*-[Ru(bpy)<sub>2</sub>(INH)<sub>2</sub>]<sup>2+</sup> (**4**) and *cis*-[Ru(phen)<sub>2</sub>(INH)<sub>2</sub>]<sup>2+</sup> (**6**), the lowest-lying triplet state was found to be  $^3\text{MLCT}$  in character which had no  $\sigma^*$ -antibonding character. It is thought that the favourable leaving properties (i.e. better  $\pi$ -acceptor) of the NA ligand lowers the energy of the  $^3\text{MC}$  state, thus enhancing its photoactivity. Interestingly it was found that different photoproducts were formed depending on the power of the light source used. In the case of *cis*-[Ru(bpy)<sub>2</sub>(INH)<sub>2</sub>][PF<sub>6</sub>]<sub>2</sub> (**4**), when photoirradiated with a higher power light source no *trans*-[Ru(bpy)<sub>2</sub>(H<sub>2</sub>O)<sub>2</sub>]<sup>2+</sup> photoproduct was observed, however when a lower light power light source was used it was present. It is hypothesised that this is due to the fact that a higher power light source promotes photooxidation of *trans*-[Ru(bpy)<sub>2</sub>(H<sub>2</sub>O)<sub>2</sub>]<sup>2+</sup> to *trans*-[Ru(bpy)<sub>2</sub>(H<sub>2</sub>O)(OH)]<sup>2+</sup> by molecular oxygen. The photochemical/photophysical pathways of complex *cis*-[Ru(bpy)<sub>2</sub>(NA)<sub>2</sub>]<sup>2+</sup> (**5**) were explored by transient-absorption spectroscopy. The rate determining step was found to be the diffusional separation of the penta-coordinate intermediate (PCI) and the leaving ligand NA ( $\tau_s = 377$  ps) allowing a water molecule to bind with formation of the photoproduct *cis*-[Ru(bpy)<sub>2</sub>(NA)(H<sub>2</sub>O)]<sup>2+</sup>.

## 4.6. References

1. Durham, B.; Caspar, J. V.; Nagle, J. K.; Meyer, T. J. *J. Am. Chem. Soc.*, **1982**, *104* (18), 4803-4810.



2. Juris, A.; Balzani, V.; Barigelletti, F.; Campagna, S.; Belser, P.; von Zelewsky, A. *Coord. Chem. Rev.*, **1988**, *84*, 85-277.
3. Wagenknecht, P. S.; Ford, P. C. *Coord. Chem. Rev.*, **2011**, *255* (5–6), 591-616.
4. Liu, F.; Meyer, G. J. *Inorg. Chem.*, **2005**, *44* (25), 9305-9313.
5. Medlycott, E. A.; Hanan, G. S. *Coord. Chem. Rev.*, **2006**, *250* (13–14), 1763-1782.
6. Zayat, L.; Salierno, M.; Etchenique, R. *Inorg. Chem.*, **2006**, *45* (4), 1728-1731.
7. Malouf, G.; Ford, P. C. *J. Am. Chem. Soc.*, **1977**, *99* (22), 7213-7221.
8. Cherry, W. R.; Henderson, L. J. *Inorg. Chem.*, **1984**, *23* (7), 983-986.
9. Frisch, M. J.; Trucks, G. W.; Schlegel, H. B.; Scuseria, G. E.; Robb, M. A.; Cheeseman, J. R.; Montgomery, J. A.; Vreven Jr., T.; Kudin, K. N.; Burant, J. C.; Millam, J. M.; Iyengar, S. S.; Tomasi, J.; Barone, V.; Mennucci, B.; Cossi, M.; Scalmani, G.; Rega, N.; Petersson, G. A.; Nakatsuji, H.; Hada, M.; Ehara, M.; Toyota, K.; Fukuda, R.; Hasegawa, J.; Ishida, M.; Nakajima, T.; Honda, Y.; Kitao, O.; Nakai, H.; Klene, M.; Li, X.; Knox, J. E.; Hratchian, H. P.; Cross, J. B.; Adamo, C.; Jaramillo, J.; Gomperts, R.; Stratmann, R. E.; Yazyev, O.; Austin, A. J.; Cammi, R.; Pomelli, C.; Ochterski, J. W.; Ayala, P. Y.; Morokuma, K.; Voth, G. A.; Salvador, P.; Dannenberg, J. J.; Zakrzewski, V. G.; Dapprich, S.; Daniels, A. D.; Strain, M. C.; Farkas, O.; Malick, D. K.; Rabuck, A. D.; Raghavachari, K.; Foresman, J. B.; Ortiz, J. V.; Cui, Q.; Baboul, A. G.; Clifford, S.; Cioslowski, J.; Stefanov, B. B.; Liu, G.; Liashenko, A.; Piskorz, P.; Komaromi, I.; Martin, R. L.; Fox, D. J.; Keith, T.; Al-Laham, M. A.; Peng, C. Y.; Nanayakkara, A.; Challacombe, M.; Gill, P. M. W.; Johnson, B.; Chen, W.; Wong, M. W.; Gonzalez, C.; Pople, J. A. *Gaussian 03*, Revision B.05; Gaussian, Inc.: Pittsburgh PA, 2003.
10. Becke, A. D. *J. Chem. Phys.*, **1993**, *98* (7), 5648-5652.
11. Lee, C.; Yang, W.; Parr, R. G. *Physical Review B*, **1988**, *37* (2), 785-789.
12. Hay, P. J.; Wadt, W. R. *J. Chem. Phys.*, **1985**, *82* (1), 270-283.

13. Petersson, G. A.; Al-Laham, M. A. *J. Chem. Phys.*, **1991**, *94* (9), 6081-6090.
14. Petersson, G. A.; Bennett, A.; Tensfeldt, T. G.; Al-Laham, M. A.; Shirley, W. A.; Mantzaris, J. *J. Chem. Phys.*, **1988**, *89* (4), 2193-2218.
15. Cossi, M.; Rega, N.; Scalmani, G.; Barone, V. *J. Comput. Chem.*, **2003**, *24* (6), 669-681.
16. Cossi, M.; Barone, V. *J. Chem. Phys.*, **2001**, *115* (10), 4708-4717.
17. Barone, V.; Cossi, M. *J. Phys. Chem. A*, **1998**, *102* (11), 1995-2001.
18. Villegas, J. M.; Stoyanov, S. R.; Huang, W.; Rillema, D. P. *Inorg. Chem.*, **2005**, *44* (7), 2297-2309.
19. Stoyanov, S. R.; Villegas, J. M.; Cruz, A. J.; Lockyear, L. L.; Reibenspies, J. H.; Rillema, D. P. *J. Chem. Theory Comput.*, **2005**, *1* (1), 95-106.
20. Browne, W. R.; O'Boyle, N. M.; McGarvey, J. J.; Vos, J. G. *Chem. Soc. Rev.*, **2005**, *34* (8), 641-663.
21. O'Boyle, N. M.; Vos, J. G. *GaussSum 1.0*, Dublin City University: Dublin, Ireland, 2005.
22. Greenough, S. E.; Roberts, G. M.; Smith, N. A.; Horbury, M. D.; McKinlay, R. G.; Zurek, J. M.; Paterson, M. J.; Sadler, P. J.; Stavros, V. G. *Phys. Chem. Chem. Phys.*, **2014**, *16* (36), 19141-55.
23. Durham, B.; Wilson, S. R.; Hodgson, D. J.; Meyer, T. J. *J. Am. Chem. Soc.*, **1980**, *102* (2), 600-607.
24. Sauaia, M. G.; Tfouni, E.; Santos, R. H. D.; Gambardella, M. M. T. D.; Del Lama, M.; Guimarães, L. F.; da Silva, R. S. *Inorg. Chem. Commun.*, **2003**, *6* (7), 864-868.
25. Budimir, N.; Fournier, F.; Bailly, T.; Burgada, R.; Tabet, J.-C. *Rapid Commun. Mass Spectrom.*, **2005**, *19* (13), 1822-1828.

- 
26. Colton, R.; D'Agostino, A.; Traeger, J. C. *Mass Spectrom. Rev.*, **1995**, *14* (2), 79-106.
27. McCusker, J. K. *Acc. Chem. Res.*, **2003**, *36* (12), 876-887.
28. Damrauer, N. H.; McCusker, J. K. *J. Phys. Chem. A*, **1999**, *103* (42), 8440-8446.
29. Liu, Y.; Turner, D. B.; Singh, T. N.; Angeles-Boza, A. M.; Chouai, A.; Dunbar, K. R.; Turro, C. *J. Am. Chem. Soc.*, **2009**, *131* (1), 26-27.
30. Grubb, M. P.; Orr-Ewing, A. J.; Ashfold, M. N. R. *Rev. Sci. Instrum.*, **2014**, *85* (6), 064104.
31. Kalyanasundaram, K., *Photochemistry of polypyridine and porphyrin complexes*. Academic Press: London, 1992.
32. Jacobs, A., *Understanding organic reaction mechanisms*. Cambridge University Press: Cambridge, 1997.
33. Salassa, L.; Garino, C.; Salassa, G.; Gobetto, R.; Nervi, C. *J. Am. Chem. Soc.*, **2008**, *130* (29), 9590-7.
34. Borfecchia, E.; Garino, C.; Salassa, L.; Ruiiu, T.; Gianolio, D.; Zhang, X.; Attenkofer, K.; Chen, L. X.; Gobetto, R.; Sadler, P. J.; Lamberti, C. *Dalton Trans.*, **2013**, *42* (18), 6564-6571.
35. Farrer, N. J.; Woods, J. A.; Salassa, L.; Zhao, Y.; Robinson, K. S.; Clarkson, G.; Mackay, F. S.; Sadler, P. J. *Angew. Chem. Int. Ed.*, **2010**, *49* (47), 8905-8908.
36. Planas, N.; Vigara, L.; Cady, C.; Miró, P.; Huang, P.; Hammarström, L.; Styring, S.; Leidel, N.; Dau, H.; Haumann, M.; Gagliardi, L.; Cramer, C. J.; Llobet, A. *Inorg. Chem.*, **2011**, *50* (21), 11134-11142.
37. Moyer, B. A.; Meyer, T. J. *J. Am. Chem. Soc.*, **1978**, *100* (11), 3601-3603.

# **Chapter 5**

## **Photobiological properties of Ru(II) polypyridyl complexes**

## Chapter 5

### Photobiological properties of Ru(II) polypyridyl complexes

#### 5.1. Introduction

Ruthenium(II) polypyridyl complexes have been studied for anticancer and antibacterial applications.<sup>1</sup> Interestingly, complexes of the type  $[\text{Ru}(N-N')_3]^{2+}$ , where  $N-N'$  is 2,2'-bipyridine or 1,10-phenanthroline, are active against *Staphylococcus aureus* and *Mycobacterium tuberculosis* at concentrations ranging between 0.5  $\mu\text{M}$  – 25  $\mu\text{M}$ .<sup>2</sup> Functionalising the  $N-N'$  ligand with increasing number of methyl groups resulted in increased activity against both bacteria, highlighting the importance of hydrophobicity.<sup>2</sup> It is important to consider the target of potential antibacterial agents. Ru(II) polypyridyl complexes of the type  $[\text{Ru}(\text{bpy})_2(\text{L})_2]^{n+}$ , where bpy is 2,2'-bipyridine and L is Cl ( $n = 0$ ) or  $\text{H}_2\text{O}$  ( $n = 2$ ), have been found to bind to DNA at N7 of guanine.<sup>3-4</sup> As a result DNA has been an interesting target for many photoactive Ru(II) polypyridyl anticancer complexes that produce  $[\text{Ru}(N-N')_2(\text{H}_2\text{O})_2]^{2+}$  in aqueous solution once photoactivated.<sup>5-7</sup> With respect to Ru(II) polypyridyl complexes as antimicrobial agents, recently efforts have been placed in investigating the intercalation into DNA and damage by the production of singlet oxygen ( $^1\text{O}_2$ ).<sup>8-11</sup>

The complexes synthesised in Chapter 3 were developed as anti-tuberculosis agents. *M. tuberculosis* is highly pathogenic and very slow growing (24 h doubling time), therefore an alternative bacterium was needed to predict the anti-tuberculosis activity of the complexes. *M. smegmatis* is comparatively fast growing (2 – 3 h doubling time), non-pathogenic and 69.8% of *M. tuberculosis* protein-coding genes have orthologues in *M. smegmatis*.<sup>12</sup> As a result *M. smegmatis* is commonly used as an *M. tuberculosis* model.

This chapter focuses on establishing the antibacterial activity of the isoniazid (INH) and nicotinamide (NA) complexes *cis*-[Ru(bpy)<sub>2</sub>(INH)<sub>2</sub>][PF<sub>6</sub>]<sub>2</sub> (**4**), *cis*-[Ru(bpy)<sub>2</sub>(NA)<sub>2</sub>][PF<sub>6</sub>]<sub>2</sub> (**5**) and *cis*-[Ru(phen)<sub>2</sub>(INH)<sub>2</sub>][PF<sub>6</sub>]<sub>2</sub> (**6**) against *E. coli*, *B. subtilis*, and *M. smegmatis*. Particular focus is on the difference in activity of the complexes in the dark and once exposed to light. Information about whether the complexes disrupt the membrane integrity of the bacteria was also obtained using the BacLight™ assay. The ability of the complexes to bind to 9-ethylguanine and L-cysteine was explored by <sup>1</sup>H-NMR and HR-MS.

## 5.2. Experimental

### 5.2.1. Materials

The complexes *cis*-[Ru(bpy)<sub>2</sub>(INH)<sub>2</sub>][PF<sub>6</sub>]<sub>2</sub> (**4**), *cis*-[Ru(bpy)<sub>2</sub>(NA)<sub>2</sub>][PF<sub>6</sub>]<sub>2</sub> (**5**) and *cis*-[Ru(phen)<sub>2</sub>(INH)<sub>2</sub>][PF<sub>6</sub>]<sub>2</sub> (**6**) were synthesised in Chapter 3. L-Cysteine, 9-ethylguanine, Middlebrook 7H9 Broth Base, glycerol, dextrose, sodium chloride, bovine serum albumin, Tween<sup>®</sup> 80, phosphate-buffered saline tablets and tryptic soy broth were purchased from Sigma Aldrich. The LIVE/DEAD<sup>®</sup> BacLight™ bacterial viability kit was purchased from Life Technologies. The bacteria *B. subtilis* 168 and *E. coli* C43(DE3) were kindly provided by Anne Smith from the Chemical Biology Department at University of Warwick, while *M. smegmatis* mc<sup>2</sup>155 was kindly provided by Professor Christopher Dowson from the School of Life Sciences at the University of Warwick. The description of each photoirradiation setup can be found in Chapter 2.

### 5.2.3. Photoirradiation in the presence of 9-ethylguanine and L-cysteine

The complex *cis*-[Ru(bpy)<sub>2</sub>(INH)<sub>2</sub>][PF<sub>6</sub>]<sub>2</sub> (**4**) was dissolved in D<sub>2</sub>O (4 mM) together with 1.1 mol equivalent excess of either 9-ethylguanine (9-EtG) or L-cysteine (Cys). The sample was placed in a 5 mm o.d. NMR tube and photoirradiated using a blue LED ( $\lambda_{\text{irr}} = 463 \text{ nm}$ ,  $50 \text{ mW cm}^{-2}$ ) at 298 K for 50 min. The <sup>1</sup>H-NMR spectrum of each sample was recorded on a Bruker AV-400 spectrometer at 298 K. The samples were incubated in the dark for 24 h at 298 K and the spectrum of each sample was recorded again. All data processing was carried out using Bruker Topspin 2.1. The <sup>1</sup>H-NMR signals were referenced to 1,4-dioxane as an internal reference ( $\delta = 3.75$ ). The structure of the photoirradiation products were confirmed by HR-MS, see Chapter 2 for details of the instrumentation.

### 5.2.4. Photoactivity against *B. subtilis* and *E. coli*

The tryptic soy broth (TSB) and phosphate buffer saline (PBS) were prepared as per manufacturer's instructions. An overnight culture of *E. coli* in TSB was centrifuged and the cell pellet was re-suspended in PBS to give a final OD of 0.015. The *E. coli* suspension was added to wells in a black 96-well plate (100  $\mu\text{L}$ ). The complex *cis*-[Ru(bpy)<sub>2</sub>(INH)<sub>2</sub>][PF<sub>6</sub>]<sub>2</sub> (**4**) dissolved in PBS was added to the wells (100  $\mu\text{L}$ ) to give final complex concentrations of 200  $\mu\text{M}$ , 100  $\mu\text{M}$  and 10  $\mu\text{M}$ . In the dark and light control wells only PBS (100  $\mu\text{L}$ ) was added. Each well was prepared in triplicate. Two black 96-well plates were prepared; one for photoirradiation and one for the dark controls. Both black 96-well plates were incubated initially in the dark for 3 h at 298 K. Subsequently, one of the black 96-well plates was photoirradiated using the 96-array blue LED ( $\lambda_{\text{irr}} = 465 \text{ nm}$ ,  $20 \text{ mW cm}^{-2}$ ) at 298 K for 2 h 20 min, while the other black 96-well plate was kept in the dark. The contents of each well (100  $\mu\text{L}$ ) were plated onto TSB agar plates and incubated overnight at 310 K. After incubation the

number of colony forming units (CFU/mL) were counted. The same procedure was performed using *B. subtilis*. The student's *t*-test was performed with two-tail distribution and unequal variance to determine *p* values (\* denotes  $p \leq 0.05$  while \*\* denotes  $p \leq 0.01$ ); the light samples were compared to the dark samples.

#### 5.2.5. Photoactivity against *M. smegmatis*

The 7H9 media was prepared from Middlebrook 7H9 broth base, glycerol, dextrose, sodium chloride, bovine serum albumin and Tween 80 as per the manufacturer's instructions. To ensure reproducibility, 20% glycerol stock solutions of *M. smegmatis* in 7H9 media were made from an overnight culture and diluted to OD 0.01. The *M. smegmatis* stock suspensions were stored at 193 K for up to 3 months.

##### 5.2.5.1. Photoirradiation using the 96-array blue LED

Prior to use, the *M. smegmatis* stock suspension was diluted to OD 0.002 with 7H9 media. The resulting solution was placed into wells of a black 96-well plate (100  $\mu$ L). The complexes *cis*-[Ru(bpy)<sub>2</sub>(INH)<sub>2</sub>][PF<sub>6</sub>]<sub>2</sub> (**4**), *cis*-[Ru(bpy)<sub>2</sub>(NA)<sub>2</sub>][PF<sub>6</sub>]<sub>2</sub> (**5**), *cis*-[Ru(phen)<sub>2</sub>(INH)<sub>2</sub>][PF<sub>6</sub>]<sub>2</sub> (**6**) and *cis*-[Ru(phen)<sub>2</sub>(NA)<sub>2</sub>][PF<sub>6</sub>]<sub>2</sub> (**7**) were dissolved in 7H9 media and were added to the wells (100  $\mu$ L) to give various final complex concentrations. In the dark and light control wells only 7H9 media (100  $\mu$ L) was added. Each well was prepared in triplicate. Two black 96-well plates were prepared. Both black 96-well plates were incubated initially in the dark for 1 h at 298 K. Subsequently, one of the black 96-well plates was irradiated using the 96-array blue LED ( $\lambda_{\text{irr}} = 465 \text{ nm}$ , 20 mW cm<sup>-2</sup>) at 298 K for various times of irradiation, while the other black 96-well plate was kept in the dark. The contents of both black 96-well plates were transferred to a clear 96-well plate which was placed into a Thermo Labsystems IEMS MF microplate reader. The growth of *M. smegmatis* was monitored



by measuring the change in OD at 600 nm at 310 K over 72 h. The percentage survival was calculated by comparing the values obtained to the appropriate control; light exposed samples were compared to the light control and the dark samples were compared to the dark controls. Details of the microplate reader setup can be found in Chapter 2. The student's *t*-test was performed with two-tail distribution and unequal variance to determine *p* values (\* denotes  $p \leq 0.05$  while \*\* denotes  $p \leq 0.01$ ); the light samples were compared to the dark sample. The minimum inhibitory concentration (MIC) is defined at the minimum concentration that produced < 5% survival of bacteria.

#### **5.2.5.2. Photoirradiation using the 32-array multi-coloured LED**

The same procedure as above was used using the 32-array multi-coloured LED ( $\lambda_{\text{irr}} = 465 \text{ nm}, 520 \text{ nm}, 589 \text{ nm}$  and  $625 \text{ nm}, 5 \text{ mW cm}^{-2}$ ).

#### **5.2.6. BacLight™ assay with *M. smegmatis***

The method was adapted from the manufacturer's instructions for the LIVE/DEAD® BacLight™ bacterial viability kit. A calibration graph of percentage live cells versus fluorescence ratio ( $F_{530 \text{ nm}}/F_{630 \text{ nm}}$ ) was created by preparing mixtures of live and dead cells. For live cells, *M. smegmatis* was suspended in 0.85% w/v NaCl, and for dead cells was suspended in 1% v/v toluene.<sup>13</sup> Both live and dead cells had an OD 0.2 and were incubated at 298 K for 1 h. Various mixtures of live and dead cells (100  $\mu\text{L}$  total volume) were placed into wells of a clear 96-well plate along with 100  $\mu\text{L}$  dye mixture (10  $\mu\text{M}$  SYTO 9 and 60  $\mu\text{M}$  propidium iodide) and 3.2  $\mu\text{L}$  DMSO. Each well was prepared in triplicate. The clear 96-well plate was incubated at 298 K in the dark for 15 min. The fluorescence at 530 nm and 630 nm was measured using an excitation wavelength of 470 nm on a Varioskan Flash Multimode microplate reader. The data were processed using SkanIt software version 2.4.3. The complexes *cis*-

[Ru(bpy)<sub>2</sub>(INH)<sub>2</sub>][PF<sub>6</sub>]<sub>2</sub> (**4**) and *cis*-[Ru(phen)<sub>2</sub>(INH)<sub>2</sub>][PF<sub>6</sub>]<sub>2</sub> (**6**) were dissolved in DMSO to give various complex concentrations and added (3.2  $\mu$ L) to live cells (100  $\mu$ L) in wells of a black 96-well plate. Each well was prepared in triplicate. Two black 96-well plates were prepared. Both were incubated at 298 K in the dark for 30 min. One black 96-well plate was photoirradiated with the 96-array blue LED ( $\lambda_{\text{irr}} = 465$  nm, 20 mW cm<sup>-2</sup>) for 1 min, while the other was kept in the dark. After photoirradiation both were incubated at 298 K in the dark for 30 min. The contents of each well was transferred to a clear 96-well plate and 100  $\mu$ L dye mixture (10  $\mu$ M STYO 9 and 60  $\mu$ M propidium iodide) was added. The clear 96-well plate was incubated at 298 K in the dark for 15 min. The fluorescence at 530 nm and 630 nm was measured using an excitation wavelength of 470 nm on a Varioskan Flash Multimode microplate reader and the fluorescence ratio ( $F_{530 \text{ nm}}/F_{630 \text{ nm}}$ ) was calculated. The students t-test was performed with two-tail distribution and unequal variance to determine *p* values (\* denotes  $p \leq 0.05$  while \*\* denotes  $p \leq 0.01$ ); each sample was compared to the positive control, isoniazid (220  $\mu$ M).

## 5.3. Results

### 5.3.1. Design of 96-array blue LED

The blue LED ( $\lambda_{\text{irr}} = 463$  nm, 50 mW cm<sup>-2</sup>) that was used for photirradiating a sample in a cuvette or an NMR tube was not suitable for photoirradiating samples in a 96-well plate. Therefore a 96-array blue LED ( $\lambda_{\text{irr}} = 465$  nm, 20 mW cm<sup>-2</sup>) was designed, Figure 5.1.

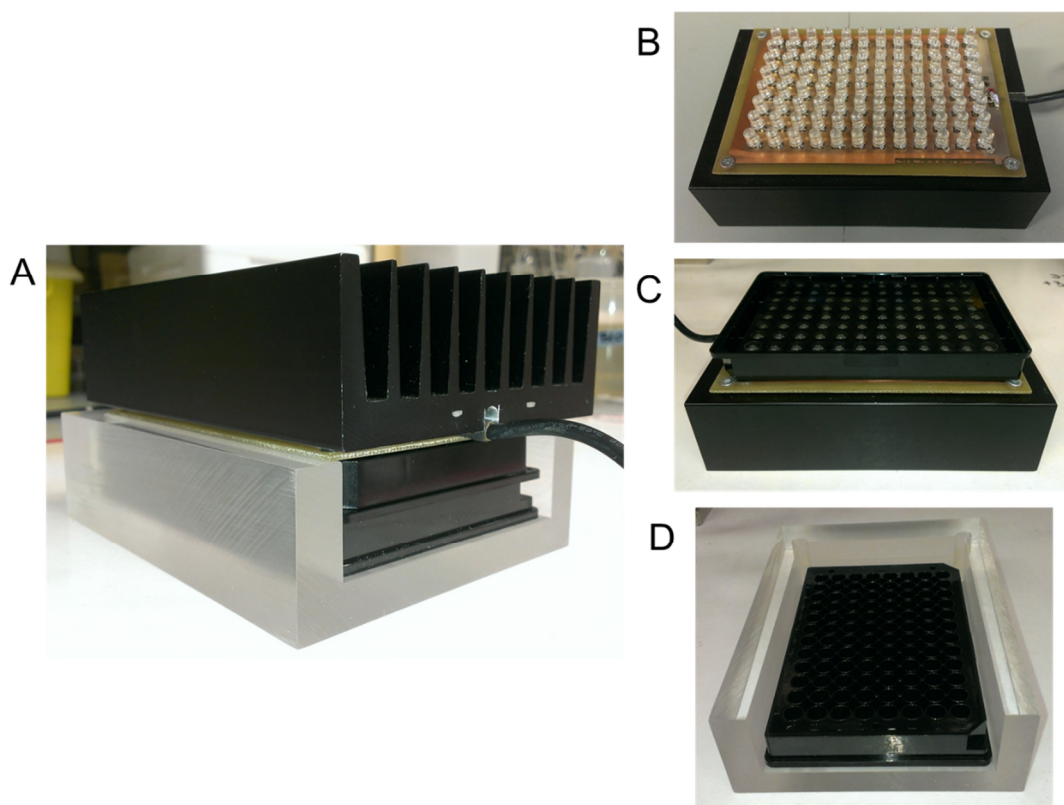


**Figure 5.1.** Complete setup of the 96-array blue LED ( $\lambda_{\text{irr}} = 465 \text{ nm}$ ,  $20 \text{ mW cm}^{-2}$ ) (A), showing the 96-array of blue LED's connected to a heat sink (B) with the black 96-well plate with glass bottom on top of the LED's (C) and the plastic holder that holds the black 96-well plate that will contain the bacteria (D).

The 96-array of blue LED's was housed on a heat sink in order to remove excess heat produced by the LED's. When in use, a black 96-well plate with a glass bottom was used to cover the LED's. A plastic holder was made that could hold the black 96-well plate that would contain the bacteria as well as allowing the 96-array of blue LED's to sit on top without sliding around, see Figure 5.1. In order to see if the heat sink was performing efficiently, heat maps of the black 96-well plate in the plastic holder were measured upon photoirradiation for various times, see Figure 5.2.

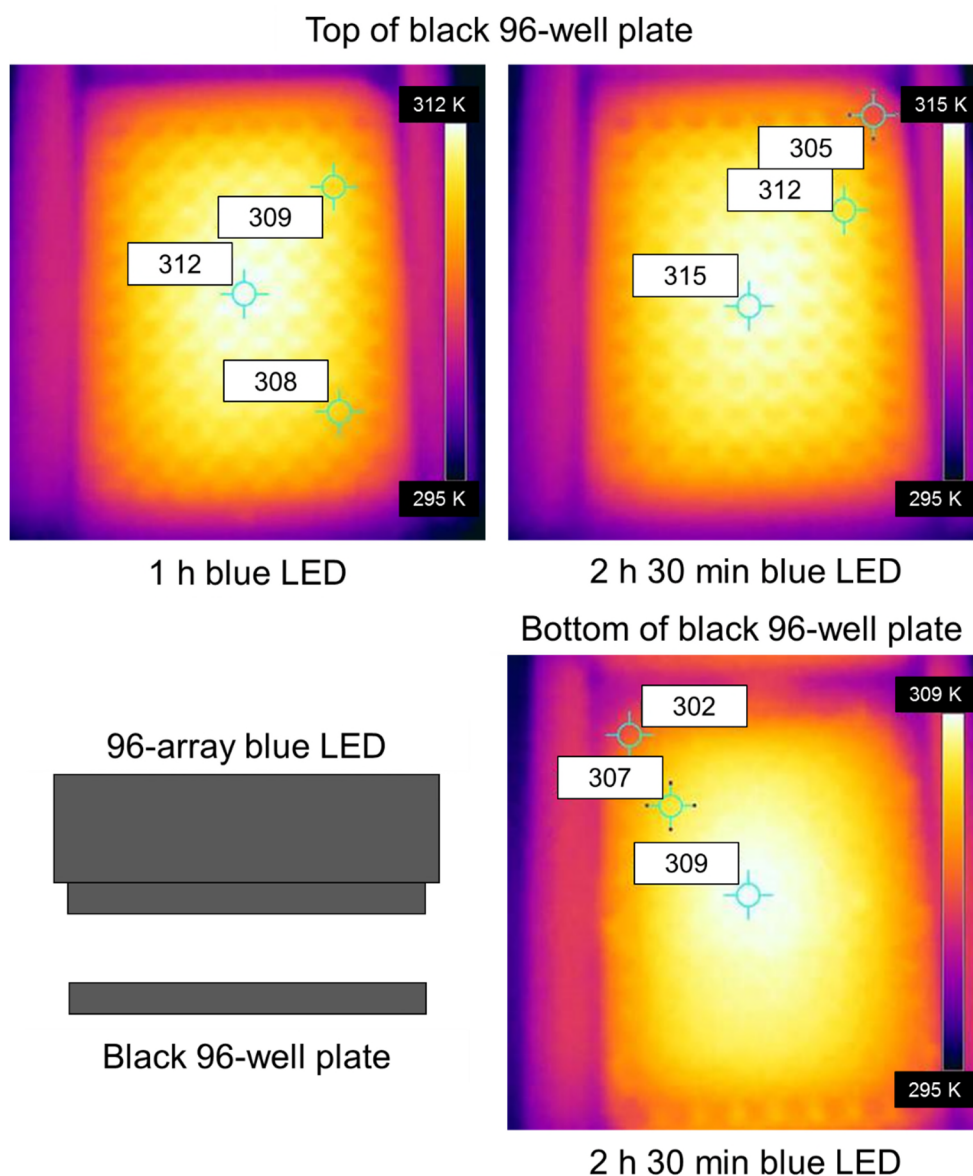


**Figure 5.2.** Heat maps to show the temperature of the black 96-well plate that will hold the bacteria after 1 h and 2 h 30 min photoirradiation with the 96-array blue LED ( $\lambda_{\text{irr}} = 465 \text{ nm}$ ,  $20 \text{ mW cm}^{-2}$ ).

After 1 h photoirradiation the middle of the black 96-well plate is the hottest region reaching 312 K. After 2 h 30 min photoirradiation the middle of the black 96-well plate raises temperature slightly to 315 K, while the outside edge of the plate is much cooler at 305 K. Interestingly the top of the black 96-well plate is 6 degrees hotter than the bottom of the plate (315 K *c.f.* 309 K) after 2 h 30 min photoirradiation.

### 5.3.2. Photoirradiation in the presence of 9-ethylguanine and L-cysteine

The complex *cis*-[Ru(bpy)<sub>2</sub>(INH)<sub>2</sub>][PF<sub>6</sub>]<sub>2</sub> (**4**) was dissolved in D<sub>2</sub>O (4 mM) and photoirradiated with a blue LED ( $\lambda_{\text{irr}} = 463 \text{ nm}$ ,  $50 \text{ mW cm}^{-2}$ ) for 50 min. The photoreaction was followed by <sup>1</sup>H-NMR, see Figure 5.3.

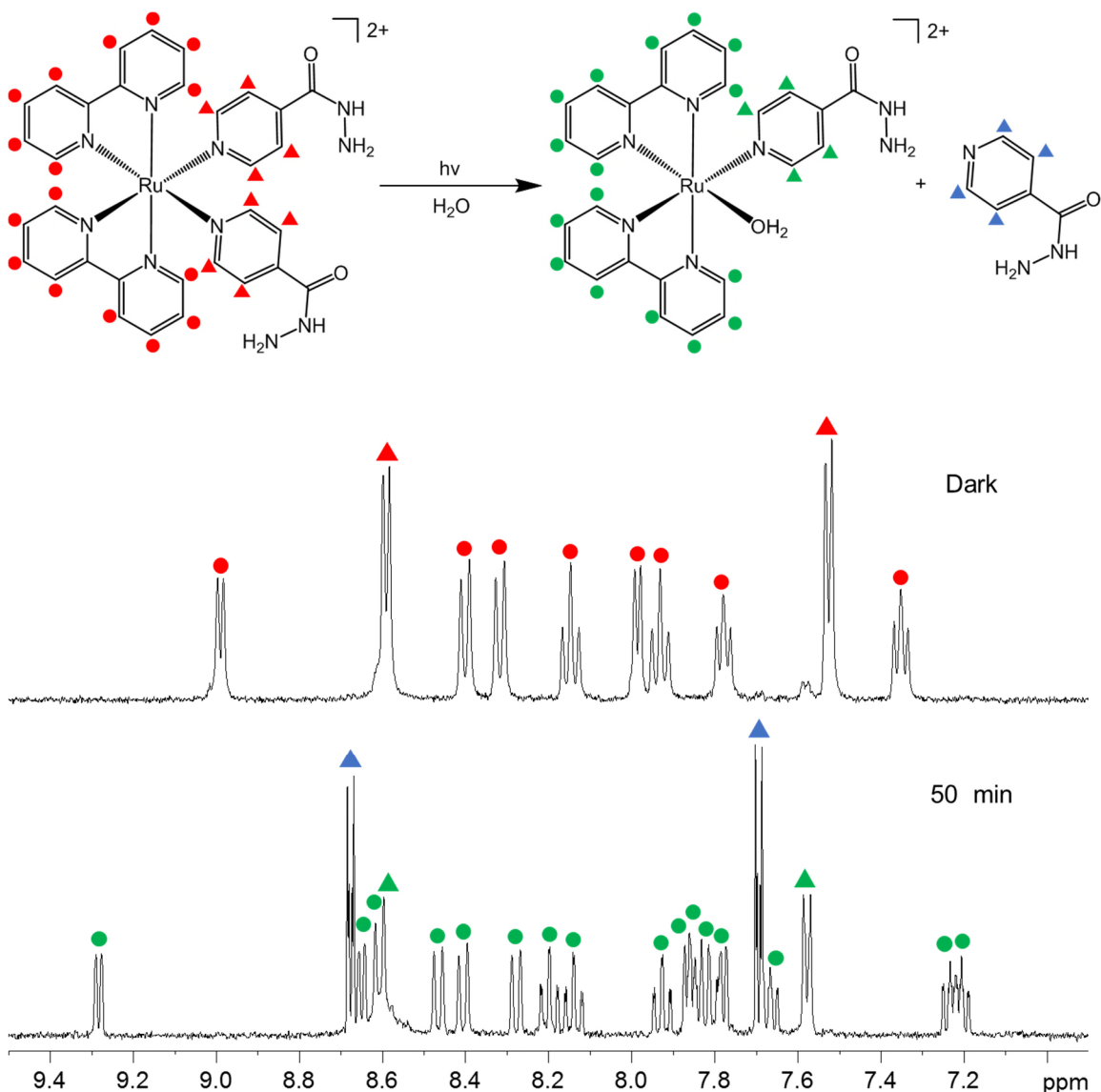


**Figure 5.3.** <sup>1</sup>H-NMR spectrum (400 MHz) of *cis*-[Ru(bpy)<sub>2</sub>(INH)<sub>2</sub>][PF<sub>6</sub>]<sub>2</sub> (**4**) (4 mM) in D<sub>2</sub>O before (top spectrum) and after 50 min photoirradiation (bottom spectrum) using the blue LED ( $\lambda_{\text{irr}} = 463 \text{ nm}$ ,  $50 \text{ mW cm}^{-2}$ ) at 298 K, with schematic of the photoreaction. *Cis*-[Ru(bpy)<sub>2</sub>(INH)<sub>2</sub>]<sup>2+</sup> = ● (with bound INH ▲), *cis*-[Ru(bpy)<sub>2</sub>(INH)(H<sub>2</sub>O)]<sup>2+</sup> = ● (with bound INH ▲), free INH = ▲.

After 50 min photoirradiation, the 10 peaks attributed to the starting material *cis*-[Ru(bpy)<sub>2</sub>(INH)<sub>2</sub>]<sup>2+</sup> decreased and two new sets of peaks increased. The first set of 2 peaks are due to the released free ligand (INH) in solution (8.68 ppm and 7.69 ppm), while the second set of 18 peaks are attributed to the formation of the photoproduct *cis*-[Ru(bpy)<sub>2</sub>(INH)(D<sub>2</sub>O)]<sup>2+</sup>. The photoirradiation of **4** was performed in the presence of L-cysteine (Cys), see Figure 5.4.

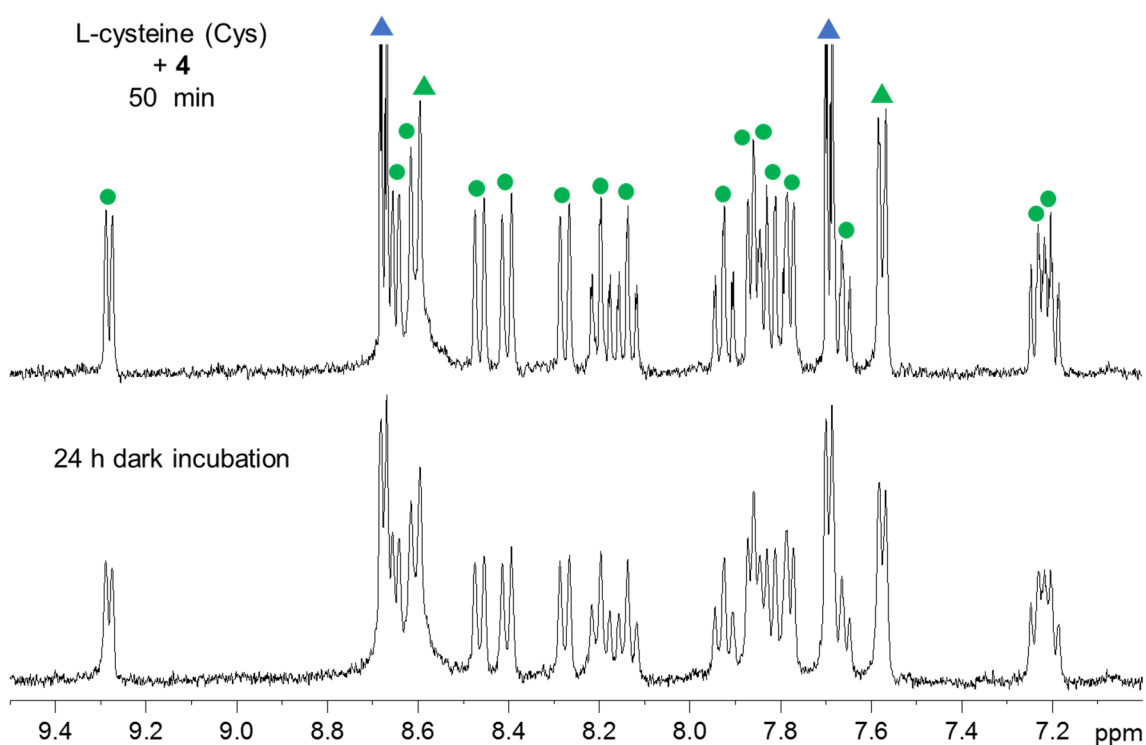


**Figure 5.4.** <sup>1</sup>H-NMR spectrum (400 MHz) of *cis*-[Ru(bpy)<sub>2</sub>(INH)<sub>2</sub>][PF<sub>6</sub>]<sub>2</sub> (**4**) (4 mM) in D<sub>2</sub>O with 1.1 mol equivalent excess L-cysteine (Cys) after 50 min photoirradiation using a blue LED ( $\lambda_{\text{irr}} = 463 \text{ nm}$ ,  $50 \text{ mW cm}^{-2}$ ) at 298 K (top) and after 24 h incubation in the dark at 298 K (bottom). *Cis*-[Ru(bpy)<sub>2</sub>(INH)(H<sub>2</sub>O)]<sup>2+</sup> = ● (with bound INH ▲), free INH = ▲.

After 50 min photoirradiation, the same two sets of peaks were observed as in the case of **4** photoirradiated in the absence of L-cysteine. After incubating the sample in the dark at 298 K for 24 h, the spectrum does not change. The photoirradiation of **4** was also performed in the presence of 9-ethylguanine (9-EtG), see Figure 5.5.

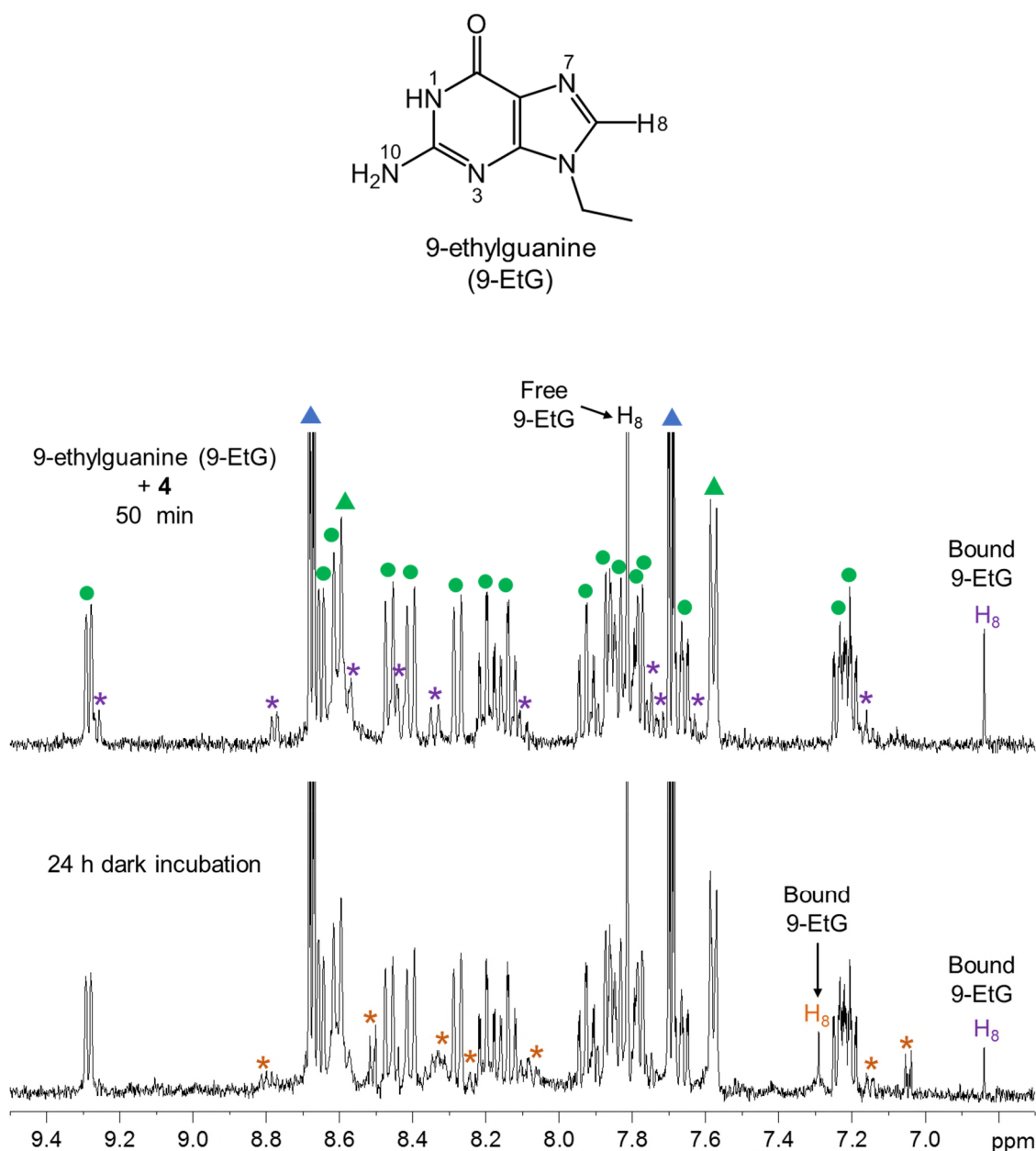


**Figure 5.5.**  $^1\text{H}$ -NMR spectrum (400 MHz) of *cis*- $[\text{Ru}(\text{bpy})_2(\text{INH})_2][\text{PF}_6]_2$  (**4**) (4 mM) in  $\text{D}_2\text{O}$  with 1.1 mol equivalent excess 9-ethylguanine (9-EtG) after 50 min photoirradiation (top spectrum) using a blue LED ( $\lambda_{\text{irr}} = 463 \text{ nm}$ ,  $50 \text{ mW cm}^{-2}$ ) at 298 K and after 24 h incubation in the dark at 298 K (bottom spectrum). *Cis*- $[\text{Ru}(\text{bpy})_2(\text{INH})(\text{H}_2\text{O})]^{2+} = \bullet$  (with bound INH  $\blacktriangle$ ), free INH =  $\blacktriangle$ , *cis*- $[\text{Ru}(\text{bpy})_2(\text{INH})(9\text{-EtG})]^{2+} = *$  (species A) and  $*$  (species B).

Initially after photoirradiation for 50 min, there was a new bound 9-EtG peak for H<sub>8</sub> found at 6.84 ppm (*c.f.* free 9-EtG H<sub>8</sub> at 7.81 ppm), along with a new set of peaks which are hidden underneath existing proton peaks, attributed to the production of the

photoadduct  $cis\text{-}[\text{Ru}(\text{bpy})_2(\text{INH})(9\text{-EtG})]^{2+}$ . All aforementioned peaks are labelled as species A (\*). The percentage binding was estimated to be  $\sim 16\%$ . Interestingly after 24 h dark incubation at 298 K, the bound 9-EtG peak for H<sub>8</sub> at 6.84 ppm decreased and a new bound 9-EtG peak H<sub>8</sub> increased at 7.29 ppm. Additionally a new set of peaks also increased, however it was difficult to identify them as they were hidden underneath existing peaks. These aforementioned peaks are labelled as species B (\*). The identity of the photoadduct  $cis\text{-}[\text{Ru}(\text{bpy})_2(\text{INH})(9\text{-EtG})]^{2+}$  was confirmed by HR-MS, see Figure 5.6. It is important to note that there was no product peak for  $cis\text{-}[\text{Ru}(\text{bpy})_2(9\text{-EtG})(\text{H}_2\text{O})]^{2+}$  or  $cis\text{-}[\text{Ru}(\text{bpy})_2(9\text{-EtG})_2]^{2+}$ .

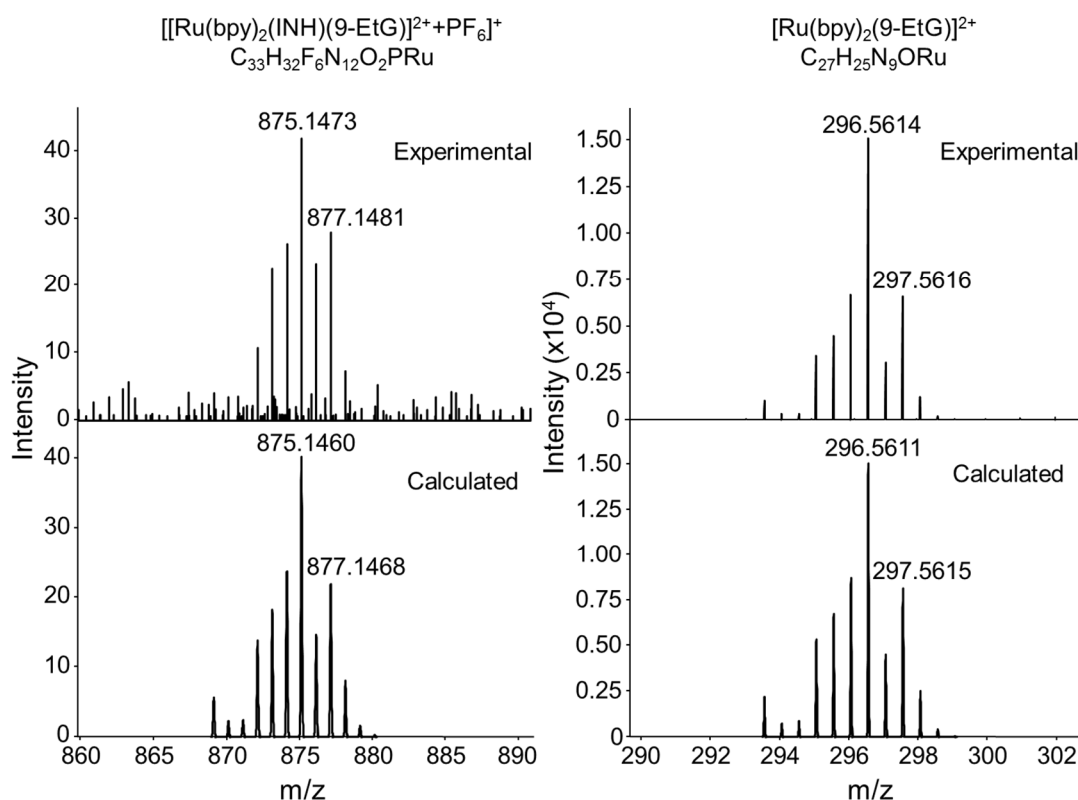


**Figure 5.6.** Calculated and experimentally observed HR-MS peaks for  $cis\text{-}[\text{Ru}(\text{bpy})_2(\text{INH})(9\text{-EtG})]^{2+}$  after  $cis\text{-}[\text{Ru}(\text{bpy})_2(\text{INH})_2][\text{PF}_6]_2$  (**4**) was photoirradiated for 50 min using a blue LED ( $\lambda_{\text{irr}} = 463 \text{ nm}$ ,  $50 \text{ mW cm}^{-2}$ ) in the presence of 1.1 mol equivalent excess of 9-ethylguanine (9-EtG) at 298 K.



### 5.3.3. Photoactivity against *B. subtilis* and *E. coli*

The complex *cis*-[Ru(bpy)<sub>2</sub>(INH)<sub>2</sub>][PF<sub>6</sub>]<sub>2</sub> (**4**) was tested against Gram-positive and Gram-negative models *B. subtilis* and *E. coli*, respectively. Complex **4** was incubated with *B. subtilis* and *E. coli* and either incubated at 298 K in the dark or photoirradiated using the 96-array blue LED ( $\lambda_{\text{irr}} = 465 \text{ nm}$ ,  $20 \text{ mW cm}^{-2}$ ) for 2 h 20 min. After placing the solutions onto agar plates and incubating at 310 K overnight, the number of colony forming units (CFU/mL) were measured, see Figure 5.7.

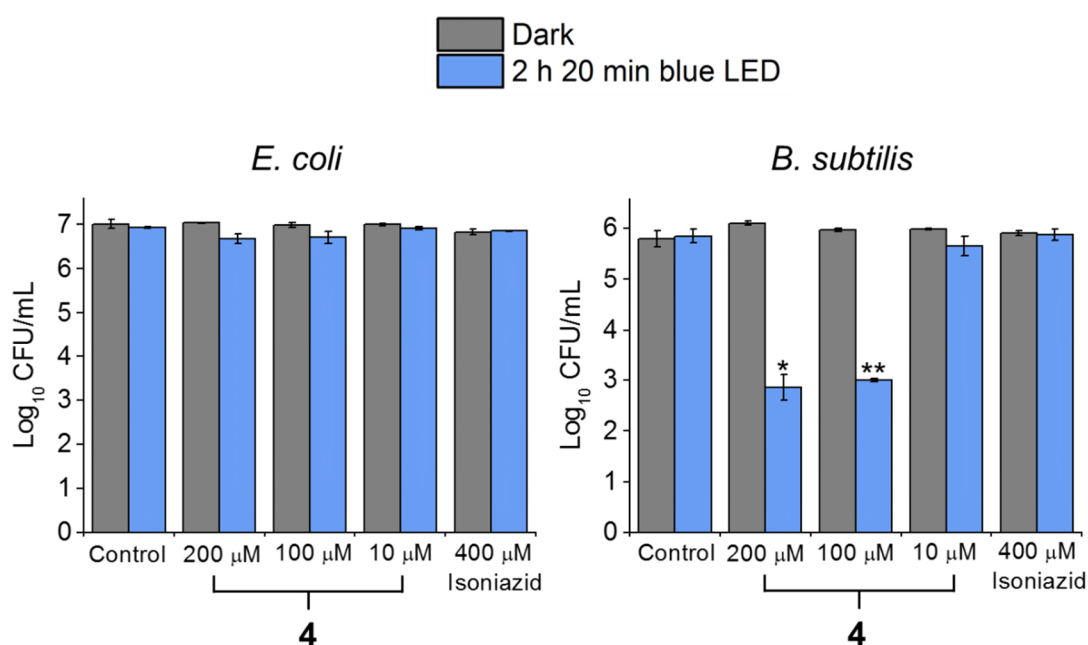


**Figure 5.7.** Activity of *cis*-[Ru(bpy)<sub>2</sub>(INH)<sub>2</sub>][PF<sub>6</sub>]<sub>2</sub> (**4**) against *E. coli* (left) and *B. subtilis* (right) when incubated in the dark (grey bars) and photoirradiated for 2 h 20 min (blue bars) using the 96-array blue LED ( $\lambda_{\text{irr}} = 465 \text{ nm}$ ,  $20 \text{ mW cm}^{-2}$ ) at 298 K. *P* values were calculated by comparing the light samples to the dark samples and are labelled as follows,  $p \leq 0.05 = *$ ,  $p \leq 0.01 = **$ .

When **4** was tested against *E. coli*, the Log<sub>10</sub> CFU/mL was found to be ~7 for all concentrations of **4** (200 μM, 100 μM and 10 μM) both in the dark and photoirradiated. Additionally the Log<sub>10</sub> CFU/mL for the control (cells not exposed to drug) and the isoniazid ligand alone (400 μM) was also ~7 both in the dark and once photoirradiated.

When **4** was tested against *B. subtilis*, for concentrations of 200  $\mu\text{M}$  and 100  $\mu\text{M}$  the  $\text{Log}_{10}$  CFU/mL was  $\sim 6$  in the dark, and decreased to  $\sim 3$  once photoirradiated. The  $\text{Log}_{10}$  CFU/mL for the control, 10  $\mu\text{M}$  **4** and ligand alone (400  $\mu\text{M}$ ) was  $\sim 6$  for both dark incubation and once photoirradiated.

#### 5.3.4. Photoactivity against *M. smegmatis*

The complexes *cis*-[Ru(bpy)<sub>2</sub>(INH)<sub>2</sub>][PF<sub>6</sub>]<sub>2</sub> (**4**), *cis*-[Ru(bpy)<sub>2</sub>(NA)<sub>2</sub>][PF<sub>6</sub>]<sub>2</sub> (**5**) and *cis*-[Ru(phen)<sub>2</sub>(INH)<sub>2</sub>][PF<sub>6</sub>]<sub>2</sub> (**6**) were tested against *M. smegmatis* using either the 96-array blue LED ( $\lambda_{\text{irr}} = 465 \text{ nm}$ , 20  $\text{mW cm}^{-2}$ ) or the 32-array multi-coloured LED ( $\lambda_{\text{irr}} = 465 \text{ nm}$ , 520  $\text{nm}$ , 589  $\text{nm}$  and 625  $\text{nm}$ , 5  $\text{mW cm}^{-2}$ ).

##### 5.3.4.1. Photoirradiation using the 96-array blue LED

Initially *M. smegmatis* was photoirradiated for 1 min, 30 min, 1 h and 2 h using the 96-array blue LED ( $\lambda_{\text{irr}} = 465 \text{ nm}$ , 20  $\text{mW cm}^{-2}$ ) at 298 K in the absence of any complex. The growth of each sample was monitored over a 72 h period at 310 K and was compared to the dark control to calculate the survival (%), see Figure 5.8.

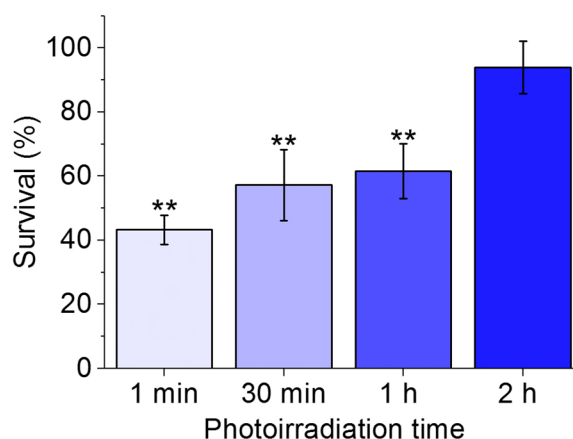


**Figure 5.8.** Photoirradiation of *M. smegmatis* using the 96-array blue LED ( $\lambda_{\text{irr}} = 465 \text{ nm}$ , 20  $\text{mW cm}^{-2}$ ) at 298 K. *P* values were calculated by comparing the light samples to the dark control and are labelled as follows,  $p \leq 0.05 = *$ ,  $p \leq 0.01 = **$ .

Interestingly 1 min photoirradiation only observed 43% survival, while 30 min and 1 h photoirradiation observed 57% and 62% survival respectively. After 2 h irradiation there was 94 % survival. The complexes *cis*-[Ru(bpy)<sub>2</sub>(INH)<sub>2</sub>][PF<sub>6</sub>]<sub>2</sub> (**4**), *cis*-[Ru(bpy)<sub>2</sub>(NA)<sub>2</sub>][PF<sub>6</sub>]<sub>2</sub> (**5**) and *cis*-[Ru(phen)<sub>2</sub>(INH)<sub>2</sub>][PF<sub>6</sub>]<sub>2</sub> (**6**) were incubated in the dark for 1 h at 298 K with *M. smegmatis* and the samples were photoirradiated for 1 min, 30 min, 1 h and 2 h at 298 K, see Figure 5.9.

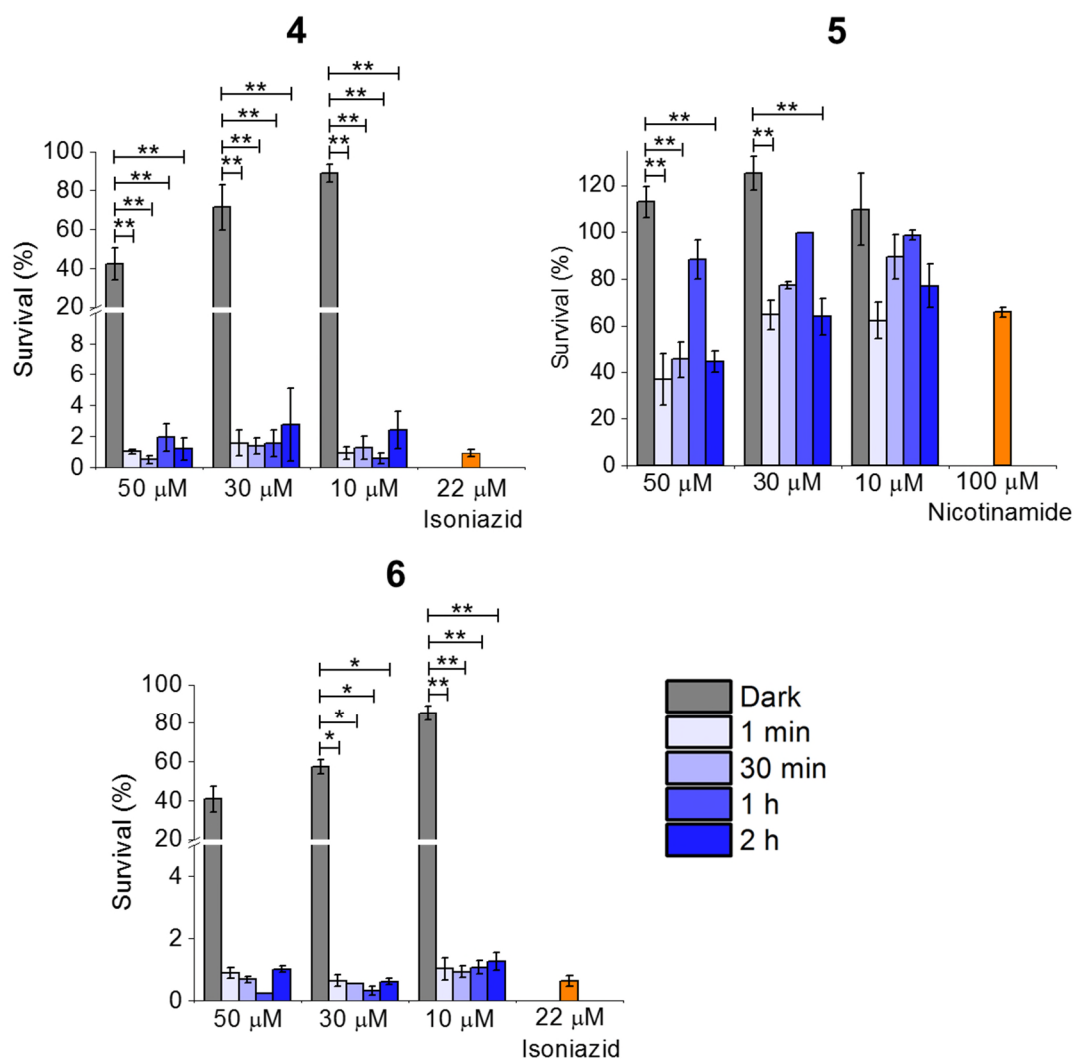


**Figure 5.9.** Activity of *cis*-[Ru(bpy)<sub>2</sub>(INH)<sub>2</sub>][PF<sub>6</sub>]<sub>2</sub> (**4**), *cis*-[Ru(bpy)<sub>2</sub>(NA)<sub>2</sub>][PF<sub>6</sub>]<sub>2</sub> (**5**) and *cis*-[Ru(phen)<sub>2</sub>(INH)<sub>2</sub>][PF<sub>6</sub>]<sub>2</sub> (**6**) against *M. smegmatis* when incubated in the dark (grey bars) and photoirradiated (1 min – 2 h displayed in blue colour gradient) using the 96-array blue LED ( $\lambda_{irr} = 465$  nm, 20 mW cm<sup>-2</sup>) at 298 K. *P* values were calculated by comparing the light samples to the dark samples and are labelled as follows,  $p \leq 0.05 = *$ ,  $p \leq 0.01 = **$ .

The survival for each complex at each photoirradiation time point was compared to the light control in the absence of complex, while the survival for each complex in the dark was compared to the dark control in the absence of complex to calculate the survival (%). For *cis*-[Ru(bpy)<sub>2</sub>(INH)<sub>2</sub>][PF<sub>6</sub>]<sub>2</sub> (**4**) in the dark, the survival of *M. smegmatis* increased at lower concentrations of complex, with survival of 42%, 71% and 89% for 50  $\mu$ M, 30  $\mu$ M and 10  $\mu$ M, respectively. The same trend was observed for *cis*-[Ru(phen)<sub>2</sub>(INH)<sub>2</sub>][PF<sub>6</sub>]<sub>2</sub> (**6**) in the dark, with survival of 41%, 57% and 85% for 50  $\mu$ M, 30  $\mu$ M and 10  $\mu$ M respectively. For *cis*-[Ru(bpy)<sub>2</sub>(NA)<sub>2</sub>][PF<sub>6</sub>]<sub>2</sub> (**5**) in the dark, the survival was > 100% at all complex concentrations.

The survival after 1 min, 30 min, 1 h and 2 h photoirradiation for complex **4** was < 4% at all complex concentrations, and similarly for complex **6** was < 2%. There appears to be no trend between irradiation time and survival for complexes **4** and **6**. The monodentate ligand for **4** and **6** is isoniazid (INH) and at 22  $\mu$ M produced a survival of < 2%. This is the minimum inhibitory concentration (MIC) for isoniazid, comparable to literature values (*c.f.* 29  $\mu$ M).<sup>14</sup> For complex **5** the general trend observed for each photoirradiation time point was increased survival with decreasing complex concentration, e.g after 2 h photoirradiation the survival was 45%, 64% and 77% for 50  $\mu$ M, 30  $\mu$ M and 10  $\mu$ M respectively. However, the survival of bacteria for all complex concentrations of **5** and all time points of photoirradiation was > 30%. Interestingly for each complex concentration of **5**, the survival of bacteria generally increased in the order of 1 min < 2 h < 30 min < 1 h. The monodentate ligand for **5** is nicotinamide (NA) and at a concentration of 100  $\mu$ M produces a survival of 66%. The minimum inhibitory concentration (MIC) was determined for *cis*-[Ru(bpy)<sub>2</sub>(INH)<sub>2</sub>][PF<sub>6</sub>]<sub>2</sub> (**4**) and *cis*-[Ru(phen)<sub>2</sub>(INH)<sub>2</sub>][PF<sub>6</sub>]<sub>2</sub> (**6**) when photoirradiated for 1 min, see Figure 5.10. For both complexes **4** and **6** in the dark at

complex concentrations of 0.5  $\mu\text{M}$  – 10  $\mu\text{M}$  the survival was  $> 60\%$ . The MIC when photoirradiated for 1 min was found to be 4  $\mu\text{M}$  for complex **4** and 8  $\mu\text{M}$  for complex **6**.

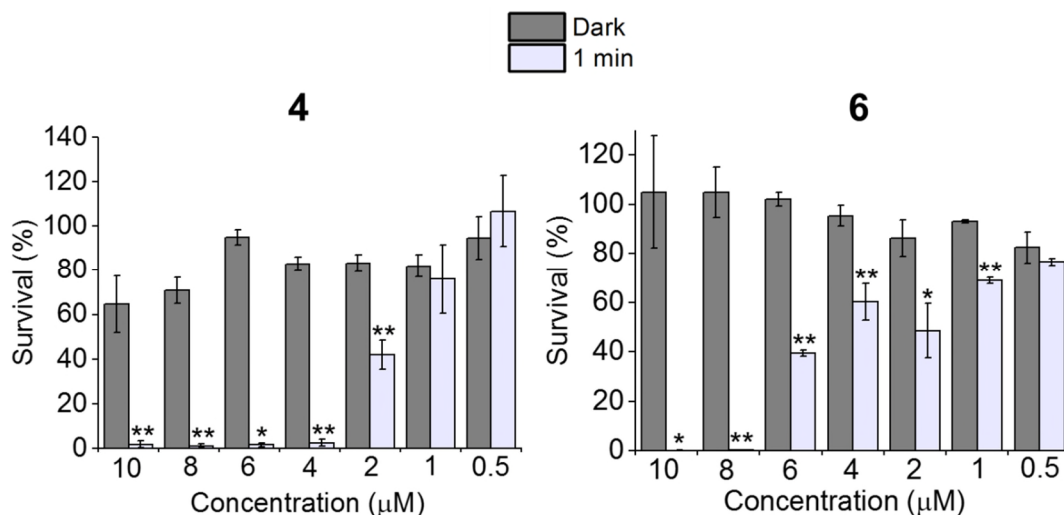


**Figure 5.10.** Activity of *cis*-[Ru(bpy)<sub>2</sub>(INH)<sub>2</sub>][PF<sub>6</sub>]<sub>2</sub> (**4**) (left) and *cis*-[Ru(phen)<sub>2</sub>(INH)<sub>2</sub>][PF<sub>6</sub>]<sub>2</sub> (**6**) (right) against *M. smegmatis* when incubated in the dark (grey bars) and photoirradiated for 1 min (light blue bar) using the 96-array blue LED ( $\lambda_{\text{irr}} = 465 \text{ nm}$ ,  $20 \text{ mW cm}^{-2}$ ) at 298 K. *P* values were calculated by comparing the light samples to the dark samples and are labelled as follows,  $p \leq 0.05 = *$ ,  $p \leq 0.01 = **$ .

#### 5.3.4.2. Photoirradiation using the 32-array multi-coloured LED

Initially *M. smegmatis* was photoirradiated for 30 min using the 32-array multi-coloured LED ( $\lambda_{\text{irr}} = 465 \text{ nm}$ , 520 nm, 589 nm and 625 nm,  $5 \text{ mW cm}^{-2}$ ) at 298 K in the absence of any complex. The growth of each sample was monitored over a 72 h period at 310 K and was compared to the dark control to calculate the survival (%), see Figure 5.11. The survival of *M. smegmatis* when exposed to blue (465 nm), green (520 nm), yellow (589 nm) and red (625 nm) light was  $> 85\%$  in all cases.

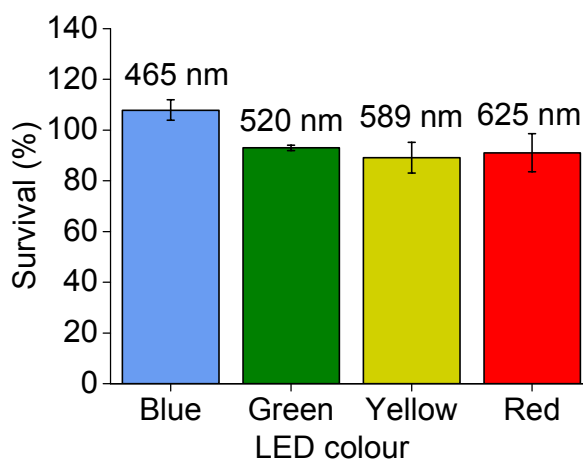


**Figure 5.11.** Photoirradiation of *M. smegmatis* using the 32-array multi-coloured LED ( $\lambda_{\text{irr}} = 465 \text{ nm}$ ,  $520 \text{ nm}$ ,  $589 \text{ nm}$  and  $625 \text{ nm}$ ,  $5 \text{ mW cm}^{-2}$ ) at  $298 \text{ K}$  for  $30 \text{ min}$ .  $P$  values were calculated by comparing the light samples to the dark control and are labelled as follows,  $p \leq 0.05 = *$ ,  $p \leq 0.01 = **$ .

The complexes *cis*-[Ru(bpy)<sub>2</sub>(INH)<sub>2</sub>][PF<sub>6</sub>]<sub>2</sub> (**4**) and *cis*-[Ru(phen)<sub>2</sub>(INH)<sub>2</sub>][PF<sub>6</sub>]<sub>2</sub> (**6**) were incubated with *M. smegmatis* in the dark for  $1 \text{ h}$  at  $298 \text{ K}$  and the samples were photoirradiated for  $30 \text{ min}$  at  $298 \text{ K}$ . The survival for each complex at each photoirradiation wavelength was compared to the light control in the absence of complex to calculate the survival (%), see Figure 5.12.

For both complexes **4** and **6**, the general trend is increased survival as the wavelength of photoirradiation increased. For complex **4**, the survival when exposed to blue, green, yellow and red light was  $0.5\%$ ,  $4\%$ ,  $94\%$  and  $96\%$  respectively, while for complex **6** was  $0.6\%$ ,  $1\%$ ,  $81\%$  and  $101\%$  respectively. The dark survival for both complex **4** and **6** was  $> 80\%$ .

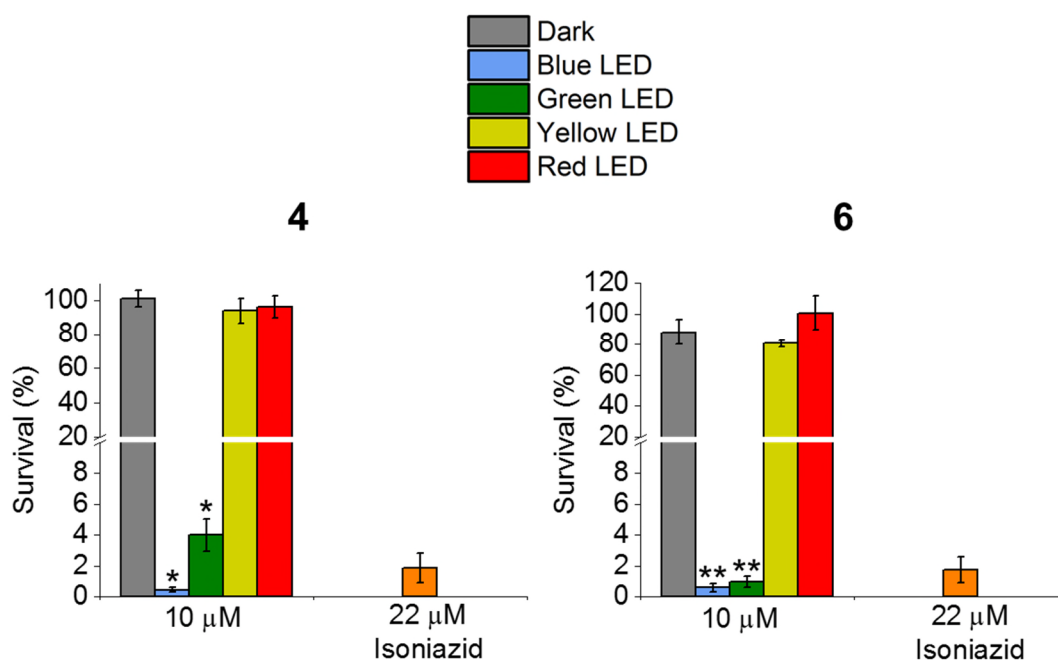


**Figure 5.12.** Activity of *cis*-[Ru(bpy)<sub>2</sub>(INH)<sub>2</sub>][PF<sub>6</sub>]<sub>2</sub> (**4**) and *cis*-[Ru(phen)<sub>2</sub>(INH)<sub>2</sub>][PF<sub>6</sub>]<sub>2</sub> (**6**) against *M. smegmatis* when incubated in the dark (grey bars) using the 32-array multi-coloured LED ( $\lambda_{\text{irr}} = 465 \text{ nm}$ ,  $520 \text{ nm}$ ,  $589 \text{ nm}$  and  $625 \text{ nm}$ ,  $5 \text{ mW cm}^{-2}$ ) at  $298 \text{ K}$  for  $30 \text{ min}$ .  $P$  values were calculated by comparing the light samples to the dark samples and are labelled as follows,  $p \leq 0.05 = *$ ,  $p \leq 0.01 = **$ .

### 5.3.5. Baclight™ assay with *M. smegmatis*

The principle of the Baclight™ assay is that the dye SYTO 9 enters and binds to nucleic acids (observes fluorescence,  $\lambda_{\text{em}} = 530 \text{ nm}$ ,  $\lambda_{\text{ex}} = 470 \text{ nm}$ ) of all bacteria independent of membrane integrity, while ethidium bromide only enters and binds to nucleic acids (observes fluorescence,  $\lambda_{\text{em}} = 630 \text{ nm}$ ,  $\lambda_{\text{ex}} = 470 \text{ nm}$ ) of bacteria which have damaged membranes. Therefore the ratio between green and red fluorescence ( $F_{530 \text{ nm}}/F_{630 \text{ nm}}$ ) can be used to investigate the membrane integrity.

The Baclight™ assay was performed with *M. smegmatis* in the presence of *cis*-[Ru(bpy)<sub>2</sub>(INH)<sub>2</sub>][PF<sub>6</sub>]<sub>2</sub> (**4**) and *cis*-[Ru(phen)<sub>2</sub>(INH)<sub>2</sub>][PF<sub>6</sub>]<sub>2</sub> (**6**) both in the dark and after photoirradiation for  $1 \text{ min}$  with 96-array blue LED ( $\lambda_{\text{irr}} = 465 \text{ nm}$ ,  $20 \text{ mW cm}^{-2}$ ), see Figure 5.13. For the purpose of the calibration graph, intact membranes are

associated with “live cells” while damaged membranes are associated with “dead” cells.

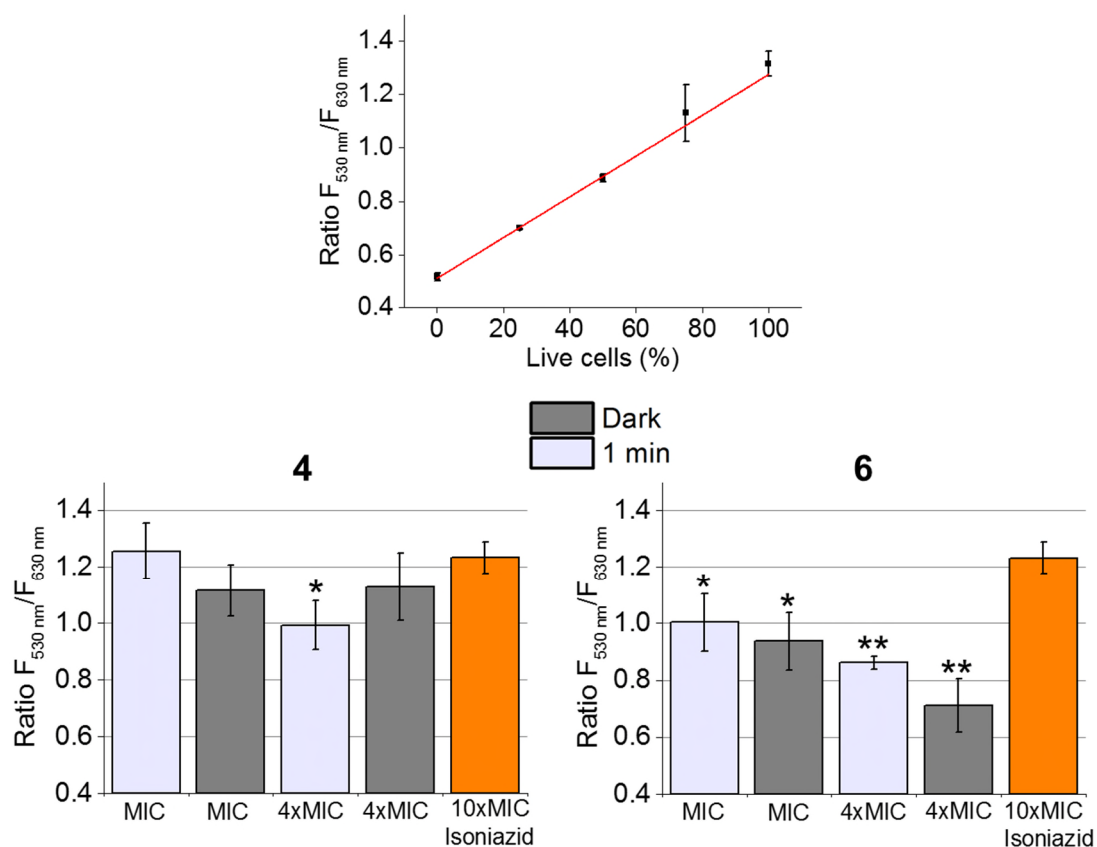


**Figure 5.13.** Calibration graph of percentage live cells verses  $F_{530\text{ nm}}/F_{630\text{ nm}}$  ratio (top) and  $F_{530\text{ nm}}/F_{630\text{ nm}}$  ratios obtained after various concentrations of *cis*-[Ru(bpy)<sub>2</sub>(INH)<sub>2</sub>][PF<sub>6</sub>]<sub>2</sub> (4) (bottom left) and *cis*-[Ru(phen)<sub>2</sub>(INH)<sub>2</sub>][PF<sub>6</sub>]<sub>2</sub> (6) (bottom right) were exposed to *M. smegmatis* when incubated in the dark (grey bars) and photoirradiated for 1 min (light blue bars) using the 96-array blue LED ( $\lambda_{\text{irr}} = 465\text{ nm}$ ,  $20\text{ mW cm}^{-2}$ ) at 298 K. *P* values were calculated by comparing the light and dark samples to the 10xMIC isoniazid (220  $\mu\text{M}$ ) control and are labelled as follows,  $p \leq 0.05 = *$ ,  $p \leq 0.01 = **$ .

Isoniazid (INH) was used as a positive control for no membrane damage, and at a concentration of 10xMIC (220  $\mu\text{M}$ ) an  $F_{530\text{ nm}}/F_{630\text{ nm}}$  ratio of 1.23 was observed. For complex 4 at both concentrations (MIC is 4  $\mu\text{M}$  and 4xMIC is 16  $\mu\text{M}$ ) in the dark and after photoirradiation, the  $F_{530\text{ nm}}/F_{630\text{ nm}}$  ratio was  $\geq 1$ . Interestingly only the photoirradiated 4xMIC sample was significantly different from the isoniazid positive



control with an  $F_{530\text{ nm}}/F_{630\text{ nm}}$  ratio of 0.99. For complex **6** at both concentrations (MIC is 8  $\mu\text{M}$  and 4xMIC is 32  $\mu\text{M}$ ) in the dark and once photoirradiated, the  $F_{530\text{ nm}}/F_{630\text{ nm}}$  ratio is  $\leq 1$  and in all cases the ratios were significantly different to the isoniazid positive control. At MIC concentration, the ratio of  $F_{530\text{ nm}}/F_{630\text{ nm}}$  in the dark and once photoirradiated was  $\sim 1.0$  while at 4xMIC concentration was  $\sim 0.8$ . In general for each complex there was no difference in  $F_{530\text{ nm}}/F_{630\text{ nm}}$  ratio between dark and photoirradiated at each concentration.

## 5.4. Discussion

### 5.4.1. Light sources

A further description of all the light sources used for this work can be found in Chapter 2. The blue LED ( $\lambda_{\text{irr}} = 463\text{ nm}$ ,  $50\text{ mW cm}^{-2}$ ) was sufficient for photoirradiating a sample in a cuvette or an NMR tube as the light beam was uniformly distributed over the entire sample area ( $\sim 6\text{ cm} \times 1\text{ cm}$ ). However this would not be the case for a 96-well plate, as the sample area was much larger ( $\sim 11\text{ cm} \times 7.5\text{ cm}$ ). Therefore a 96-array blue LED was developed ( $\lambda_{\text{irr}} = 465\text{ nm}$ ,  $20\text{ mW cm}^{-2}$ ) in order to photoirradiate samples in a 96-well plate. In this way, each well receive a uniformly distributed dose of light. This was further aided by placing a black 96-well plate with a glass bottom on top of the LED's. This not only created a "channel" for the light to pass through and thus avoided light leaking through into the next well, but it also aided with aseptic working as the glass acts as a protective barrier so the bacteria never come into contact with the LED's. A heat sink was added to the system in order to reduce the transfer of heat produced by the LED's to the samples. Heat maps of the black 96-well plate that would contain the bacteria after photoirradiation aided assessment of the effectiveness of the heat sink. After 2 h 30 min of photoirradiation, the temperature of the black 96-well plate did not exceed 315 K. This temperature should not hinder the growth of *M.*

*smegmatis* as the bacteria can grow at 298 K and up to 323 K.<sup>15</sup> A 32-array multi-coloured LED ( $\lambda_{\text{irr}} = 465 \text{ nm}, 520 \text{ nm}, 589 \text{ nm}$  and  $625 \text{ nm}$ ,  $5 \text{ mW cm}^{-2}$ ) was also developed in order to screen for the optimal wavelength of activation. The system was used in an analogous manner to the 96-array blue LED. A heat sink was not necessary for this setup, as the LED's are 4 times less powerful than those in the 96-array blue LED setup and thus heat production should be negligible.

#### 5.4.2. Photoirradiation in the presence of 9-ethylguanine and L-cysteine

L-Cysteine is an amino acid and 9-ethylguanine is a guanine nucleobase. Both are building blocks of biomolecules such as proteins (L-cysteine) and DNA (guanine). If a metal complex can bind to either, it may disrupt the biological action of either proteins or DNA *in vitro*.

The complex *cis*-[Ru(bpy)<sub>2</sub>(INH)<sub>2</sub>][PF<sub>6</sub>]<sub>2</sub> (**4**) in aqueous solution (4 mM, D<sub>2</sub>O) was photoirradiated with a blue LED ( $\lambda_{\text{irr}} = 463 \text{ nm}$ ,  $50 \text{ mW cm}^{-2}$ ) in the presence of L-cysteine (Cys) and 9-ethylguanine (9-EtG) and the reaction followed by <sup>1</sup>H-NMR at 298 K. In the absence of Cys and 9-EtG, after 50 min photoirradiation the photoproduct *cis*-[Ru(bpy)<sub>2</sub>(INH)(D<sub>2</sub>O)]<sup>2+</sup> had formed, characterised by the INH free ligand peaks (found at 8.68 ppm and 7.69 ppm) and a new set of 18 peaks corresponding to the Ru(II) photoproduct. Interestingly when **4** was photoirradiated for 50 min in the presence of L-cysteine the photoadduct *cis*-[Ru(bpy)<sub>2</sub>(INH)(Cys)]<sup>2+</sup> was not formed. Even after 24 h dark incubation at 298 K, L-cysteine did not bind as was evident from the lack of changes in the <sup>1</sup>H-NMR resonances for the photoproduct. Conversely when **4** was photoirradiated for 50 min in the presence of 9-EtG, a new set of peaks (species A) occurred which can be attributed to the photoadduct *cis*-[Ru(bpy)<sub>2</sub>(INH)(9-EtG)]<sup>2+</sup>, see Figure 5.5. The H<sub>8</sub> resonance of 9-ethylguanine shifted upfield from 7.81 ppm to 6.84 ppm as a result of binding to the metal. The percentage

of binding was low (16%) which can be attributed to the bulky nature of the 9-EtG ligand and the photoproduct  $cis-[Ru(bpy)_2(INH)(D_2O)]^{2+}$ . The bulky nature of 9-EtG has been noted previously, for example reacting  $cis-[Ru(bpy)_2(H_2O)_2]^{2+}$  with an excess of 9-EtG in aqueous solution at 310 K gives only the mono-adduct  $cis-[Ru(bpy)_2(9-EtG)(H_2O)]^{2+}$ .<sup>16</sup> In order to form bis-adducts vigorous conditions are needed, such as an ethanol reflux for an extended period of time.<sup>17</sup> After the resulting photoirradiation mixture of **4** and 9-EtG was incubated at 298 K in the dark for 24 h, the bound 9-EtG H<sub>8</sub> resonance at 6.84 ppm decreased and a new bound 9-EtG H<sub>8</sub> resonance increased downfield at 7.29 ppm (species B). This new product is related to the photoproduct  $cis-[Ru(bpy)_2(INH)(9-EtG)]^{2+}$ , which was detected by HR-MS, see Figure 5.6. In fact no other photoadduct was found in HR-MS, such as  $cis-[Ru(bpy)_2(9-EtG)_2]^{2+}$  or  $cis-[Ru(bpy)_2(9-EtG)(H_2O)]^{2+}$ . The presence of two bound 9-EtG H<sub>8</sub> peaks is due to the high energy rotation barrier of the 9-EtG ligand and therefore is a result of the atropisomers (species A and B) that can be formed (see Chapter 3 for in depth discussion about the concept of atropisomerism due to hindered rotation). It has been noted previously that in complexes of the type  $cis-[Ru(bpy)_2(9-EtG)(X)]^{n+}$  and  $cis-[Ru(bpy)_2(9-MeG)_2]^{2+}$ , where X is either Cl (n = 1) or H<sub>2</sub>O (n = 2) and 9-MeG is 9-methylguanine, rotation of the purine moieties does not occur because of their bulky nature.<sup>16-17</sup> Interestingly in the case of  $cis-[Ru(bpy)_2(9-MeG)_2]^{2+}$ , due to the different orientations of each MeG unit, there are two H<sub>8</sub> proton resonances that are separated by ~ 1.2 ppm (at 8 ppm and 6.8 ppm).<sup>17</sup> This correlates well with data obtained above. It is hypothesised that the first resonance seen at 6.84 ppm is from the kinetic atropisomer (species A) and the second resonance seen at 7.29 ppm after a longer period of time (24 h dark incubation at 298 K) is from the thermodynamic atropisomer (species B), see Figure 5.14.

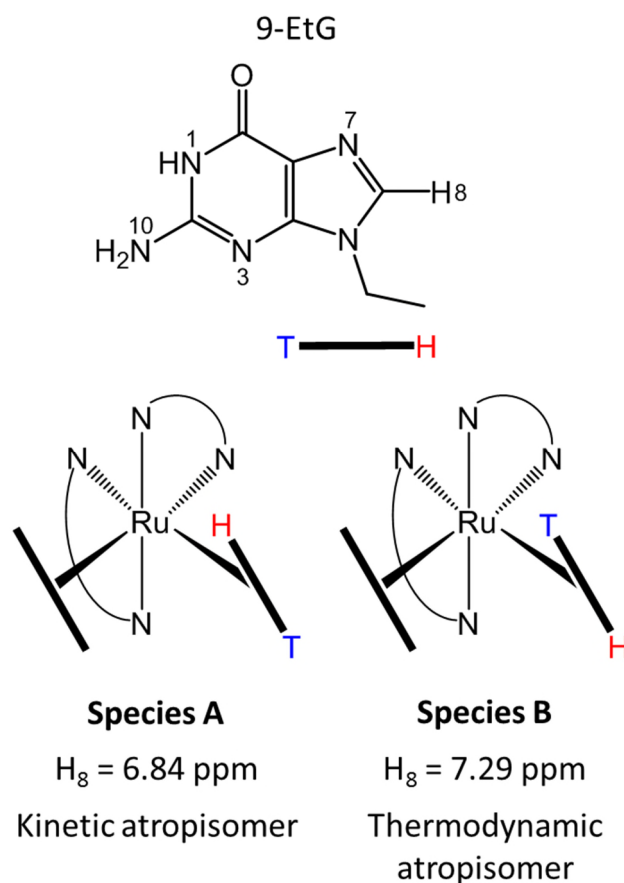


**Figure 5.14.** Diagram of the proposed *cis*-[Ru(bpy)<sub>2</sub>(INH)(9-EtG)]<sup>2+</sup> atropisomers.

It is thought that in the kinetic atropisomer the bulky “tail” portion of 9-EtG is placed in between the bipyridyl rings, as this orientation is more favourable sterically. In the kinetic atropisomer the H<sub>8</sub> will be shielded by INH ring and thus is upfield-shifted. In the thermodynamic atropisomer it is hypothesised that the carbonyl oxygen in 9-EtG interacts favourably with the  $\pi$ -system of the INH ligand. Previously it has been found that such interaction between carbonyl oxygen and an aromatic  $\pi$ -system is enthalpically favourable.<sup>16, 18-19</sup> Furthermore in the case of *cis*-[Ru(azpy)<sub>2</sub>(9-EtG)(H<sub>2</sub>O)]<sup>2+</sup>, where azpy is 2-phenylazopyridine, an intramolecular hydrogen bond between the carbonyl oxygen of 9-EtG and H<sub>2</sub>O stabilized the conformation.<sup>20</sup> In order

to confirm the presence of atropisomers, variable temperature  $^1\text{H}$ -NMR and NOESY studies would need to be performed to investigate the rotation of the 9-EtG ligand.

#### 5.4.3. Photoactivity against *E. coli* and *B. subtilis*

The complex *cis*-[Ru(bpy) $_2$ (INH) $_2$ ][PF $_6$ ] $_2$  (**4**) was incubated with *E. coli* and *B. subtilis* in the dark for 1 h at 298 K and subsequently photoirradiated with the 96-array blue LED ( $\lambda_{\text{irr}} = 465 \text{ nm}$ ,  $20 \text{ mW cm}^{-2}$ ) for 2 h 20 min at 298 K. In the case of *E. coli* no activity was found in the dark or once photoirradiated at all complex concentrations (10  $\mu\text{M}$  – 100  $\mu\text{M}$ ), see Figure 5.7. The monodentate ligand of **4** is isoniazid (INH) and at a concentration of 400  $\mu\text{M}$  has no activity. When complex **4** was incubated with *B. subtilis* activity was observed only at 200  $\mu\text{M}$  and 100  $\mu\text{M}$  when photoirradiated, see Figure 5.7. Interestingly against *B. subtilis*, isoniazid (400  $\mu\text{M}$ ) has no effect. The activity of **4** in *B. subtilis* could be due to a) the activity of the Ru(II) photoproducts or b) the complex (**4**) may aid isoniazid to become active (potentially by enhanced uptake), or both may have an effect.

The reason for the difference in activity of **4** against *E. coli* and *B. subtilis* is most likely due to the differences in the bacterial cell walls. Gram-positive bacteria (i.e. *B. subtilis*) are generally permeable to a variety of antibiotics due to a porous peptidoglycan layer in its cell wall.<sup>21</sup> Furthermore, the presence of negatively-charged teichoic acids in the cell wall may facilitate the uptake of positively charged antibiotics into the cell envelope.<sup>22</sup> Gram-negative bacteria (i.e. *E. coli*) have a more complex cell envelope consisting of an outer membrane as well as a peptidoglycan layer. The outer membrane is composed of lipopolysaccharides and phospholipids, and molecular diffusion across this barrier is very hindered.<sup>22</sup> Porins offer another pathway for an antimicrobial compound to gain entry through the outer membrane, however they only permit molecules with a mass of <600 Da.<sup>22</sup> Interestingly polycationic species are very

effective at killing gram-negative bacteria as they can alter the outer membrane.<sup>9, 23</sup> Therefore it is hypothesised that *cis*-[Ru(bpy)<sub>2</sub>(INH)<sub>2</sub>][PF<sub>6</sub>]<sub>2</sub> (**4**) is not active in *E. coli* due to reduced uptake, however uptake experiments need to be performed to confirm this.

#### 5.4.4. Photoactivity against *M. smegmatis*

##### 5.4.4.1. Effect of blue light alone on survival of *M. smegmatis*

Prior to incubation of the photoactive complexes with *M. smegmatis*, an assessment of the effect of light on the growth of the bacteria was performed. When the bacteria were photoirradiated using the 96-array blue LED ( $\lambda_{\text{irr}} = 465 \text{ nm}$ ,  $20 \text{ mW cm}^{-2}$ ) at 298 K, the bacterial survival increased with increasing photoirradiation time (e.g. bacterial survival was 43% after 1 min and 94% after 2 h), see Figure 5.8. This was very unusual as in the literature there are many examples of blue light (with a wavelength of 400 nm - 470 nm and powers ranging from  $20 \text{ mW/cm}^2$  –  $100 \text{ mW/cm}^2$ ) having a bactericidal effect against bacteria such as methicillin-resistant *Staphylococcus aureus* (MRSA), *Propionibacterium acnes* (the causative agent of acnes), *Pseudomonas aeruginosa*, *Helicobacter pylori* and *Streptococcus mutans* (oral bacteria) both *in vitro* and *in vivo*.<sup>24-32</sup> In all of the aforementioned cases, increasing the time of photoirradiation caused a decrease in bacterial survival, contrary to the results obtained in this work for *M. smegmatis*. Interestingly, in one instance in the literature when *M. smegmatis* was photoirradiated with high doses of 405 nm blue light, the bacteria were not effectively killed (the kill extent decreased from 97% for  $150 \text{ J/cm}^2$  light dose to 61% for  $180 \text{ J/cm}^2$  light dose).<sup>33</sup> The reason for this was unknown. This is more consistent with the results found in this work. It is hypothesised that low doses of blue light in *M. smegmatis* are bactericidal, while at higher doses of blue light photoreactivation occurs whereby a repair system is utilised. Blue light ( $> 400 \text{ nm}$ )

may be harmful to bacteria due to the production of reactive oxygen species from endogenous photosensitisers, such as porphyrin containing cytochrome.<sup>34</sup> However when *Mycobacteria*, including *mycobacterium smegmatis* and *mycobacterium tuberculosis*, have been exposed to UV-irradiation and subsequently photoirradiated with white light, the bacteria photoreactivate and the growth of bacteria is restored (the mechanism may involve a photoreactivating enzyme, however the identity of this is unknown).<sup>35-39</sup> The degree of photoreactivation increases with increasing dose of white light, which correlates with the results obtained in this work where increasing the dose of blue light promotes a higher survival.

#### 5.4.4.2. Photoactivity of complexes against *M. smegmatis*

The complexes *cis*-[Ru(bpy)<sub>2</sub>(INH)<sub>2</sub>][PF<sub>6</sub>]<sub>2</sub> (**4**), *cis*-[Ru(bpy)<sub>2</sub>(NA)<sub>2</sub>][PF<sub>6</sub>]<sub>2</sub> (**5**) and *cis*-[Ru(phen)<sub>2</sub>(INH)<sub>2</sub>][PF<sub>6</sub>]<sub>2</sub> (**6**) were tested against *M. smegmatis* in the dark and photoirradiated with the 96-array blue LED ( $\lambda_{\text{irr}} = 465 \text{ nm}$ ,  $20 \text{ mW cm}^{-2}$ ) for 1 min, 30 min, 1 h and 2 h. In the dark, complexes **4** and **6** were most active. As the concentration of the complexes increased, the survival of bacteria decreased, owing to the dark toxicity of the complexes, see Figure 5.9. For both complexes at a concentration of 50  $\mu\text{M}$  the survival of the bacteria was  $\sim 40\%$  while at 10  $\mu\text{M}$  was  $\sim 90\%$ . Complex **5** showed no dark toxicity at all concentrations ranging from 10  $\mu\text{M}$  – 50  $\mu\text{M}$ . The reason for this dark toxicity could be due to the presence of an active ligand, which in the case of **4** and **6** is isoniazid (INH). The hydrazide group of isoniazid is activated by an enzyme called KatG, see Chapter 1 for an in depth description of isoniazid activation. Since the hydrazide portion of isoniazid is still exposed once INH is bound to ruthenium, it may still be activated by the enzyme to a small extent.

Once complexes **4** and **6** were photoirradiated with blue light, the activity of the complexes increased dramatically. For complexes **4** and **6** at concentrations of 10  $\mu\text{M}$

– 50  $\mu\text{M}$ , the survival of the bacteria was  $< 4\%$  and  $< 2\%$  respectively when photoirradiated for 1 min, 30 min, 1 h and 2 h, see Figure 5.9. This is comparable to the survival ( $< 2\%$ ) when the bacteria were exposed to the minimum inhibitory concentration (MIC) of isoniazid (22  $\mu\text{M}$ ). The MIC for complexes **4** and **6** when photoirradiated for 1 min was found to be 4  $\mu\text{M}$  (survival in dark was  $\sim 80\%$ ) and 8  $\mu\text{M}$  (survival in dark was  $\sim 100\%$ ), respectively, see Figure 5.10. This dramatic increase in activity from dark exposure to light exposure suggests that *in vitro* isoniazid can be released from the ruthenium(II) centre by at least 1 min blue light photoirradiation, and that isoniazid retains its activity. Interestingly the MIC for **4** and **6** after 1 min photoirradiation is lower than that for isoniazid; 5.5x lower in the case of **4** and 2.75x lower in the case of **6**. This could be due to, a) the synergism between the damaging 1 min blue photoirradiation and the released isoniazid ligand, b) the synergism between the active Ru(II) photoproducts and the released isoniazid ligand, c) the increased uptake of the isoniazid ligand into the bacteria as a result of the metal complex, or a mixture of (a), (b) and (c).

The survival of bacteria for all complex concentrations of **5** and all time points of photoirradiation was  $> 30\%$ , thus complex **5** is much less active than complexes **4** and **6** with an MIC  $> 50 \mu\text{M}$ . This is due to the reduced activity of the monodentate ligand nicotinamide (NA); at a concentration of 100  $\mu\text{M}$  a survival of 66% was observed. For **5** at a complex concentration 50  $\mu\text{M}$ , after 2 h photoirradiation the survival of bacteria was found to be 45%, which is 21% lower than the survival for the maximum amount of ligand than can be released (i.e. 100  $\mu\text{M}$ ). This supports the hypothesis that the Ru(II) centre is contributing to the activity (either by increasing the uptake of ligand or by production of active photoproducts), as at this time point of photoirradiation the light alone does not affect the survival of bacteria.



Complexes **4** and **6** were photoirradiated in the presence of *M. smegmatis* using the 32-array multi-coloured LED ( $\lambda_{\text{irr}} = 465 \text{ nm}, 520 \text{ nm}, 589 \text{ nm}$  and  $625 \text{ nm}, 5 \text{ mW cm}^{-2}$ ) for 30 min to investigate wavelength dependence on the activity. Interestingly for this light source, all wavelengths did not harm the bacteria; survival was  $> 85\%$  in all cases, see Figure 5.11. This reduced antibacterial effect is due to the reduction in power of the light source. For complex **4** the antibacterial activity with different wavelengths decreases in the order of blue  $>$  green  $>$  yellow  $\approx$  red, and for complex **6** blue  $\approx$  green  $>$  yellow  $>$  red. This general trend correlates well with results in Chapter 4, where for complexes **4** and **6** photoactivity decreases in the order blue  $>$  green  $>$  yellow  $>$  red. At longer wavelengths of photoirradiation, the photoactivity of the complex is reduced, thus the antibacterial activity of the complex decreases.

#### 5.4.4.3. *Baclight*<sup>TM</sup> assay

The *Mycobacterium* cell wall contains an array of mycolic acids and glycolipids that causes the membrane to have a low fluidity, which makes it difficult for antibiotics to diffuse through the membrane.<sup>22</sup> It is proposed that isoniazid enters the cell by passive diffusion.<sup>40</sup> However a drug does not necessarily need to diffuse through the cell wall and enter to the bacterium to cause damage. For example, antibacterial agents such as vancomycin bind to targets in the cell wall, and daptomycin forms harmful pores in the membrane.<sup>41</sup> The *Baclight*<sup>TM</sup> assay can be used to assess if an antibacterial agent is causing membrane damage by forming pores. Isoniazid is selective and inhibits an enzyme (InhA) that is responsible for cell wall mycolic acid synthesis, as a result it can be used as a positive control in *Baclight*<sup>TM</sup> assay as it affects a specific pathway, and does not permeabilize the membrane by forming pores.<sup>42</sup> As described in Section 5.2.6., the ratio between green and red fluorescence ( $F_{530 \text{ nm}}/F_{630 \text{ nm}}$ ) can be used to investigate the membrane integrity. By constructing an *M. smegmatis* calibration

graph, bacteria with no membrane damage exhibited a ratio of  $\sim 1.2$ , while bacteria with damaged membranes exhibited a value of  $\sim 0.5$ , see Figure 5.14. For 10xMIC concentration of isoniazid (220  $\mu\text{M}$ ) the  $F_{530\text{ nm}}/F_{630\text{ nm}}$  ratio was 1.23, consistent with no membrane damage. For complex *cis*-[Ru(bpy)<sub>2</sub>(INH)<sub>2</sub>][PF<sub>6</sub>]<sub>2</sub> (**4**) at both MIC (4  $\mu\text{M}$ ) and 4xMIC (16  $\mu\text{M}$ ) in the dark and once photoirradiated with 96-array blue LED ( $\lambda_{\text{irr}} = 465\text{ nm}$ , 20 mW cm<sup>-2</sup>) for 1 min, the  $F_{530\text{ nm}}/F_{630\text{ nm}}$  ratio was  $\geq 1$ . This suggests for complex **4**, no/very little membrane damage occurs. For complex *cis*-[Ru(phen)<sub>2</sub>(INH)<sub>2</sub>][PF<sub>6</sub>]<sub>2</sub> (**6**) at both MIC (8  $\mu\text{M}$ ) and 4xMIC (32  $\mu\text{M}$ ) in the dark and once photoirradiated with 96-array blue LED for 1 min, the  $F_{530\text{ nm}}/F_{630\text{ nm}}$  ratio was  $\leq 1$ . Therefore complex **6** appears to damage the membrane by creating pores. Increasing the complex concentration resulted in more damage, i.e. lower  $F_{530\text{ nm}}/F_{630\text{ nm}}$  ratio. It is hypothesised that complex **6** enters the cell wall and forms pores because of its increased hydrophobicity (comparing complex **4** which has 2,2'-bipyridine and complex **6** which has 1,10-phenanthroline as the chelating ligand). Interestingly this membrane damage does not affect the MIC obtained for complex **6** when compared to complex **4**, as both complexes observe very similar MIC's.

## 5.5. Summary

The photobiological properties of complexes *cis*-[Ru(bpy)<sub>2</sub>(INH)<sub>2</sub>][PF<sub>6</sub>]<sub>2</sub> (**4**), *cis*-[Ru(bpy)<sub>2</sub>(NA)<sub>2</sub>][PF<sub>6</sub>]<sub>2</sub> (**5**) and *cis*-[Ru(phen)<sub>2</sub>(INH)<sub>2</sub>][PF<sub>6</sub>]<sub>2</sub> (**6**) were explored. The complex *cis*-[Ru(bpy)<sub>2</sub>(INH)<sub>2</sub>][PF<sub>6</sub>]<sub>2</sub> (**4**) did not bind to L-cysteine after formation of the photoproduct *cis*-[Ru(bpy)<sub>2</sub>(INH)H<sub>2</sub>O]<sup>2+</sup> by photoirradiating the sample with blue light, however binding occurred with 9-ethyguanine (9-EtG) to form the photoadduct *cis*-[Ru(bpy)<sub>2</sub>(INH)(9-EtG)]<sup>2+</sup>. The extent of binding was small ( $\sim 16\%$ ), however the binding was evident from <sup>1</sup>H-NMR and HR-MS data. Interestingly for *cis*-[Ru(bpy)<sub>2</sub>(INH)(9-EtG)]<sup>2+</sup>, two atropisomers were detected in solution. Due to the

bulky nature of 9-EtG there is a high energy rotation barrier for the 9-EtG ligand. One atropisomer formed instantly (kinetic atropisomer) and the other formed over time (thermodynamic atropisomer) as the complex was incubated in the dark for 24 h at 298 K. The complex *cis*-[Ru(bpy)<sub>2</sub>(INH)<sub>2</sub>][PF<sub>6</sub>]<sub>2</sub> (**4**) was inactive against *E. coli*, however it showed some activity once photoirradiated with blue light for 2 h 20 min against *B. subtilis* at concentrations of 100 µM and 200 µM. The complexes *cis*-[Ru(bpy)<sub>2</sub>(INH)<sub>2</sub>][PF<sub>6</sub>]<sub>2</sub> (**4**) and *cis*-[Ru(phen)<sub>2</sub>(INH)<sub>2</sub>][PF<sub>6</sub>]<sub>2</sub> (**6**) were found to be active against *M. smegmatis*, with MIC values of 4 µM and 8 µM respectively after 1 min photoirradiation with blue light. This was a 5.5 x and 2.75x increase in potency (for **4** and **6** respectively) when compared to the ligand, isoniazid, alone which has an MIC of 22 µM. The activity of the **4** and **6** was significantly reduced in the dark, where survival of the bacteria is > 80% at the MIC value, showing that the active ligand (isoniazid) had successfully been released *in vitro* after photoirradiation with blue light. Blue light (463 nm) was the optimum wavelength for maximum activity for both **4** and **6**, while the complexes were not active once photoirradiated with red light. The complex *cis*-[Ru(phen)<sub>2</sub>(INH)<sub>2</sub>][PF<sub>6</sub>]<sub>2</sub> (**6**) forms pores in the cell wall of *M. smegmatis*, while *cis*-[Ru(bpy)<sub>2</sub>(INH)<sub>2</sub>][PF<sub>6</sub>]<sub>2</sub> (**4**) does not, as detected by the BacLight™ assay. This may be due to the increased hydrophobicity of **6** when compared to **4**.

## 5.6. References

1. Kilah, N. L.; Meggers, E. *Aust. J. Chem.*, **2012**, 65 (9), 1325-1332.
2. Dwyer, F. P.; Reid, I. K.; Shulman, A.; Laycock, G. M.; Dixon, S. *Aust. J. Exp. Biol. Med.*, **1969**, 47 (2), 203-218.
3. Novakova, O.; Kasparkova, J.; Vrana, O.; van Vliet, P. M.; Reedijk, J.; Brabec, V. *Biochemistry*, **1995**, 34 (38), 12369-12378.

4. Grover, N.; Welch, T. W.; Fairley, T. A.; Cory, M.; Thorp, H. H. *Inorg. Chem.*, **1994**, *33* (16), 3544-3548.
5. Wachter, E.; Heidary, D. K.; Howerton, B. S.; Parkin, S.; Glazer, E. C. *Chem. Commun.*, **2012**, *48* (77), 9649-51.
6. Sears, R. B.; Joyce, L. E.; Ojaimi, M.; Gallucci, J. C.; Thummel, R. P.; Turro, C. J. *Inorg. Biochem.*, **2013**, *121*, 77-87.
7. Garner, R. N.; Gallucci, J. C.; Dunbar, K. R.; Turro, C. *Inorg. Chem.*, **2011**, *50* (19), 9213-5.
8. Srishailam, A.; Kumar, Y.; Gabra, N. D.; Reddy, P. V.; Deepika, N.; Veerababu, N.; Satyanarayana, S. *J. Fluoresc.*, **2013**, *23* (5), 897-908.
9. Malik, Z.; Ladan, H.; Nitzan, Y. *J. Photochem. Photobiol., B*, **1992**, *14* (3), 262-6.
10. Gorle, A. K.; Feterl, M.; Warner, J. M.; Wallace, L.; Keene, F. R.; Collins, J. *G. Dalton Trans.*, **2014**, *43* (44), 16713-25.
11. Bolhuis, A.; Hand, L.; Marshall, J. E.; Richards, A. D.; Rodger, A.; Aldrich-Wright, J. *Eur. J. Pharm. Sci.*, **2011**, *42* (4), 313-7.
12. Altaf, M.; Miller, C. H.; Bellows, D. S.; O'Toole, R. *Tuberculosis*, **2010**, *90* (6), 333-337.
13. Ahmed, E.; Lamine, B. M.; Zouaoui, B.; Khedoudja, K.; Bouziane, A. *J. Biotechnol. Biomaterial.*, **2012**, *2* (3), 1-5.
14. Wube, A. A.; Bucar, F.; Hochfellner, C.; Blunder, M.; Bauer, R.; Hufner, A. *Eur. J. Med. Chem.*, **2011**, *46* (6), 2091-101.
15. Smith, M. C. M.; Sockett, R. E., *Genetic methods for diverse prokaryotes*. Academic Press: London, 1999; Vol. 29.

- 
16. van Vliet, P. M.; Haasnoot, J. G.; Reedijk, J. *Inorg. Chem.*, **1994**, 33 (9), 1934-1939.
  17. Zobi, F.; Hohl, M.; Zimmermann, I.; Alberto, R. *Inorg. Chem.*, **2004**, 43 (9), 2771-2772.
  18. Imai, Y. N.; Inoue, Y.; Nakanishi, I.; Kitaura, K. *J. Comput. Chem.*, **2009**, 30 (14), 2267-76.
  19. Thomas, K. A.; Smith, G. M.; Thomas, T. B.; Feldmann, R. J. *PNAS*, **1982**, 79 (16), 4843-4847.
  20. Hotze, A. C. G.; Velders, A. H.; Ugozzoli, F.; Biagini-Cingi, M.; Manotti-Lanfredi, A. M.; Haasnoot, J. G.; Reedijk, J. *Inorg. Chem.*, **2000**, 39 (17), 3838-3844.
  21. Ghuysen, J. M.; Hakenbeck, R., *Bacterial Cell Wall*. Elsevier: The Netherlands, 1994; Vol. 27.
  22. Franklin, T. J.; Snow, G. A., *Biochemistry and Molecular Biology of Antimicrobial Drug Action*. 6th edition ed.; Springer: New York, USA, 2005.
  23. Vaara, M.; Vaara, T. *Antimicrob. Agents Chemother.*, **1983**, 24 (1), 114-122.
  24. Kawada, A.; Aragane, Y.; Kameyama, H.; Sangen, Y.; Tezuka, T. *J. Dermatol. Sci.*, **2002**, 30 (2), 129-135.
  25. Elman, M.; Slatkine, M.; Harth, Y. *J. Cosmet. Laser Ther.*, **2003**, 5 (2), 111-117.
  26. Feuerstein, O. *Adv. Dent. Res.*, **2012**, 24 (2), 103-107.
  27. Dai, T.; Gupta, A.; Huang, Y.-Y.; Yin, R.; Murray, C. K.; Vrahas, M. S.; Sherwood, M. E.; Tegos, G. P.; Hamblin, M. R. *Antimicrob. Agents Chemother.*, **2013**, 57 (3), 1238-1245.
  28. Enwemeka, C. S.; Williams, D.; Hollosi, S.; Yens, D.; Enwemeka, S. K. *Laser Surg. Med.*, **2008**, 40 (10), 734-737.

- 
29. Bumah, V. V.; Masson-Meyers, D. S.; Cashin, S. E.; Enwemeka, C. S. *Photomed. Laser Surg.*, **2013**, *31* (11), 547-53.
  30. Tzung, T.-Y.; Wu, K.-H.; Huang, M.-L. *Photodermatol. Photoimmunol. Photomed.*, **2004**, *20* (5), 266-269.
  31. Ganz, R. A.; Viveiros, J.; Ahmad, A.; Ahmadi, A.; Khalil, A.; Tolkoff, M. J.; Nishioka, N. S.; Hamblin, M. R. *Laser Surg. Med.*, **2005**, *36* (4), 260-265.
  32. Ashkenazi, H.; Malik, Z.; Harth, Y.; Nitzan, Y. *FEMS Immunol. Med. Microbiol.*, **2003**, *35* (1), 17-24.
  33. Guffey, J. S.; Payne, W.; James, L.; Qian, Z. *Wounds*, **2013**, *25* (5), 131-135.
  34. Lubart, R.; Lipovski, A.; Nitzan, Y.; Friedmann, H. *Laser Ther.*, **2011**, *20* (1), 17-22.
  35. David, H. L.; Jones, W. D.; Newman, C. M. *Infect. Immun.*, **1971**, *4* (3), 318-319.
  36. Peccia, J.; Hernandez, M. *Appl. Environ. Microbiol.*, **2001**, *67* (9), 4225-4232.
  37. McCarthy, C. M.; Schaefer, J. O. *Appl. Microbiol.*, **1974**, *28* (1), 151-153.
  38. Dhople, A. M.; Nakamura, M. *Kurume Medical Journal*, **1977**, *24* (4), 217-221.
  39. Sellers, M. I.; Nakamura, R.; Tokunaga, T. *J. Gen. Virol.*, **1970**, *7* (3), 233-47.
  40. Bardou, F.; Raynaud, C.; Ramos, C.; Laneelle, M. A.; Laneelle, G. *Microbiology*, **1998**, *144* (Pt 9), 2539-44.
  41. Mason, B.; Parker, D. L.; Lott, R. S., *Capstone pharmacy review*. Jones & Bartlett Learning: Massachusetts, USA, 2014.
  42. Timmins, G. S.; Deretic, V. *Mol. Microbiol.*, **2006**, *62* (5), 1220-1227.

## **Chapter 6**

# **Extending photoactivation of Ru(II) polypyridyl complexes into the phototherapeutic window**

---

## Chapter 6

### Extending photoactivation of Ru(II) polypyridyl complexes into the phototherapeutic window

#### 6.1. Introduction

In the clinic, the optimum wavelength of light used to activate a photoactive therapeutic agent is known as the phototherapeutic window (between 600 nm – 1000 nm), as discussed in Chapter 1. Thus a photoactive therapeutic agent should have a strong absorption band in this region. The Ru(II) polypyridyl complexes based on *cis*-[Ru(*N-N'*)<sub>2</sub>(L)<sub>2</sub>]<sup>2+</sup>, where *N-N'* is 2,2'-bipyridine or 1,10-phenanthroline and L is isoniazid or nicotinamide, studied in previous chapters (complexes **1** – **7**) were activated by blue or green light (465 nm – 520 nm), just outside the phototherapeutic window. One methodology to extend the photoactivation of Ru(II) polypyridyl complexes into the phototherapeutic window is by two-photon activation. Two-photon activation occurs when a compound absorbs two photons simultaneously to achieve a higher energy transition. In order to achieve this, a femtosecond pulsed laser light source needs to be utilised in order to achieve a high density and flux of photons. Efficient two-photon chromophores generally have extended  $\pi$ -conjugated systems with opposing donor and acceptor groups.<sup>1-2</sup> The  $\pi$ -conjugated and electron donor ligand MOPEP, 4-[2-(4-methoxyphenyl)ethynyl]pyridine, was added to a square planar platinum(II) complex, *cis*-[Pt(Cl)<sub>2</sub>(MOPEP)<sub>2</sub>], which rendered the complex two-photon active once photoirradiated with 600 nm laser light.<sup>3</sup> Interestingly complexes such as *cis*-[Ru(bpy)<sub>2</sub>(4AP)<sub>2</sub>]<sup>2+</sup>, where bpy is 2,2'-bipyridine and 4AP is 4-aminopyridine, have been found to release a ligand of 4AP in one-photon (with  $\geq 480$  nm light) and two-photon regimes (with 800 nm laser light).<sup>4-5</sup> In comparison, the



addition of highly conjugated fluorene-substituted 1,10-phenanthroline ligands (FPhen) to give  $[\text{Ru}(\text{FPhen})_3]^{2+}$  highly enhanced the two-photon activation efficiency.<sup>6</sup>

This Chapter focuses on the synthesis of *cis*- $[\text{Ru}(\text{bpy})_2(\text{MOPEP})_2][\text{PF}_6]_2$  (**9**), see Figure 6.1, and investigating its two-photon activity.

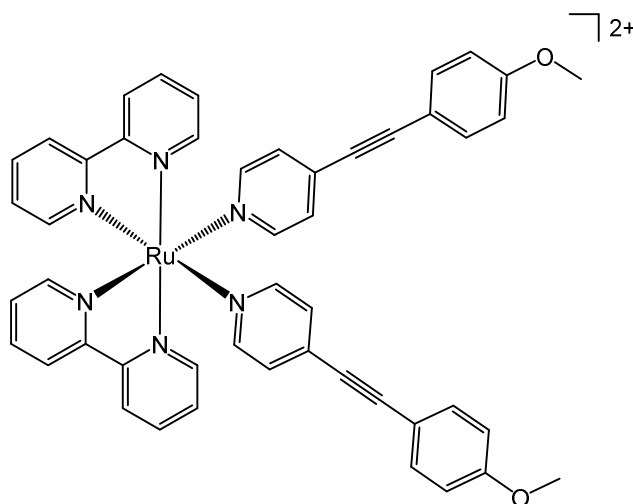


**Figure 6.1.** Structure of *cis*- $[\text{Ru}(\text{bpy})_2(\text{MOPEP})_2][\text{PF}_6]_2$  (**9**).

Comparisons with the control compound *cis*- $[\text{Ru}(\text{bpy})_2(\text{py})_2][\text{PF}_6]_2$  (**10**) were made. Due to lack of solubility in aqueous solution, experiments were conducted in acetonitrile. Additionally the two photon activation of *cis*- $[\text{Ru}(\text{bpy})_2(\text{INH})_2][\text{PF}_6]_2$  (**4**) in aqueous solution was explored. The release of ligands was followed by UV-visible spectroscopy and transient absorption spectroscopy using a femtosecond pulsed laser and a non-laser light source. The DNA binding properties of *cis*- $[\text{Ru}(\text{bpy})_2(\text{MOPEP})_2][\text{PF}_6]_2$  (**9**) were also investigated since MOPEP's extended aromatic system was expected to promote DNA intercalation.

## 6.2. Experimental

### 6.2.1. Materials

The synthesis of *cis*-[Ru(bpy)<sub>2</sub>(INH)<sub>2</sub>][PF<sub>6</sub>]<sub>2</sub> (**4**) can be found in Chapter 3. The synthesis of the starting material [Ru(bpy)<sub>2</sub>(Cl)<sub>2</sub>], where bpy is 2,2'-bipyridine, can be found in Chapter 2. 1-Ethynyl-4-methoxybenzene, 4-bromopyridine, PdCl<sub>2</sub>(PPh<sub>3</sub>)<sub>2</sub>, tetrabutylammonium fluoride hydrate, NH<sub>4</sub>PF<sub>6</sub>, Trizma<sup>®</sup> base, NaCl, pyridine and acetonitrile were purchased from Sigma Aldrich. UltraPure<sup>™</sup> Calf thymus (CT) DNA was purchased from Life Technologies. Description of the photoirradiation setups can be found in Chapter 2.

### 6.2.2. Preparation of MOPEP (**8**)

The synthesis of MOPEP (4-[2-(4-methoxyphenyl)ethynyl]pyridine) was adapted from previously published methods.<sup>3, 7</sup> 1-Ethynyl-4-methoxybenzene (310  $\mu$ L, 2.4 mmol), 4-bromopyridine (388 mg, 2 mmol), PdCl<sub>2</sub>(PPh<sub>3</sub>)<sub>2</sub> (42 mg, 0.06 mmol) and tetrabutylammonium fluoride hydrate (1.57 g, 6 mmol) were stirred under N<sub>2</sub> at 353 K for 19 h. After cooling to room temperature (298 K), water (60 mL) was added and the solution was extracted with diethyl ether. The diethyl ether layer was washed with brine, and diethyl ether was removed under reduced pressure. The resulting orange powder was recrystallized from petroleum ether (bp 40-60 °C) to give a pale yellow powder. Yield 22% (92 mg, 0.4 mmol). Elemental analysis calculated for C<sub>14</sub>H<sub>11</sub>NO %C: 80.36, %H: 5.30, %N: 6.69; found %C: 79.48, %H: 5.27, %N: 5.90. ESI-MS calculated for C<sub>14</sub>H<sub>12</sub>NO [M+H]<sup>+</sup> *m/z* 210.1, found *m/z* 210.0. <sup>1</sup>H-NMR (chloroform-*d*<sub>3</sub>, 400 MHz)  $\delta$ <sub>H</sub>: 3.9 (3H, s), 6.9 (2H, d, *J* = 8.8 Hz), 7.5 (4H, m), 8.6 (2H, d, *J* = 6.2 Hz).

### 6.2.3. Preparation of *cis*-[Ru(bpy)<sub>2</sub>(MOPEP)<sub>2</sub>][PF<sub>6</sub>]<sub>2</sub> (9)

*Cis*-[Ru(bpy)<sub>2</sub>(Cl)<sub>2</sub>] (18.4 mg, 0.04 mmol) and MOPEP (8) (40 mg, 0.2 mmol) were added to 8 mL of 1:3 water:ethanol mixture and the solution was refluxed under nitrogen while stirring for 20 h. The reaction vessel was covered in foil to avoid light exposure. After cooling to room temperature (298 K), the solution was filtered and NH<sub>4</sub>PF<sub>6</sub> (32.2 mg, 0.2 mmol) was added to produce a red powder. The powder was dissolved in methanol and the red product was precipitated by addition of diethyl ether. Yield 32% (14 mg, 0.01 mmol). Elemental analysis calculated for C<sub>48</sub>H<sub>38</sub>F<sub>12</sub>N<sub>6</sub>O<sub>2</sub>P<sub>2</sub>Ru.2MeOH %C: 50.64, %H: 3.91, %N: 7.09; found %C: 50.21, %H: 3.40, %N: 6.86. ESI-MS calculated for C<sub>48</sub>H<sub>38</sub>N<sub>6</sub>O<sub>2</sub>Ru [M]<sup>2+</sup> *m/z* 416.1, found *m/z* 416.0. <sup>1</sup>H-NMR (acetone-*d*<sub>6</sub>, 400MHz) δ<sub>H</sub>: 3.9 (6H, s), 7.0 (4H, d, *J* = 8.9 Hz), 7.5 (4H, d, *J* = 6.6 Hz), 7.5 (4H, d, *J* = 8.9 Hz), 7.6 (2H, ddd, *J* = 7.6, 5.4 and 1.1 Hz), 8.0 (2H, ddd, *J* = 7.6, 5.6 and 1.1 Hz), 8.1 (2H, td, *J* = 7.9 and 1.3 Hz), 8.3 (2H, d, *J* = 5.3 Hz), 8.3 (2H, td, *J* = 7.9 and 1.1 Hz), 8.6 (2H, d, *J* = 8.2 Hz), 8.7 (6H, m), 9.4 (2H, d, *J* = 5.4 Hz).

### 6.2.4. Preparation of *cis*-[Ru(bpy)<sub>2</sub>(py)<sub>2</sub>][PF<sub>6</sub>]<sub>2</sub> (10)

Water (10 mL) was degassed by bubbling nitrogen through the solution for 15 min. *Cis*-[Ru(bpy)<sub>2</sub>(Cl)<sub>2</sub>] (50 mg, 0.1 mmol) was added and solution heated at 353 K under nitrogen while stirring for 15 min. The reaction vessel was covered in foil to avoid light exposure. Pyridine (100 μL, 1 mmol) was added and solution heated at 353 K for 5 h. After cooling to room temperature (298 K), the solution was filtered and NH<sub>4</sub>PF<sub>6</sub> (84 mg, 0.5 mmol) was added to give an orange precipitate. The precipitate was collected by filtration and washed with water and diethyl ether. Yield 46% (40 mg, 0.05 mmol). Elemental analysis calculated for C<sub>30</sub>H<sub>26</sub>F<sub>12</sub>N<sub>6</sub>P<sub>2</sub>Ru.2H<sub>2</sub>O %C: 40.14, %H: 3.37, %N: 9.36; found %C: 39.23, %H: 2.78, %N: 8.65. ESI-MS calculated for

$\text{C}_{30}\text{H}_{26}\text{N}_6\text{Ru} [\text{M}]^{2+}$   $m/z$  286.1, found 286.0.  $^1\text{H}$ -NMR (acetone- $d_6$ , 400 MHz)  $\delta_{\text{H}}$ : 7.45 (4H, m), 7.54 (2H, ddd,  $J = 7.69, 5.62$  and  $1.27$  Hz), 7.96 (4H, m), 8.08 (2H, td,  $J = 7.85$  and  $1.43$  Hz), 8.28 (4H, m), 8.60 (2H, d,  $J = 8.17$  Hz), 8.67 (6H, m), 9.33 (2H, d,  $J = 5.58$  Hz).

### 6.2.5. Photoirradiation using non-laser light source

MOPEP (**8**), *cis*-[Ru(bpy) $_2$ (MOPEP) $_2$ ][PF $_6$ ] $_2$  (**9**) and *cis*-[Ru(bpy) $_2$ (py) $_2$ ][PF $_6$ ] $_2$  (**10**) were dissolved in acetonitrile to give a concentration of either 40  $\mu\text{M}$  or 10  $\mu\text{M}$ . The solutions (600  $\mu\text{L}$ ) were placed into a 1 cm path length quartz cuvette and photoirradiated using a blue LED ( $\lambda_{\text{irr}} = 463$  nm, 50 mW  $\text{cm}^{-2}$ ) and the KiloArc light source ( $\lambda_{\text{irr}} = 600$  nm and 800 nm) at 298 K for various times of photoirradiation. The UV-visible spectrum of each sample was recorded on a Cary 300-Scan spectrophotometer. The absorbance over the range 200 – 800 nm was recorded at 298 K. The data were processed using OriginPro 9.1 and, where applicable, plots of change in absorbance versus time were fitted to the exponential equation  $A = A_0 + Ce^{Rt}$  (where  $A$  is absorbance,  $t$  is time and  $C$ ,  $A_0$  and  $R$  are calculated parameters) to give the half-life of formation ( $t_{1/2}$ , s).

### 6.2.6. Photoirradiation using laser light source

The laser experiments were performed in collaboration with Dr Simon E. Greenough from the Chemistry Department at University of Warwick.

An acetonitrile solution (178  $\mu\text{M}$ ) of *cis*-[Ru(bpy) $_2$ (MOPEP) $_2$ ][PF $_6$ ] $_2$  (**9**) was photoirradiated using the laser set-up described in Chapter 2. The average absorbance at 373 nm - 378 nm was monitored at various time points of photoirradiation (up to 30 min), using different powers of 800 nm and 600 nm laser light (0.5 mW, 0.6 mW, 0.7 mW, 0.8 mW, 0.9 mW and 1 mW). Plots of  $\ln(\text{Abs})$  versus time were made and fitted

to a linear regression to obtain a pseudo-first order rate constant ( $k_{\text{obs}}$ ) for each power of laser light. For *cis*-[Ru(bpy)<sub>2</sub>(INH)<sub>2</sub>][PF<sub>6</sub>]<sub>2</sub> (**4**), an aqueous solution (690  $\mu\text{M}$ ) was photoirradiated using the transient laser-set up described in Chapter 2. The integrated area (between 350 nm – 675 nm) at a pump-probe (probe  $\lambda_{\text{irr}} = 800$  nm) delay of 100 ps was recorded at each power of laser light (12 mW, 15 mW, 18 mW, 21 mW, 24 mW). log-log plots were constructed of either  $\log(k_{\text{obs}})$  or  $\log(\text{integrated area})$  versus  $\log(\text{power})$ , where a slope of 1 indicates a one-photon process, and a slope of 2 indicates a two-photon process. This is due to the quadratic relationship between two-photon activation (TPA) and the excitation power (I) where  $\text{TPA} \propto I^2$ .<sup>8</sup>

#### 6.2.7. Interaction with DNA

Calf thymus (CT) DNA (50  $\mu\text{M}$ , with respect to nucleotides), *cis*-[Ru(bpy)<sub>2</sub>(MOPEP)<sub>2</sub>][PF<sub>6</sub>]<sub>2</sub> (**9**) (5  $\mu\text{M}$ , complex initially dissolved in 5% v/v DMSO and diluted accordingly) and NaCl (50 mM) were dissolved in Tris buffer (5 mM). The Tris buffer was prepared from Trizma<sup>®</sup> base diluted with dd.H<sub>2</sub>O and pH adjusted using HCl to give a final pH of 7.4. The control experiment contained no complex **9**. Both the sample (CT DNA and complex **9**) and the control sample (CT-DNA only) were incubated in the dark at 298 K for 1 h. Thermal denaturation of CT-DNA in the presence or absence of complex **9** was investigated by recording the change in absorbance at 260 nm while increasing the temperature from 298 K to 371 K. The data were processed using OriginPro 9.1, and for each sample plots of absorbance at 260 nm versus temperature were fitted to a Boltzmann sigmoidal equation to afford the melting temperature ( $T_m$ ) at the inflection point of the curve.

### 6.3. Results

#### 6.3.1. Photoirradiation using non-laser light source

The UV-visible spectra of *cis*-[Ru(bpy)<sub>2</sub>(MOPEP)<sub>2</sub>][PF<sub>6</sub>]<sub>2</sub> (**9**) and *cis*-[Ru(bpy)<sub>2</sub>(py)<sub>2</sub>][PF<sub>6</sub>]<sub>2</sub> (**10**) in acetonitrile are shown in Figure 6.2 with extinction coefficients listed in Table 6.1.

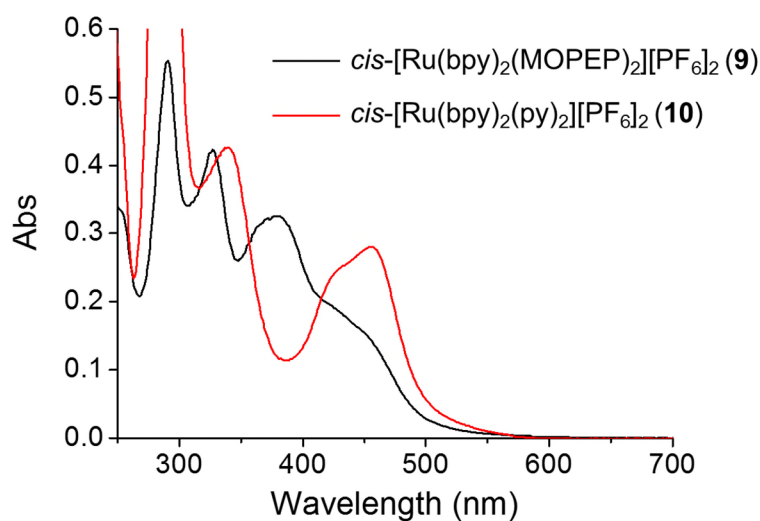


**Figure 6.2.** UV-visible spectrum of *cis*-[Ru(bpy)<sub>2</sub>(MOPEP)<sub>2</sub>][PF<sub>6</sub>]<sub>2</sub> (**9**) (10  $\mu$ M) and *cis*-[Ru(bpy)<sub>2</sub>(py)<sub>2</sub>][PF<sub>6</sub>]<sub>2</sub> (**10**) (40  $\mu$ M) in acetonitrile in the dark at 298 K.

**Table 6.1.** Extinction coefficients for MOPEP (**8**), *cis*-[Ru(bpy)<sub>2</sub>(MOPEP)<sub>2</sub>][PF<sub>6</sub>]<sub>2</sub> (**9**) and *cis*-[Ru(bpy)<sub>2</sub>(py)<sub>2</sub>][PF<sub>6</sub>]<sub>2</sub> (**10**) in acetonitrile in the dark at 298 K.

	Wavelength (nm)	Extinction coefficient (M <sup>-1</sup> cm <sup>-1</sup> )
<b>8</b>	298	30000
	310	30000
	354	1000
<b>9</b>	291	60000
	327	40000
	380	30000
	424	20000
<b>10</b>	340	10000
	425	6000
	455	7000

Interestingly for **9** there was a very broad band at 380 nm with a shoulder at 424 nm, whereas for **10** there is a relatively narrower band at 425 nm. At  $< 350$  nm the spectra are similar with respect to the position of the bands (e.g. band at 327 nm for **9** and 340 nm for **10**). The major difference between **9** and **10** is their extinction coefficients. In the case of MOPEP (**8**), there was a band at  $\sim 300$  nm with an extinction coefficient of  $30000 \text{ M}^{-1} \text{ cm}^{-1}$ . Similarly for *cis*-[Ru(bpy)<sub>2</sub>(MOPEP)<sub>2</sub>][PF<sub>6</sub>]<sub>2</sub> (**9**), all bands had extinction coefficients in the range of  $10^4 \text{ M}^{-1} \text{ cm}^{-1}$ . In the case of *cis*-[Ru(bpy)<sub>2</sub>(py)<sub>2</sub>][PF<sub>6</sub>]<sub>2</sub> (**10**), all bands had extinction coefficients in the range of  $10^3 \text{ M}^{-1} \text{ cm}^{-1}$ , which is 10x smaller than for **8** or **9**.

Changes in the absorption spectra of MOPEP (**8**) and *cis*-[Ru(bpy)<sub>2</sub>(MOPEP)<sub>2</sub>][PF<sub>6</sub>]<sub>2</sub> (**9**) were investigated in acetonitrile (ACN) using a blue LED ( $\lambda_{\text{irr}} = 463 \text{ nm}$ ,  $50 \text{ mW cm}^{-2}$ ) for various times at 298 K, see Figure 6.3.

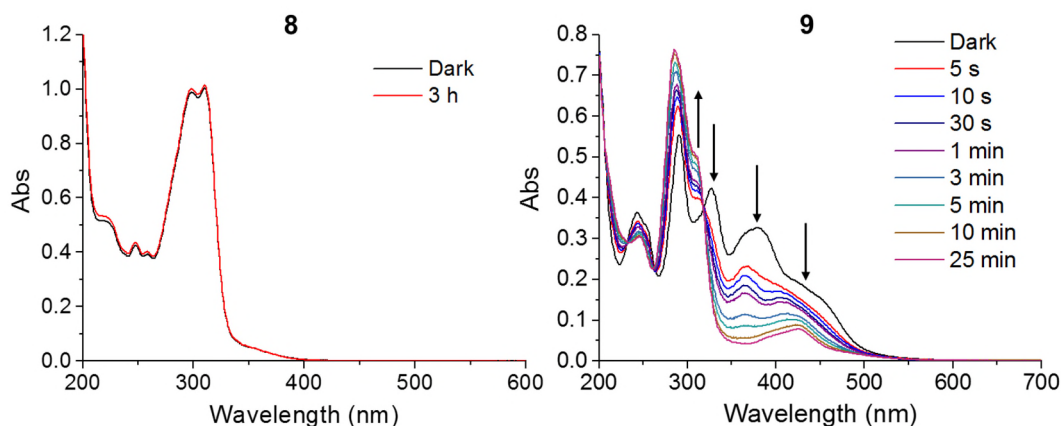


**Figure 6.3.** UV-visible spectrum of MOPEP (**8**) (40  $\mu\text{M}$ ) and *cis*-[Ru(bpy)<sub>2</sub>(MOPEP)<sub>2</sub>][PF<sub>6</sub>]<sub>2</sub> (**9**) (10  $\mu\text{M}$ ) in acetonitrile photoirradiated using a blue LED ( $\lambda_{\text{irr}} = 463 \text{ nm}$ ,  $50 \text{ mW cm}^{-2}$ ) for various times at 298 K.

MOPEP (**8**) was stable when photoirradiated for 3 h with no changes observed in the UV-visible spectrum. For *cis*-[Ru(bpy)<sub>2</sub>(MOPEP)<sub>2</sub>][PF<sub>6</sub>]<sub>2</sub> (**9**) there were dramatic

changes in the UV-visible spectrum upon photoirradiation. The bands at 380 nm and 327 nm (including the shoulder at 424 nm) decreased, while the band at 291 nm increased. Interestingly a shoulder at 310 nm constantly increased, attributable to the continued photorelease of the MOPEP ligand and the absorption of free MOPEP in solution. As a result there was an isosbestic point at 318 nm. The increase in the absorbance at 310 nm was followed at various points of photoirradiation, see Figure 6.4.

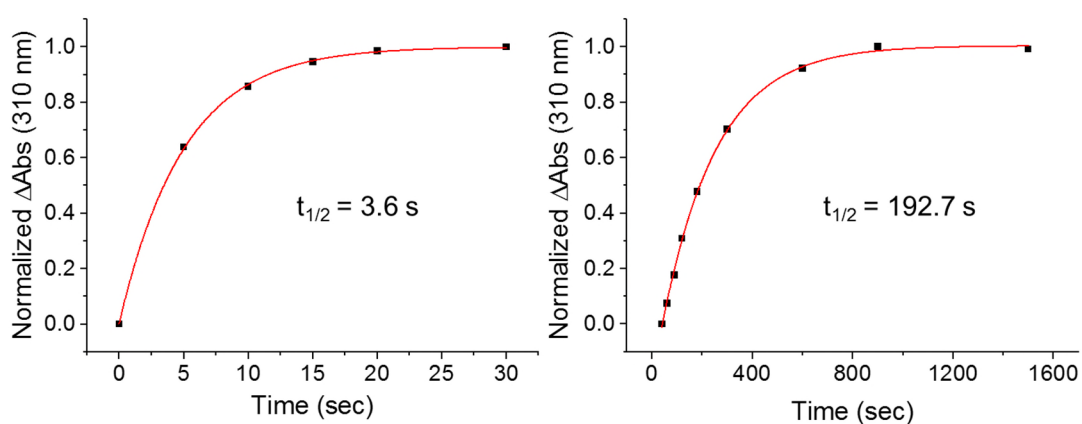


**Figure 6.4.** Kinetic traces for the increase in absorbance of the shoulder at 310 nm after photoirradiation of *cis*-[Ru(bpy)<sub>2</sub>(MOPEP)<sub>2</sub>][PF<sub>6</sub>]<sub>2</sub> (**9**) in acetonitrile using a blue LED ( $\lambda_{\text{irr}} = 463 \text{ nm}$ ,  $50 \text{ mW cm}^{-2}$ ) for various times at 298 K.

After 30 s photoirradiation the first MOPEP ligand was released, producing the photoproduct *cis*-[Ru(bpy)<sub>2</sub>(MOPEP)(ACN)]<sup>2+</sup>. This was evident by the change in absorbance at 310 nm reaching its first plateau, and when fitted to a single exponential function gave half-life for formation of photoproduct  $t_{1/2} = 3.6 \text{ s}$ . Further photoirradiation for 25 min released the second MOPEP ligand, producing the photoproduct *cis*-[Ru(bpy)<sub>2</sub>(ACN)<sub>2</sub>]<sup>2+</sup>. The change in absorbance at 310 nm reached a second plateau, and when fitted to a single exponential function gave  $t_{1/2} = 192.7 \text{ s}$ .



Both *cis*-[Ru(bpy)<sub>2</sub>(MOPEP)<sub>2</sub>][PF<sub>6</sub>]<sub>2</sub> (**9**) and *cis*-[Ru(bpy)<sub>2</sub>(py)<sub>2</sub>][PF<sub>6</sub>]<sub>2</sub> (**10**) were photoirradiated in acetonitrile using the KiloArc light source ( $\lambda_{\text{irr}}$  = 600 nm and 800 nm) for various times at 298 K, see Figure 6.5.

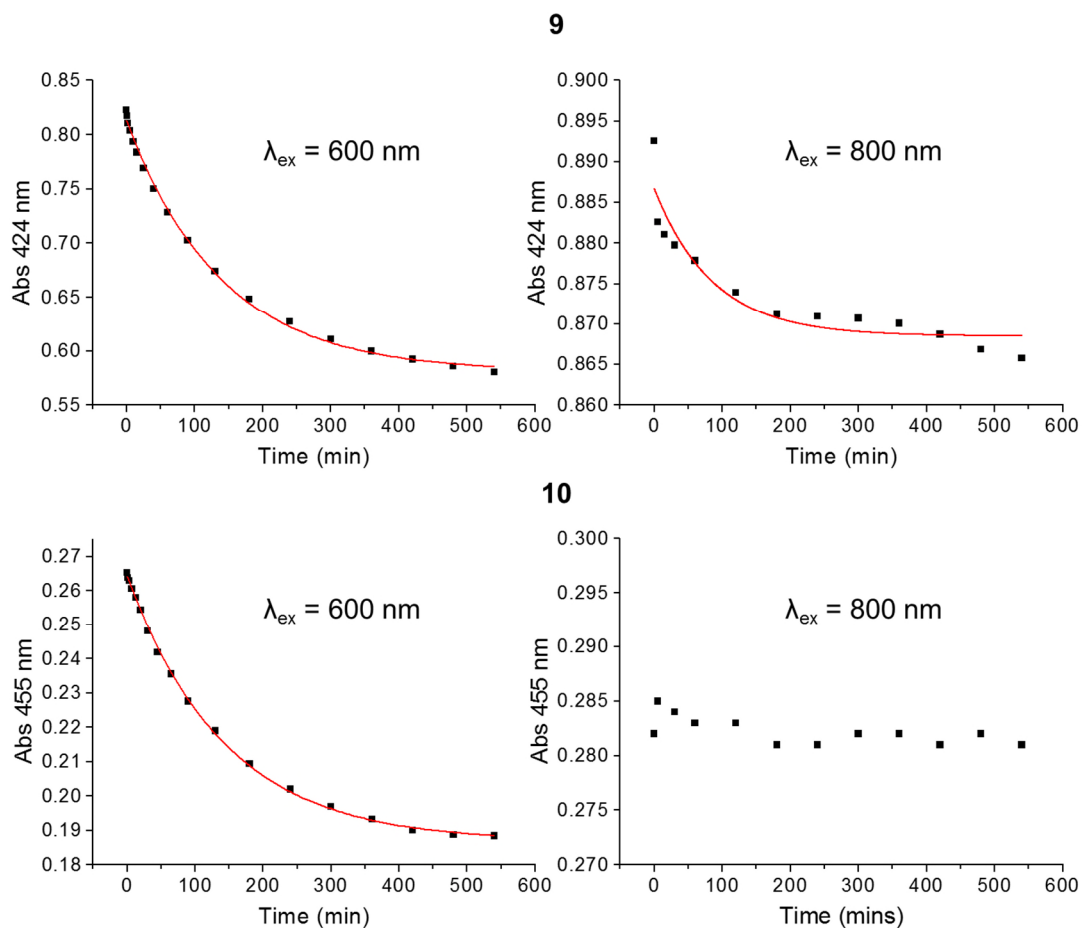


**Figure 6.5.** Kinetic traces for the decrease in absorption at 424 nm and 455 nm after photoirradiation of *cis*-[Ru(bpy)<sub>2</sub>(MOPEP)<sub>2</sub>][PF<sub>6</sub>]<sub>2</sub> (**9**) (top) and *cis*-[Ru(bpy)<sub>2</sub>(py)<sub>2</sub>][PF<sub>6</sub>]<sub>2</sub> (**10**) (bottom) in acetonitrile (40  $\mu$ M) using the KiloArc light source ( $\lambda_{\text{irr}}$  = 600 nm and 800 nm) for various times at 298 K..

For both **9** and **10**, once photoirradiated with 600 nm light the absorbance band at 424 nm and 455 nm respectively, decreased mono-exponentially over the time frame 0 – 9 h. Interestingly *cis*-[Ru(bpy)<sub>2</sub>(MOPEP)<sub>2</sub>][PF<sub>6</sub>]<sub>2</sub> (**9**) was slightly active when photoirradiated using 800 nm light, as was evident from the decrease in the absorption band at 424 nm. Conversely in the case of *cis*-[Ru(bpy)<sub>2</sub>(py)<sub>2</sub>][PF<sub>6</sub>]<sub>2</sub> (**10**), no activity

was observed at 800 nm photoirradiation as there were no changes in the absorbance band at 455 nm.

### 6.3.2. Photoirradiation using laser light source

Changes in the absorption spectrum of *cis*-[Ru(bpy)<sub>2</sub>(MOPEP)<sub>2</sub>][PF<sub>6</sub>]<sub>2</sub> (**9**) were investigated in acetonitrile (ACN) using a laser light source ( $\lambda_{\text{irr}} = 600$  nm and 800 nm) for various times of photoirradiation and powers of the laser light (0.5 mW – 1 mW) at 298 K. Changes in the absorption spectrum were monitored and fitted to a pseudo-first order rate equation to obtain the pseudo-first order rate constant  $k_{\text{obs}}$ . Log-log plots were made of  $\log(k_{\text{obs}})$  versus  $\log(\text{power})$  to investigate if a one-photon (resulting in a slope of 1) or two-photon (resulting in a slope of 2) process was occurring at that specific wavelength of photoirradiation, see Figure 6.6.

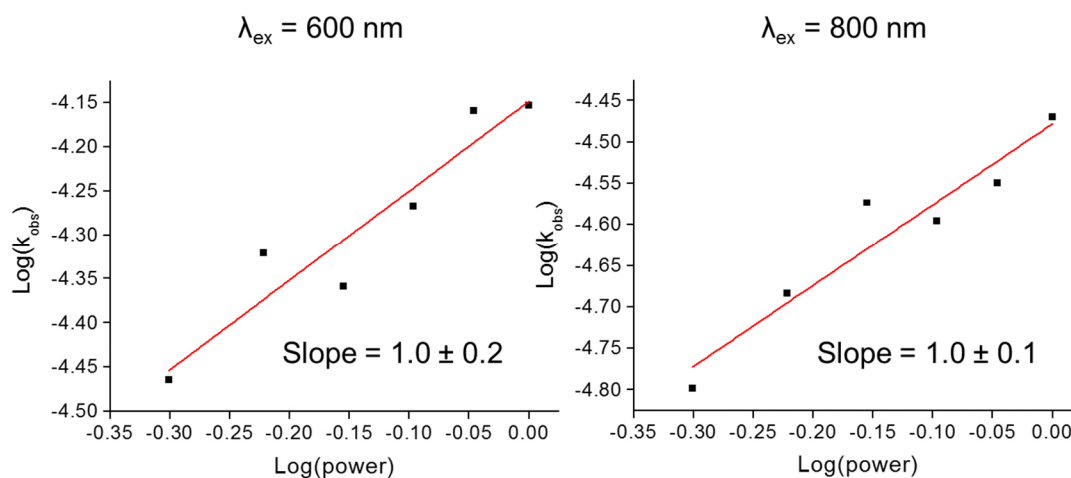


**Figure 6.6.**  $\text{Log}(k_{\text{obs}})$ - $\log(\text{power})$  plots for *cis*-[Ru(bpy)<sub>2</sub>(MOPEP)<sub>2</sub>][PF<sub>6</sub>]<sub>2</sub> (**9**) photoirradiated in acetonitrile using a laser light source at 600 nm (left) and 800 nm (right) at 298 K.

At both wavelengths of photoirradiation (600 nm and 800 nm), the slope of the  $\log(k_{\text{obs}})$  versus  $\log(\text{power})$  plots indicated that photorelease was a one-photon process (slope =  $1.0 \pm 0.1$ ). The same analysis was carried out for *cis*-[Ru(bpy)<sub>2</sub>(INH)<sub>2</sub>][PF<sub>6</sub>]<sub>2</sub>

(4) in aqueous solution using the transient absorption spectroscopy approach, see Figure 6.7. After photoirradiation (800 nm) with 100 ps pump-probe delay, there is an absorption of the  $^3\text{MLCT}$  state at 358 nm, a ground state bleach feature at  $\sim 420$  nm and an absorption due to the penta-coordinate intermediate at  $> 550$  nm. A more in-depth discussion of such features is given in Chapter 4. The integrated area between 350 nm – 675 nm was recorded at each power of laser light (12 mW – 24 mW), and log-log plots were constructed of  $\log(\text{integrated area})$  versus  $\log(\text{power})$ . Interestingly this analysis indicated that the photorelease is a two-photon process (slope =  $1.90 \pm 0.09$ ).

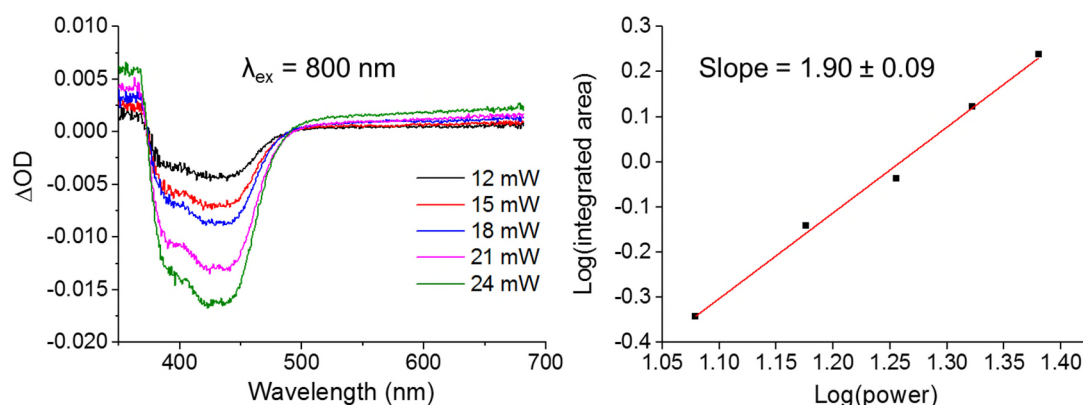


**Figure 6.7.** Dependence of the transient absorption spectrum of *cis*-[Ru(bpy) $_2$ (INH) $_2$ ][PF $_6$ ] $_2$  (4) in aqueous solution on the power of a laser light source at 800 nm (left), and plot of  $\log(\text{integrated area})$ - $\log(\text{power})$  (right).

### 6.3.3. Interaction with DNA

Double stranded DNA has an absorption band at 260 nm. When heated, the double-stranded DNA is denatured, and as a result the absorption band at 260 nm increases due to the formation of single-stranded DNA. This increase in absorbance can be plotted versus temperature to produce a melting curve, see Figure 6.8. When fitted to a Boltzmann sigmoidal equation, the inflection point is known as the melting

temperature ( $T_m$ ), the point at which 50% of the DNA is denatured into single strands. The melting temperature of CT-DNA was determined in the absence and presence of *cis*-[Ru(bpy)<sub>2</sub>(MOPEP)<sub>2</sub>][PF<sub>6</sub>]<sub>2</sub> (**9**) (1:10 complex:DNA ratio) after 1 h dark incubation at 298 K, see Table 6.2. Interestingly there was only a 0.5 K increase in melting temperature upon addition of complex **9** (from 352.5 K to 353 K).

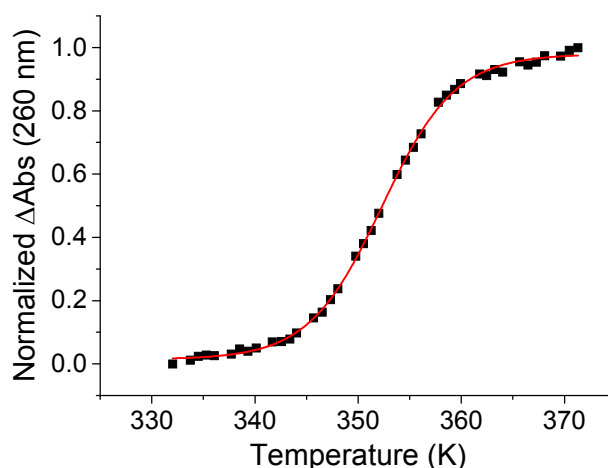


**Figure 6.8.** Melting curve for CT-DNA in 5 mM Tris buffer and 50 mM NaCl, fitted to a Boltzmann sigmoidal equation.

**Table 6.2.** Melting temperature ( $T_m$ ) of CT-DNA in the absence and presence of *cis*-[Ru(bpy)<sub>2</sub>(MOPEP)<sub>2</sub>][PF<sub>6</sub>]<sub>2</sub> (**9**) when incubated in the dark for 1 h at 298 K.

	Melting temperature (K)
CT-DNA	352.5 ± 0.2
CT-DNA and complex <b>9</b>	353 ± 1

## 6.4. Discussion

### 6.4.1. Two-photon activation

The complex *cis*-[Ru(bpy)<sub>2</sub>(MOPEP)<sub>2</sub>][PF<sub>6</sub>]<sub>2</sub> (**9**) was synthesised and exhibited efficient photorelease upon photoirradiation using blue light ( $\lambda_{irr}$  = 463 nm, 50 mW cm<sup>-2</sup>) in acetonitrile at 298 K. When photoirradiated at a concentration of 10  $\mu$ M, the

first MOPEP ligand was released with  $t_{1/2} = 3.6$  s and the second MOPEP ligand was released with  $t_{1/2} = 192.7$  s. The previously synthesised complex *cis*-[Pt(Cl)<sub>2</sub>(MOPEP)<sub>2</sub>] is active with UVA light (330 – 380 nm) to release the MOPEP ligands, however MOPEP itself photodecomposes after exposure to UVA light.<sup>3</sup> Notably the MOPEP ligand alone did not degrade after photoirradiation with blue light ( $\lambda_{irr} = 463$  nm, 50 mW cm<sup>-2</sup>) for 3 h.

Both *cis*-[Ru(bpy)<sub>2</sub>(MOPEP)<sub>2</sub>][PF<sub>6</sub>]<sub>2</sub> (**9**) and *cis*-[Ru(bpy)<sub>2</sub>(py)<sub>2</sub>][PF<sub>6</sub>]<sub>2</sub> (**10**) were photoactive when photoirradiated with 600 nm non-laser light (over a longer time period of 9 h) in acetonitrile, however only *cis*-[Ru(bpy)<sub>2</sub>(MOPEP)<sub>2</sub>][PF<sub>6</sub>]<sub>2</sub> (**9**) was active with 800 nm non-laser light. This confirms that when photoirradiated with 800 nm non-laser light, the photoactivation of **9** is a one-photon process, as two-photon activation cannot be achieved using a non-laser light source. Furthermore when *cis*-[Ru(bpy)<sub>2</sub>(MOPEP)<sub>2</sub>][PF<sub>6</sub>]<sub>2</sub> (**9**) was photoirradiated with a laser light source at 600 nm and 800 nm in acetonitrile, the log( $k_{obs}$ ) vs log(power) plots confirmed that one-photon activation was occurring at these wavelengths. The reason for this is apparent from Figure 6.9.

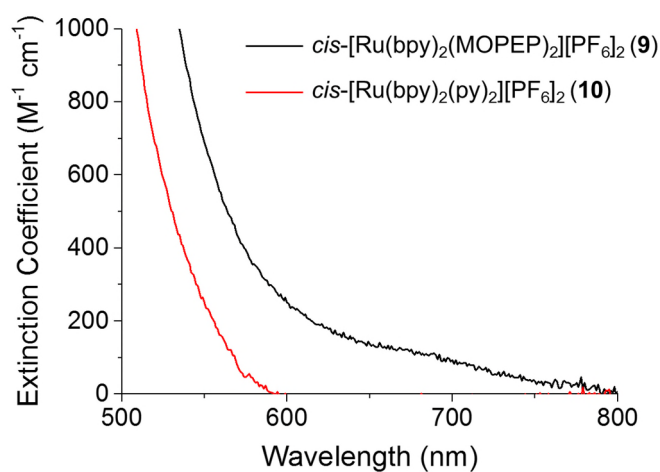


**Figure 6.9.** UV-visible absorption spectrum of *cis*-[Ru(bpy)<sub>2</sub>(MOPEP)<sub>2</sub>][PF<sub>6</sub>]<sub>2</sub> (**9**) and *cis*-[Ru(bpy)<sub>2</sub>(py)<sub>2</sub>][PF<sub>6</sub>]<sub>2</sub> (**10**) in acetonitrile at 298 K.

In the case of *cis*-[Ru(bpy)<sub>2</sub>(py)<sub>2</sub>][PF<sub>6</sub>]<sub>2</sub> (**10**) there is no absorbance at 800 nm, however for *cis*-[Ru(bpy)<sub>2</sub>(MOPEP)<sub>2</sub>][PF<sub>6</sub>]<sub>2</sub> (**9**) there is a shoulder that extends from 600 nm to 800 nm (with an extinction coefficient of  $\sim 100 \text{ M}^{-1} \text{ cm}^{-1}$  at 700 nm). This explains why **9** is one-photon active at 800 nm and **10** is not, as photoirradiating a complex into its one-photon absorption band will induce a one-photon process.

Conversely when *cis*-[Ru(bpy)<sub>2</sub>(INH)<sub>2</sub>][PF<sub>6</sub>]<sub>2</sub> (**4**) was photoirradiated with a laser light source at 800 nm in aqueous solution, the log(integrated area) vs log(power) showed that two-photon activation was occurring at this wavelength. This is a similar behaviour to the complex *cis*-[Ru(bpy)<sub>2</sub>(4AP)<sub>2</sub>]<sup>2+</sup>, where 4AP is 4-aminopyridine, that is two-photon active with 800 nm laser excitation. Interestingly in aqueous solution *cis*-[Ru(bpy)<sub>2</sub>(INH)<sub>2</sub>][PF<sub>6</sub>]<sub>2</sub> (**4**) does not have a measurable absorbance at 800 nm, see Figure 6.10, and so does not observe one-photon activation at this wavelength. It was found in Chapter 4 that complex **4** is not photoactive with wavelengths > 610 nm with a non-laser light source.

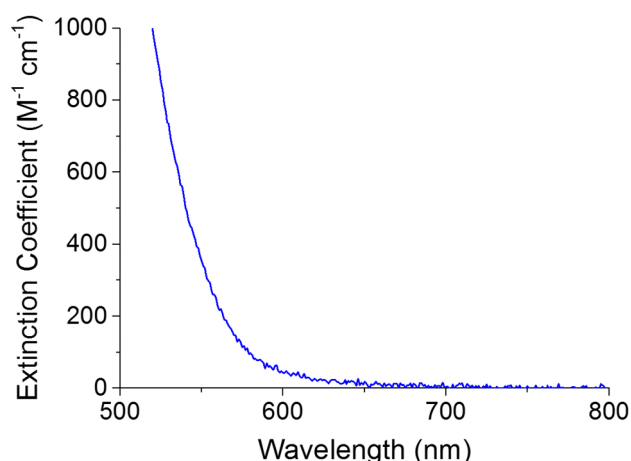


**Figure 6.10.** UV-visible absorption spectrum of *cis*-[Ru(bpy)<sub>2</sub>(INH)<sub>2</sub>][PF<sub>6</sub>]<sub>2</sub> (**4**) in aqueous solution at 298 K.

The reason for the shoulder at 600 nm – 800 nm for *cis*-[Ru(bpy)<sub>2</sub>(MOPEP)<sub>2</sub>][PF<sub>6</sub>]<sub>2</sub> (**9**) could be due to the stronger electron-donating ability of the MOPEP ligand (*c.f.* pyridine or isoniazid) which may produce a lower energy <sup>1</sup>MLLCT<sub>(Ru/MOPEP-bpy)</sub> transition (and thus extend the shoulder of the band). For example, in the complex *cis*-[Ru(bpy)<sub>2</sub>(4AP)<sub>2</sub>]<sup>2+</sup>, where 4AP is 4-aminopyridine, the lowest singlet excited state was <sup>1</sup>MLLCT<sub>(Ru/4AP-bpy)</sub> in character, potentially a result of the electron-donating amino functionality.<sup>9</sup> Additionally the extended aromatic nature of the MOPEP ligand may enhance the extinction coefficient of this absorption band, allowing photoactivation to occur in the shoulder of the band at longer wavelengths.

For a further understanding of why *cis*-[Ru(bpy)<sub>2</sub>(INH)<sub>2</sub>][PF<sub>6</sub>]<sub>2</sub> (**4**) is two-photon active at 800 nm and *cis*-[Ru(bpy)<sub>2</sub>(MOPEP)<sub>2</sub>][PF<sub>6</sub>]<sub>2</sub> (**9**) is one photon at 800 nm, computational approaches would need to be adopted to elucidate two-photon activation cross sections.<sup>3</sup>

#### 6.4.2. Interaction with DNA

For complexes of the type *cis*-[Ru(*N-N'*)<sub>2</sub>(H<sub>2</sub>O)<sub>2</sub>]<sup>2+</sup> and [Ru(*N-N'*)<sub>3</sub>]<sup>2+</sup>, where *N-N'* is a bipyridyl based ligand, both covalent and intercalative binding to DNA increases the melting temperature (T<sub>m</sub>) by 1 – 14 degrees.<sup>10-13</sup> However the T<sub>m</sub> of calf thymus DNA (CT-DNA) increased only by 0.5 K in the presence of *cis*-[Ru(bpy)<sub>2</sub>(MOPEP)<sub>2</sub>][PF<sub>6</sub>]<sub>2</sub> (**9**) (from 352.5 K to 353 K), suggesting there is no interaction between **9** and CT-DNA. Even though the MOPEP ligand is an extended  $\pi$ -conjugated planar ligand, the monodentate ligands in *cis*-[Ru(bpy)<sub>2</sub>(L)<sub>2</sub>]<sup>2+</sup>, where L is a pyridine based ligand, rotate freely about the Ru-N bond at 298 K and higher temperatures, depending on the bulky nature of the ligand involved. A more detailed discussion of rotation in such complexes is given in Chapter 3. This rotation may hinder any interaction with DNA, and may explain the result above. Metal complexes that tend to intercalate into DNA

have extended  $\pi$ -conjugated planar ligands that are rigid (e.g. bidentate/tridentate ligands) and contain fused aromatic rings.<sup>14</sup>

## 6.5. Summary

The complex *cis*-[Ru(bpy)<sub>2</sub>(MOPEP)<sub>2</sub>][PF<sub>6</sub>]<sub>2</sub> (**9**) was synthesised and its photoactivity explored in acetonitrile using both a non-laser and laser light source. Both complex **9** and the control complex *cis*-[Ru(bpy)<sub>2</sub>(py)<sub>2</sub>][PF<sub>6</sub>]<sub>2</sub> (**10**), where py is pyridine, were photoactive in a one-photon regime by photoirradiating with a non-laser light source at 600 nm. However only complex **9** was photoactive in a one-photon regime when photoirradiated with a non-laser light source at 800 nm. Interestingly this one-photon behaviour was confirmed when photoirradiated using a laser light source. This behaviour is due to an extended absorption band shoulder observed for complex **9** between 600 nm and 800 nm, which results in an extinction coefficient of  $\sim 100 \text{ M}^{-1} \text{ cm}^{-1}$  at 700 nm. Interestingly *cis*-[Ru(bpy)<sub>2</sub>(INH)<sub>2</sub>][PF<sub>6</sub>]<sub>2</sub> (**4**) was two-photon active once photoirradiated with a laser light source at 800 nm in aqueous solution.

The results obtained in this chapter show that complexes of the type *cis*-[Ru(bpy)<sub>2</sub>(L)<sub>2</sub>]<sup>2+</sup>, where L is a pyridine based ligand, can be photoactive in either a one-photon or two-photon regime when photoirradiated with laser light at 800 nm, depending on the properties of the ligand L.

## 6.6. References

1. He, G. S.; Tan, L.-S.; Zheng, Q.; Prasad, P. N. *Chem. Rev.*, **2008**, *108* (4), 1245-1330.
2. Pawlicki, M.; Collins, H. A.; Denning, R. G.; Anderson, H. L. *Angew. Chem. Int. Ed.*, **2009**, *48* (18), 3244-3266.



3. Zhao, Y.; Roberts, G. M.; Greenough, S. E.; Farrer, N. J.; Paterson, M. J.; Powell, W. H.; Stavros, V. G.; Sadler, P. J. *Angew. Chem. Int. Ed.*, **2012**, *51* (45), 11263-11266.
4. Zayat, L.; Calero, C.; Alborés, P.; Baraldo, L.; Etchenique, R. *J. Am. Chem. Soc.*, **2003**, *125* (4), 882-883.
5. Nikolenko, V.; Yuste, R.; Zayat, L.; Baraldo, L. M.; Etchenique, R. *Chem. Commun.*, **2005**, (13), 1752-1754.
6. Four, M.; Riehl, D.; Mongin, O.; Blanchard-Desce, M.; Lawson-Daku, L. M.; Moreau, J.; Chauvin, J.; Delaire, J. A.; Lemercier, G. *Phys. Chem. Chem. Phys.*, **2011**, *13* (38), 17304-17312.
7. Liang, Y.; Xie, Y.-X.; Li, J.-H. *J. Org. Chem.*, **2006**, *71* (1), 379-381.
8. Masters, B. R.; So, P. T. C., *Handbook of Biomedical Nonlinear Optical Microscopy*. Oxford University Press: New York, 2008.
9. Salassa, L.; Garino, C.; Salassa, G.; Gobetto, R.; Nervi, C. *J. Am. Chem. Soc.*, **2008**, *130* (29), 9590-9597.
10. Wilson, W. D.; Tanious, F. A.; Fernandez-Saiz, M.; Rigl, C. T., Evaluation of Drug-Nucleic Acid Interactions by Thermal Melting Curves. In *Drug-DNA Interaction Protocols*, Fox, K. R., Ed. Springer New York: 1997; Vol. 90, pp 219-240.
11. Grover, N.; Welch, T. W.; Fairley, T. A.; Cory, M.; Thorp, H. H. *Inorg. Chem.*, **1994**, *33* (16), 3544-3548.
12. Neyhart, G. A.; Grover, N.; Smith, S. R.; Kalsbeck, W. A.; Fairley, T. A.; Cory, M.; Thorp, H. H. *J. Am. Chem. Soc.*, **1993**, *115* (11), 4423-4428.
13. Gao, F.; Chao, H.; Zhou, F.; Yuan, Y.-X.; Peng, B.; Ji, L.-N. *J. Inorg. Biochem.*, **2006**, *100* (9), 1487-1494.
14. Liu, H.-K.; Sadler, P. J. *Acc. Chem. Res.*, **2011**, *44* (5), 349-359.

# **Chapter 7**

## **Conclusions and future work**

## Chapter 7

### Conclusions and future work

#### 7.1. Conclusions

This thesis is concerned with the synthesis, design, photochemical and photobiological properties of potential antibacterial ruthenium(II) polypyridyl complexes.

In Chapter 3, two sets of novel antibacterial compounds were synthesised based on *cis*-[Ru(*N-N'*)<sub>2</sub>(L)<sub>2</sub>][PF<sub>6</sub>]<sub>2</sub> and *cis*-[Ru(*N-N'*)(L)X][PF<sub>6</sub>], where *N-N'* is 2,2'-bipyridine (bpy) or 1,10-phenanthroline (phen), L is isoniazid (INH) or nicotinamide (NA) (anti-tuberculosis compounds) and X is either Cl or I. Their dark solution chemistry was explored utilizing UV-visible spectroscopy and <sup>1</sup>H-NMR. Complexes *cis*-[Ru(bpy)<sub>2</sub>(INH)<sub>2</sub>][PF<sub>6</sub>]<sub>2</sub> (**4**), *cis*-[Ru(bpy)<sub>2</sub>(NA)<sub>2</sub>][PF<sub>6</sub>]<sub>2</sub> (**5**), *cis*-[Ru(phen)<sub>2</sub>(INH)<sub>2</sub>][PF<sub>6</sub>]<sub>2</sub> (**6**) and *cis*-[Ru(phen)<sub>2</sub>(NA)<sub>2</sub>][PF<sub>6</sub>]<sub>2</sub> (**7**) were stable in the dark in aqueous solution, however *cis*-[Ru(bpy)<sub>2</sub>(NA)Cl][PF<sub>6</sub>] (**1**) hydrolysed to form the aqua species *cis*-[Ru(bpy)<sub>2</sub>(NA)(H<sub>2</sub>O)]<sup>2+</sup>. Interestingly the presence of 5% DMF, 5% DMSO or 5% acetone resulted in the binding of the organic species, complicating the hydrolysis process. By <sup>1</sup>H-NMR, the rotation of the NA ligand in *cis*-[Ru(bpy)<sub>2</sub>(NA)Cl][PF<sub>6</sub>] (**1**) and *cis*-[Ru(bpy)<sub>2</sub>(NA)I][PF<sub>6</sub>] (**2**) was hindered on the NMR timescale (500 MHz) at 298 K, with two atropisomers observable at 185 K. Further investigations using Density Functional Theory (DFT) showed that the hindered rotation is due to hydrogen bonding between a NA proton and the halide. This may have implications if a biomolecule adds to the complex *cis*-[Ru(bpy)<sub>2</sub>(NA)(H<sub>2</sub>O)]<sup>2+</sup>, as the hindered rotation may affect the binding.

In Chapter 4, the photochemical and photophysical properties of **1** and **4** – **7** were explored by UV-visible spectroscopy, liquid chromatography (LC), time-dependent DFT (TD-DFT) and transient-absorption spectroscopy. The production of *cis*-[Ru(*N*-*N'*)<sub>2</sub>(L)(H<sub>2</sub>O)]<sup>2+</sup> after photoirradiation of **4** – **7** using a blue LED ( $\lambda_{\text{irr}} = 463 \text{ nm}$ ,  $50 \text{ mW cm}^{-2}$ ) in aqueous solution at 298 K was monitored by UV-visible spectroscopy. Complexes containing 1,10-phenanthroline (phen) were more photoactive than complexes containing 2,2'-bipyridine (bpy) (i.e. *cis*-[Ru(phen)<sub>2</sub>(NA)<sub>2</sub>][PF<sub>6</sub>]<sub>2</sub> (**7**) > *cis*-[Ru(bpy)<sub>2</sub>(NA)<sub>2</sub>][PF<sub>6</sub>]<sub>2</sub> (**5**) and *cis*-[Ru(phen)<sub>2</sub>(INH)<sub>2</sub>][PF<sub>6</sub>]<sub>2</sub> (**6**) > *cis*-[Ru(bpy)<sub>2</sub>(INH)<sub>2</sub>][PF<sub>6</sub>]<sub>2</sub> (**4**)) while complexes containing nicotinamide (NA) were more photoactive than complexes containing isoniazid (INH) (i.e. *cis*-[Ru(bpy)<sub>2</sub>(NA)<sub>2</sub>][PF<sub>6</sub>]<sub>2</sub> (**5**) > *cis*-[Ru(bpy)<sub>2</sub>(INH)<sub>2</sub>][PF<sub>6</sub>]<sub>2</sub> (**4**) and *cis*-[Ru(phen)<sub>2</sub>(NA)<sub>2</sub>][PF<sub>6</sub>]<sub>2</sub> (**7**) > *cis*-[Ru(phen)<sub>2</sub>(INH)<sub>2</sub>][PF<sub>6</sub>]<sub>2</sub> (**6**)). By utilizing TD-DFT, the following qualitative assessments were made; a) phen containing complexes observed a higher number of <sup>1</sup>MLCT states, possibly contributing to their increased photoactivity and b) the improved  $\pi$ -accepting properties of NA when compared to INH causes the dissociative <sup>3</sup>MC state to lower in energy in NA-containing complexes, thus increasing their photoactivity. Liquid chromatography-mass spectrometry (LC-MS) analysis showed that the photoproduction of *cis*-[Ru(bpy)<sub>2</sub>(H<sub>2</sub>O)<sub>2</sub>]<sup>2+</sup> from **4** was complicated by the photoisomerisation to *trans*-[Ru(bpy)<sub>2</sub>(H<sub>2</sub>O)<sub>2</sub>]<sup>2+</sup> and the resulting oxidation to *trans*-[Ru(bpy)<sub>2</sub>(H<sub>2</sub>O)(OH)]<sup>2+</sup>. Furthermore the production of *trans*-[Ru(bpy)<sub>2</sub>(H<sub>2</sub>O)<sub>2</sub>]<sup>2+</sup> was affected by the power of the light source.

In Chapter 5, the photobiological properties of **4** – **6** were explored by assessing their binding ability to L-cysteine and 9-ethylguanine, and investigating their activity *in vitro* against *E. coli*, *B. subtilis* and the *M. tuberculosis* model *M. smegmatis*. By <sup>1</sup>H-NMR, photoirradiating the complex *cis*-[Ru(bpy)<sub>2</sub>(INH)<sub>2</sub>][PF<sub>6</sub>]<sub>2</sub> (**4**) in the presence of

L-cysteine (in order to produce  $cis$ -[Ru(bpy)<sub>2</sub>(INH)(H<sub>2</sub>O)]<sup>2+</sup>) showed no binding, however in the presence of 9-ethylguanine (9-EtG) binding occurred to produce  $cis$ -[Ru(bpy)<sub>2</sub>(INH)(9-EtG)]<sup>2+</sup>. Interestingly, due to the bulky nature of 9-ethylguanine, different atropisomers were observable over a 24 h period at 298 K. Complex **4** was inactive against *E. coli* and only active in *B. subtilis* at concentrations ranging from 100 – 200 μM once photoactivated with blue light. When tested against *M. smegmatis*, complexes  $cis$ -[Ru(bpy)<sub>2</sub>(INH)<sub>2</sub>][PF<sub>6</sub>]<sub>2</sub> (**4**) and  $cis$ -[Ru(phen)<sub>2</sub>(INH)<sub>2</sub>][PF<sub>6</sub>]<sub>2</sub> (**6**) were both inactive in the dark with a bacterial survival of > 80 % at concentrations <10 μM. Once photoirradiated for 1 min with blue light, complexes **4** and **6** gave a minimum inhibitory concentration (MIC) of 4 μM and 8 μM, respectively, which is at least 3x the potency of the ligand alone (MIC of isoniazid is 22 μM). Interestingly the activity can be extended to green light. This proof-of-concept has shown that the isoniazid ligand can be successfully photoreleased from a ruthenium(II) complex *in vitro* and retain its activity. The complex  $cis$ -[Ru(phen)<sub>2</sub>(INH)<sub>2</sub>][PF<sub>6</sub>]<sub>2</sub> (**6**) was found to produce pores in the cell wall of *M. smegmatis* as was evident from the BacLight™ assay, while  $cis$ -[Ru(bpy)<sub>2</sub>(INH)<sub>2</sub>][PF<sub>6</sub>]<sub>2</sub> (**4**) does not, however this does not seem to affect the activity.

In Chapter 6, the complex  $cis$ -[Ru(bpy)<sub>2</sub>(MOPEP)<sub>2</sub>][PF<sub>6</sub>]<sub>2</sub> (**9**), where MOPEP is 4-[2-(4-methoxyphenyl)ethynyl]pyridine (MOPEP), was synthesised in an attempt to try and efficiently extend the photoactivation of the complex into the red region (>600 nm) by two-photon activation. Surprisingly the complex was found to be one-photon active with 600 nm and 800 nm light. This was due to the MOPEP ligand extending the absorption band shoulder of complex **9** to give an extinction coefficient of ~ 100 M<sup>-1</sup> cm<sup>-1</sup> at 700 nm.

## 7.2. Future work

This section highlights future research areas based on the complexes synthesised in this thesis either by modification of the chelating scaffold (Section 7.2.1. and 7.2.2.) or investigating the potential modes of action of ruthenium(II) polypyridyl complexes in bacteria (Section 7.2.3. and 7.2.4.).

### 7.2.1. Addition of an antibacterial scaffold

The work carried out here has shown that complexes *cis*-[Ru(bpy)<sub>2</sub>(INH)<sub>2</sub>][PF<sub>6</sub>]<sub>2</sub> (**4**) and *cis*-[Ru(phen)<sub>2</sub>(INH)<sub>2</sub>][PF<sub>6</sub>]<sub>2</sub> (**6**), where bpy is 2,2'-bipyridine, phen is 1,10-phenanthroline and INH is isoniazid, photoreleased INH using blue/green light and are active against *Mycobacterium smegmatis* after photoirradiation. Modification of the chelating ligand (bpy) may enhance further the activity of the complex.

The addition of a ferrocene substituent to chloroquine (currently used to treat malaria) affords a complex, Ferroquine, which is 22 times more potent than chloroquine itself against *Plasmodium falciparum* (causative agent of malaria).<sup>1</sup> Thus addition an existing drug to the scaffold of a metal complex can afford a complex with improved activity. Ascidiemin (ASC) is a natural product found be a “hit” in a screen of compounds against *Mycobacterium aurum* A<sup>+</sup> (a *Mycobacterium tuberculosis* model).<sup>2</sup> Although it is a natural product it can be synthesised in 3 steps.<sup>3</sup> ASC has a structure based on 1,10-phenanthroline, and therefore has a suitable structure to chelate to a metal. Synthesis of the complex *cis*-[Ru(ASC)<sub>2</sub>(INH)<sub>2</sub>]<sup>2+</sup>, where INH is isoniazid, may therefore afford a complex that has a triple action; 1) ASC scaffold may still have its pharmacophore exposed and thus retain its activity, 2) INH can be released by photoactivation and 3) the Ru(II) aqua species obtained after photoactivation may covalently bind to DNA and intercalate into DNA due to the

extended aromatic system of ASC. Interestingly attachment of ASC may afford three isomers, see Figure 7.1, due to the asymmetric nature of ASC. Such isomers have been explored in complexes of the type  $[\text{Ru}(\text{azpy})_2(\text{Cl})_2]$ , where azpy is 2-phenylazopyridine.<sup>4</sup>

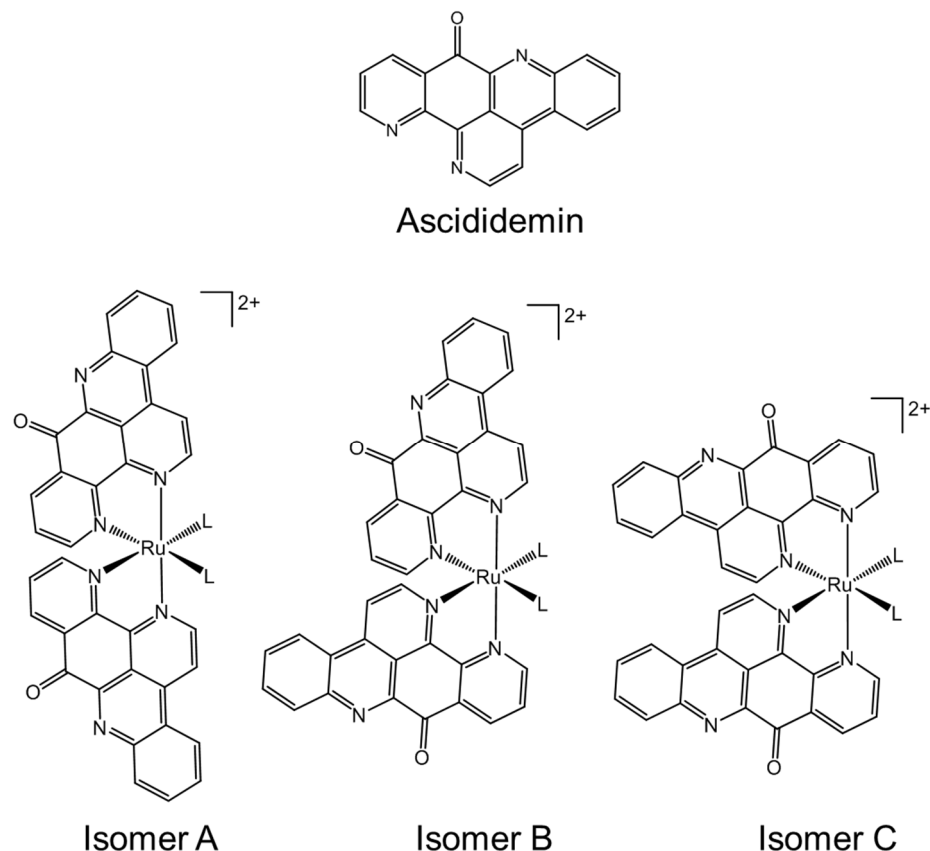


**Figure 7.1.** Structure of asciddemin (ASC) and potential isomers (only  $\Lambda$  enantiomers are shown) after coordination of ASC to ruthenium(II) to afford the complex  $\text{cis-}[\text{Ru}(\text{ASC})_2(\text{L})_2]^{2+}$ , where L is a pyridine based ligand.

### 7.2.2. Addition of red-light shifting moieties to the chelating scaffold

In Chapter 6 the addition of MOPEP, 4-[2-(4-methoxyphenyl)ethynyl]pyridine, as a monodentate ligand to give  $\text{cis-}[\text{Ru}(\text{bpy})_2(\text{MOPEP})_2][\text{PF}_6]_2$  (**9**) rendered the complex photoactive with 600 nm – 800 nm light. However this complex is limited by the fact that an existing biologically active ligand cannot be released from the structure by

light. Therefore substituents that shift the wavelength of activation could be attached to the chelating scaffold to allow the attachment and photorelease of biologically active ligands, see Figure 7.2. In the case of MOPEP this can be achieved synthetically by the same method as in Chapter 6, but with 4,4'-Dibromo-2,2'-bipyridine as the starting material.

Another methodology could be the attachment of a fluorophore that absorbs at  $>600$  nm. For example, the rhodamine B fluorophore was added to the chelating ligand of a Ru(II) complex so that low energy light (570 nm) can be efficiently harvested by the fluorophore and transferred to the Ru(II) complex via energy transfer.<sup>5</sup> BODIPY dyes (4,4-difluoro-4-bora-3a,4a-diaza-s-indacene) absorb at  $>500$  nm and possess a high quantum yield of fluorescence.<sup>6</sup> The complex  $[(\eta^6\text{-}p\text{-cymene})\text{Ru}(\text{bpy})(\text{BODIPY-py})]^{2+}$ , where BODIPY-py is BODIPY attached to pyridine, has been reported to photorelease BODIPY-py upon exposure to  $>500$  nm light.<sup>7</sup> It is proposed that BODIPY could be attached to the 2,2'-bipyridine ligand by a previously published one-pot method using 2,2'-bipyridine-4,4'-dicarboxaldehyde.<sup>8</sup>

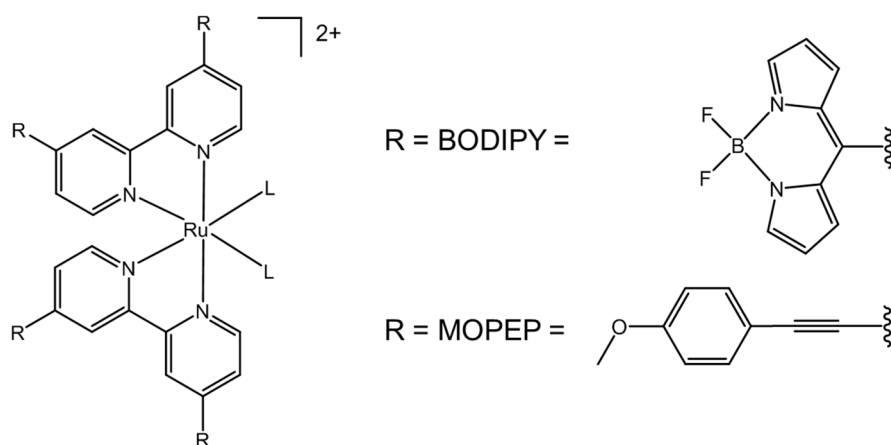


**Figure 7.2.** Structure of the proposed red-light shifting antennae (BODIPY and MOPEP) to be attached to the 2,2'-bipyridine scaffold.



### 7.2.3. Further biological testing

In Chapter 5 complexes *cis*-[Ru(bpy)<sub>2</sub>(INH)<sub>2</sub>][PF<sub>6</sub>]<sub>2</sub> (**4**) and *cis*-[Ru(phen)<sub>2</sub>(INH)<sub>2</sub>][PF<sub>6</sub>]<sub>2</sub> (**6**) were tested against *M. smegmatis* and were active with blue light. However the minimum inhibitory concentration (MIC) with green light should be assessed, along with finding the minimum time of photoirradiation to yield an appreciable MIC value (less than that for isoniazid). Additionally further studies need to elucidate which photoproduct is active. This may be accomplished by dosing the bacteria with pre-synthesised photoproducts, e.g. *cis*-[Ru(bpy)<sub>2</sub>(H<sub>2</sub>O)<sub>2</sub>]<sup>2+</sup>. However care needs to be taken as they may have different uptake mechanisms than the original complex and so may not be representative. Cell uptake experiments may help in this case, and would help to understand how much of the complex is taken up and if this needs to be improved by changing ligands around the metal. For example the attachment of an antibacterial peptide to the chelating ligand scaffold may enhance uptake and additionally provide another mechanism of action.<sup>9</sup>

Interestingly one avenue that could be explored is the potential binding of *cis*-[Ru(bpy)<sub>2</sub>(H<sub>2</sub>O)<sub>2</sub>]<sup>2+</sup> to hydrogenases. The complex [Ru(bpy)<sub>2</sub>(NH<sub>2</sub>phen)]<sup>2+</sup>, where NH<sub>2</sub>phen is 5-amino-1,10-phenanthroline, has been bound covalently to carboxylates on the surface of an hydrogenase from *T. roseopersicina* and was found to produce hydrogen by photoirradiation via the transfer of electrons from the Ru(II) complex to the hydrogenase.<sup>10</sup> However hydrogen production by a hydrogenase in *Mycobacterium smegmatis* has been linked to the long term survival of the bacterium in hypoxic conditions.<sup>11</sup> It would be interesting to investigate whether *cis*-[Ru(bpy)<sub>2</sub>(H<sub>2</sub>O)<sub>2</sub>]<sup>2+</sup> can bind to hydrogenase, and whether this would have a positive (i.e. disrupting the efficient functioning of hydrogenase) or negative effect (i.e. by aiding the production of H<sub>2</sub>) on the growth of *Mycobacteria*.

#### 7.2.4. Affecting the NADH/NAD<sup>+</sup> ratio by photoactive ruthenium(II) complexes

As mentioned previously in Chapter 1, the target of isoniazid is an enzyme called InhA, and isoniazid inhibits InhA by forming an adduct with NAD<sup>+</sup> (INH-NAD) that can competitively bind in place of NADH. Interestingly mutations in NADH hydrogenase (Ndh) in *Mycobacterium smegmatis* conferred resistance to isoniazid by increasing the intracellular ratio of NADH/NAD<sup>+</sup>, where excess NADH levels competitively inhibit the binding of INH-NAD adduct to InhA, see Figure 7.3.<sup>12-13</sup> For a detailed description of the mechanism of action of isoniazid see Chapter 1.

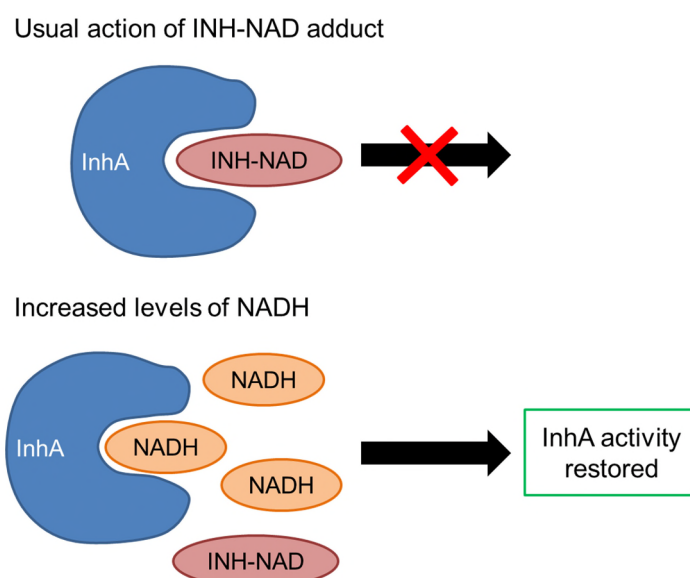


**Figure 7.3.** Diagram to depict the usual action of the INH-NAD adduct inhibiting the InhA enzyme (top) with the competitive binding of NADH when levels of NADH are increased restoring the activity of InhA (bottom).

Ruthenium(II) arene complexes, such as  $[(\eta^6\text{-hmb})\text{Ru}(\text{bpm})\text{Cl}]^+$  where hmb is hexamethylbenzene and bpm is 2,2'-bipyrimidine, aquate in aqueous solution to form the aqua complex  $[(\eta^6\text{-hmb})\text{Ru}(\text{bpm})(\text{H}_2\text{O})]^{2+}$  and can convert NADH to NAD<sup>+</sup> via metal-hydride formation.<sup>14</sup> Interestingly the pyridine (py) analogues, such as  $[(\eta^6\text{-hmb})\text{Ru}(\text{bpm})(\text{py})]^{2+}$ , are photoactive with visible light and release py to form the aqua

complex.<sup>15</sup> This methodology was used to oxidise NADH to NAD<sup>+</sup> by photoirradiating  $[(\eta^6\text{-hmb})\text{Ru}(\text{bpm})(\text{py})]^{2+}$  with UVA light (300 – 400 nm), however photodegradation of NADH by UVA light was potentially contributing to the conversion.<sup>16</sup> It is proposed that the synthesis of  $[(\eta^6\text{-hmb})\text{Ru}(\text{bpm})(\text{INH})]^{2+}$  may help to circumvent the issue of isoniazid resistance by initial photorelease of INH using visible light and formation of  $[(\eta^6\text{-hmb})\text{Ru}(\text{bpm})(\text{H}_2\text{O})]^{2+}$ , followed by oxidation of NADH to NAD<sup>+</sup> to circumvent isoniazid resistance if Ndh mutations are causing an excess of NADH. However one issue with this methodology is that Ru(II) arene complexes are most active with harmful UVA light, while visible light reactions require long irradiation times (in some cases up to 12 h).<sup>15</sup> Therefore another set of complexes could be synthesised based on  $[\text{Ru}(\text{bpy})(\text{terpy})(\text{py})]^{2+}$  (where terpy is 2,2':6',2''-terpyridine), as it was shown that upon photoirradiation with >500 nm light the complex can release py, form the aqua complex  $[\text{Ru}(\text{bpy})(\text{terpy})(\text{H}_2\text{O})]^{2+}$  and subsequently reduce a NAD model (1-benzyl-3-carbamoyl-pyridinium cation) by the formation of a metal-hydride species.<sup>17</sup> Both methodologies are shown in Figure 7.4A with the proposed mechanism of NADH oxidation in Figure 7.4B.

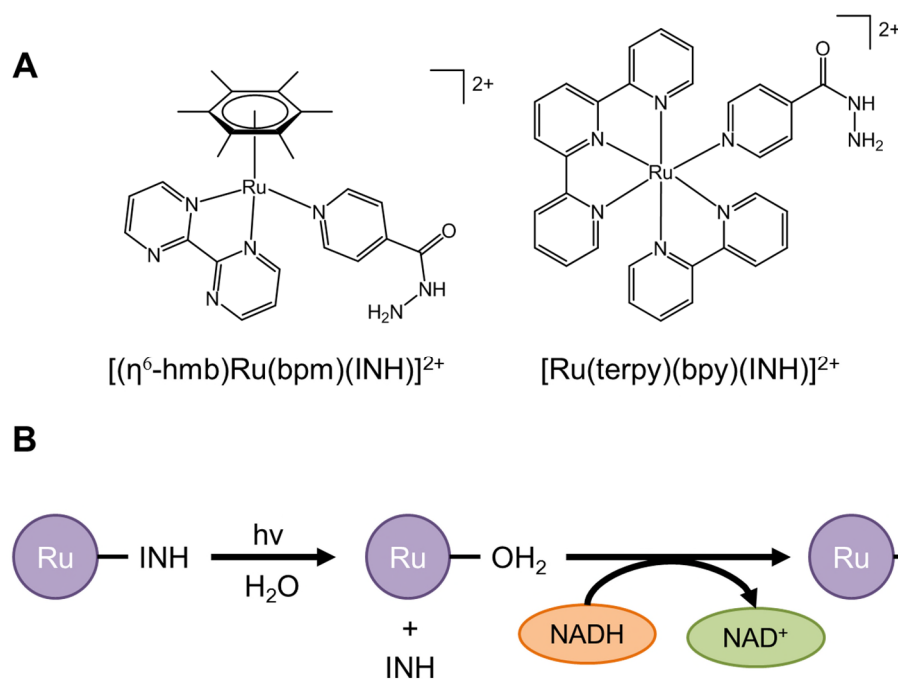


**Figure 7.4.** Structures of potential photoactive ruthenium(II) NADH oxidising agents (A) and proposed mechanism of action of such complexes (B)<sup>14</sup>.

## 7.5. References

1. Biot, C.; Glorian, G.; Maciejewski, L. A.; Brocard, J. S.; Domarle, O.; Blampain, G.; Millet, P.; Georges, A. J.; Abessolo, H.; Dive, D.; Lebibi, J. *J. Med. Chem.*, **1997**, 40 (23), 3715-3718.
2. Chung, G. A.; Aktar, Z.; Jackson, S.; Duncan, K. *Antimicrob. Agents Chemother.*, **1995**, 39 (10), 2235-8.
3. Yin, H.; Shan, N.; Wang, S.; Yao, Z.-J. *J. Org. Chem.*, **2014**, 79 (20), 9748-9753.
4. Krause, R. A.; Krause, K. *Inorg. Chem.*, **1980**, 19 (9), 2600-2603.
5. Bahreman, A.; Cuello-Garibo, J.-A.; Bonnet, S. *Dalton Trans.*, **2014**, 43 (11), 4494-4505.
6. Loudet, A.; Burgess, K. *Chem. Rev.*, **2007**, 107 (11), 4891-4932.

7. Zhou, Q.-X.; Lei, W.-H.; Hou, Y.-J.; Chen, Y.-J.; Li, C.; Zhang, B.-W.; Wang, X.-S. *Dalton Trans.*, **2013**, 42 (8), 2786-2791.
8. Bartelmess, J.; Weare, W. W. *Dyes Pigments*, **2013**, 97 (1), 1-8.
9. Bahar, A. A.; Ren, D. *Pharmaceuticals*, **2013**, 6 (12), 1543-1575.
10. Zadvornyy, O. A.; Lucon, J. E.; Gerlach, R.; Zorin, N. A.; Douglas, T.; Elgren, T. E.; Peters, J. W. *J. Inorg. Biochem.*, **2012**, 106 (1), 151-155.
11. Berney, M.; Greening, C.; Conrad, R.; Jacobs, W. R.; Cook, G. M. *Proc. Natl. Acad. Sci.*, **2014**, 111 (31), 11479-11484.
12. Vilchèze, C.; Weisbrod, T. R.; Chen, B.; Kremer, L.; Hazbón, M. H.; Wang, F.; Alland, D.; Sacchettini, J. C.; Jacobs, W. R. *Antimicrob. Agents Chemother.*, **2005**, 49 (2), 708-720.
13. Miesel, L.; Weisbrod, T. R.; Marcinkeviciene, J. A.; Bittman, R.; Jacobs, W. R. *J. Bacteriol.*, **1998**, 180 (9), 2459-2467.
14. Betanzos-Lara, S.; Liu, Z.; Habtemariam, A.; Pizarro, A. M.; Qamar, B.; Sadler, P. J. *Angew. Chem. Int. Ed.*, **2012**, 51 (16), 3897-3900.
15. Betanzos-Lara, S.; Salassa, L.; Habtemariam, A.; Novakova, O.; Pizarro, A. M.; Clarkson, G. J.; Liskova, B.; Brabec, V.; Sadler, P. J. *Organometallics*, **2012**, 31 (9), 3466-3479.
16. Betanzos-Lara, S. Design, Synthesis and Activation of Ruthenium Arene Anticancer Complexes. PhD Thesis, University of Warwick, 2010.
17. Ishitani, O.; Inoue, N.; Koike, K.; Ibusuki, T. *J. Chem. Soc., Chem. Commun.*, **1994**, (4), 367-368.